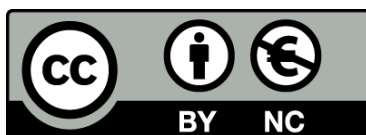




UNIVERSITAT_{DE}
BARCELONA

Catalyst and reactor design for carbon dioxide methanation

Andreina Alarcón Avellán



Aquesta tesi doctoral està subjecta a la llicència **Reconeixement- NoComercial 4.0. Espanya de Creative Commons**.

Esta tesis doctoral está sujeta a la licencia **Reconocimiento - NoComercial 4.0. España de Creative Commons**.

This doctoral thesis is licensed under the **Creative Commons Attribution-NonCommercial 4.0. Spain License**.

DOCTORAL THESIS

Catalyst and reactor design for carbon dioxide methanation

Author:

Andreina Alexandra Alarcón Avellán

Directors:

Dra. Teresa Andreu Arbella

Dr. Jordi Guilera Sala



UNIVERSITAT DE
BARCELONA

CATALYST AND REACTOR DESIGN FOR CARBON DIOXIDE METHANATION

Programa de Doctorado en Nanociencia

Autor:

Andreina Alexandra Alarcón Avellán

Directores:

Dra. Teresa Andreu Arbella

Dr. Jordi Guilera Sala

Tutor:

Dr. Joan Ramón Morante Leonart



UNIVERSITAT DE
BARCELONA



UNIVERSITAT DE
BARCELONA



Shaping Energy for a Sustainable Future

FACULTY OF PHYSICS

ENERGY STORAGE, HARVESTING
AND CATALYSIS GROUP

Catalyst and reactor design for carbon dioxide methanation

Andreina Alexandra Alarcón Avellán



Aquesta tesi doctoral està subjecta a la llicència Reconeixement-NoComercial 4.0. Espanya de Creative Commons.

Esta tesis doctoral está sujeta a la licencia Reconocimiento-NoComercial 4.0. España de Creative Commons.

This doctoral thesis is licensed under the Creative Commons Attribution-NonCommercial 4.0. Spain License.

Dra. Teresa Andreu Arbella, Lecturer professor at Department of Materials Science and Chemical Physics of the University of Barcelona.

Dr. Jordi Guilera Sala, Researcher at Catalonia Institute for Energy Research (IREC)

CERTIFY:

That the thesis entitled “**Catalyst and reactor design for carbon dioxide methanation**”, submitted by Andreina Alexandra Alarcón Avellán to apply for the degree of Doctor, in the Nanoscience Program from University of Barcelona, has been developed under their supervision in the Catalonia Institute for Energy Research (IREC).

Barcelona, January 2021

Andreina Alexandra Alarcón Avellán
Doctoral Student

Dra. Teresa Andreu Arbella
Director

Dr. Jordi Guilera Sala
Director

Acknowledgements

I would like to express my sincere gratitude to my research supervisors Dra. Teresa Andreu and Dr. Jordi Guilera. Thanks to both for giving me the opportunity to continue with my postgraduate studies at IREC and advising me on all aspects of my research work and thesis preparation. Thanks to Teresa for scientific advice and knowledge and for many insightful discussions and suggestions. Her sincerity, continuous motivation, and love for science and teaching have deeply inspired me. I am profoundly grateful to Jordi for his confidence and suggestion of this topic to me. His patient guidance in the interesting world of catalysis and reaction engineering and supervision in the laboratory have been fundamental during the development of this thesis. His willingness to share his knowledge and experience, and to give his time so generously has been very much appreciated. I only can say that it was a great privilege to work and study under their supervision.

I also wish to thank various people for their contribution to this thesis project: Dr. José A. Díaz for sharing his expertise and guiding me during his stay at IREC.; Dr. Rodrigo Soto for performing TEM and HRTEM images, for providing assistance and useful material for the image analysis, and for his enthusiastic encouragement and positive critiques to improve the manuscript.; to MSc. Jaime del Valle for his compromise and valuable work during his master's internship.; and, to Dr. Marco Argudo and Dra. Diouldé Sylla for their technical assistance with the materials characterization equipment and recommendation to carry out the measurements and to analyse data.

My grateful thanks are also extended to Dr.-Ing. Tim Böltken for giving the opportunity to become part of the INERATEC team as an international intern. Thanks to M.Sc.-Ing. Friedemann Timm for his supervision during my experimental study performed in the laboratory from the Institute for Micro Process Engineering (IMVT) at Karlsruhe Institute of Technology (KIT). This was an amazing experience that helped me to grow both professionally and personally.

I would like to acknowledge Escuela Superior Politecnica del Litoral (ESPOL) for providing the financial support for my PhD studies.

I would like to thank all members of ESEH group, who have worked at IREC since I started as a master's intern in 2017. To Felipe, Javier, Kele, Antonio, Jordi B., Jordi J., Nina, Sebastian, Paolo, Martí, Carles, Hemesh, Marisa, Viktoriia, Tandava, Marcelo, Monalisa and José Miguel for contributing to a relaxing working environment and for sharing special times outside IREC.

Special thanks to Viktoriia for being an unconditional friend. Thanks also to my Ecuadorian friends Mercedes and Emilia, for encouraging me and helping in everything. To Jacque, for sharing with me crazy travels and memorable adventures

during my holidays. Many thanks to my “Choco” Group for always being in contact with me despite the distance.

I am very grateful to my parents for their love, wise advice, and support during my postgraduate studies abroad. Thanks to my sister, for her optimism and constant encouragement, especially during these last months. I love them so much, and I would not have made it this far without them. This thesis is dedicated to my aunt Norma, who will always be in my thoughts.

Andreina Alarcón
Barcelona, January 2021

Index

List of acronyms and symbols	i
Preface	v
List of publications included in this thesis.....	viii
Author's contribution to the publications included in this thesis.....	ix
Summary of results	xi
Resumen de resultados	xiii
Chapter 1: General introduction	1
1. Synthetic natural gas production through CO ₂ methanation process.....	3
1.1. Fundamental concepts.....	6
1.1.1. Thermodynamics.....	6
1.1.2. Reaction mechanisms.....	11
1.1.3. Reaction kinetics	13
1.1.4. Transport phenomena limitations.....	16
1.1.5. Reactor design.....	17
1.1.6. Modelling of fixed-bed exchanger reactor technology	22
1.2. Catalyst design	24
1.2.1. Active phase.....	24
1.2.2. Catalyst support	26
1.2.3. Promoter	30
1.2.4. Preparation method	31
1.2.5. Shape and size	32
1.3. P2G experiences: Process strategies at lab, pilot and demo plant	33
1.4. Challenges	37
1.5. Scope of this research	40
1.6. References.....	41
Chapter 2: Design and optimization of micro-sized catalysts	47
2.1. Metal-oxide promoted Ni/Al ₂ O ₃ as micro-size catalysts	49
2.2. Optimization of nickel and ceria catalyst content	51

Chapter 3: Evaluation of the catalyst in relevant industrial environment	71
3.1. Higher tolerance to sulfur poisoning in CO ₂ methanation by the presence of CeO ₂	74
3.2. Pushing the limits of SNG process intensification: High GHSV operation at pilot scale	76
Chapter 4: Reactor design and modelling for SNG production	101
4.1. CO ₂ conversion to synthetic natural gas: Reactor design over Ni-Ce/Al ₂ O ₃ catalyst	104
4.2. An insight into the heat management for the CO ₂ methanation based on free convection	106
Chapter 5: Conclusions, outlook and recommendations	131
Appendix 1: Tables of the state-of-art of the proposed kinetic models and catalysts	139
Table A1.1. An overview of the Kinetic rate expressions of CO ₂ methanation on Ni-based catalysts	142
Table A1.2. A summary of the bimetallic catalysts	148
Table A1.3. A summary of the metal-supported catalysts	149
Table A1.4. A summary of the metal-oxide promoted Ni/Al ₂ O ₃ catalysts	157
Table A1.5. Preparation methods for the synthesis of Ni-based catalysts	158
Appendix 2: Supporting information	163
Curriculum vitae	209

List of acronyms and symbols

Abbreviations

RES	Renewable energy sources
P2G	Power-to-Gas
CAES	Compressed air energy storage
PHES	Pumped hydro energy storage
SNG	Synthetic natural gas
RWGS	Reverse water gas shift reaction
PL	Power-law
LHHW	Langmuir-Hinshelwood-Hougen-Watson
FIXBR	Fixed-bed reactor
FBR	Fluidized bed reactor
TPR	Three-phase reactor
MR	Microreactor
AFIXBR	Adiabatic fixed-bed reactor
CFIXBR	Cooled fixed-bed reactor
MFIXBR	Multitubular fixed-bed exchanger reactor
TFR	Three-phase reactor
SCBR	Slurry bubble column reactor
OCF	Open cell foam
Se	Semenov number
CFD	Computational fluid dynamics
GHSV	Gas hourly space velocity
OMA	Ordered mesoporous alumina
AC	Active carbon
CNTs	Nanotubes
SOGs	Surface oxygen groups
NPs	Nanoparticles
MOFs	Metal-organic frameworks
ATPG	Attapulguite
IWI	Incipient wetness impregnation
WI	Wet impregnation
DBD	Dielectric barrier discharge plasma
EISA	Evaporation-induced self-assembly
KIT	Karlsruhe Institute of Technology
ESC	Electrolyte supported cells
HEX	Heat exchanger
LMER	Laboratory for materials in renewable energy
COSYMA	Container-based system for methanation

REEs	Rare earth elements
LRREs	Light rare-earth elements
SEM	Scanning electron microscopy
TEM	Transmission electron microscopy
EDX	Energy dispersive x-ray spectrometer
BET	Brunauer-Emmett-Teller
BJH	Barrett-Joyner-Halenda
XRD	X-ray diffraction
ICDD	International centre for diffraction data
TCD	Thermal conductivity detector
H ₂ -TPR	Hydrogen-Temperature programmed reduction
TGA-DSC	Thermogravimetric analysis and differential scanning calorimetry
TPO	Temperature programmed oxidation
HRTEM	High-resolution transmission electron microscopy
FT	Fourier Transform
DRIFTS	Diffuse reflectance infrared Fourier transform spectroscopy
VOCs	Volatile Organic Compounds
CFD	Computational fluid dynamics
3D	Three-dimensional
3DFD	Three-dimensional fiber deposition
NIST	The National Institute of Standards and Technology

Greek symbols

$\gamma, \eta, \delta, \theta, \kappa, \alpha$ Phase of alumina

Subscripts and superscripts

atm	Atmosphere
*	Metallic site
ads	Adsorbed
cat.	catalyst

Nomenclature

Units

ΔH_R^{298K}	Enthalpy	[-kJ·mol ⁻¹]
ΔG_R^{298K}	Gibbs free energy	[-kJ·mol ⁻¹]
K	Equilibrium constant	[-]
T	Temperature	[K/°C]
R	Universal gas constant	[L·atm·mol ⁻¹ ·K ⁻¹]
n_i	Number of moles of species <i>i</i>	-
ΔG_i^0	Standard Gibbs free energy of formation of species <i>i</i>	[-kJ·mol ⁻¹]
P	Pressure	[atm/bar·g]

y_i	Mole fraction of species i in the gas mixture	[-]
$\hat{\Phi}_i$	Fugacity coefficient of species i in the gas mixture	[-]
X_{CO_2}	CO ₂ conversion	[%]
S_{CH_4}	CH ₄ selectivity	[%]
E_a	Activation energy	[-kJ·mol ⁻¹]
d_p	Particle diameter catalyst	[μm]
d_{pore}	Pore diameter catalyst	[nm]
GHSV	Gas hourly space velocity	[h ⁻¹]
$m_{\text{cat.}}$	Catalyst mass	[g]
$\rho_{\text{cat.}}$	Apparent bulk density	[g·mL ⁻¹]
F	Reactants stoichiometric mixture flow	[NmL·min ⁻¹]
T_{inlet}	Temperature of the gas inlet	[K]
T_{wall}	Temperature of the tube wall	[K]
T_{air}	Air temperature	[K]
T_{max}	Maximum temperature of the reaction	[K]
V_{inlet}	Velocity of the gas inlet	[m·s ⁻¹]
L	Reactor tube length	[mm]
d_i	Reactor tube inner diameter	[mm]



Preface

*Publications
and
summary of the thesis*

The work included in this PhD thesis covers part of the research developed between 2017 and 2020 by the PhD candidate Andreina Alexandra Alarcón Avellán at the Catalonia Institute for Energy Research – IREC, in Sant Adrià del Besòs, Barcelona. The research has been performed under the framework of the Nanoscience PhD program from University of Barcelona (UB) and funded by the CoSin project (COMRDI15-1-0037), LLAVOR project (LLAV-2018-00066) and the Walter Valdano Raffo program from Escuela Superior Politécnica del Litoral, Ecuador.

The research is focused on catalyst and reactor design for carbon dioxide methanation, especially on development of micro-size catalyst and fixed-bed reactor configurations. This dissertation covers all the aspects from catalyst synthesis, characterization, testing and implementation in relevant industrial environments to reactor design analysis, CFD modelling and experimental validation.

The thesis includes five chapters. In Chapter 1, a general introduction of the background is presented, and the objectives are formulated. The core of the dissertation, Chapters 2 to 4, are based on six peer-reviewed scientific articles, in which the PhD candidate is first author and co-author, in agreement with the requirements of the Nanoscience doctoral program of the University of Barcelona for a thesis presented as a compilation of publications. The main conclusions and future work are described in Chapter 5. Lastly, two appendixes are included at the final of the thesis. An overview of the kinetic models, catalysts and preparation methods reported for CO₂ methanation is presented in Appendix 1, while the supporting information of each scientific article is shown in Appendix 2.

List of publications included in this thesis

The research result in my PhD stage are listed in the following six peer-reviewed scientific articles:

1. Jordi Guilera, Jaime del Valle, **Andreina Alarcón**, José Antonio Díaz, Teresa Andreu. Metal-oxide promoted Ni/Al₂O₃ as CO₂ methanation micro-size catalysts. *Journal of CO₂ Utilization* 30, (2019) 11-17.
<https://doi.org/10.1016/j.jcou.2019.01.003>.
2. **Andreina Alarcón**, Jordi Guilera, José Antonio Díaz, Teresa Andreu. Optimization of nickel and ceria catalyst content for synthetic natural gas production through CO₂ methanation. *Fuel Processing Technology* 193, (2019) 114-122.
<https://doi.org/10.1016/j.fuproc.2019.05.008>.
3. **Andreina Alarcón**, Jordi Guilera, Rodrigo Soto, Teresa Andreu. Higher tolerance to sulfur poisoning in CO₂ methanation by the presence of CeO₂. *Applied Catalysis B: Environmental* 263, (2020) 118346.
<https://doi.org/10.1016/j.apcatb.2019.118346>.
4. **Andreina Alarcón**, Jordi Guilera, Teresa Andreu. CO₂ conversion to synthetic natural gas: reactor design over Ni–Ce/Al₂O₃ catalyst. *Chemical Engineering Research and Design* 140, (2018) 155-165.
<https://doi.org/10.1016/j.cherd.2018.10.017>.
5. Jordi Guilera, Tim Boeltken, Friedemann Timm, Ignasi Mallo, **Andreina Alarcón**, Teresa Andreu. Pushing the limits of SNG process intensification: high GHSV operation at pilot scale. *ACS Sustainable Chemistry & Engineering* 2020, 8, 22, 8409–8418.
<https://doi.org/10.1021/acssuschemeng.0c02642>.
6. **Andreina Alarcón**, Jordi Guilera, Teresa Andreu. An insight into the heat management for the CO₂ methanation based on free convection. *Fuel processing and Technology* 2020.
<https://doi.org/10.1016/j.fuproc.2020.106666>.

Author's contribution to the publications included in this thesis

The works presented in this thesis were carried out in the Energy Storage, Harvesting and Catalysis Group of the Catalonia Institute for Energy Research (IREC). None of these publications have been previously presented by other co-authors for their doctoral thesis. The contribution of thesis's author for each publication is shown below. Along with each publication, the impact factor and category by the Journal Citation Report (JCR) of the journal is also provided.

1. Metal-oxide promoted Ni/Al₂O₃ as CO₂ methanation micro-size catalysts.
 - Impact factor 2019: 5.189
 - 1st quartile in: Chemical engineering.
 - Andreina Alarcón contributed in the synthesis, performed material characterization, participated in results discussion and manuscript revision.
2. Optimization of nickel and ceria catalyst content for synthetic natural gas production through CO₂ methanation.
 - Impact factor 2019: 4.507
 - 1st quartile in Chemical engineering
 - Andreina Alarcón designed the experiments, performed the synthesis together with the material characterization. She also evaluated the catalytic activity and stability of the catalysts and wrote the manuscript.
3. Higher tolerance to sulfur poisoning in CO₂ methanation by the presence of CeO₂.
 - Impact factor 2020: 14.229
 - 1st quartile in: Catalyst
 - Andreina Alarcón designed the experiments, performed the synthesis together with material characterization. She also evaluated the catalytic activity and stability of the catalysts and wrote the manuscript.
4. Pushing the limits of SNG process intensification: high GHSV operation at pilot scale.
 - Impact factor 2020: 6.97
 - 1st quartile in: Chemical engineering
 - Andreina Alarcón performed the synthesis and the material characterization. She also performed preliminary catalytic test, participated in results discussion and manuscript revision.

5. CO₂ conversion to synthetic natural gas: reactor design over Ni–Ce/Al₂O₃ catalyst.
 - Impact factor 2018: 3.073
 - 1st quartile in: Chemical engineering
 - Andreina Alarcón designed the experiments, performed catalytic tests for the reaction kinetics, developed the computational fluid dynamics (CFD). She also performed simulation for optimization of the reactor design and wrote the manuscript.

6. An insight into the heat management for the CO₂ methanation based on free convection.
 - Impact factor 2020: 4.982
 - 1st quartile in: Chemical engineering
 - Andreina Alarcón designed the experiments, performed the synthesis and the catalytic tests. She also developed the computational fluid dynamics (CFD) model, performed the simulation and experimental validation of the proposed reactor design, and wrote the manuscript.

Dra. Teresa Andreu Arbella and Dr. Jordi Guilera Sala certify that the information provided above is true.

Barcelona, January 2021

Dra. Teresa Andreu Arbella
Director

Dr. Jordi Guilera Sala
Director

Summary of results

The transformation of the current energy model towards a more sustainable mix, independent of fossil fuels, requires the exploration of new technologies that are capable of taking advantage of excess electricity (e^-) derived from renewable energy sources (wind and solar) and to use new alternative sources of carbon (CO_2) for the generation and storage of clean fuels. An alternative that combines both is the Power-to-Gas (P2G) technology, whose concept is based on a two-stage process. In the first stage, excess electricity from renewable energies is converted to hydrogen by electrolysis. Then, in a second stage, the H_2 produced is transformed to CH_4 through methanation with CO_2 . The CH_4 produced is referred to as synthetic natural gas (SNG) and allows large amounts of renewable energy to be distributed from the energy sector to the end-use sectors.

The thermo-catalytic CO_2 methanation process, known as the Sabatier reaction, is considered the most efficient route for large-scale SNG production in P2G applications. However, developing a cost-effective CO_2 methanation technology is one of the biggest challenges facing the P2G concept. For CO_2 methanation, the use of a catalyst that is active and capable of working under moderate conditions for a long period of time is key to achieve an adequate reaction rate. Furthermore, a reactor that presents a simple configuration and is capable of controlling the high temperatures formed by the exothermic nature of the Sabatier reaction is required to avoid thermodynamic limitations and catalyst degradation. Both catalyst and reactor can be considered as the core of CO_2 methanation technology and are widely investigated to promote the intensification of the process.

In this context, this thesis focused on the design of a catalyst and a reactor for the production of SNG by means of CO_2 methanation. The thesis objectives were addressed in three main aspects, which are: i) design a high performance catalyst based on metal oxide promoted $\text{Ni}/\gamma\text{-Al}_2\text{O}_3$ and determine its reaction mechanism; ii) evaluate the stability of the catalyst and the tolerance to sulfur for its implementation in a relevant industrial environment (CoSin project); and finally, iii) develop a CFD model based on experimental kinetic data to understand the role of operating conditions and propose a new reactor configuration.

In the first Chapter of this thesis it is presented a general introduction of the SNG production through CO_2 methanation process. In the second Chapter, it is proposed a $\text{Ni}/\gamma\text{-Al}_2\text{O}_3$ promoted metal oxide catalyst. The addition of a promoter (X: CeO_2 , La_2O_3 , Y_2O_3 , Sm_2O_3 or ZrO_2) on a system composed by Ni as active phase and $\gamma\text{-Al}_2\text{O}_3$ microspheres ($d_p=400\text{-}500\ \mu\text{m}$) as support was studied as the design strategy to develop a micro-sized $\text{Ni-X}/\gamma\text{-Al}_2\text{O}_3$ catalyst. The effect of promoters was studied in a temperature range of $250\text{-}350\ \text{°C}$ to select the most interesting metal-oxide. The ternary catalyst based on $\text{Ni-CeO}_2/\gamma\text{-Al}_2\text{O}_3$ was proposed as the most feasible due to

its high catalytic performance in relation to its economic competitiveness. In order to find the optimal composition for Ni-CeO₂/γ-Al₂O₃, the simultaneous optimization of its components was evaluated through a systematic experimental design. The catalyst composed by 25 wt.% Ni, 20 wt.% CeO₂ and 55 wt.% γ-Al₂O₃ proved to be the most active and stable using moderate reaction conditions (T=300 °C, P=5 bar·g and GHSV=40,000 h⁻¹). The successful performance of the micro-sized catalyst was attributed to its enhanced Ni dispersion and reduction, its high metallic area, and the formation of moderate base sites.

In Chapter three, the thermal stability and tolerance to sulfur impurities on the Ni/γ-Al₂O₃ catalyst promoted with CeO₂ is further studied using the following reaction conditions: i) high temperatures (T=500 °C), and ii) the presence of H₂S on the reactants (1-5 ppm). The catalytic results showed that Ni-CeO₂/γ-Al₂O₃ was capable of maintaining high thermal stability and greater tolerance of H₂S compared to a conventional Ni/γ-Al₂O₃ catalyst. The strong metal-promoter interaction and the favourable formation of cerium oxide sulfide (Ce₂O₂S) were revealed as the main causes of its successful stability and tolerance to H₂S, respectively. Additionally, it was evaluated the technical feasibility of the implementation of Ni-CeO₂/γ-Al₂O₃ (105 g) on microstructured reactors in a two-stage industrial methanation process, CoSin project. The desired gas composition (≥92.5% CH₄) at the outlet of the second microreactor was successfully obtained using a pressure of 5 bar·g and a decreasing temperature profile in both the first (T=450-400 °C) and the second microreactor (T=375-275 °C). The high stability recorded during the 2000 h of experimentation demonstrated that Ni-CeO₂/γ-Al₂O₃ can be a competitive catalyst for CO₂ methanation.

Regarding to reactor design, in Chapter four, the design of a fixed-bed multitubular reactor on a Ni-CeO₂-Al₂O₃ catalyst was proposed for mid-scale SNG production. A CFD mathematical model based on experimental kinetic data was developed. The optimization of the temperature profile in the reactor tube was carried out through a sensitivity analysis. A reactor tube with a diameter of 9.25 mm and a length of 250 mm was proposed, which should be operated at T_{inlet}=473 K, T_{wall}=373 K, GHSV=14,400 h⁻¹ and P=5 atm. At these conditions, CO₂ conversions of 99% were achieved with T_{max} of 673 K. On the other hand, for small-scale SNG production, a reactor with a heat management approach based on free convection was proposed. The pre-evaluation of the reactor design (di=4.6 mm and L=250 mm) through experiments and the optimization of the reaction conditions (GHSV, T_{inlet}, P, T_{air}) through a CFD mathematical model were carried out using the micro-sized Ni-CeO₂/γ-Al₂O₃. The optimal conditions were found at: GHSV=11,520 h⁻¹, T_{inlet}=503 K, P=5 atm, and T_{air}=298 K. The feasibility of the reactor proposal was experimentally validated. As results, a competitive conversion (X_{CO₂}=93%) was obtained with a decreasing temperature profile (T=830-495 K).

Resumen de resultados

La transformación del modelo energético actual hacia un mix más sostenible, independiente de los combustibles fósiles, requiere la exploración de nuevas tecnologías que sean capaces de aprovechar el exceso de electricidad (e^-) derivado de fuentes de energía renovables (eólica y solar) y utilizar nuevas fuentes alternativas de carbono (CO_2) para la generación y almacenamiento de combustibles limpios. Una alternativa que combina ambas es la tecnología Power-to-Gas (P2G), cuyo concepto se basa en un proceso de dos etapas. En la primera etapa, el exceso de electricidad procedente de energías renovables se convierte en hidrógeno por electrólisis. Luego, en una segunda etapa, el H_2 producido se transforma en CH_4 mediante metanación con CO_2 . El CH_4 producido se conoce como gas natural sintético (SNG) y permite distribuir grandes cantidades de energía renovable desde el sector energético a los sectores de uso final.

El proceso termo-catalítico de metanación de CO_2 , conocido como la reacción de Sabatier, se considera la ruta más eficiente para la producción de SNG a gran escala en aplicaciones P2G. Sin embargo, el desarrollo de una tecnología de metanación de CO_2 rentable es uno de los mayores desafíos que enfrenta el concepto P2G. Para la metanación de CO_2 , en miras a lograr una velocidad de reacción adecuada, es clave el empleo de un catalizador que sea activo y capaz de trabajar en condiciones moderadas durante un largo período de tiempo. Además, se requiere un reactor que presente una configuración simple y sea capaz de controlar las altas temperaturas generadas por la naturaleza exotérmica de la reacción de Sabatier, evitando así limitaciones termodinámicas y la degradación del catalizador. Tanto el catalizador como el reactor pueden ser considerados como el núcleo de la tecnología de la metanación de CO_2 y aún se investigan para promover la intensificación del proceso.

En este contexto, la presente tesis se enfocó en el diseño de un catalizador y un reactor para la producción de SNG mediante la metanación de CO_2 . Los objetivos abordaron tres aspectos principales, los cuales fueron: i) diseñar un catalizador de alto rendimiento basado en $\text{Ni}/\gamma\text{-Al}_2\text{O}_3$ promovido por óxido metálico y determinar su mecanismo de reacción; ii) evaluar la estabilidad del catalizador y la tolerancia al azufre para su implementación en un entorno industrial relevante (proyecto CoSin); y finalmente, iii) desarrollar un modelo CFD basado en datos cinéticos experimentales para comprender el papel de las condiciones de operación y proponer una nueva configuración de reactor.

En el primer Capítulo de esta tesis se presenta una introducción general de la producción de SNG mediante el proceso de metanación de CO_2 . En el segundo Capítulo, se propone un catalizador de $\text{Ni}/\gamma\text{-Al}_2\text{O}_3$ promovido por óxido metálico. Se estudió la adición de un promotor (X: CeO_2 , La_2O_3 , Y_2O_3 , Sm_2O_3 ó ZrO_2) en un sistema compuesto por Ni como la fase activa y micro-esferas de $\gamma\text{-Al}_2\text{O}_3$ ($d_p=400\text{-}500\ \mu\text{m}$)

como el soporte se estudió como la estrategia de diseño para desarrollar un microcatalizador ($\text{Ni-X}/\gamma\text{-Al}_2\text{O}_3$). Se estudió el efecto de los promotores en un rango de temperatura de 250-350 ° C para seleccionar el óxido metálico más interesante. El catalizador ternario basado en $\text{Ni-CeO}_2/\gamma\text{-Al}_2\text{O}_3$ se propuso como el más factible por su alto rendimiento catalítico en relación a su competitividad económica. Con la finalidad de encontrar la composición óptima para el $\text{Ni-CeO}_2/\gamma\text{-Al}_2\text{O}_3$, se evaluó la simultánea optimización de sus componentes mediante un diseño experimental sistemático. El catalizador compuesto por 25 wt.% Ni, 20 wt.% CeO_2 y 55 wt.% $\gamma\text{-Al}_2\text{O}_3$ demostró ser el más activo y estable usando condiciones de reacción moderadas ($T=300$ °C, $P=5$ bar g y $\text{GHSV}=40,000$ h^{-1}). El exitoso rendimiento del microcatalizador se atribuyó a su alta dispersión y reducción de Ni, a su alta área metálica, y a la formación de sitios básicos moderados.

En el Capítulo tres, se estudia la estabilidad y tolerancia al azufre sobre el catalizador de $\text{Ni}/\gamma\text{-Al}_2\text{O}_3$ promovido con CeO_2 usando las siguientes como condiciones de reacción: i) altas temperaturas ($T=500$ °C), y ii) la presencia de impurezas de H_2S en los reactivos (1-5 ppm). Los resultados catalíticos mostraron que el $\text{Ni-CeO}_2/\gamma\text{-Al}_2\text{O}_3$ es capaz de mantener una alta estabilidad y mayor tolerancia de H_2S en comparación a un catalizador convencional de $\text{Ni}/\gamma\text{-Al}_2\text{O}_3$. La fuerte interacción metal-promotor y la formación favorable de sulfuro de óxido de cerio ($\text{Ce}_2\text{O}_2\text{S}$) se revelaron como las causas principales de su exitosa estabilidad y tolerancia a la impureza de H_2S , respectivamente. Adicionalmente, se evaluó la viabilidad técnica de la implementación del $\text{Ni-CeO}_2/\gamma\text{-Al}_2\text{O}_3$ (105 g) en reactores microestructurados que formaban parte de un proceso industrial de dos etapas, proyecto CoSin. A la salida del segundo microreactor, se obtuvo con éxito la composición de gas deseada ($\geq 92.5\%$ CH_4) utilizando una presión de 5 bar g y un perfil de temperatura decreciente tanto en el primero ($T=450\text{-}400$ °C) como en el segundo microreactor ($T=375\text{-}275$ °C). La alta estabilidad registrada durante las 2000 h de experimentación demostró que el $\text{Ni-CeO}_2/\gamma\text{-Al}_2\text{O}_3$ es un catalizador competitivo para la metanación de CO_2 .

Con respecto al diseño del reactor, en el Capítulo cuatro, se propone el diseño de un reactor multitubular de lecho fijo sobre un catalizador de $\text{Ni-CeO}_2\text{-Al}_2\text{O}_3$ para la producción SNG a mediana escala. Se desarrolló un modelo matemático CFD basado en datos cinéticos experimentales. La optimización del perfil de temperatura en el tubo del reactor se realizó mediante un análisis de sensibilidad. Se propuso un tubo de reactor con un diámetro de 9.25 mm y una longitud de 250 mm, el cual debe ser operado a $T_{\text{inlet}}=473$ K, $T_{\text{wall}}=373$ K, $\text{GHSV}=14,400$ h^{-1} y $P=5$ atm. A estas condiciones, se lograron conversiones de 99% con una T_{max} de 673 K. Por otro lado, para la producción de SNG a pequeña escala, se propuso un reactor con un enfoque de gestión de calor basado en la convección libre. La pre-evaluación del diseño del reactor ($d_i=4.6$ mm y $L=250$ mm) mediante experimentos y la optimización de las condiciones de reacción mediante un modelo matemático CFD se realizaron usando

el microcatalizador de Ni-CeO₂-Al₂O₃. Las condiciones óptimas se encontraron a: GHSV=11,520 h⁻¹, T_{inlet}=503 K, P=5 atm, y T_{air}=298 K. La viabilidad de la propuesta de reactor se validó experimentalmente. Como resultado, se obtuvo una competitiva conversión (X_{CO2}=93%) con un perfil de temperatura decreciente (T=830-495 K).

Chapter

General Introduction

1. Synthetic natural gas production through CO₂ methanation process

The use of energy throughout human history has been linked to all phases of global development [1]. Most of the energy that is used to power modern civilizations has been derived from the chemical energy found in fossil fuels (oil, coal, and natural gas), which benefits from their high energy density, low cost and ease of access. At the present time, these fossil resources represent the 85% of the global primary energy [2]; however, they have negative impacts on the environment and human health. Fossil fuels are the largest source of carbon dioxide (CO₂), a greenhouse gas which contributes to global warming and climate change. Without CO₂ mitigation, the average temperature on the planet may increase as much as three to five degrees Celsius in this century, according to the Intergovernmental Panel on Climate Change [3]. These concerns are triggering the world must balance the role of energy in social and economic development; with the need to decarbonise, reduce our dependence on fossil fuels, and transition towards low-carbon energy sources.

Renewable energy sources (RES), such as solar and wind are practically CO₂-neutral, and they play a key role in the shift towards green growth, a low-carbon economy, and a greater share of renewables in the energy mix [4]. However, due to their variable and unpredictable nature, the integration of both solar and wind energy into the electricity grid is a challenge, since the existing grids and their capacities were established to comply with less or non-variable energy sources, dispatchable power generation, and predictable load peaks. Consequently, long term and large capacity electricity storage is required, as well as reserve production capacity [5].

Several options have been proposed for large-scale energy storage, including flywheels, batteries, pumped hydro energy storage, compressed air energy storage and thermochemical energy storage. Compared to all storage technologies (see Figure 1.1), chemical energy storage in the form of synthetic gas (as methane (CH₄)) produced via Power-to-Gas technologies (P2G) has the greatest potential for the seasonal energy storage of low-carbon electricity [6–8]. Indeed, CH₄ caverns can store approximately 1000 kWh·Nm⁻³ at 100 atm, while compressed air has a significantly lower energy density of 0.4–20 kWh·Nm⁻³ and pumped hydro can only store 0.5–1.3 kWh·Nm⁻³. This latter is also limited by geographical constraints and it is preferentially used for weekly storage. Therefore, P2G technology can be considered an energy-efficient approach that offers a wide opportunity for conserving primary energy sources as well as reducing greenhouse gas emissions.

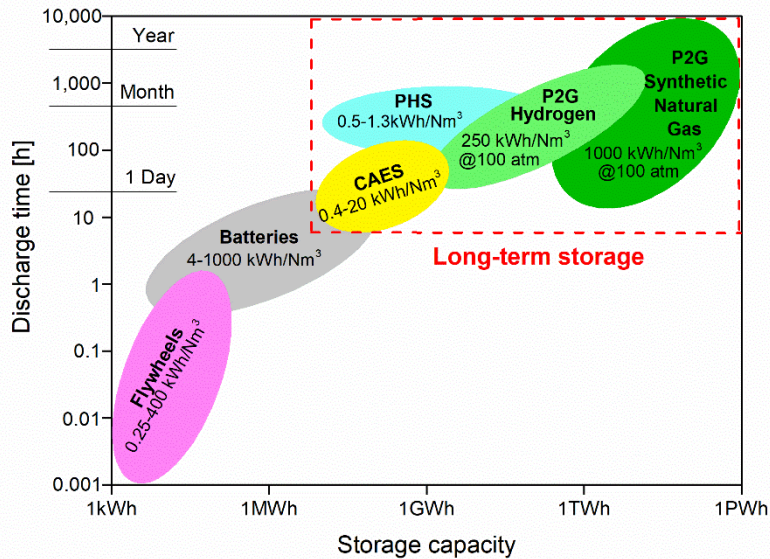


Figure 1.1. Comparison of electricity storage technologies in terms storage capacity, discharge time and energy density. Adapted from Anajovic et al. [9]. CAES=compressed air energy storage, PHES=pumped hydro energy storage, P2G=power-to-gas.

The P2G concept relies on the ability to transform the supply electrical energy from RES into valuable energy carries by means of 1-step process (Power-to-Hydrogen) or 2-step processes (Power-to-Methane), as it is shown Figure 1.2. In the 1-step process, the electricity excess is used to split water into hydrogen (H_2) and oxygen (O_2) through electrolysis. Consecutively, the produced renewable H_2 is combined with CO_2 to produce CH_4 through methanation process. In this 2-step process, the sources of CO_2 used as feedstock are derived from power plants (coal or natural gas), industries (cement, steel, chemical, etc.), biogenic sources (biogas produced from organic waste, bioethanol fermentation, biomass combustion, etc.) and direct air capture. The produced methane is also known as synthetic natural gas (SNG). Compared to hydrogen which requires specialized infrastructure, if the SNG composition meets the gas quality requirements of the natural gas grid (e.g. $\geq 95\%$ for Spain), it could be directly injected into a natural gas pipeline at the point of production. In addition, the SNG can be stored for long-term (days, weeks, or even months), used in the transportation sector and burned for heat and power production.

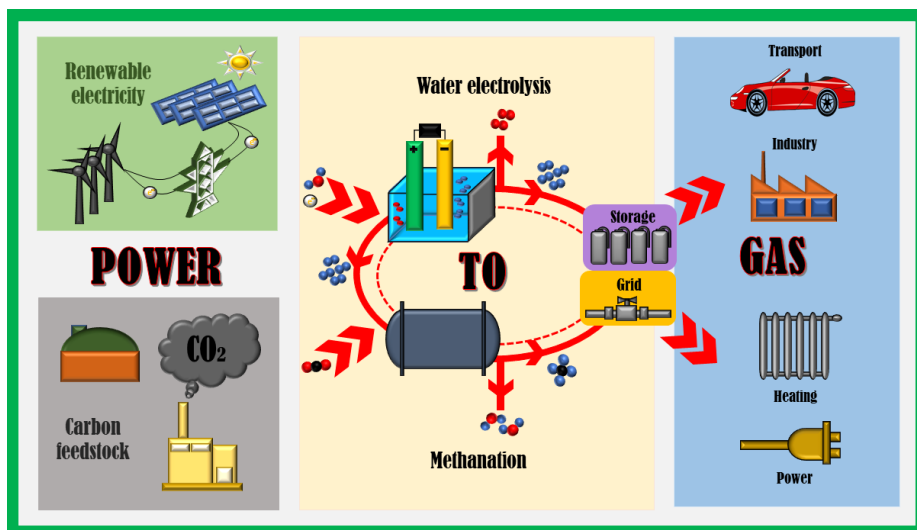


Figure 1.2. Schematic illustration of the Power-to-Gas concept for synthetic natural gas production.

Thermochemical, biological, plasmolysis, electrochemical and photoelectrochemical are the main methanation technologies proposed for the production of synthetic natural gas [10–13]. Among them, thermochemical CO₂ methanation process via Sabatier reaction is the most mature and intensive technology for P2G plants at industrial scale [14,15]. In the thermochemical route, high volumetric productivity can be reached in comparison with another technologies (e.g. biological [16]). This process is very old, since the CO₂ methanation reaction was already proposed by the French chemistry Paul Sabatier and Jean-Baptiste Senderens in 1902 [17]. In the context P2G, Sabatier reaction is typically conducted on a catalytic reactor under moderate temperature and pressure, in which H₂ and CO₂ react over a catalytic metal-based system to form CH₄ and H₂O, as it is shown in Figure 1.3.

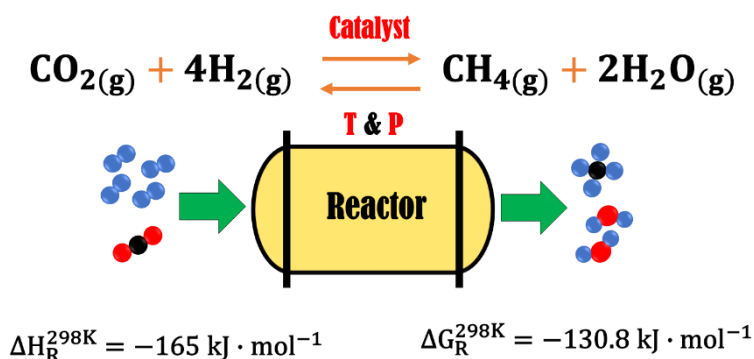


Figure 1.3. Schematic illustration of the thermochemical CO₂ methanation process.

The overall Sabatier reaction is reversible, highly exothermic and characterized by a volume reduction of 40% of the reacting gases. Thermodynamically, the reaction is highly favourable because of its large negative values of enthalpy ($\Delta H_R^{298K} = -165 \text{ kJ} \cdot \text{mol}^{-1}$) and Gibbs free energy ($\Delta G_R^{298K} = -130.8 \text{ kJ} \cdot \text{mol}^{-1}$). However, the involvement of eight-electrons in the process makes it kinetically limited [18]. Accordingly, an active and stable metal-based catalytic system needs to be utilized to attain an acceptable reaction rate and methane selectivity. Since the reaction has an exothermic nature, a reactor design with a proper temperature control is mandatory to avoid backwards reaction and catalysts deactivation. According to Le Chatelier's principle, low temperatures and high pressures shift the equilibrium to the products side. Consequently, a balance between thermodynamic and kinetic barriers should be found in order to guarantee an efficient methane production via thermochemical CO₂ methanation technology. This requirement imposes high challenges: i) on the development of innovative heterogeneous catalytic systems with proficient catalytic performance, high stability and tolerance to impurities; and, ii) on the proposal of advanced reactors with novel thermal approaches to manage the heat released by the reaction during the Sabatier process.

In this context, the aim of this introduction is to present current academic and industrial progress of the CO₂ methanation process with a special interest to the main aspects to drive CO₂ methanation technology to widespread applications. Therefore, fundamentals of the CO₂ methanation reaction, strategies applied to design high-active and stable CO₂ methanation catalysts are reviewed. Finally, CO₂ methanation reactor configuration and implementation strategies were analysed, as well as future prospective challenges for efficient and scalable CO₂ methanation technology are discussed.

1.1. Fundamental concepts

1.1.1. Thermodynamics

The CO₂ methanation process carried out through the exothermic Sabatier reaction (Eq. 1) occurs in a parallel combination between the endothermic reverse water gas shift reaction (RWGS) (Eq. 2) and the exothermic CO methanation reaction (Eq. 3).



Under certain process conditions, the formation of carbon over catalyst surface can be derived from by-reactions, such as: the exothermic Boudouard reaction (Eq. 4), the endothermic methane cracking reaction (Eq. 5), the exothermic CO reaction (Eq. 6) and the exothermic CO₂ reduction reaction (Eq. 7).



Besides carbon, the formation of saturated hydrocarbons can occur according to the following reactions (Eq. 8 and 9):



In order to analyse the thermodynamics of the main reactions involved in the CO₂ methanation process, Van't Hoff equation (Eq. 10) was used to calculate equilibrium constants (*K*) for each reaction in function of temperature.

$$\frac{d(\ln(K))}{dT} = \frac{\Delta H_{\text{R}}}{RT^2} \quad \text{Eq. 10}$$

where *T* is the temperature, Δ*H_R* the molar enthalpy changes of reaction at temperature *T*, and *R* the gas constant. According to values of $\frac{d(\ln(K))}{dT}$, reaction can be classified as either spontaneous or not-spontaneous:

- If $\frac{d(\ln(K))}{dT} < 0$, reaction is favourable or spontaneous
- If $\frac{d(\ln(K))}{dT} > 0$, reaction is unfavourable or not spontaneous

Figure 1.4 shows the equilibrium constant values of the main reactions involved in the CO₂ methanation process as a function of temperature. As it can be observed, the catalytic hydrogenation of CO₂ to CH₄ through both exothermic reactions (Eq. 1 and Eq. 3) is favourable when temperature decreases. In particular, CH₄ formation by Eq. 1 is promoted in the temperature range from 473-823 K. A further increase on the temperature (*T* ≥ 823 K) is unfavourable for the process since Eq. 2 is more dominate and promotes the formation of CO. With respect to the set of by-reactions (Eq. 4-7), Eq. 4, 6 and 7 are favoured at low temperatures, while Eq. 5 is favoured at high temperatures. Besides, it can be seen that the Eq. 4 has an equilibrium constant much larger than Eq. 5, 6, and 7. Therefore, it is necessary to consider that the Boudouard reaction lies in the temperature range where the conversion of CO₂ to CH₄ is favoured.

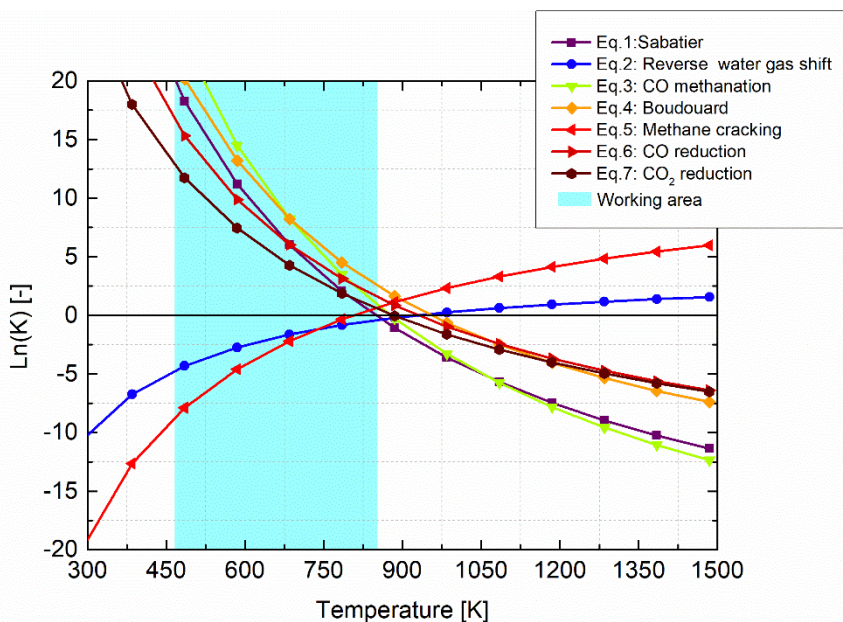


Figure 1.4. The equilibrium constant (K) of the possible reactions involved in methanation process as a function of temperature. The values calculated were based on thermochemical data in gas and solid phase of the main species (H_2 , CO_2 , CH_4 , H_2O , CO and C) [19] and using the Van't Hoff equation: $d(\ln(k))/dT = \Delta H_R/RT^2$.

Temperature reaction is not the only important parameter to evaluate the CO_2 methanation process. According to thermodynamics, the equilibrium of the Sabatier process in regard to CO_2 conversion, selectivity and yield to CH_4 , CO and C can be also influenced by the effects of the pressure, the H_2/CO_2 molar ratio and the addition of other reactants (e.g. H_2O and CH_4). The minimization of the Gibbs free energy of the system is a non-stoichiometric method can be applied to calculate the equilibrium composition of the chemical species in a reactive system. This method is based on the principle that the total Gibbs energy of the system has its minimum value at chemical equilibrium, and only requires the definition of all the chemical species involved in the process (both reactants and products).

In this line, thermodynamic calculations using a Gibbs energy minimization model were performed to understand the potential behaviour of the Sabatier process. The model was developed in excel and its minimization was executed using a Solver plugin with GRG nonlinear optimizer [20]. The thermochemical data in gas and solid phase of the main species (H_2 , CO_2 , CH_4 , H_2O , CO and C) was used to calculate the Gibbs free energy [19]. The Gibbs function (Eq. 11) as a function of pressure and temperature can be written follows as:

$$nG(T, P) = \sum n_i \Delta G_i^0 + \sum n_i RT \ln P + \sum n_i RT y_i + \sum n_i RT \ln \hat{\Phi}_i \quad \text{Eq. 11}$$

where n_i is the number of moles of species i , ΔG_i^0 is the standard Gibbs free energy of formation of species i , R is the universal gas constant, P is the total pressure of the gas mixture, y_i is the mole fraction of species i in the gas mixture, $\hat{\Phi}_i$ is the fugacity coefficient of species i in the gas mixture. The equilibrium model results shown below were in concordance with previous reported thermodynamic equilibrium analysis [21–26].

The CO_2 equilibrium conversions and selectivities to CH_4 , CO and C as a function of temperature at pressures between 1 and 30 atm and using a $\text{H}_2/\text{CO}_2=4$ are presented in Figure 1.5. CO_2 conversions ($X_{\text{CO}_2} \geq 95\%$) close to equilibrium can be obtained at low temperatures ($T \leq 623$ K) and high pressures ($P > 1$ atm) (see Figure 1.5 (a)). However, high operating pressures ($P \geq 20$ atm) are neither technically nor economically feasible, and low operating temperatures ($T \leq 473$ K) require highly active metal-based catalytic systems. In contrast, high temperatures ($T \geq 823$ K) shift the equilibrium to the reactants side, leading to the reduction of CO_2 conversions. Besides, at this condition the carbon monoxide (CO) is promoted by RWGS reaction. Consequently, higher CO selectivities and lower CH_4 selectivities are obtained (see Figure 1.5 (b)).

Regarding H_2/CO_2 effects, carbon formation is not expected at a H_2/CO_2 molar ratio of 4 (see Figure 1.5 (b)). A similar trend was observed by Gao et al. [21], who also claimed that the catalyst deactivation by carbon deposition is strongly influenced when the hydrogenation of CO_2 is performed at low molar ratios ($\text{H}_2/\text{CO}_2 < 4$) and using temperatures below 823 K. In addition, it was informed that a H_2/CO_2 molar ratio above 4 increase the selectivity to hydrogen-rich species (methane) with a decrease in coke as hydrogen is a well-known coke removing agent [22]. From thermodynamic point of view, a H_2/CO_2 molar ratio of 4, low temperatures (473-623 K) and high pressures (1-30 atm) should be considered as the operating window to achieve an efficient methane production during the CO_2 methanation process.

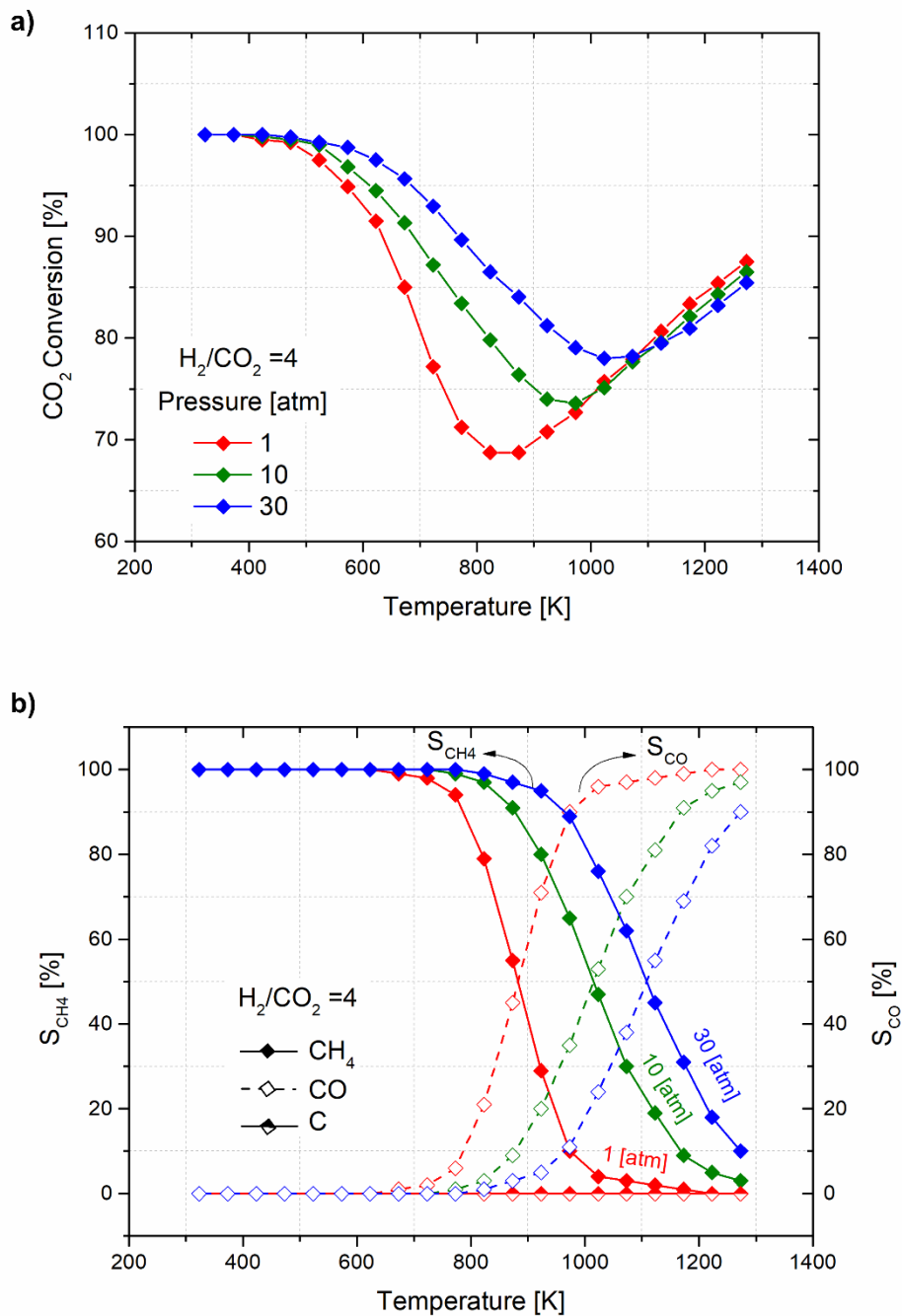


Figure 1.5. a) CO₂ equilibrium conversions and b) selectivities to CH₄, CO and C as a function of temperature at pressures between 1 and 30 atm and using a H₂/CO₂=4.

1.1.2. Reaction mechanisms

Although the methanation process has been investigated extensively for many years, the elementary steps involved in the overall Sabatier reaction catalysed by metals remain controversial. In view of the studies reported to date over Ni-based catalyst (see Table 1.1), reaction mechanisms for the hydrogenation of CO₂ can be classified in three main types (see Figure 1.6):

- **Dissociative mechanism**, where the dissociation of CO₂ to CO_{ads} (CO₂+**→CO*+O*) and the dissociation of CO_{ads} to C_{ads} (CO*+*→C*+O*) are identified as the rate-limiting step for CH₄ formation.
- **Associative mechanism**, where the formation of formates (CO₂*+H*→HCOO*+*) is recognized as the rate-limiting step.
- **Hybridized mechanism**, where a mixture between the two previous ones is considered.

The hydrogenation of CO₂ via dissociative mechanism occurs on the active metal nanoparticles. This reaction pathway starts from the dissociative adsorption of both hydrogen (H₂) and carbon dioxide (CO₂) on the metallic sites (*) to form adsorbed hydrogen adatoms (H_{ads}), as well as adsorbed carbonyl species (CO_{ads}) and adsorbed oxygen (O_{ads}). Then, CO_{ads} can be transformed to methane (CH₄) following the same pathway as CO methanation, where the CO_{ads} is i) directly hydrogenated to methane (CH₄) or further ii) dissociated to form adsorbed carbidic carbon species (C_{ads}) and O_{ads}. [27–29]. In the first route, H_{ads} is associated with carbonyl species, such as linear CO [30] and bridged CO [31] to form adsorbed formyl (HCO_{ads}), HCOH_{ads} and COH_{ads}. Consecutively, these intermediate species are hydrogenated to CH₄. In the second route, the dissociated C_{ads} [32] is directly hydrogenated to CH₄, where COH_{ads}, CH_{2ads} and CH_{3ads} are the intermediate species formed during the process.

The associative mechanism suggests that the formation of intermediate species are highly dependent of the reaction conditions, metal/support interaction [33–36], and physicochemical properties of the catalyst (e.g. metal loading [37], structural properties [38], and distribution of the basic/acidic sites [39–42]). In this route, adsorbed H₂ is dissociated on metallic sites (*) to form adsorbed hydrogen adatoms (H_{ads}), while adsorbed CO₂ is activated on the support to form adsorbed hydrogen carbonate (HCO_{3ads}) under the presence of an adsorbed group hydroxyl (OH_{ads}), and adsorbed carbonate species (CO_{3ads}) in form of monodentate (m-CO_{3ads}), bidentate (b-CO_{3ads}), polydentate (p-CO_{3ads}) and bridged carbonate [43–48]. Later, these CO_{3ads} are hydrogenated to adsorbed formate (HCOO_{ads}) or formyl (CHO_{ads}) species. From these two species, formate formation is mainly identified as the rate-limiting step, and its successive hydrogenation to adsorbed formaldehyde-like (H₂CO_{ads}) and methoxy

($\text{H}_3\text{CO}_{\text{ads}}$) species allow that CH_4 can be formed and released from catalyst surface as a final product.

Hybridized mechanisms can be defined as the combination of both CO and formate route. These can be divided in two subcategories resulting in i) the migration of dissociated carbonyl species and/or ii) the dissociation of formate species. The first one suggests that CO_2 and H_2 are adsorbed and dissociated on metal sites to form CO_{ads} , O_{ads} and H_{ads} atoms, followed by migration onto the support surface [49]. The CO then interacts with oxide surfaces of the support to form bridged carbonyl and linear carbonyl, while the presence of H atom facilitates the formation of bidentate formate. These three species could be responsible for the formation of methane, being the bidentate formate species the main route to formation of methane. The second one suggested that CO_2 is adsorbed on support to form $\text{HCO}_3_{\text{ads}}$ or CO_3_{ads} , followed by their hydrogenation to HCOO_{ads} . Then, adsorbed formate can be dissociated and hydrogenated on the sites actives to form methane [50–52].

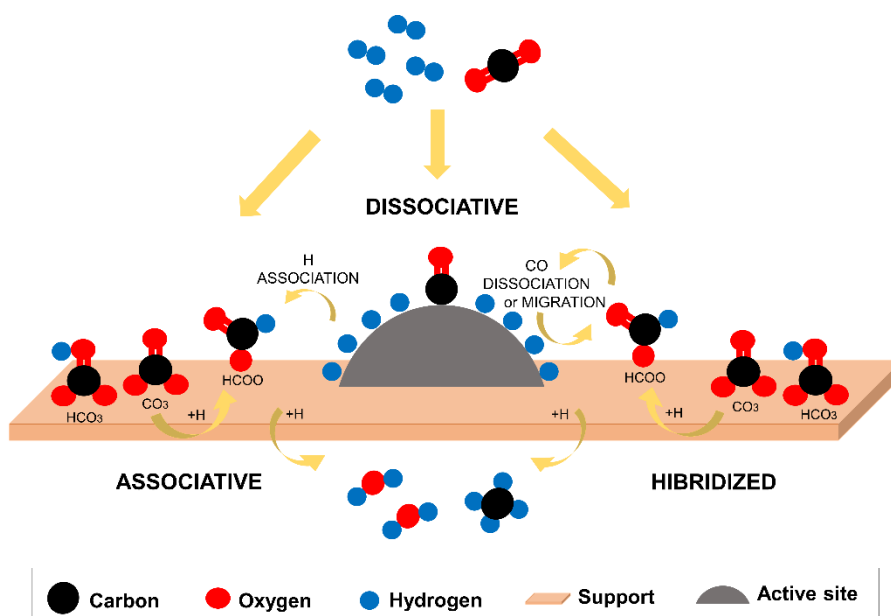


Figure 1.6. Schematic illustration of proposed reaction mechanisms of CO_2 methanation process.

Table 1.1. Proposed reaction mechanisms of CO₂ methanation on Ni-based catalysts.

Catalyst	Reaction mechanism	Species formation	Reference
Ni/SO ₂			[27]
Ni (100)	Dissociative	Lineal and bridged CO	[28]
Ni/Al ₂ O ₃			[30]
Ni/Sepeolite			[31]
Ni/CeO _{2-x}			[33–35,37,43]
Ni/MgO			[36]
Ni/TiO ₂	Associative	Monodentate, Bidentate and Bridged formate	[38]
Ni/CeO ₂ -ZrO ₂			[39–42]
Ni/SO ₂			[44]
Ni/Hβ40			[45]
CeO ₂ -modified Ni-A			[46]
Ni/Al@MnAl ₂ O ₄			[47]
W-doped Ni-Mg			[48]
Ni/Y-doped ZrO ₂			[49]
Ni/MSN	Hybridized	Bidentate formate	[50]
g-C ₃ N ₄ -modified Ni-CeO ₂			[51]
Ni-CeO ₂ /Ce _x Zr _{1-x} O ₂			[52]
NiUSY zeolites			

1.1.3. Reaction kinetics

An important part of studying chemical reactions is to monitor the rate at which they occur. Reaction kinetics is the field of science dealing with the rate of a chemical reaction. This is the rate at which the reactants are consumed to form products. In addition to the rate of the reaction, kinetics can be also used to make conclusion regarding the mechanism or sequence of steps by which reaction exactly occur at molecular level. Understanding the kinetics of Sabatier reaction is critical for being able to control the process and obtain the desired products.

Kinetic rate expressions for describing the hydrogenation of CO₂ to CH₄ can be developed employing Power-law (PL) and Langmuir-Hinshelwood-Hougen-Watson (LHHW) kinetics approaches. PL kinetics are easier to be developed with respect to LHHW kinetics. The reaction rate equations through this kinetic approach can be obtained by a simple adjusting the reaction constant and the reaction rate in the range at which reaction parameters were measured. In contrast, kinetics expressions

derived from LHHW approaches are more complex and a reaction mechanism is mandatory to adapt the reaction rates. An overview of kinetic reaction expressions on nickel-based catalyst using these kinetic approaches are summarized in Table A1.1. Eq. 12 is used for a better understanding and interpretation of the mathematical description of the proposed reaction rates.

$$r = \frac{(\text{rate constant}) * (\text{driving} - \text{force}) * (\text{equilibrium term})}{(\text{adsorption term})} \quad \text{Eq. 12}$$

The first kinetic studies for the hydrogenation of CO₂ to CH₄ were performed in 1950s [53–55]. On the basis of these results, the most plausible mechanisms for CO₂ methanation reaction were proposed. Additional kinetic models were latter developed in view of the potential significance of the CO₂ methanation reaction for the industrial fuel production [56–59]. Among them, the intrinsic kinetics proposed by Xu et al. [59] for steam reforming of methane has provided finding which are relevant for further work on methanation kinetics. They developed reaction rates for the reversible water gas shift (RWGS), CO methanation and CO₂ methanation at reactions conditions close to those used industrially.

In the Power-to-Gas context, Koschany et al. [60] developed kinetic models using three approaches: simple PL with and without inhibition of water, and LHHW. They emphasize that the kinetics at differential conversions and pure H₂/CO₂ feed markedly differ from the regime closer to equilibrium. PL with inhibition and LHHW models were capable to reflect the kinetics over a wide range of conditions from differential conversion to thermodynamic equilibrium. Hubble et al. [61] also proposed a LHHW kinetic model based on a mechanism in which adsorbed CO₂ dissociated to CO and O surface species. The subsequent dissociation of adsorbed CO was considered as the rate-limiting step.

Macro- and even micro-intrinsic kinetics were proposed to design, simulate and optimize conventional and advanced reactor configurations for industrial Power-to-Gas applications [62–69]. For instance, Molina et al. [62] proposed a kinetic model for CO₂ methanation using a simple PL rate expression over a commercial catalyst. The experimental kinetic parameters were implemented for the optimization of a wall-cooled fixed-bed exchanger reactor. With the same goal, Ducamp et al. [63] developed a kinetic model over a commercial catalyst. The rate equations were defined through the adaptation of the activity coefficients and adsorption constants of the three kinetic rates from the Xu and Froment model. Most recently, Miguel et al. [64] proposed a LHHW kinetic model based on a formyl intermediate mechanism with a hydroxyl group being the most abundant species.

Besides direct path (CO₂ methanation rate equation), kinetic studies with indirect path (RWGS rate equation + CO methanation rate equation) have been performed in order

to account for the presence/formation of CO. Marroco et al. [65] proposed a kinetic model in where rate equations were developed applying a simple power law, a power law with an inhibition term, and a LHHW approach. The most suitable fitting of experimental data was achieved by using the LHHW expression and the PL (with inhibition influence of adsorbed water or hydroxyl). On the other hand, kinetic model proposed by Champon et al. [66] was performed over a commercial catalyst and their rate equations were also developed following a LHHW approach.

Regarding the micro-intrinsic kinetics rate equations, these were developed over structured reactor configuration. Farsi et al. [67] developed a kinetic model using a microstructured packed bed reactor. The kinetic model for two-step CO₂ methanation process was developed using a LHHW formalism. The best agreement to the experimental data was obtained when the direct water adsorption in the inhibition term was assumed. Hernandez et al. [68] developed kinetic rate equations using a catalytic plate reactor. The proposed models suggested that the rate determining step includes the reaction of an oxygenated complex (COH* or HCOO*) with an active site (*) or an adsorbed hydrogen (H*). Furthermore, water was assumed to be adsorbed as a hydroxyl species (OH*), while methane did not influence the reaction. Recently, Morosanu et al. [69] proposed a power law model for aging evolution of a commercial catalyst. This was developed considering that the loss of activity during the sintering process can be correlated with the loss of normalized surface area or dispersion of the active phase.

In summary, the majority of kinetic model proposed for CO₂ methanation were developed over commercial Ni-based catalysts. These PL and LHHW kinetics were mainly proposed for the modelling, design, and optimization of conventional and advanced reactor technologies. Concerning the activation energies (E_a), the proposed values ranged between 55 and 240 kJ·mol⁻¹. A comparison between them is tricky since different reaction conditions were selected to develop the kinetic models. However, it is possible to claim that energy must be provided to initiate the exothermic Sabatier reaction. As it can be seen in Figure 1.7, the activation energy is higher when the reaction occurs in absence of a catalyst as shown by the red curve. In contrast, the presence of a catalyst decreases the activation energy which is indicated by the green reaction pathway. However, a sufficiently high temperature (depending catalyst) makes Sabatier reaction take place until all reactants are consumed. Therefore, active catalysts able to work at relatively moderate conditions should be designed to overcome the energy barrier of the exothermic Sabatier reaction.

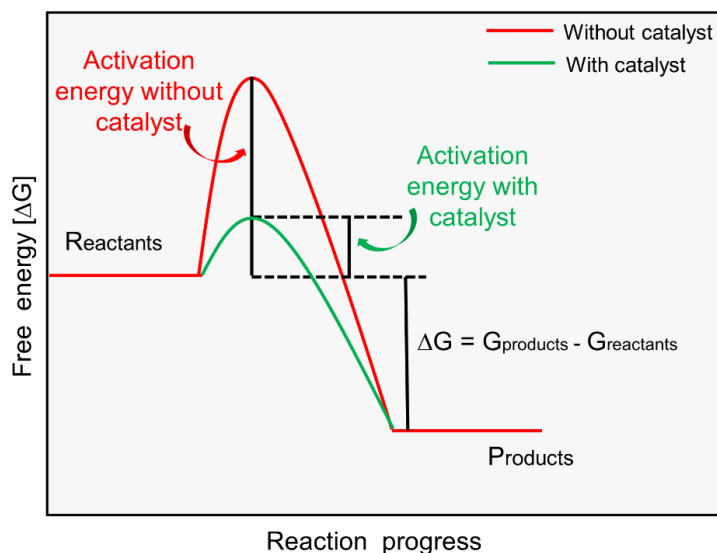


Figure 1.7. Activation energy with and without catalyst.

1.1.4. Transport phenomena limitations

In a heterogeneous catalytic system, transport phenomena limitations have a significant effect on the rate of reaction and product formation due to differences between reactant and product phases (gas) compared with the catalyst phase (solid). For a solid-catalyzed reaction, the reactants first diffuse through the stagnant boundary layer surrounding the catalyst particles (external transfer effect). Then, the reactants diffuse into and through the pores within the catalyst particles, with reaction taking place only on the catalytic surface of the pores (internal transfer effect). A schematic description of this two-step diffusion process is shown in Figure 1.8. These two mass transport limitations are potentially favoured when large-size particles and low velocities of the fluid flow are used. Consequently, both external and internal transfer must be considered in a catalytic reaction system since they limit the rate of the reaction. In addition to mass transfer effects, heat transfer throughout the catalyst particle and the stagnant boundary layer can also affect the rate of the reaction.

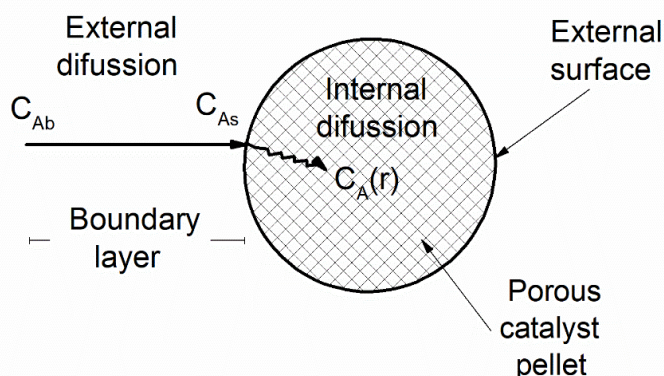


Figure 1.8. Schematic representation of the mass transfer and reaction step for a catalyst pellet. Adapted from Folger et al. [70].

Since a balance between transport phenomena and rate of the reaction is frequently considered the most effective means of operating a catalytic reaction [71]. The fundamental understanding of these transport phenomena is essential for CO₂ methanation process scale-up. For the Sabatier reaction, serious efforts in order to minimize or eliminate mass and heat transfer resistances are needed due to its exothermic nature. Strong gradients of temperature and concentrations of reacting components can arise within the reactor in the gas volume as well as inside the catalyst structure. Consequently, the implementation of a catalyst with proper shape and size on a reactor design with effective control of temperature is critical to overcome transport phenomena in the Sabatier process.

1.1.5. Reactor design

Reactor design suitable for SNG production via CO₂ methanation process should have an efficient heat management to prevent temperature increase in the catalytic bed and thermodynamic limit. High temperatures may result in damaging of the catalyst and the reactor itself, or in the initiation of undesired parallel or consecutive reactions. Therefore, another great challenge in CO₂ methanation technology is to design reactors able to manage the heat naturally released by the exothermic Sabatier reaction. Currently, there are various reactor designs developed for CO₂ methanation, which according to their configuration can be classified as follows: fixed-bed reactor (FIXBR), fluidized bed reactor (FBR), three-phase reactor (TPR) and microreactor (MR).

FIXBR represents the simplest reactor design option and most used. This approach can operate in adiabatic or polytropic conditions. Adiabatic fixed-bed reactors (AFIXR) are designed with a cooled product gas recirculation system to limit the strong

exothermicity of the reaction [72] (see Figure 1.9). This simple design can be disadvantageous when too many AFIXBRs are required to reach the target conversion.

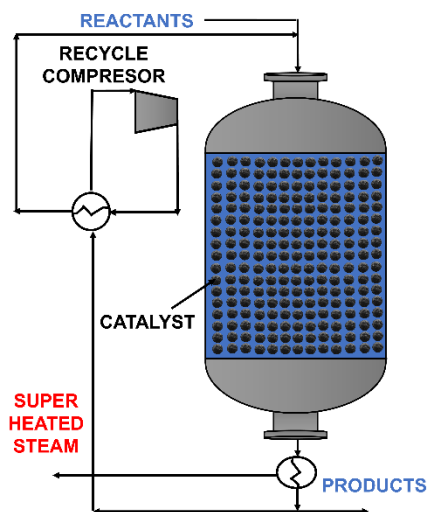


Figure 1.9. Adiabatic fixed-bed reactor.

FIXBR in polytropic operation condition involves the design of a cooled fixed-bed reactor (CFIXBR). The most common is the multitubular fixed-bed exchanger reactor (MFIIXBR). As it can be observed in Figure 1.10, its design consists of a series of tubes mounted inside a cylindrical shell. The tubes are filled with catalytic particles. The gas flow goes downward through the tubes from the upper to the lower head. In the tubes, gas and the catalytic particles react. The heat that results from the reaction is absorbed by a cooling fluid (e.g. water, steam, oil, and molten salt) in the shell side of the reactor [73]. Compared to an adiabatic reactor, a cooled fixed-bed reactor offers the advantages of intensive heat removal and therefore suitable conditions in the reactor tube, which in turn facilitate hot spot avoidance and a high level of temperature control over cooling performance. However, some limitations are found when high cooling operating conditions are required ($T \geq 375$ K & $P \geq 30$ atm) to reach the reaction temperature targeted [74]. Therefore, the design of a multitubular fixed-bed reactor is always a compromise between selectivity, yield and investment- and operating costs.

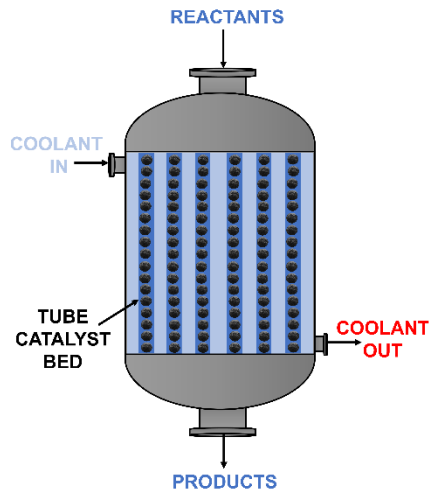


Figure 1.10. Multitubular fixed-bed reactor.

FBR is an alternative design to operate in isothermal conditions. The reactor configuration consists of a vertical column with an in-tube heat exchanger bundle, as it is represented in Figure 1.11. The fluidization occurs when the solid catalyst particles are suspended in the upward-flowing stream of the gases. Due to the turbulent gas flow and rapid circulation, this design offers a higher efficiency in heat exchange, and thus a higher control temperature with respect to fixed bed reactors [75]. However, the main issue is associated with the fluidized bed. For instance, particle blowout caused by an uncontrolled gas velocity can lead to the deterioration of the reactor by abrasion and attrition.

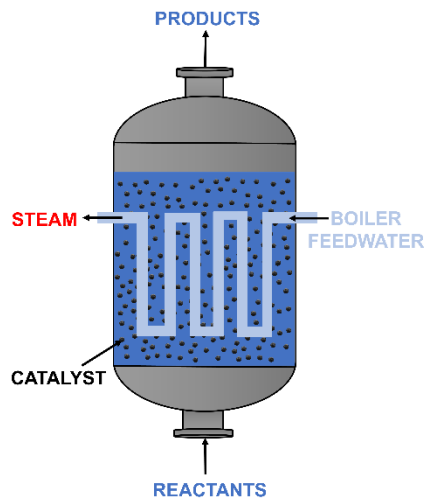


Figure 1.11. Fluidized bed reactor.

TFR also is known as a slurry bubble column reactor (SCBR) [76]. The design involves the use of fine catalyst particles ($d_p < 100 \mu\text{m}$) which are suspended in an inert liquid medium (dibenzyltoluene) by the gases flow [77], as it is shown in Figure 1.12. The stable isothermal operation in a SCBR is achieved thanks to the catalyst removal during the process. Further advantage is the possibility to operate in both semi and continuous. On the other hand, their limitations include severe backmixing, decomposition and evaporation of the suspension liquids, and the necessity of a catalyst filtration step. However, an important feature of this reactor design is that they allow the continuous catalyst replacement in the case of its quick deactivation [78].

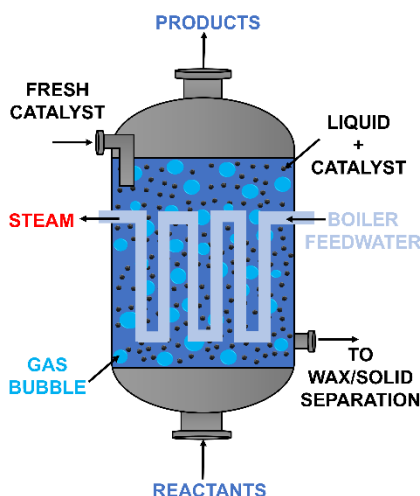


Figure 1.12. Three-phased or slurry bubble column reactor.

MRs are advanced reactor designed for the intensification of the CO_2 methanation process. The design involves a compact and miniaturized configuration. Compared to conventional reactors, these offers an high heat management thanks to its large surface area to volume ratio [79,80]. Microchannel [81] and Monolith honeycomb [82] are the main microreactor design proposal for CO_2 methanation. In a microchannel reactor (see Figure 1.13), the diameter of the channels is in the range of 50 to 5000 μm [83] and the catalyst can either be packed in them or deposited to the walls as a coating [84]. This is considered as a heat exchanger reactor type since the overall unit design combines a reactor and a heat exchanger. In addition to its enhanced heat/mass transfer, it has a quick response time (start-up and shut-down) [85]. Despite its easy scale-up, the high manufacturing cost limits its widespread application. A further drawback is the removal the catalyst of the walls, leading also to high operation costs. The implementation of structured catalysts, e.g. micro-size particles or open cell foam (OCF) coated with material catalytic has been recently proposed to overcome this problem [86].

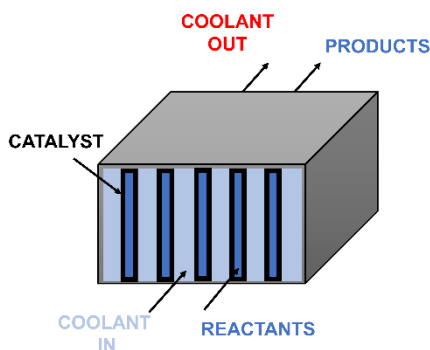


Figure 1.13. Microchannel reactor.

With regard to monolith honeycomb reactor, this design offers an extruded structure more practical with an enhanced heat transfer and high radial heat conductivity [76]. In a honeycomb structure, each monolith can contain thousands of parallel channels or holes, which are defined by many thin walls. The channels can be square, hexagonal, round, or other shapes. The hole density may be from 30 to 200 per cm^2 , and the separating walls can be 0.05 to 0.3 mm. A suitable hole density is mandatory since the surface area is mainly influenced by this parameter. Honeycomb structures can be also used into the tubes of a conventional multitubular fixed bed reactor. However, one crucial point for the development of structured honeycomb reactors is the deposition of a suitable and stable catalytic layer on the metallic or ceramic support [87].

Among the proposed reactor configurations, fixed-bed, fluidized bed and microstructured reactors are the three designs available in the market. The rest of reactor technologies continue in demonstration or research & development (R&D) stages. Lurgi from Air Liquide [88], TREMP™ from Haldor Topsøe [89], Vesta from Clariant and Foster Wheeler [90], and DAVY™ from Johnson Matthey [91] are the accessible technologies to carry out methanation process using adiabatic fixed-bed reactors. Alternatively, cooled fixed-bed reactors are provided by Etogas [92] and Man [93], while cooled microstructured reactors by INERATEC [94], Velocys [95] or ATMOSTAT [96].

1.1.6. Modelling of fixed-bed exchanger reactor technology

Modelling and simulation of chemical reactors is crucial to design and technology scale-up as it allows to understand the role of the design parameters and operational conditions without performing an excessive number of experiments, avoiding a trial-and-error approach. Competitive fixed-bed exchanger reactor for Sabatier process can be designed by means of the development of mathematical models. In the last 10 years, various one- and two-dimensional mathematical models have been developed to study the Sabatier process and propose reactor design able to achieve high CO₂ conversion in safe condition. A brief description and main findings reported in the proposed mathematical model are exposed as follows.

Kiewidt et al. [97] developed a one-dimensional pseudo-homogeneous model to evaluate the temperature behaviour of a single-stage externally-cooled fixed-bed reactor. They suggested that the thermal optimization of the Sabatier process over a single-stage externally cooled fixed-bed reactor depends slightly on the inlet temperature, and strongly on possible thermal requirements of the catalyst. Through the optimization of Semenov number (Se), they achieved methane-yields above 90% for typical reaction conditions of 573 K and 10 atm. Another mathematical model based on a wall-cooled fixed-bed reactor was proposed by Molina et al. [62]. They demonstrated that the reduction of the tube diameter leads to high efficiency in terms of heat dissipation and both the inlet temperature and gas velocity can be increased, which improves the amount of SNG produced per tube.

The combination of both modelling and experimental validation of a cooled fixed-bed reactor was reported by Ducamp et al. [63]. A two-dimensional heterogeneous computational fluid dynamics (CFD) model was developed using experimental characterization of heat transfer and kinetic parameters. They confirmed with the model that at the peak temperature location, the reacting mixture was at thermodynamic equilibrium ($X_{\text{CO}_2}=69\%$ at $T=793\text{ K}$ and $P=4\text{ atm}$). Strong diffusion limitations were also identified in the catalyst particles which locally reduced the efficiency of the reaction to 10%. Fache et al. [98] proposed an one-dimensional dynamic pseudo-homogeneous model for optimization of fixed-bed methanation reactors with safe and efficient operation under transient and steady-state conditions. The mathematical model developed for reactor optimization was based on a fixed-bed exchanger reactor composed by four-dilution zones. They indicated that a proper catalyst dilution profile can increase the steady state efficiency and stability of the reactor. Nevertheless, the dilution profile considered in this work had a negative impact on transient efficiency and stability.

Molioli et al. [99] developed a one-dimensional heterogeneous fixed-bed reactor model in order to evaluate the most important elements for the activation and heat

management of the Sabatier process on Ru/Al₂O₃. For adiabatic reactors, feed temperature was found at 487 K for a space velocity of 3000 h⁻¹ and a pressure of 10 atm. On the other hand, the properties of cooled reactors were obtained by the interrelationship between cooling and feed temperature. They proposed a staged feeding strategy to limit the maximum temperature in the reactor and ensure the stable operation of the system. On the other hand, the operation range extension via hot-spot control for catalytic CO₂ methanation reactors was investigated by Bremer et al. [74]. A dynamic one-dimensional pseudo-homogeneous fixed-bed reactor model was developed. They applied stabilizing control to moderate the reactive zone (hot spot) via adaptive coolant temperature variations. By using this alternative heat management approach, they attained unconventional operating points in regions of steady-state multiplicity that offer reduced catalyst temperatures (<773 K) while maintaining elevated reactor performance.

Design of an air-cooled Sabatier reactor was modelled and experimentally validated by Currie et al. [100]. A transient one-dimensional pseudo-homogenous model was developed to simulate the reactor. They suggested that the selection of proper reaction conditions (P=10 atm and GHSVs=500-3000 h⁻¹) was a key point to achieve CO₂ conversion as high as 90–95% and complete selectivity to CH₄ formation. Zhang et al. [101] developed a CFD model to simulate CO₂ methanation in a shell-and-tube reactor with multiphase coupled heat transfer. The steady-state CFD model was based on the open-source toolbox OpenFOAM. Three different methanation rate models were adopted to validate the practical applicability of the developed solver. They claim that the solver can capture the trends of temperature profiles along both axial and radial directions. Most recently, the design of an optimal fixed-bed reactor concept for CO₂ methanation process in small-scale applications was proposed by Molioli et al. [102]. The model-based optimization of the Sabatier reaction was developed by controlling the heat transfer. They found that the reactor can be divided into three zones: an initial zone for reaction activation; a central zone to remove excess heat; and a final zone to achieve high conversion reaching the thermodynamic equilibrium curve. They suggested that the optimal reactor can be designed by point-by-point manipulation. Therefore, modelling is a powerful tool for justification and prediction of the optimal reactor design for efficient SNG production which meets the criteria required for industrial-scale applications.

1.2. Catalyst design

It is well-known that heterogeneous catalysts play an important role in industrial chemical production due to their easy separation, handling, recycling and the possibility of continuous operation of the reactor. Heterogeneous catalysts are composed by several elements such as support, promoter and active catalytic materials of metal or metal oxide [103]. The kinetic rates of the Sabatier reaction are reliant on the nature of the applied catalyst; thus, a special attention is required in its design, formulation and preparation method. In order to be industrially relevant, this must allow the reaction to proceed at a suitable rate under conditions that are economically desirable, at as low a temperature and pressure as possible.

The design of heterogeneous catalytic systems with optimal performance (active, selective and stable) for CO₂ methanation reaction involves a consideration of some properties, including physical, chemical and mechanical [104]. Besides the properties shown in Figure 1.14, catalytic material selection as well as its shape and size are important aspects for the optimization during the catalyst design.

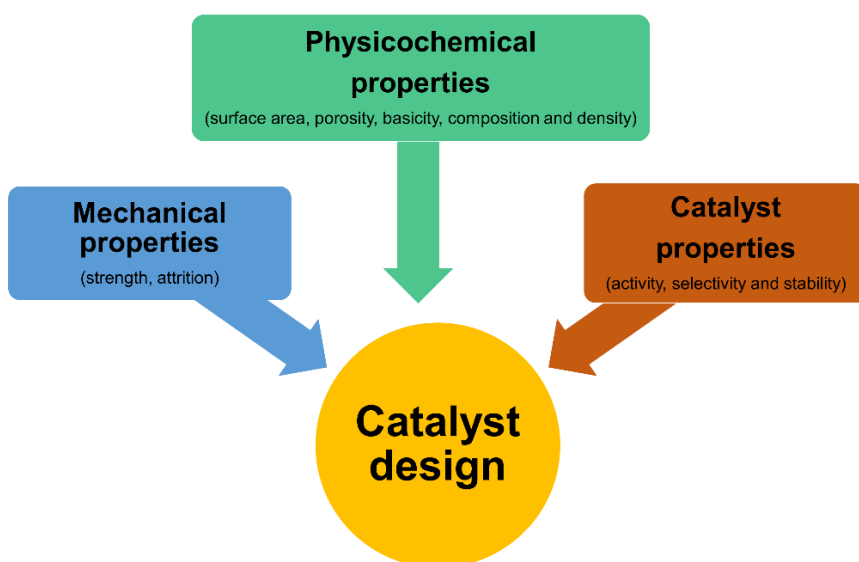


Figure 1.14. The main properties to be considered for the CO₂ methanation catalyst design.

1.2.1. Active phase

The activity, selectivity and stability are the most relevant properties to be addressed in the pursuit of optimally performing catalytic systems. Heterogeneous catalysts composed by metals primarily from VIII-XI group (noble metals (ruthenium (Ru) [105–107], rhodium (Rh) [108], platinum (Pt) [109], palladium (Pd) [110]) and

transition metals (nickel (Ni) [111], iron (Fe) [112], cobalt (Co) [113–116])) have been confirmed to be active materials for CO₂ methanation reaction. In terms of activity and selectivity, these metal materials can be ordered as follows:



Catalysts based on Ru are the most active for CO₂ methanation operating at low temperatures ($T \leq 523$ K) [117–119], but their effective implementation is limited by the high price of Ru. Nevertheless, they can have a narrow niche market as industrial process if affordable alternatives are available. From the proposed transition metal materials, Fe is inexpensive compared to Co, but both have lower selectivity to methane and they are typically used for Fischer–Tropsch process [120]. Fe-based catalysts require of high pressures to reach similar selectivities than Ni [112]. Ni-based catalysts are the most widely used at industrial levels [121]. This is because nickel is an abundant material with a high activity and selectivity in relation to its low cost. However, the main limitation of catalysts based on Ni are their early deactivation by sintering [122] or coke deposition [30] because of the high temperatures formed by the nature of the Sabatier reaction; and by poisoning [123–125] when the supplied CO₂ is derived from carbon feedstocks as for example coal power plant [126]. Therefore, great efforts have been made to develop an effective Ni-based catalyst which exhibits a high activity, a high thermal stability and a high tolerance to impurities in CO₂ methanation.

The combination of nickel metal with a second active metal material has been a catalyst design strategy recently explored to improve the catalytic performance of the Ni-based catalysts. The key parameter determining the intrinsic properties of the bimetallic catalyst (Ni-X/Al₂O₃; X: second active metal) is evidently the ratio between the two metals. These are separately active for the Sabatier reaction, but at different ratios can display a synergistic effect. Metals such as Fe, Pt, Pd, Rh, Co and Ru have been the most active material used together with Ni-based catalysts for CO₂ methanation process, as it is listed in Table A1.2.

Bimetallic catalysts based on Ni-Fe as active phase and supported on different metal oxides were evaluated by Pandey et al. [127]. The maximum enhancement was achieved when γ -Al₂O₃ was used as the support. They suggested that the competitive yield in the bimetallic catalysts was due to the formation of Ni–Fe alloy (Ni₃Fe), while the maximum enhancement for the γ -Al₂O₃ supported catalysts was due to the ability of the support to adsorb CO₂. The metal sites of the most active γ -Al₂O₃ supported Ni–Fe catalyst were approximately 1.63 times more active than metal sites of the γ -Al₂O₃ supported Ni catalyst.

Mihet et al. [128] investigated the effect of other metals (X=Pt, Pd and Rh) on Ni-X/ γ -Al₂O₃ catalyst. Among the evaluated bimetallic catalysts, Ni-Pt and Ni-Pd are the most

active ones in the temperature range of 452–541 K. The beneficial effect of Pt or Pd were ascribed to the different distribution of the active centers for hydrogen chemisorption. A catalytic enhancement at low temperature was also reported for bimetallic catalysts based on Ni-Co and supported on ordered mesoporous alumina (γ -Al₂O₃-OMA) [129]. The kinetic study demonstrates that the synergistic effect between the Ni and Co bimetallic active centers was beneficial to reduce the apparent activation energy by coordinating the activation of H₂ and CO₂ process over Ni and Co active centers.

Ru as second metal on Ni/ γ -Al₂O₃ catalysts was recently reported by Chen et al. [130]. The bimetallic Ni-Ru catalyst was more active compared with the monometallic Ni or Ru catalysts. The optimum reaction temperature was found to be 673 K. This behaviour was also detected by Zhen et al. [131]. The high catalytic performance over their bimetallic Ni-Ru/ γ -Al₂O₃ catalyst was associated to the segregation phenomenon of Ru on the catalyst surface.

1.2.2. Catalyst support

Another important factor that must be considered for catalyst design is the mechanical resistance, morphology and porosity of the support. The selection of a support which stabilises the resulting Ni nanoparticles is crucial for determining CO₂ methanation catalyst activity and stability. Metal oxides, such as alumina (Al₂O₃) [132], cerium oxide (CeO₂) [133–135], silicon dioxide (SiO₂) [136] [137], titanium dioxide (TiO₂) [138], zirconium dioxide ZrO₂ [139–143], magnesium oxide (MgO) [144], yttrium oxide (Y₂O₃) [145,146], lanthanum oxide (La₂O₃) [147] and samarium oxide (Sm₂O₃) [30]; composite oxides (CeO₂-ZrO₂ [148–151], Y₂O₃-ZrO₂ [152], Al₂O₃-ZrO₂ [153], Al₂O₃-ZrO₂-TiO₂-CeO₂ [154], MIL-101-Al₂O₃ [155], CeO₂-Gd₂O₃ [156], CaO-Al₂O₃ [157]; ordered porous materials (SBA-15, MCM-41 [158], MSC [159]) ; carbon [160–165] and zeolites [166–171] are used as material supports for Ni-based catalysts.

Among metal oxide materials, Al₂O₃ is commonly used as a support for catalytic applications [172]. Despite it can be found in a variety of metastable structures including the γ , η , δ , θ , κ , and α phase, gamma-alumina (γ -Al₂O₃) is the most competitive support for CO₂ methanation catalyst due to its high surface area, developed pore structure, porosity and well characterized surface acid–base properties [173]. The main drawback is its tendency to sinter in the presence of water at high temperatures and their low CO₂ absorption [174].

Lanthanide metal oxides are also reported to be promising material supports, specially cerium oxide (CeO₂). This is a well-known light rare earth element, which can be used as a sintering-resistant support thanks to its potential redox chemistry between Ce³⁺ and Ce⁴⁺, high oxygen affinity and absorption/excitation energy bands associated with

electronic structure [133] [175]. In particular, it enhances Ni dispersion on its surface and provides surface oxygen vacancies to generate active CO species and promote CO₂ methanation [176]. Tada et al. [133] examined the effects of the support materials (α -Al₂O₃, TiO₂, MgO and CeO₂) on CO₂ conversion and CH₄ selectivity. From all evaluated supports, Ni/CeO₂ showed high CO₂ conversion especially at low temperatures compared to Ni/ α -Al₂O₃. They suggested that the surface coverage by CO₂-derived species on CeO₂ surface and the partial reduction of CeO₂ surface could result in the high CO₂ conversion over Ni/CeO₂. Regarding Y₂O₃, La₂O₃, Sm₂O₃, these metal oxides presented an enhanced catalytic performance than Ni/ γ -Al₂O₃ catalysts [30]; however, these rare earths are less abundant than cerium and thus more expensive.

The combination of conventional supports Al₂O₃ with other metal oxides is a strategy currently attracting considerable interest since it can be an alternative to design inexpensive catalysts. CeO₂-ZrO₂ [148–151], Y₂O₃-ZrO₂ [152], Al₂O₃-ZrO₂ [153], Al₂O₃-ZrO₂-TiO₂-CeO₂ [154], MIL-101-Al₂O₃ [155], CeO₂-Gd₂O₃ [156], CaO-Al₂O₃ [157] composite oxides supported Ni-based catalysts have been reported to be active for CO₂ methanation. Among them, the quaternary system supports proposed by Abate et al. [154] showed competitive catalytic performance and stability at high gas hour space velocities. The enhanced catalytic performance and stability of their composite oxide (55 wt.% γ -Al₂O₃-15 wt.% ZrO₂-15wt.% TiO₂-15 wt.% CeO₂) supported Ni-based catalyst was achieved due to the improvements in reducibility nature of the catalysts.

Zeolites are aluminosilicate molecular sieves that have a great applicability as basic catalyst and catalyst supports. In CO₂ methanation, Ni/zeolite catalysts have been demonstrated to have proficient catalytic performances [177]. Most works suggested that a proper selection of the preparation conditions is crucial to improve metallic dispersion and avoid growth/agglomeration of metal particles on the external surface of the zeolites [166,167,170,178]. In a recent study, Wei et al. [169] demonstrated that the selection of precursor can also influence the properties of a nickel modified catalyst. They observed that nickel citrate combined with a rather low calcination temperature leads to Ni modified 13X and 5A zeolite catalysts which can be easily reduced at lower temperature compared to the other Ni 13X and 5A zeolite catalysts made with acetate and nitrate. From all their catalysts, the 5 wt.% Ni13X-cit zeolite catalyst prepared with nickel citrate showed high activity and CH₄ selectivity in the Sabatier reaction at remarkably low temperatures and the catalyst displayed good stability.

Carbon materials in form of active carbon (AC) [160] and nanotube (CNTs) [161–164] also have been considered as support due to their admirable chemical inertness, thermal conductivity, large surface area and stability. Feng et al. [161] claimed that

compared with Al_2O_3 -supported catalysts, the CNTs- supported catalysts shown an enhanced catalytic activity. However, they also reported that the catalytic activity of Ni/CNTs catalyst decreased as the reaction progresses, which was mainly due to the sintering of nickel particles. In order to improve the stability in their Ni/CNTs catalyst, they modified the support with the addition of Ce. Similar problems were detected by Feng et al. [160] on a Ni/AC catalyst. In this case, an improvement of stability was observed when Ca was added to catalytic system. Most recently, the catalytic activity of CNT supported Ni and Ni-ZrO₂ catalysts were evaluated by Romero-Sáez et al. [162]. Between them, Ni-ZrO₂/CNT prepared by sequential impregnation showed an interesting catalytic activity but also stability. This was attributed to the available NiO nanoparticles, which were deposited either on the surface or next to the ZrO₂ nanoparticles, increasing the extent of the Ni-ZrO₂ interface thus improving the catalytic performance. Li et al. [163] revealed that oxygen- functionalized carbon nanotubes (CNTs) are promising supports for CO₂ hydrogenation to methane. They confirmed that the formation of covalent bonding between the interfacial Ni atom and C or O elements of surface oxygen groups (SOGs), causing the electrons to be transferred from Ni atoms to CNT support because of the intrinsic electronegativity of -COOH (electronic effect) were the origin of N-CNT interaction. In addition, they exposed that the addition of Mn to Ni-CNT catalyst was positive in terms of activity. The Mn promoter enhanced CO₂ adsorption and conversion. Efficient and selective CO₂ methanation over N-CNT has been also reported by Wang et al. [164]. The competitive catalytic performance observed on their Ni-NPs/N-CNT was ascribed to the high thermal conductivity of the support and the high basic surface character of the N-doped nanocarrier that fosters the generation of local gradients of CO₂ concentrations in proximity of the material active sites.

Materials with ordered structure such as SBA-15, MCM-41[158,179], MSM [159], MOF-5 [180], 3D-KIT-6 [181] are also potential to manufacture CO₂ methanation catalysts. These material supports are reported to have valuable structural and textural properties for the dispersion of metal species and the prevention of sintering processes. In a recent study, Aziz et al. [159] compared conventional Ni/ γ -Al₂O₃ catalyst with other Ni/X catalysts (X=MSM, MCM-41, protonated Y zeolite, SiO₂). They observed that the enhancement of catalytic activity of CO₂ methanation followed the order: Ni/MSN > Ni/MCM-41 > Ni/HY > Ni/SiO₂ > Ni/ γ -Al₂O₃. The notable catalytic performance of the Ni/MSN was attributed to both intra- and inter-particle porosity which facilitated the transport of reactant and product molecules during the reaction. Metal-organic frameworks (MOFs) are structures materials with very high surface areas (>1000 m²·g⁻¹) and considered as emerged supports for CO₂ methanation catalysts. Zhen et al. [180] investigated Ni@MOF-5 catalyst via controlling active species dispersion. The promising catalytic activity and stability of their 10Ni@MOF-5 under low temperature condition was attributed to the high dispersed Ni active sites (41.8%) over MOF-5 (2961 m²·g⁻¹). 3D-mesoporous KIT-6 as support has been

evaluated by Cao et al. [181]. The formation of highly dispersed nanoparticles for enhancing catalytic performance was evidenced by transmission electron microscopy (TEM). They identified that Ni nanoparticles were uniformly scattered into the internal pores, stimulating the production of small Ni nanoparticles due to the valid confinement effect of 3D mesopores and intense interaction between active Ni and KIT-6. Furthermore, the addition of V_2O_5 species remarkably enhanced CO_2 conversion, and enabled the equilibrium conversion temperature to shift from 723 to 673 K.

Other mesoporous materials such as olivine [182], core shell $Al@Al_2O_3$ [183], attapulgite (ATPG) [184] and KCC-1 [185] have been recently reported as supports. Wang et al. [182] proved that Ni/Olivine catalysts has a strong resistance to coke deposition and abrasion, thus this catalytic system could be a promising methanation catalyst, especially for fluidized bed operation. On the other hand, core shell $Al@Al_2O_3$ has been found to provide high density of medium basic sites and enhanced CO_2 adsorption capacity [183]. Regarding ATPG, this is an industrial mineral material with a layered chain transition structure and is rich in magnesium silicate, which contains abundant alkaline sites to absorb acid CO_2 during methanation reaction. However, Liang et al. [184] demonstrated that the increase of nickel loading to attapulgite significantly decreased the abundance of alkaline sites, remarkably enhanced the catalytic activity, and suppressed the formation of CO. As an alternative to conventional mesoporous silica materials, fibrous silica nanosphere support (KCC-1) with unique dendrimeric mesopore structure has been recently proposed by Lv et al. [185]. They demonstrated that the dendrimeric mesoporous channels of the fibrous KCC-1 support was in favour of the improvement of the Ni dispersion by providing large accessible surface area for the Ni species. The promising 20Ni/KCC-1 catalyst shown much higher catalytic activity and better sintering-proof property of the metallic Ni nanoparticles than the 20Ni/SiO₂ and 20Ni/MCM-41 reference catalysts.

A summary of the supported Ni-based catalysts implemented to carry out the CO_2 methanation process is shown in Table A1.3. According to this information, a comparison of the productivity for all the reported support material was performed. Figure 1.15 suggests that the productivity trend as a function of GHSV and CO_2 conversion follows the order: KIT-6 > $Al@Al_2O_3$ > CNTs > TiO_2 > Y_2O_3 > CeO_2-ZrO_2 > MSN > ZrO_2 > GDC > MCM-41 > Zeolite > $Y_2O_3-ZrO_2$ > Al_2O_3 > $CaO_2-Al_2O_3$ > La_2O_3 > $Al_2O_3-ZrO_2$ > CeO_2 > $Al_2O_3-ZrO_2-TiO_2-CeO_2$ > SiO_2 > Attapulgite > Olivine > MOF-5 > KCC-1 > MIL101- Al_2O_3 . The notable productivity of the KIT-6 can be probably attributed to its large pores with channel interconnection, leading to an enhance Ni dispersion. However, one of the main disadvantages of KIT-6 is its high-cost syntheses. KIT-6 materials are achieved typically using expensive Si sources (e.g. TEOS) under strongly acid solution. Therefore, a supported catalyst for CO_2 methanation with efficient productivity and low-cost is still a demand.

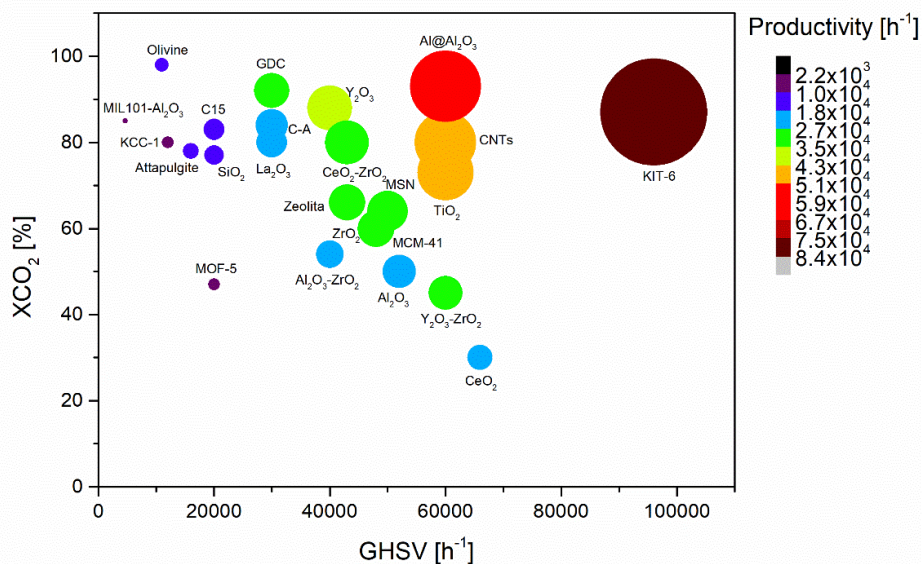


Figure 1.15. Comparison of productivity of the different support material used in Ni catalyst showing the relationship between GHSV [h^{-1}] and CO_2 conversion [%]. Productivity [h^{-1}]= X_{CO_2} [%]*GHSV [h^{-1}]* S_{CH_4} [%]. Note: GHSVs were calculated assuming for all samples a $\rho_{\text{cat}}=1\text{g}\cdot\text{mL}^{-1}$. Productivity of ZrO_2 is overlapped with MCM-41; C-A: $\text{CaO}\text{-Al}_2\text{O}_3$; and, C15: $\text{Al}_2\text{O}_3\text{-ZrO}_2\text{-TiO}_2\text{-CeO}_2$.

1.2.3. Promoter

Catalytic performance of the conventional Ni-based catalysts can be enhanced by the addition of so-called promoters. These are elements or compounds incorporated in small amount in the catalyst composition in order to improve the physicochemical properties of catalysts. Promoters are usually classified as two types: i) physical promoters that help in stabilizing the surface area of the composite material or that increase its mechanical resistance, and ii) chemical promoters that modify the activity and selectivity of the active phase. A summary of promoted Ni/ $\gamma\text{-Al}_2\text{O}_3$ catalysts for CO_2 methanation process is shown in Table A1.4.

In addition to its uses as a bulk support material, CeO_2 has been explored as a promoter [186–188]. Most of the studies claimed that the 2-2.5 wt.% CeO_2 to Ni/ $\gamma\text{-Al}_2\text{O}_3$ catalyst led to a remarkable improvement of the initial activity and stability. This can be attributed to the fact that the CeO_2 increased the surface area of the catalyst by means of the reduction the nickel particles [188]. La_2O_3 is another metal oxide that act as a promoter. Its addition also strongly increases the activity of Ni/ $\gamma\text{-Al}_2\text{O}_3$ as a result of the strong metal support interaction and basicity [189,190]. Besides La and Ce, alternative lanthanide promoters (Pr, Eu and Gd) were evaluated by Ahmad et al. [191]. From all promoted catalysts, the Ni/ $\gamma\text{-Al}_2\text{O}_3$ promoted by praseodymium

exhibited the best catalytic performance. A higher metal dispersion and smaller average particle size were the positive effects caused by addition of Pr.

The effects of Mn addition on Ni/ γ -Al₂O₃ catalyst has been evaluated by Zhao et al. [192]. The main contribution detected by using a 1.7 wt.% of this promoter were described as follows: the addition of Mn ii) created high medium-strength basic sites, ii) improved the catalyst reducibility and iii) the Ni active sites dispersion. A similar result was recently reported for another 3 wt.% Mn-promoted Ni/ γ -Al₂O₃ catalyst [193]. The enhanced catalytic performed was also observed on Ca doped ordered mesoporous Ni-Al composite oxide catalysts. Xu et al. [194] revealed that the addition of the Ca greatly enhanced the surface basicity, which could favour the chemisorption and activation of CO₂. In a recently study by Isah et al. [195], Zeolite was found to enhance the activity and coking resistant of Ni/ γ -Al₂O₃ catalyst. The addition of 2 wt.% of zeolite to Ni/ γ -Al₂O₃ increased the specific surface area of the catalyst while sustaining similar Ni metal surface area to the non-promoted one.

1.2.4. Preparation method

Highly active and stable catalytic systems with effective physical and chemical properties can be prepared by using an appropriate method. Various innovative preparation methods, beyond the traditional impregnation method, have been developed for the synthesis of nanoparticles with controllable nanoscale sizes and shapes. These methods allow to reach performance optimization by controlling synthetic procedures and conditions. Figure 1.16 shows an overview of the preparation methods used to synthesize CO₂ methanation catalysts.



Figure 1.16. An overview of the preparation methods used to synthesize CO₂ methanation catalysts.

Among the methods listed in Figure 1.16, the impregnation method is the simplest and used more frequently to synthesize Ni-based catalysts. This term denotes a procedure whereby a certain volume of solution containing the precursor of the active element of the catalyst is contacted with the solid support. According to the relation between volume of the solution and the pore volume of the support, the impregnation method can be classified as follows: i) incipient wetness impregnation (IWI) and ii) wet impregnation (WI). In the first case, the volume of the solution either equal or is less than the pore volume of the support, while in the second one an excess of the solution is always used. In addition to these impregnation methods, co- and sequential are particularly used for the impregnation of multiple metals. As it can be seen in Table A1.5, high catalytic performance, stability, metal-support interface and basicity in the Ni-based catalysts were achieved when the impregnation methods wet, co- and sequential were used [162,196,197][198]. The IWI method is recommended to apply high loading of precursors. However, special attention should be paid in the concentration of the metal salts. For Ni-based catalyst, an increase in solution concentration can result in a lower solution pH which influences the dissolution of the support.

Ni-based catalysts with small metal nanoparticles ($d_p \leq 10$ nm) and high metal dispersion (Ni dispersion $\leq 39.5\%$) have been obtained using methods, such as deposition-precipitation [199], solution combustion synthesis [143], dielectric barrier discharge (DBD) plasma [138], evaporation-induced self-assembly process (EISA) [200], colloidal and Sol-gel [201]. This latter methods together with hydrothermal [178] also are the most promising to synthesize heterogeneous catalysts with an accurate particle size control and complete mesopore structure. Regarding template methods, a high resistance to carbon deposition was found in the catalysts prepared by self-sacrificial [202], while a high metal-support interaction was identified in the catalysts prepared by hard-template [203]. On the other hand, electrochemical [204] and ammonia evaporation [205] are two methods able to enhance the textural properties, specially BET surface area. Despite the great efforts have been made to synthesize heterogeneous catalysts with accurate nanoparticle size control and complete mesoporous structure, their final shape limits their industrial application.

1.2.5. Shape and size

Most of the promising CO₂ methanation catalysts developed through the aforementioned methods lead to powder catalysts, with particle size lower than 200 μm , as it can be seen in Table A1.5. At industrial levels, powder catalysts are not technical feasible to be used in the conventional fixed-bed reactors because their small particle sizes promote the pressure drop across the catalyst bed. To avoid high pressure drop, the use of relatively large particles (1-3 mm) can be required. The extrusion moulding of the powder catalysts in a pellet shape is an alternative to

advance their use in this type of reactor. Indeed, commercial methanation catalysts are currently manufactured in spherical (3-6 mm) [206], cylindrical (5.4x3.6 mm) [207] and ring (5x2.5 mm) [208] shapes, as it can be observed in Figure 1.17.



Figure 1.17. Commercial catalysts with different shapes for CO₂ methanation.

Microreactors for CO₂ methanation process have recently received a great deal of attention because of increased heat removal at moderate pressure drop. Micro- and milli-fixed bed reactors are the design in which small catalyst particles (e.g. 300-1000 μm [209]) can be loaded into the packed bed. The proposed commercial catalysts evidently should be first crushed and then sieved to be implemented. Therefore, the design of active micro-sized catalysts with appropriate shape is required to intensify CO₂ methanation process in these advanced reactors.

Solutions based on the use of monolith [210–214] as catalyst support have also been considered in the literature, together with other shapes such as foam [215,216], sponge [217], spiral plate [218], ceramic fiber [219] and tubular [213]. These are also known as structured catalysts in where a layer of catalytic material ($\leq 1\text{mm}$) is deposited on the 3D-shape support through a washcoating method. Most recently, 3D printing process using 3D-Fiber Deposition (3DFD) method was reported for the manufacture of 3D-shape supports [220]. This technique is based on continuous extrusion (layer-by-layer construction) of a ceramic or metallic support structure.

1.3. P2G experiences: Process strategies at lab, pilot and demo plant.

There are many research and demonstration projects devote to spread the P2G technology around Europe [221]. In Power-to-Methane applications, lab, pilot, and demo plant in different sites have been designed to evaluate their technical feasibility. A detailed review of the description about 40 relevant projects in where SNG is produced by thermocatalytic methanation and biological methanation was reported by Bailera et al. [222]. Between 2009 and 2017, fixed-bed reactors operated under adiabatic, isothermal and polytropic conditions were the designs widely used to carry

out the CO₂ methanation process. Nevertheless, novel reactor design and process strategies have been recently proposed as part of the SNG process intensification. The most relevant projects are presented as follows:

- **STORE&GO**

The Horizon 2020 project STORE&GO [223] evaluated the technological, economic, social and legal integration of P2G as a storage modality for flexible sustainable energy systems in three different European countries. A first demo plant (700 kW) was located in Falkenhagen (Germany). The methanation process is based on a honeycomb reactor concept developed at the Engler-Bunte-Institut of the Karlsruhe Institute of Technology (KIT). The plant currently produces up to 1,400 m³ of SNG per day. A second demo plant was located in Solothurn (Switzerland). It employs a special methanation method. Microorganisms, the so-called Archaea, convert the hydrogen obtained in the electrolyser with carbon dioxide into methane. The third demo plant (200 kW) was built in Troia (Italy), and shown that direct air capture of CO₂ can also represent a technical option. The plant combines a microreactor for methanation with an innovative liquefaction plant.

- **JUPITER 1000**

The Jupiter 1000 project [224] was the first industrial demonstrator of Power-to-Gas in France to recover surplus electricity from renewable sources and recycle CO₂. The demo plant with a power rating of 1MWe was equipped with two electrolyzers and a methanation process with carbon capture for hydrogen (200 m³·h⁻¹) and SNG (25 m³·h⁻¹) production, respectively. Alkaline and PEM electrolyzers were developed by McPhy, while the METHAMOD methanation reactor developed in the LACRE laboratory (ATMOSTAT and CEA joint laboratory) was the key element of the methanation system. A total of 10 reactors were needed for SNG production. More than 15 TWh of gas per year could well be produced using the Power-to-Gas system by 2050.

- **HELMETH**

The HELMETH project [225] evidenced the technical feasibility of combining a pressurized high-temperature steam electrolysis with a CO₂ methanation module in stand-alone and thermally integrated operation. The SOEC system is made of 3 sunfire stacks, each containing 30 electrolyte supported cells (ESC) with an active area of 127.8 cm² per cell. The methanation module was composed by two fixed-bed reactors connected in series with a water condensation and separation stage in between and an overall of five additional heat exchangers (HEX) to pre-heating inlet gases and for control cooling system of the reactors. The pressurized SOEC system showed steam conversions up to 90% and operating pressures of max. 15. The SNG production (over 97 vol% CH₄) was achieved using relatively low inlet temperature

($T_{\text{inlet}} \leq 523$ K) and high pressures ($P=30$ atm). Overall efficiency based on stand-alone tests was 76% with a potential increase to 80% in industrial scale.

- **Small-scale demonstrator (SSDS) pilot plant**

The Laboratory for Materials in Renewable Energy (LMER) designed, built and evaluated at lab scale a fixed-bed reactor to be used a part of the small-scale demonstrator of renewable energy to synthetic hydrocarbon conversion of EPFL Valais/Wallis [226]. The one-stage methanation process was designed to convert $50 \text{ g}\cdot\text{h}^{-1}$ of hydrogen, which corresponds to a production of $100 \text{ g}\cdot\text{h}^{-1}$ of methane. The reactor was designed to operate at temperatures up to 673 K and pressures up to 10 atm with a structural safety factor of 4. The total power of the reactor amounts to around 2 kW, split into 1.54 kW contained in the produced methane and 0.44 kW supplied in the form of heat. At target flow rate of $50 \text{ g}\cdot\text{h}^{-1} \text{ H}_2$, CO_2 conversion of 97% was reached using a temperature set point of 553 K.

- **P2G movable modular plant**

The ENEA Casaccia Research Center built and put in operation a pilot scale experimental facility dedicated to study and test the methanation process ($0.2\text{--}1 \text{ Nm}^3\cdot\text{h}^{-1}$ of produced SNG) [227]. The small-size pilot plant was equipped with a methanation unit constituted by a multi-tubular fixed bed reactor able to work in cooled or adiabatic conditions. The catalyst bed diameter was about 15 mm while the maximum length can reach 400 mm. The methanation facility can operate in the range of 1–5 atm. The optimal reactor operating parameters to achieve high conversions (94%) were found at $T_{\text{inlet}} = 563$ K and pressure of 5 atm.

- **COSYMA (COntainer-based SYstem for MethAnation)**

The Swiss Competence Center for Energy Research SCCER BIOSWEET, with financial support Swiss Innovation Agency Innosuisse, built a COSYMA set-up at pilot-scale to demonstrate the feasibility of the catalytic direct methanation of biogas in a fluidised bed reactor [228]. The pilot-scale COSYMA set-up was evaluated using real biogas from the plant of energie360° in Zurich at Werdhölzli. During the long-duration experiment (1100 h), it was achieved an average yield of 96% and average bulk concentrations of 88 vol% CH_4 , 11 vol% H_2 and 1 vol% CO_2 in the product gas, which was close to equilibrium. A slow deactivation process was monitored and found to be only moderate. Organic sulphur compounds were identified as the main source of deactivation.

- **InnoEnergy - CO_2 -SNG**

The CO_2 -SNG project [229] proved the feasibility of Synthetic natural gas (SNG) by using CO_2 from amine scrubbing with H_2 obtained from water electrolysis. TAURON Wytwarzanie S.A was responsible for building and testing the CO_2 -SNG pilot plant at

the Łaziska power plant in Poland. A two-stage process was designed for the production of $4.5 \text{ Nm}^3\cdot\text{h}^{-1}$ of SNG. The methanation unit was equipped with two microchannel reactors and their cooling circuits, a gas pressure and flow controllers of gases. The microstructured reactors were developed by CEA and delivered by ATMOSTAT. The maximum CO_2 conversion achieved during the experimental campaign was of 98% (at process parameters: inlet gas mass flow rate $=10 \text{ kg}\cdot\text{h}^{-1}$, pressure 3.0 atm, I inlet reactor temperature: 573 K, II inlet reactor temperature: 623 K). The produced SNG consisted of about 82% of methane, 13% of hydrogen and 5%.

- **Naturgy - CoSin**

The CoSin project [230] demonstrated the technical economic viability of SNG production at a sewage treatment plant in Barcelona, Spain. Cetaqua and Labaqua were the responsible for the membrane biogas unit, IREC and Naturgy for the methanation unit and catalyst development. As it can be seen in Figure 1.18, three renewable carbon dioxide sources, such as biogas, partially upgraded biogas and carbon dioxide released by a membrane upgrading unit were combined with renewable hydrogen produced from an alkaline electrolysis (37 kWh_e) of tap water to produce SNG using an innovative microstructured heat-exchange reactor. The methanation process consisted of a 2-step synthesis unit, including gas pre-heating, catalytic reaction and water condensation. The microstructured reactor technology was designed at KIT and delivered by the KIT spin-off INERATEC. The plant start-up was first performed using an industrial nickel-based catalyst, while new formulations were planned for next experimentation steps. The quality of the produced synthetic natural gas met the injection requirements of the gas grid ($\text{CH}_4 \geq 95\%$, $\text{H}_2 \leq 5\%$ and $\text{CO}_2 \leq 2.5\%$). The first reactor acts as the kinetic reactor, where most CO_2 conversion occurs ($T \approx 673 \text{ K}$). The second reactor acts as the equilibrium reactor ($T \approx 573 \text{ K}$) in which injectable gas quality was ensured. The use of biogas or partially upgraded biogas reduced the reaction hot-spots and increased the methane content at the outlet of the first reactor. An optimum balance of gas grid injection requirements and costs was found at 5 atm of methanation process pressure.

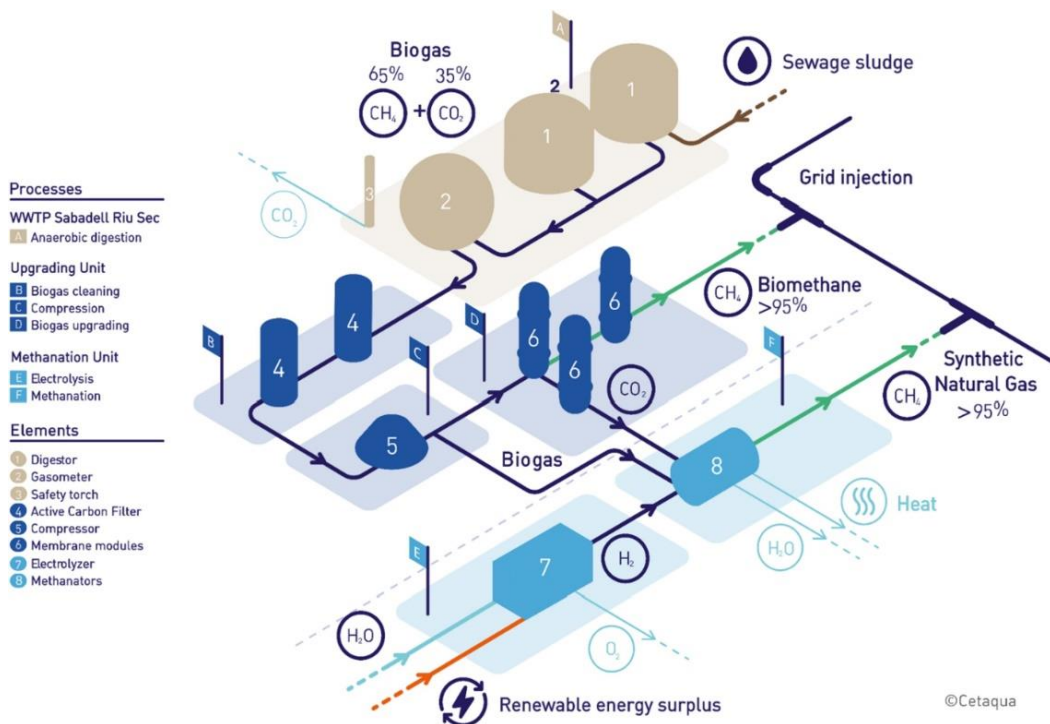


Figure 1.18. Scheme of CoSin pilot plant. Reproduced from Guilera et al. [230].

1.4. Challenges

Power-to-Gas (P2G) seems an attractive chemical energy storage technology for the transition to a sustainable low-carbon future energy system. The concept involves renewable power conversion to hydrogen through electrolysis with the possibility of further combining it with CO₂ to produce methane (synthetic natural gas, SNG). The production of methane via the thermochemical CO₂ methanation process is particularly interesting because offers an easily transportable fuel with a wide proven market for power, heat and mobility final use applications. Although Power-to-Gas is a pre-commercial technology, the high cost and low efficiency of the CO₂ methanation technology available in the market limit its large application at an industrial scale. In the last decade, novel heterogeneous catalytic systems, advanced reactor designs and several industrial process strategies have been explored in order to propose a scalable and cost-efficient CO₂ methanation technology.

According to the state-of-art hereby presented, Ni-based catalysts are preferred to be developed at industrial levels because of their excellent catalytic performance, easy availability, and low price. Nevertheless, conventional Ni/γ-Al₂O₃ catalysts often suffer the problem of poor stability from carbon deposition, sintering, and chemical poisoning. Therefore, the biggest challenge for CO₂ methanation over Ni-based catalysts is their poor stability. In this regard, strategy such as the addition of a second

active metal, the implementation of other metal oxides or mesoporous materials with controllable pore sizes, the addition of a promoter material to modify conventional γ -Al₂O₃ support, and different preparation methods have been investigated.

Ni-based catalyst combined with a second active metal material (Ru, Ph, Pt, Fe, Co) or simply supported on other metal oxides (specially from lanthanides group) present enhanced CO₂ methanation performances and stabilities compared to conventional Ni/ γ -Al₂O₃ catalysts. However, the interest in these materials from an industrial point of view is limited due to their high costs. Lanthanides are rare earth elements (REEs) less abundant, and thus more expensive. The addition of these lanthanide metal oxides as a promoter provides a most promising alternative to design stable and cost-effective Ni-based catalysts for CO₂ methanation from the perspective of improving the basicity, dispersion, and reducibility. The current catalyst design strategy consists in using of low amounts of promoter phase (<5 wt.%) and constant amount of the active phase content, which may lead to an ineffective catalyst formulation and, therefore, reduced performance with time. Therefore, efforts should be put in the exploration of new catalyst design strategies in where optimum formulations can be found to achieve competitive SNG production. The use of high promoter content as well as the simultaneous optimization of the main component of the catalytic system can be two novel design strategies to enhance performance and overcome deactivation problems of Ni-based catalysts.

Furthermore, it was demonstrated that the preservation and improvement of the metal activity can be achieved by selecting appropriate preparation methods as they influence the nature of the catalysts (such as particle size, metal dispersion, BET surface area, etc.). However, despite of the fact that some innovative preparation methods have been proposed, the synthesis scalability is still a challenge. The incipient wetness impregnation method (IWI), is usually implemented to synthesize catalysts on a large scale, but the prepared catalysts often exhibit weak metal support interactions with a low metal dispersion, especially when a high metal content is used. Wet impregnation (WI) is an alternative method for dealing with this problem. However, challenges arise when excessive amount of solution is used. Therefore, an appropriate catalyst preparation procedure is required to guarantee a homogeneous impregnation by the WI method.

Another key factor for the large scale of CO₂ methanation catalysts is their final size and shape. Internal mass transfer imitations are directly influenced by the size particle. Catalyst with an optimum size particle should be designed to minimize pore diffusion effects (small size particles) and pressure drop across the reactor (large size particles). At present, most of the reported catalysts are powder material that can be only used in the microreactor technology available in the market. These active small particles (<200 μ m) can be deposited on the microstructure surface by a washcoating

method. However, challenges arise when maintenance catalyst exchange tasks are required. The feasibility of structuring powder catalyst by coating powder catalyst over structured 3D-shape supports (such as monoliths, foam, sponge, ceramic-fiber paper, spiral plate, etc.), and using extrusion molding and 3D-printing process have been recently evaluated. The major problem in these structured catalysts is also related with the coating of the catalyst layer on the structured support. Depending on the 3D-support materials, pre- and post-treatments are mandatory to guarantee a good catalyst deposition. Therefore, active micro-sized catalysts with an appropriate shape and easy replacement procedure should be explored to intensify the process in these advanced compact reactor type.

Besides of stable CO₂ methanation catalysts with high catalytic performances at moderate temperature reaction conditions (T=523-623 K), CO₂ methanation reactor should be able to control the formation of the unpredictable high temperatures. An inefficient heat-management may result in damaging of the catalyst and the reactor itself, or in the initiation of undesired parallel or consecutive reactions. Several reactor configurations have been proposed to carry out the CO₂ methanation process, including Fixed-bed reactor under adiabatic (AFIXBR) or polytropic operation (multitubular fixed-bed reactor (MFI XBR)), fluidized bed reactor (FBR), three-phase reactor operation (TPR) and microreactor (MR). Among them, MFI XBR is the commonly used design at industrial level due to its simple and low cost. However, this reactor concept presents limitations associated to its low heat and mass transfer, leading to a poor efficient process. The reactor design optimization, especially reactor dimensions can be key parameters to be considered to eliminate or reduce transport phenomena in the reaction system. Since microreactors are designs with low heat and mass transfer limitations due to their high surface-to-volume ratio and a short distance to the wall, conventional fixed-bed reactors can be adapted as micro- and milli-fixed bed reactors. These simple reactor designs lead to an alternative low-cost reactor type with potential utilization in decentralized P2G applications.

In P2G application, the industrial process strategies proposal to achieve the equilibrium conversion can be classified as follows: i) a multi(\geq two)-stage process using adiabatic fixed-bed reactors with temperatures up to 973 K, ii) a two-stage process using multitubular fixed-bed and microstructured reactors with temperatures up to 823 K, and iii) a one-stage process using isothermal fluidised, multitubular fixed-bed and microstructured reactors. The first and second option are typically applied for large-size CO₂ methanation applications, while the third is used for small-size. Furthermore, during the last decade, several mathematical models have been developed in order to understand the role of the design parameters and operational conditions. New reactor designs with novel heat-management approaches and simple processes shall advance to push the CO₂ methanation technology, together with the catalyst design.

1.5. Scope of this research

This thesis is focused on the catalyst and reactor design for SNG production through the CO₂ methanation process. The main objectives of this thesis are:

- i. Design a high-performance catalyst based on metal oxide promoted Ni/ γ -Al₂O₃ and determine its reaction mechanism.
- ii. Evaluate the catalyst stability and sulfur tolerance for their implementation in a relevant industrial environment.
- iii. Develop a CFD model based on experimental kinetic data to understand the role of the operation conditions and propose a novel reactor configuration.

In line with these objectives, this thesis is organized as compilation of research articles as follows.

- **Chapter 2** shows the catalyst design strategy applied to develop an active-stable ternary catalytic system for CO₂ methanation process. The evaluation of a series of metal-oxide as the promoter phase (X) of the designed ternary catalytic system (Ni-X/Al₂O₃ catalyst) is presented. Moreover, an optimum global formulation (micro-sized catalyst composed by 25 wt.% Ni-20 wt.% CeO₂-55 wt.% γ -Al₂O₃) is proposed.
- **Chapter 3** presents catalytic performance evaluation and long-term stability of the optimized micro-sized catalyst under the industrial adverse condition. The presence of impurities derived from carbon sources as biogas is evaluated. In addition, the scale-up of the active micro-sized catalyst and its industrial implementation in combination with an advanced microreactor for the SNG process intensification is also presented.
- **Chapter 4** describes a CFD mathematical model coupled with kinetic experiments to simulate CO₂ methanation process and optimize over Ni-CeO₂-Al₂O₃ catalyst a multitubular reactor design for the SNG production at industrial scale. Furthermore, modelling, simulation and experimental validation of a novel reactor design with a heat management approach based on free convection for the small-scale SNG production is proposed.

The most relevant conclusions, outlook and recommendations of this work are summarized in **Chapter 5**. Besides, two **Appendixes** are added at the end of the thesis to disclose experimental data, procedures and results, not included in the main text, and to deepen on the state-of-the-art of the technology. **Appendix 1** presents five tables, in which the state-of-the-art of the proposed kinetics models, and catalysts for CO₂ methanation is presented. **Appendix 2** includes the supporting information of the published articles.

1.6. References

- [1] R. Fouquet, *Nature Energy*. 1 (2016) 16098.
- [2] BP, *Statistical review of world energy 2019*, 68th edition, 2019.
- [3] Allen, M.R., O.P. Dube, W. Solecki, F. Aragón-Durand, W. Cramer, S. Humphreys, M. Kainuma, J. Kala, N. Mahowald, Y. MuLugetta, R. Perez, M. Wairiu, K. Zickfeld, *An IPCC Special Report on the impacts of global warming of 1.5°C above pre-industrial levels and related global greenhouse gas emission pathways.*, 2018.
- [4] N.L. Panwar, S.C. Kaushik, S. Kothari, *Renewable and Sustainable Energy Reviews*. 15 (2011) 1513–1524.
- [5] O. Ellabban, H. Abu-Rub, F. Blaabjerg, *Renewable and Sustainable Energy Reviews*. 39 (2014) 748–764.
- [6] A. Maroufmashat, M. Fowler, *Energies*. 10 (2017).
- [7] H. Blanco, A. Faaij, *Renewable and Sustainable Energy Reviews*. 81 (2018) 1049–1086.
- [8] C.J. Quarton, S. Samsatli, *Applied Energy*. 257 (2020) 113936.
- [9] A. Ajanovic, R. Haas, *Wiley Interdisciplinary Reviews: Energy and Environment*. 8 (2019) e318.
- [10] N. Ali, M. Bilal, M.S. Nazir, A. Khan, F. Ali, H.M.N. Iqbal, *Science of the Total Environment*. 712 (2020).
- [11] R. Değbek, F. Azzolina-Jury, A. Travert, F. Maugé, *Renewable and Sustainable Energy Reviews*. 116 (2019).
- [12] K. Ghaib, K. Nitz, F.-Z. Ben-Fares, *ChemBioEng Reviews*. 3 (2016) 266–275.
- [13] V. Kumaravel, J. Bartlett, S.C. Pillai, *ACS Energy Letters*. (2020) 486–519.
- [14] J. Guilera, J. Ramon Morante, T. Andreu, *Energy Conversion and Management*. 162 (2018) 218–224.
- [15] M. Di Salvo, M. Wei, *Energy*. 182 (2019) 1250–1264.
- [16] M. Thema, T. Weidlich, M. Hörl, A. Bellack, F. Mörs, F. Hackl, M. Kohlmayer, J. Gleich, C. Stabenau, T. Trabold, M. Neubert, F. Ortlo, R. Brotsack, D. Schmack, H. Huber, D. Hafenbradl, J. Karl, M. Sterner, *Energies*. 12 (2019) 1–32.
- [17] A.G. Morachevskii, *Russian Journal of Applied Chemistry*. 77 (2004) 1909–1912.
- [18] I. Kuznecova, J. Gusca, *Energy Procedia*. 128 (2017) 255–260.
- [19] NIST Standard Reference Database 13, (1985). <https://janaf.nist.gov/>.
- [20] Y. Lwin, *International Journal of Engineering Education*. 16 (2000) 335–339.
- [21] J. Gao, Y. Wang, Y. Ping, D. Hu, G. Xu, F. Gu, F. Su, *RSC Advances*. 2 (2012) 2358–2368.
- [22] A. Swapnesh, V.C. Srivastava, I.D. Mall, *Chemical Engineering and Technology*. 37 (2014) 1765–1777.
- [23] S. Sahebdehfar, M. Takht Ravanchi, *Journal of Petroleum Science and Engineering*. 134 (2015) 14–22.
- [24] C. V. Miguel, M.A. Soria, A. Mendes, L.M. Madeira, *Journal of Natural Gas Science and Engineering*. 22 (2015) 1–8.
- [25] A. Catarina Faria, C. V. Miguel, L.M. Madeira, *Journal of CO2 Utilization*. 26 (2018) 271–280.
- [26] E.I. Koysoumpa, S. Karellas, *Renewable and Sustainable Energy Reviews*. 94 (2018) 536–550.
- [27] G.D. Weatherbee, C.H. Bartholomew, *Journal of Catalysis*. 77 (1982) 460–472.
- [28] D.E. Peebles, D.W. Goodman, J.M. White, *Journal of Physical Chemistry*. 87 (1983) 4378–4387.
- [29] S. Fujita, H. Terunuma, M. Nakamura, N. Takezawa, *Industrial & Engineering Chemistry Research*. 30 (1991) 1146–1151.
- [30] H. Muroyama, Y. Tsuda, T. Asakoshi, H. Masitah, T. Okanishi, T. Matsui, K. Eguchi, *Journal of Catalysis*. 343 (2016) 178–184.
- [31] C. Cerdá-Moreno, A. Chica, S. Keller, C. Rautenberg, U. Bentrup, *Applied Catalysis B: Environmental*. 264 (2020).
- [32] S. Fujita, M. Nakamura, T. Doi, N. Takezawa, *Applied Catalysis A: General*. 104 (1993) 87–100.
- [33] S.M. Lee, Y.H. Lee, D.H. Moon, J.Y. Ahn, D.D. Nguyen, S.W. Chang, S.S. Kim, *Industrial & Engineering Chemistry Research*. (2019) [acs.iecr.9b00983](https://doi.org/10.1021/acs.iecr.9b00983).
- [34] R. Ye, Q. Li, W. Gong, T. Wang, J. James, L. Lin, Y. Qin, Z. Zhou, H. Adidharma, J. Tang, A.G. Russell, M. Fan, Y. Yao, *Applied Catalysis B: Environmental*. 268 (2019) 118474.
- [35] A. Cárdenas-Arenas, A. Quindimil, A. Davó-Quiñonero, E. Bailón-García, D. Lozano-Castelló, U. De-La-Torre, B. Pereda-Ayo, J.A. González-Marcos, J.R. González-Velasco, A. Bueno-López, *Applied Catalysis B: Environmental*. 265 (2020) 118538.
- [36] J. Huang, X. Li, X. Wang, X. Fang, H. Wang, X. Xu, *Journal of CO2 Utilization*. 33 (2019) 55–63.
- [37] Z. Zhang, Y. Tian, L. Zhang, S. Hu, J. Xiang, Y. Wang, L. Xu, Q. Liu, S. Zhang, X. Hu, *International Journal of Hydrogen Energy*. 44 (2019) 9291–9306.
- [38] R. Zhou, N. Rui, Z. Fan, C. Liu, *International Journal of Hydrogen Energy*. 41 (2016) 22017–22025.

- [39] P.A.U. Aldana, F. Ocampo, K. Kobl, B. Louis, F. Thibault-Starzyk, M. Daturi, P. Bazin, S. Thomas, A.C. Roger, *Catalysis Today*. 215 (2013) 201–207.
- [40] Q. Pan, J. Peng, T. Sun, S. Wang, S. Wang, *Catalysis Communications*. 45 (2014) 74–78.
- [41] J. Ashok, M.L. Ang, S. Kawi, *Catalysis Today*. 281 (2017) 304–311.
- [42] A. Solis-Garcia, J.F. Louvier-Hernandez, A. Almendarez-Camarillo, J.C. Fierro-Gonzalez, *Applied Catalysis B: Environmental*. 218 (2017) 611–620.
- [43] Z. Bian, Y.M. Chan, Y. Yu, S. Kawi, *Catalysis Today*. (2018).
- [44] C. Liang, L. Zhang, Y. Zheng, S. Zhang, Q. Liu, G. Gao, D. Dong, Y. Wang, L. Xu, X. Hu, *Fuel*. 262 (2020).
- [45] X. Guo, H. He, A. Traitangwong, M. Gong, V. Meeyoo, P. Li, C. Li, Z. Peng, S. Zhang, *Catalysis Science and Technology*. 9 (2019) 5636–5650.
- [46] Le, Kim, Jeong, Park, *Catalysts*. 9 (2019) 599.
- [47] Y. Yan, Y. Dai, H. He, Y. Yu, Y. Yang, 'Applied Catalysis B, Environmental'. 196 (2016) 108–116.
- [48] H. Takano, Y. Kirihaata, K. Izumiya, N. Kumagai, H. Habazaki, K. Hashimoto, *Applied Surface Science*. 388 (2016) 653–663.
- [49] M.A.A. Aziz, A.A. Jalil, S. Triwahyono, S.M. Sidik, *Applied Catalysis A: General*. 486 (2014) 115–122.
- [50] Y. Yu, Y.M. Chan, Z. Bian, F. Song, J. Wang, Q. Zhong, S. Kawi, *International Journal of Hydrogen Energy*. 43 (2018) 15191–15204.
- [51] Y. Yu, Z. Bian, F. Song, J. Wang, Q. Zhong, S. Kawi, *Topics in Catalysis*. 61 (2018) 1514–1527.
- [52] A. Westermann, B. Azambre, M.C. Bacariza, I. Graça, M.F. Ribeiro, J.M. Lopes, C. Henriques, *Applied Catalysis B: Environmental*. 174–175 (2015) 120–125.
- [53] G.G. Binder, R.R. White, *Chem. Eng. Prog.* 46 (1950) 563–574.
- [54] J.N. Dew, R.R. White, C.M. Sliepcevich, Hydrogenation of carbon dioxide on Nickel-Kieselguhr catalyst, in: de Vries (Ed.), *Fourth Chemical and Petroleum Engineering Conference*, Georg Thieme Verlag, Stuttgart, 1954: pp. 140–146.
- [55] T. Herwijnen, H. Doesburg, W.A. de Jong, *Journal of Catalysis*. 28 (1973) 391–402.
- [56] J.H. Chiang, J.R. Hopper, *Industrial and Engineering Chemistry Product Research and Development*. 22 (1983) 225–228.
- [57] H. Inoue, M. Funakoshi, *Journal of Chemical Engineering of Japan*. 17 (1984) 602–610.
- [58] T. Kai, T. Takahashi, S. Furusaki, *The Canadian Journal of Chemical Engineering*. 66 (1988) 0–4.
- [59] J. Xu, G.F. Froment, *AIChE Journal*. 35 (1989) 88–96.
- [60] F. Koschany, D. Schlereth, O. Hinrichsen, *Applied Catalysis B: Environmental*. 181 (2016) 504–516.
- [61] R.A. Hubble, J.Y. Lim, J.S. Dennis, *Faraday Discussions*. 192 (2016) 529–544.
- [62] M. Martinez Molina, C. Kern, A. Jess, *Chemical Engineering & Technology*. 39 (2016) 2404–2415.
- [63] J. Ducamp, A. Bengaouer, P. Baurens, Modelling and experimental validation of a CO₂ methanation annular cooled fixed-bed reactor exchanger, in: *Canadian Journal of Chemical Engineering*, 2017: pp. 241–252.
- [64] C. V. Miguel, A. Mendes, L.M. Madeira, *Journal of CO₂ Utilization*. 25 (2018) 128–136.
- [65] P. Marocco, E.A. Morosanu, E. Giglio, D. Ferrero, C. Mebrahtu, A. Lanzini, S. Abate, S. Bensaid, S. Perathoner, M. Santarelli, R. Pirone, G. Centi, *Fuel*. 225 (2018) 230–242.
- [66] I. Champon, A. Bengaouer, A. Chaise, S. Thomas, A. Roger, *Journal of CO₂ Utilization*. 34 (2019) 256–265.
- [67] S. Farsi, W. Olbrich, P. Pfeifer, R. Dittmeyer, *Chemical Engineering Journal*. 388 (2020) 124233.
- [68] J.A. Hernandez Lalinde, P. Roongruangsree, J. Ilsemann, M. Bäumer, J. Kopyscinski, *Chemical Engineering Journal*. 390 (2020).
- [69] E.A. Morosanu, F. Salomone, R. Pirone, S. Bensaid, *Catalysts*. 10 (2020).
- [70] H.S. Folger, M.N. Gurmen, *Essentials of Chemical Reaction Engineering*. (2008) 813–866.
- [71] M. Boudart, E.S. Lewis, J. Wiley, (n.d.).
- [72] S. Rönsch, S. Matthischke, M. Müller, P. Eichler, *Chemie-Ingenieur-Technik*. 86 (2014) 1198–1204.
- [73] T.J. Schildhauer, S.M.A. Biollaz, *Chimia*. 69 (2015) 603–607.
- [74] J. Bremer, K. Sundmacher, *Reaction Chemistry and Engineering*. 4 (2019) 1019–1037.
- [75] C. Jia, Y. Dai, Y. Yang, J.W. Chew, *Particuology*. 49 (2020) 55–64.
- [76] M. Held, D. Schollenberger, S. Sauersschell, S. Bajohr, T. Kolb, *Chemie-Ingenieur-Technik*. 92 (2020) 595–602.
- [77] J. Lefebvre, S. Bajohr, T. Kolb, *Renewable Energy*. 151 (2020) 118–136.
- [78] J. Lefebvre, M. Götz, S. Bajohr, R. Reimert, T. Kolb, *Fuel Processing Technology*. 132 (2015) 83–90.
- [79] R. Dittmeyer, T. Boeltken, P. Piermartini, M. Selinsek, M. Loewert, F. Dallmann, H. Kreuder, M. Cholewa, A. Wunsch, M. Belimov, S. Farsi, P. Pfeifer, *Current Opinion in Chemical Engineering*.

- 17 (2017) 108–125.
- [80] S. Pérez, J.J. Aragón, I. Peciña, E.J. Garcia-Suarez, *Topics in Catalysis*. (2019).
- [81] N. Engelbrecht, S. Chiuta, R.C. Everson, H.W.J.P. Neomagus, D.G. Bessarabov, *Chemical Engineering Journal*. 313 (2017) 847–857.
- [82] D. Schollenberger, S. Bajohr, M. Gruber, R. Reimert, T. Kolb, *Chemie-Ingenieur-Technik*. 90 (2018) 696–702.
- [83] P. Pfeifer, M. Belimov, WO2017211864-Micro-reactor and method implementation for methanation, 2017. <https://patentscope.wipo.int/search/en/detail.jsf?docId=WO2017211864&tab=PCTBIBLIO>.
- [84] M. Gruber, C. Wieland, P. Habisreuther, D. Trimis, D. Schollenberger, S. Bajohr, O. VonMorstein, S. Schirmeister, *Chemie Ingenieur Technik*. 90 (2018) 615–624.
- [85] N. Engelbrecht, R.C. Everson, D. Bessarabov, *Fuel Processing Technology*. 208 (2020) 106508.
- [86] M. Frey, T. Romero, A.C. Roger, D. Edouard, *Chemical Engineering Science*. 195 (2019) 271–280.
- [87] T. Stiegler, K. Meltzer, A. Tremel, M. Baldauf, P. Wasserscheid, J. Albert, *Energy Technology*. 7 (2019) 1900047.
- [88] M. Weiss, S. Walter, U. Berger, *Lurgi's Methanation Technology for Production of SNG from Coal*, in: *Gasification Technologies Conference*, 2008.
- [89] J.H. Jensen, J.M. Poulsen, N.U. Andersen, *From coal to clean energy*, 2011.
- [90] L. Romano, F. Ruggeri, *Energy Procedia*. 81 (2015) 249–254.
- [91] J. Matthey, (2020). <https://matthey.com/en/products-and-services/chemical-processes/core-technologies/methanation-technology>.
- [92] H.Z.E. GmbH, *EtoGas Power-to-Gas Technology Converting Electricity into Renewable Gases Converting Volatile Electricity into Renewable , Synthetic Gases for a Carbon-Neutral Economy*, 2017.
- [93] MAN Diesel & Turbo, (2020) 11.
- [94] INERATEC, (2020). <https://ineratec.de/technologien/?lang=en&lang=en>.
- [95] J.J. Lerou, A.L. Tonkovich, L. Silva, S. Perry, J. McDaniel, *Chemical Engineering Science*. 65 (2010) 380–385.
- [96] ATMOSTAT, (2020). <https://www.atmostat-alcen.com/en/products/exchangers-reactors>.
- [97] L. Kiewidt, J. Thöming, *Chemical Engineering Science*. 132 (2015) 59–71.
- [98] A. Fache, F. Marias, V. Guerré, S. Palmade, *Chemical Engineering Science*. 192 (2018) 1124–1137.
- [99] E. Moioli, N. Gallandat, A. Züttel, *Reaction Chemistry & Engineering*. 4 (2019) 100–111.
- [100] R. Currie, S. Mottaghi-tabar, Y. Zhuang, D.S.A. Simakov, *Industrial & Engineering Chemistry Research*. 58 (2019) 12964–12980.
- [101] W. Zhang, H. Machida, H. Takano, K. Izumiya, K. Norinaga, *Chemical Engineering Science*. (2019) 115276.
- [102] E. Moioli, N. Gallandat, A. Züttel, *Chemical Engineering Journal*. (2019) 121954.
- [103] W. Wang, S. Wang, X. Ma, J. Gong, *Chemical Society Reviews*. 40 (2011) 3703–3727.
- [104] J.A. Dumesic, G.W. Huber, M. Boudart, *Introduction: Principles of heterogeneous catalysis*, n.d.
- [105] S. Sharma, Z. Hu, P. Zhang, E.W. McFarland, H. Metiu, *Journal of Catalysis*. 278 (2011) 297–309.
- [106] Y. Yan, Q. Wang, C. Jiang, Y. Yao, D. Lu, J. Zheng, Y. Dai, H. Wang, Y. Yang, *Journal of Catalysis*. 367 (2018) 194–205.
- [107] G. Garbarino, D. Bellotti, P. Riani, L. Magistri, G. Busca, *International Journal of Hydrogen Energy*. 40 (2015) 9171–9182.
- [108] A. Karelövic, P. Ruiz, *ACS Catalysis*. 3 (2013) 2799–2812.
- [109] H. Choi, S. Oh, J.Y. Park, *Catalysis Today*. 352 (2020) 212–219.
- [110] N.M. Martin, P. Velin, M. Skoglundh, M. Bauer, P.A. Carlsson, *Catalysis Science and Technology*. 7 (2017) 1086–1094.
- [111] G. Garbarino, P. Riani, L. Magistri, G. Busca, *International Journal of Hydrogen Energy*. 39 (2014) 11557–11565.
- [112] T. Franken, A. Heel, *Journal of CO2 Utilization*. 39 (2020).
- [113] P. Riani, G. Garbarino, T. Cavattoni, F. Canepa, G. Busca, *International Journal of Hydrogen Energy*. 44 (2019) 27319–27328.
- [114] G. Garbarino, T. Cavattoni, P. Riani, G. Busca, *Catalysis Today*. 345 (2020) 213–219.
- [115] H. Liu, S. Xu, G. Zhou, K. Xiong, Z. Jiao, S. Wang, *Fuel*. 217 (2018) 570–576.
- [116] G. Amica, S.R. Azcona, S. Aparicio, F.C. Gennari, *Physical Chemistry Chemical Physics : PCCP*. (2020) 14720–14730.
- [117] T. Sakpal, L. Lefferts, *Journal of Catalysis*. 367 (2018) 171–180.
- [118] S. Tada, O.J. Ochieng, R. Kikuchi, T. Haneda, H. Kameyama, *International Journal of Hydrogen Energy*. 39 (2014) 10090–10100.

- [119] S. Navarro-Jaén, J.C. Navarro, L.F. Bobadilla, M.A. Centeno, O.H. Laguna, J.A. Odriozola, *Applied Surface Science*. 483 (2019) 750–761.
- [120] Z. Qi, L. Chen, S. Zhang, J. Su, G.A. Somorjai, *Applied Catalysis A: General*. 602 (2020).
- [121] J.A. Moulijn, P.W.N.M. van Leeuwen, R.A. van Santen, *Catalysis: An integrated approach to homogeneous, heterogeneous and industrial catalyst*, 1993.
- [122] S. Ewald, M. Kolbeck, T. Kratky, M. Wolf, O. Hinrichsen, *Applied Catalysis A: General*. 570 (2019) 376–386.
- [123] M. Wolf, L.H. Wong, C. Schüller, O. Hinrichsen, *Journal of CO2 Utilization*. 36 (2020) 276–287.
- [124] D. Méndez-Mateos, V.L. Barrio, J.M. Requies, J.F. Cambra, *RSC Advances*. 10 (2020) 16551–16564.
- [125] B. Legras, V. V. Ordonsky, C. Dujardin, M. Virginie, A.Y. Khodakov, *ACS Catalysis*. 4 (2014) 2785–2791.
- [126] K. Müller, M. Fleige, F. Rachow, D. Schmeißer, *Energy Procedia*. 40 (2013) 240–248.
- [127] D. Pandey, G. Deo, *Journal of Industrial and Engineering Chemistry*. 33 (2016) 99–107.
- [128] M. Mihet, M.D. Lazar, *Catalysis Today*. 306 (2018) 294–299.
- [129] L. Xu, X. Lian, M. Chen, Y. Cui, F. Wang, W. Li, B. Huang, *International Journal of Hydrogen Energy*. 43 (2018) 17172–17184.
- [130] R.-Y. Chein, C.-C. Wang, *Catalysts*. 10 (2020) 1112.
- [131] W. Zhen, B. Li, G. Lu, J. Ma, *RSC Advances*. 4 (2014) 16472–16479.
- [132] M. Rahmani, M. Rezaei, F. Meshkani, *Chemical Engineering and Technology*. 38 (2015) 1637–1645.
- [133] S. Tada, T. Shimizu, H. Kameyama, T. Haneda, R. Kikuchi, *International Journal of Hydrogen Energy*. 37 (2012) 5527–5531.
- [134] T.A. Le, T.W. Kim, S.H. Lee, E.D. Park, *Catalysis Today*. 303 (2018) 159–167.
- [135] L.R. Winter, E. Gomez, B. Yan, S. Yao, J.G. Chen, *Applied Catalysis B: Environmental*. 224 (2018) 442–450.
- [136] H.C. Wu, Y.C. Chang, J.H. Wu, J.H. Lin, I.K. Lin, C.S. Chen, *Catalysis Science and Technology*. 5 (2015) 4154–4163.
- [137] G. Zhou, H. Liu, Y. Xing, S. Xu, H. Xie, K. Xiong, *Journal of CO2 Utilization*. 26 (2018) 221–229.
- [138] R. Zhou, N. Rui, Z. Fan, C. jun Liu, *International Journal of Hydrogen Energy*. 41 (2016) 22017–22025.
- [139] M. Yamasaki, H. Habazaki, K. Asami, K. Izumiya, K. Hashimoto, *Catalysis Communications*. 7 (2006) 24–28.
- [140] H. Takano, H. Shinomiya, K. Izumiya, N. Kumagai, H. Habazaki, K. Hashimoto, *International Journal of Hydrogen Energy*. 40 (2015) 8347–8355.
- [141] O.E. Everett, P.C. Zonetti, O.C. Alves, R.R. de Avillez, L.G. Appel, *International Journal of Hydrogen Energy*. 45 (2020) 6352–6359.
- [142] J. Ren, X. Qin, J.Z. Yang, Z.F. Qin, H.L. Guo, J.Y. Lin, Z. Li, *Fuel Processing Technology*. 137 (2015) 204–211.
- [143] K. Zhao, W. Wang, Z. Li, *Journal of CO2 Utilization*. 16 (2016) 236–244.
- [144] Y. Yan, Y. Dai, H. He, Y. Yu, Y. Yang, 'Applied Catalysis B, Environmental'. 196 (2016) 108–116.
- [145] Y. Yan, Y. Dai, Y. Yang, A.A. Lapkin, *Applied Catalysis B: Environmental*. 237 (2018) 504–512.
- [146] C. Italiano, J. Llorcab, L. Pinoa, M. Ferraro, V. Antonuccia, A. Vitaa, *Applied Catalysis A: General*. (2020).
- [147] H. Song, J. Yang, J. Zhao, L. Chou, *Chinese Journal of Catalysis*. 31 (2010) 21–23.
- [148] P.A.U. Aldana, F. Ocampo, K. Kobl, B. Louis, F. Thibault-Starzyk, M. Daturi, P. Bazin, S. Thomas, A.C. Roger, *Catalysis Today*. 215 (2013) 201–207.
- [149] V. Meeyoo, N. Panchan, N. Phongprueksathat, A. Traitangwong, X. Guo, C. Li, T. Rirksomboon, *Catalysts*. 10 (2020) 1–10.
- [150] L. Pastor-Pérez, V. Patel, E. Le Saché, T.R. Reina, *Journal of the Energy Institute*. 93 (2020) 415–424.
- [151] F. Ocampo, B. Louis, L. Kiwi-Minsker, A.C. Roger, *Applied Catalysis A: General*. 392 (2011) 36–44.
- [152] J.K. Kesavan, I. Luisetto, S. Tuti, C. Meneghini, C. Battocchio, G. Iucci, *Journal of Materials Science*. 52 (2017) 10331–10340.
- [153] Y. Zhan, Y. Wang, D. Gu, C. Chen, L. Jiang, K. Takehira, *Applied Surface Science*. 459 (2018) 74–79.
- [154] S. Abate, C. Mebrahtu, E. Giglio, F. Deorsola, S. Bensaid, S. Perathoner, R. Pirone, G. Centi, *Industrial & Engineering Chemistry Research*. 55 (2016) 4451–4460.
- [155] O. Grad, M. Mihet, G. Blanita, M. Dan, L. Barbu-Tudoran, M.D. Lazar, *Catalysis Today*. (2020).
- [156] P. Frontera, A. Malara, V. Modafferi, V. Antonucci, P. Antonucci, A. Macario, *The Canadian Journal of Chemical Engineering*. (2020).
- [157] Q. Liu, S. Wang, G. Zhao, H. Yang, M. Yuan, X. An, H. Zhou, Y. Qiao, Y. Tian, *International*

- Journal of Hydrogen Energy. 43 (2018) 239–250.
- [158] M.C. Bacariza, I. Graça, S.S. Bebiano, J.M. Lopes, C. Henriques, Chemical Engineering Science. 175 (2018) 72–83.
- [159] M.A.A. Aziz, A.A. Jalil, S. Triwahyono, R.R. Mukti, Y.H. Taufiq-Yap, M.R. Sazegar, Applied Catalysis B: Environmental. 147 (2014) 359–368.
- [160] Y. Feng, W. Yang, S. Chen, W. Chu, Cerium promoted nano nickel catalysts Ni-Ce/CNTs and Ni-Ce/Al₂O₃ for CO₂ methanation, in: Integrated Ferroelectrics, 2014: pp. 116–125.
- [161] Y. Feng, W. Yang, W. Chu, Integrated Ferroelectrics. 172 (2016) 40–48.
- [162] M. Romero-Sáez, A.B. Dongil, N. Benito, R. Espinoza-González, N. Escalona, F. Gracia, Applied Catalysis B: Environmental. 237 (2018) 817–825.
- [163] J. Li, Y. Zhou, X. Xiao, W. Wang, N. Wang, W. Qian, W. Chu, ACS Applied Materials and Interfaces. 10 (2018) 41224–41236.
- [164] W. Wang, C. Duong-Viet, H. Ba, W. Baaziz, G. Tuci, S. Caporali, L. Nguyen-Dinh, O. Ersen, G. Giambastiani, C. Pham-Huu, ACS Applied Energy Materials. 2 (2019) 1111–1120.
- [165] R. Goyal, W.J. Lee, S. Sameer, B. Sarkar, K. Chiang, A. Bordoloi, Catalysis Today. 343 (2020) 48–55.
- [166] I. Graça, L. V. González, M.C. Bacariza, A. Fernandes, C. Henriques, J.M. Lopes, M.F. Ribeiro, Applied Catalysis B: Environmental. 147 (2014) 101–110.
- [167] S. Walspurger, G.D. Elzinga, J.W. Dijkstra, M. Sarić, W.G. Haije, Chemical Engineering Journal. 242 (2014) 379–386.
- [168] A. Borgschulte, E. Callini, N. Stadie, Y. Arroyo, M.D. Rossell, R. Erni, H. Geerlings, A. Züttel, D. Ferri, Catalysis Science and Technology. 5 (2015) 4613–4621.
- [169] L. Wei, W. Haije, N. Kumar, J. Peltonen, M. Peurla, H. Grenman, W. de Jong, Catalysis Today. (2020).
- [170] N. Czuma, K. Zarębska, M. Motak, M.E. Gálvez, P. Da Costa, Fuel. 267 (2020).
- [171] M.C. Bacariza, R. Bértolo, I. Graça, J.M. Lopes, C. Henriques, Journal of CO₂ Utilization. 21 (2017) 280–291.
- [172] G. Paglia, C.E. Buckley, A.L. Rohl, R.D. Hart, K. Winter, A.J. Studer, B.A. Hunter, J. V. Hanna, Chemistry of Materials. 16 (2004) 220–236.
- [173] M. Trueba, S.P. Trasatti, European Journal of Inorganic Chemistry. (2005) 3393–3403.
- [174] J. Gao, Q. Liu, F. Gu, B. Liu, Z. Zhong, F. Su, RSC Advances. 5 (2015) 22759–22776.
- [175] M. Li, H. Amari, A.C. van Veen, Applied Catalysis B: Environmental. 239 (2018) 27–35.
- [176] G. Zhou, H. Liu, K. Cui, A. Jia, G. Hu, Z. Jiao, Y. Liu, X. Zhang, Applied Surface Science. 383 (2016) 248–252.
- [177] M.C. Bacariza, I. Graça, J.M. Lopes, C. Henriques, ChemCatChem. 11 (2019) 2388–2400.
- [178] Y. Chen, B. Qiu, Y. Liu, Y. Zhang, Applied Catalysis B: Environmental. 269 (2020).
- [179] W. Xiao-liu, Y. Meng, Z.H.U. Ling-jun, Z.H.U. Xiao-nan, W. Shu-rong, Journal of Fuel Chemistry and Technology. 48 (2020).
- [180] W. Zhen, B. Li, G. Lu, J. Ma, Chemical Communications. 51 (2015) 1728–1731.
- [181] H. Cao, W. Wang, T. Cui, H. Wang, G. Zhu, X. Ren, Energies. 13 (2020).
- [182] G. Wang, S. Xu, L. Jiang, C. Wang, International Journal of Hydrogen Energy. 41 (2016) 12910–12919.
- [183] T.A. Le, J. Kim, J.K. Kang, E.D. Park, Catalysis Today. 19 (2019) 3252–3262.
- [184] C. Liang, Z. Gao, H. Lian, X. Li, S. Zhang, Q. Liu, D. Dong, X. Hu, International Journal of Hydrogen Energy. 45 (2020) 16153–16160.
- [185] C. Lv, L. Xu, M. Chen, Y. Cui, X. Wen, C. e. Wu, B. Yang, F. Wang, Z. Miao, X. Hu, Q. Shou, Fuel. 278 (2020).
- [186] H. Liu, X. Zou, X. Wang, X. Lu, W. Ding, Journal of Natural Gas Chemistry. 21 (2012) 703–707.
- [187] L. Zhou, Q. Wang, L. Ma, J. Chen, J. Ma, Z. Zi, Catalysis Letters. 145 (2015) 612–619.
- [188] S. Rahmani, M. Rezaei, F. Meshkani, Journal of Industrial and Engineering Chemistry. 20 (2014) 4176–4182.
- [189] D.E. Rivero-Mendoza, J.N.G. Stanley, J. Scott, K.F. Aguey-Zinsou, Catalysts. 6 (2016) 1–15.
- [190] G. Garbarino, C. Wang, T. Cavattoni, E. Finocchio, P. Riani, M. Flytzani-Stephanopoulos, G. Busca, Applied Catalysis B: Environmental. 248 (2019) 286–297.
- [191] W. Ahmad, M.N. Younis, R. Shawabkeh, S. Ahmed, Catalysis Communications. 100 (2017) 121–126.
- [192] K. Zhao, Z. Li, L. Bian, Frontiers of Chemical Science and Engineering. 10 (2016) 273–280.
- [193] R. Darougehi, F. Meshkani, M. Rezaei, Journal of the Energy Institute. 93 (2020) 482–495.
- [194] L. Xu, H. Yang, M. Chen, F. Wang, D. Nie, L. Qi, X. Lian, H. Chen, M. Wu, Journal of CO₂ Utilization. 21 (2017) 200–210.
- [195] A. Isah, I. Akanyeti, A.A. Oladipo, Reaction Kinetics, Mechanisms and Catalysis. 130 (2020) 217–228.
- [196] F.W. Chang, M.S. Kuo, M.T. Tsay, M.C. Hsieh, Applied Catalysis A: General. 247 (2003) 309–

- 320.
- [197] J.K. Kesavan, I. Luisetto, S. Tuti, C. Meneghini, G. Iucci, C. Battocchio, S. Mobilio, S. Casciardi, R. Sisto, *Journal of CO2 Utilization*. 23 (2018) 200–211.
- [198] M. Guo, G. Lu, *Catalysis Communications*. 54 (2014) 55–60.
- [199] J. Liu, C. Li, F. Wang, S. He, H. Chen, Y. Zhao, M. Wei, D.G. Evans, X. Duan, *Catalysis Science and Technology*. 3 (2013) 2627–2633.
- [200] A. Aljishi, G. Veilleux, J.A.H. Lalinde, J. Kopyscinski, *Applied Catalysis A: General*. 549 (2018) 263–272.
- [201] W.L. Vrijburg, J.W.A. Van Helden, A. Parastaev, E. Groeneveld, E.A. Pidko, E.J.M. Hensen, *Catalysis Science and Technology*. 9 (2019) 5001–5010.
- [202] F. Zhang, B. Lu, P. Sun, *International Journal of Hydrogen Energy*. (2020).
- [203] L. Atzori, M.G. Cutrufello, D. Meloni, R. Monaci, C. Cannas, D. Gazzoli, M.F. Sini, P. Deiana, E. Rombi, *International Journal of Hydrogen Energy*. 42 (2017) 20689–20702.
- [204] N.A.A. Fatah, A.A. Jalil, N.F.M. Salleh, M.Y.S. Hamid, Z.H. Hassan, M.G.M. Nawawi, *International Journal of Hydrogen Energy*. (2019).
- [205] R.P. Ye, W. Gong, Z. Sun, Q. Sheng, X. Shi, T. Wang, Y. Yao, J.J. Razink, L. Lin, Z. Zhou, H. Adidharma, J. Tang, M. Fan, Y.G. Yao, *Energy*. 188 (2019).
- [206] Clariant, (2019). <https://www.clariant.com/es/Solutions/Products/2019/03/13/08/18/METH-134>.
- [207] J. Matthey, (2020). <https://matthey.com/en/products-and-services/chemical-processes/chemical-catalysts/methanation-catalysts>.
- [208] H. Topsøe, (2020). <https://www.topsoe.com/products/catalysts/pk-7r?hsLang=en>.
- [209] A. Bengaouer, J. Ducamp, I. Champon, R. Try, *Canadian Journal of Chemical Engineering*. 96 (2018) 1937–1945.
- [210] C. Fukuhara, K. Hayakawa, Y. Suzuki, W. Kawasaki, R. Watanabe, *Applied Catalysis A: General*. 532 (2017) 12–18.
- [211] A. Vita, C. Italiano, L. Pino, P. Frontera, M. Ferraro, V. Antonucci, *Applied Catalysis B: Environmental*. 226 (2018) 384–395.
- [212] J.C. Navarro, M.A. Centeno, O.H. Laguna, J.A. Odriozola, *Renewable Energy*. 161 (2020) 120–132.
- [213] F. Kosaka, T. Yamaguchi, Y. Ando, T. Mochizuki, H. Takagi, K. Matsuoka, Y. Fujishiro, K. Kuramoto, *International Journal of Hydrogen Energy*. 45 (2020) 12911–12920.
- [214] A. Ricca, L. Truda, V. Palma, *Chemical Engineering Journal*. 377 (2019) 120461.
- [215] M. Frey, D. Édouard, A.C. Roger, *Comptes Rendus Chimie*. 18 (2015) 283–292.
- [216] Y. Li, Q. Zhang, R. Chai, G. Zhao, Y. Liu, Y. Lu, F. Cao, *AIChE Journal*. 61 (2015) 4323–4331.
- [217] S. Tada, S. Ikeda, N. Shimoda, T. Honma, M. Takahashi, A. Nariyuki, S. Satokawa, *International Journal of Hydrogen Energy*. 42 (2017) 30126–30134.
- [218] C. Fukuhara, S. Ratchahat, A. Kamiyama, M. Sudoh, R. Watanabe, *Chemistry Letters*. 48 (2019) 441–444.
- [219] A. Sánchez, V.G. Milt, E.E. Miró, R. Güttel, *Industrial & Engineering Chemistry Research*. 59 (2020) 16539–16552.
- [220] V. Middelkoop, A. Vamvakeros, D. De Wit, S.D.M. Jacques, S. Danaci, C. Jacquot, Y. De Vos, D. Matras, S.W.T. Price, A.M. Beale, *Journal of CO2 Utilization*. 33 (2019) 478–487.
- [221] IEA, (2020). <https://www.iea.org/reports/hydrogen-projects-database>.
- [222] M. Bailera, P. Lisbona, L.M. Romeo, S. Espatolero, *Renewable and Sustainable Energy Reviews*. 69 (2017) 292–312.
- [223] STORE&GO, *Innovative large-scale energy storage technologies and Power-to-Gas concepts after optimisation*, 2015.
- [224] GRTgaz, (2019). <https://www.jupiter1000.eu/>.
- [225] M. Gruber, P. Weinbrecht, L. Biffar, S. Harth, D. Trimis, J. Brabandt, O. Posdziech, R. Blumentritt, *Fuel Processing Technology*. 181 (2018) 61–74.
- [226] N. Gallandat, R. Mutschler, V. Vernay, H. Yang, A. Züttel, *Sustainable Energy and Fuels*. 2 (2018) 1101–1110.
- [227] C. Bassano, P. Deiana, L. Lietti, C.G. Visconti, *Fuel*. 253 (2019) 1071–1079.
- [228] J. Witte, A. Calbry-Muzyka, T. Wieseler, P. Hottinger, S.M.A. Biollaz, T.J. Schildhauer, *Applied Energy*. 240 (2019) 359–371.
- [229] T. Chwoła, T. Spietz, L. Więclaw-Solny, A. Tatarczuk, A. Krótki, S. Dobras, A. Wilk, J. Tchórz, M. Stec, J. Zdeb, *Fuel*. 263 (2020).
- [230] J. Guilera, T. Andreu, N. Basset, T. Boeltken, F. Timm, I. Mallol, J.R. Morante, *Renewable Energy*. 146 (2020) 1301–1308.

Chapter

*Design and optimization
of micro-sized catalysts*

This chapter is devoted to the design of a high-performance heterogeneous catalyst for SNG production through CO₂ methanation reaction. The proposed catalyst formulation is based on a nickel (Ni) and alumina (γ -Al₂O₃) as cost-effective metal-active phase and support, respectively.

Commercial γ -Al₂O₃ microspheres with particle diameters between 450 and 500 μ m were selected as the mesoporous support material ($d_{\text{pore}}=10$ nm). The support presented a high surface area and relatively low cost. As part of catalyst development, their spherical shape and microscopic dimensions were considered in order to obtain a catalyst design able to work in the novel microreactor technologies that currently are available in the market.

Nickel (Ni) was selected as the metal-active phase of the catalytic system due to its excellent activity/cost ratio. Ni supported on γ -Al₂O₃ catalysts are feasible in order to achieve high catalytic activity. Nevertheless, the presence of impurities in the feed gases and the formation of high temperatures originated by the exothermic nature of the Sabatier reaction can lead to its deactivation by poisoning, fouling (carbon deposition) or thermal degradation of the metal particles. The modification of γ -Al₂O₃ support by adding promoters is a common strategy design applied to enhance both the catalytic and stability.

Various promoter materials have been recently evaluated in the literature, as it was described in Chapter 1 section 1.2.3. In the present case, the design strategy was to use a high amount of promoter material (≥ 15 wt.%) in comparison with the reported amounts (≤ 5 wt.%). The high promoter content into the Ni/ γ -Al₂O₃ microspheres can provide a highly active-stable catalyst design for the CO₂ methanation process.

The target of this chapter is to obtain the optimal catalyst formulation. In this direction, two articles are included, which are focused on:

- The evaluation of different metal-oxides in order to identify the most active promoter material.
- The optimization of the composition for the selected ternary catalytic system.

2.1. Metal-oxide promoted Ni/Al₂O₃ as micro-size catalysts

In the first article included in this chapter, the final goal was to identify the most active promoter material. With this aim, the influence of using various metal oxides at high loading level as promoters on Ni/ γ -Al₂O₃ micro-spheres catalysts were evaluated. A total of five metal oxides were selected as promoters, including four lanthanides (CeO₂, La₂O₃, Sm₂O₃, Y₂O₃) and one transition metal (ZrO₂). These materials were selected according to their positive catalytic properties reported in the literature when they were used as bulk support catalysts. The series of metal oxide promoted Ni/ γ -

Al_2O_3 micro-spheres catalysts were synthesized through the wet impregnation (WI). They were named Ni-X in where X is the promoter component ($\text{X}=\text{CeO}_2$, La_2O_3 , Sm_2O_3 , Y_2O_3 and ZrO_3). The content for Ni-active phase was set at 25 wt.% and that of promoter at 15 wt.%.

Catalytic screening tests were conducted at different temperatures to explore the promoting effect of the selected materials. Then, the catalytic stability of the most promising catalysts was evaluated, without, and under the presence of H_2S traces (0.04 ppm) for 170 h. The selected reaction conditions were representative of an industrial technically clean biogas case. Relatively low H_2S traces were considered according to the minimum detention limit of the commercial gas analyzers. As it can be observed in Figure 2.1, the strategy of the promoter addition led to evident catalytic benefits. The catalytic performance for the evaluated catalysts follows the order of Ni- $\text{La}_2\text{O}_3 >$ Ni- $\text{CeO}_2 >$ Ni- $\text{Sm}_2\text{O}_3 >$ Ni- $\text{Y}_2\text{O}_3 >$ Ni- $\text{ZrO}_2 >$ Ni $>$ commercial reference. Ni- La_2O_3 and Ni- CeO_2 were selected as the two most promising promoted catalysts and their catalytic stabilities were further evaluated.

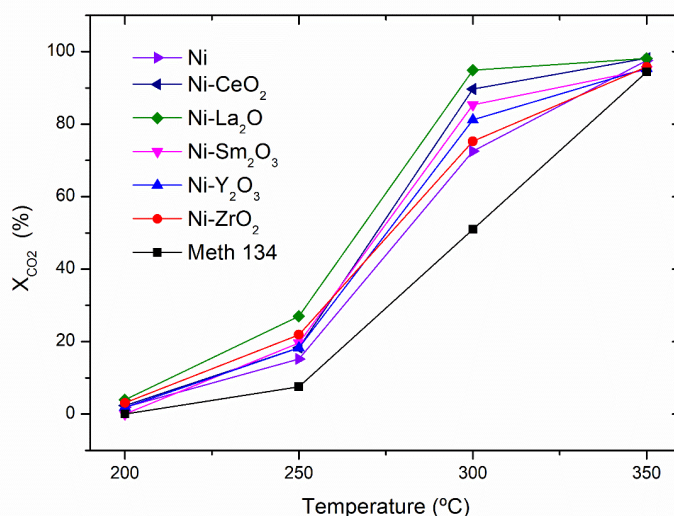


Figure 2.1. Effect of the promoter on CO_2 conversion at 5 bar-g and using different temperatures.

The long-term experiments shown in Figure 2.2 were carried out in order to evaluate during 24 h the stability of the catalysts without the presence of impurities, and then, a gas feed with 0.4 ppm of H_2S was introduced to the reactant mixture during 146 h. Ni- La_2O_3 ($X_{\text{CO}_2}=95\%$) and Ni- CeO_2 ($X_{\text{CO}_2}=89\%$) again achieved the highest initial catalytic activity and both catalysts were stable during the whole experiment. In contrast, a slight reduction of activity was detected over the non-promoted Ni catalyst ($X_{\text{CO}_2}=74\%$).

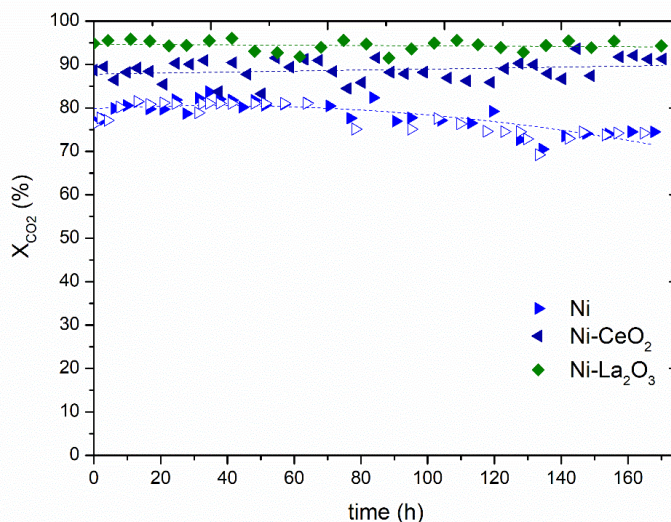


Figure 2.2. Catalytic performance along time. Closed symbols: H_2S concentration of 50 ppb. Open symbol: H_2S -free. Reaction conditions: $T=300$ °C, $H_2:CO_2$ molar ratio=4, $P=5$ bar·g, and $GHSV=40,000$ $mL \cdot g^{-1} \cdot h^{-1}$.

According to the catalyst characterization results, the deactivation of the non-promoted catalysts was due to the Ni particles sintering. On the other hand, the high catalytic performance and stability achieved in the two promoted catalysts was attributed to physicochemical properties. The addition of La_2O_3 and CeO_2 on $Ni/\gamma-Al_2O_3$ lead to a high nickel reducibility (84-91% at 500 °C), high dispersion (2.3%), high surface area (15 $m^2 \cdot g_{Ni}^{-1}$) and intermediate heat of CO_2 adsorption (-168 - 128 $kJ \cdot mol^{-1}$). Therefore, the strategy of adding a promoter was clearly beneficial in terms of both initial activity and stability.

2.2. Optimization of nickel and ceria catalyst content

In the previous section, it was evidenced that La_2O_3 and CeO_2 are two promising metal-oxide promoters. Both metal-oxides were able to improve catalytic activity and prevent the deactivation of the non-promoted $Ni/\gamma-Al_2O_3$ micro-spheres catalyst. These two lanthanide metal oxides are light rare-earth elements (LRREs) and their implementation as a promoter material, instead of a bulk support material, is from an economical point of view an attractive way to manufacture CO_2 methanation catalysts at industrial levels. From the two LRREs, CeO_2 was selected as most cost-effective promoter material than La_2O_3 . This is the 26th most abundant element in the Earth's crust, and thus more economically affordable.

In the second work, the aim was to find an optimum Ni-CeO₂/γ-Al₂O₃ formulation by the simultaneous optimization of the main components of ternary catalytic system. Generally, the influence of CeO₂ addition as promoter has been studied using a fixed amount of Ni (≤20 wt.%). However, the simultaneous optimization of Ni, CeO₂ and γ-Al₂O₃ content is proposed to design a catalyst with optimum catalytic, physicochemical and mechanical properties.

In this context, a series of Ni-CeO₂-Al₂O₃ catalysts were synthesized through the wet impregnation method. The content of Ni and CeO₂ was varied simultaneously in a range from 0 to 30 wt.%, while the content of γ-Al₂O₃ was in the range of 40-100 wt.%. The innovative systematic experimental design led to the preparation of eight samples with different composition and their catalytic performance evaluation was conducted by a screening test. The catalytic trend at 300 °C displayed in Figure 2.3, revealed that the maximum region of catalytic activity can be found around of 22-28 wt.% for Ni and 12-25 wt.% for CeO₂. In addition, material characterization suggested that a compromise between Ni, CeO₂, and γ-Al₂O₃ content was favourable to obtain a suitable catalyst for the CO₂ methanation.

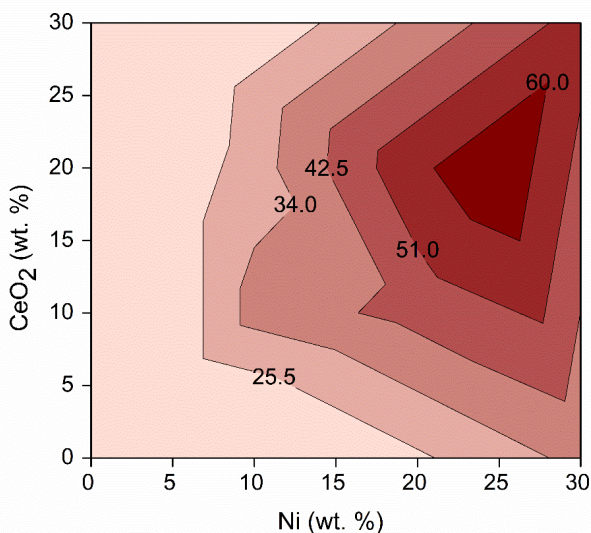


Figure 2.3. CO₂ Conversion (%) trend of the tested Ni-CeO₂ catalysts at 300 °C.

According to CO chemisorption analysis, Ni as active phase was detected to provide metallic surface. On the other hand, CeO₂ as promoter improves both the reducibility of Ni and the amount of CO₂ adsorbed on the catalyst, as it was confirmed by H₂-TPR and microcalorimetric analysis. Finally, γ-Al₂O₃ as support was favourable in terms of surface area and pore volume, and thus availability of proper Ni dispersion. Taking into consideration these findings, an optimum catalyst composed by 25 wt.% Ni, 20

wt.% CeO₂ and 55 wt.% γ -Al₂O₃ was synthesized and its catalytic performance was evaluated.

The catalytic test confirmed the highest catalytic performance predicted from the mathematical surface area response. In this direction, the 25Ni-20CeO₂ catalyst exhibited the highest catalytic activity (X_{CO_2} =67.94% with S_{CH_4} =100%) compared to rest of studied catalysts, thus the simultaneous optimization procedure was found to be useful. Their competitive catalytic performance was attributed to the synergistic effects achieved when the content of all species was optimized. Further experiments over the optimized Ni-CeO₂ were then performed in order to evaluate its catalytic stability.

The lifetime testing conducted for 120 h over the optimized Ni-CeO₂ catalyst claimed its high stability Figure 2.4. Compared to a commercial reference, METH[®]134 (X_{CO_2} =64%), the 25Ni-20CeO₂ catalyst achieved higher conversion rates (X_{CO_2} =91%) and was stable during the whole test.

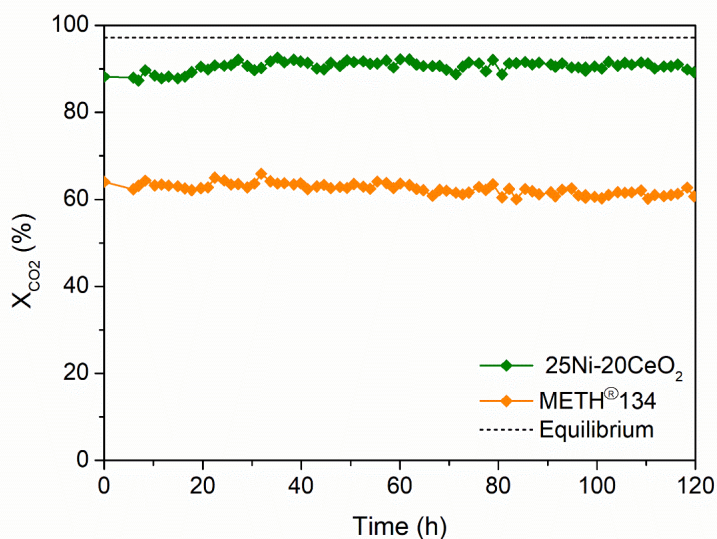
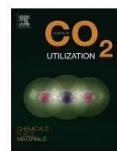


Figure 2.4. Lifetime testing comparison of 25Ni-20CeO₂ and METH[®]134 catalysts. Reaction conditions: $T=300$ °C, $P=5$ bar·g; $GHSV=36,000$ h⁻¹, $m_{cat}=0.3$ g, $\rho_{cat}=0.9$ g·mL⁻¹, and $H_2:CO_2$ molar ratio=4.



Metal-oxide promoted Ni/Al₂O₃ as CO₂ methanation micro-size catalysts

Jordi Guilera^{a,*}, Jaime del Valle^b, Andreina Alarcón^{a,c}, José Antonio Díaz^{a,d}, Teresa Andreu^{a,b}

^a Catalonia Institute for Energy Research (IREC), Jardins de les Dones de Negre 1, 08930, Sant Adrià de Besòs, Spain

^b Universitat Politècnica de Catalunya (UPC), Eduard Maristany 16, 08019, Barcelona, Spain

^c Escuela Superior Politécnica del Litoral, ESPOL, Facultad de Ingeniería en Ciencias de la Tierra, Campus Gustavo Galindo Km. 30.5 Vía Perimetral, P.O. Box 09-01-5863, Guayaquil, Ecuador

^d Universidad Politécnica de Madrid (UPM), Department of Mechanical, Chemical and Industrial Design Engineering, ETSIDI, 28012, Madrid, Spain



ARTICLE INFO

Keywords:
Carbon dioxide
Power-to-Gas
Biogas
Synthetic natural gas
Catalyst

ABSTRACT

The Power-to-Gas concept has the challenge to convert the excess of renewable electricity to synthetic natural gas, composed mainly by methane, through CO₂ methanation. The superior heat transfer capacity of micro-structured reactors offers a suitable alternative for an efficient control of the reaction temperature. In the present work, the strategy of adding large amount of metal oxide promoters (15 wt.%) to nickel supported on micro-size catalysts ($d_p = 400\text{--}500\ \mu\text{m}$) is presented. The addition of CeO₂, La₂O₃, Sm₂O₃, Y₂O₃ and ZrO₂ was clearly beneficial, as the corresponding metal-oxide promoted catalysts exhibited higher catalytic performance than Ni/Al₂O₃ and the commercial reference Meth[®] 134 ($T = 200\text{--}300\ ^\circ\text{C}$, $P = 5\ \text{bar}$). This increase of catalytic activity is attributed to the higher amount of CO₂ adsorbed on the catalyst. Among the selected promoters, La₂O₃ showed the highest catalytic activity ($X_{\text{CO}_2} = +20\%$ at $300\ ^\circ\text{C}$) due to the enhancement of nickel reducibility, nickel dispersion and the presence of moderate basic sites. In addition, Ni-La₂O₃/Al₂O₃ was stable for one week, while the unpromoted catalyst exhibited a slight decline in its activity. Accordingly, the technical catalyst proposed in this study could be used directly in compact reactors for CO₂ methanation with much higher activity than the commercial reference.

1. Introduction

Pumped hydro storage is nowadays the leading electricity grid storage technology, reaching 119 TWh in 2017 [1]. However, the potential of water pumping technology to store the energy produced by wind and solar photovoltaic power plants is limited because these facilities can only be installed in areas with a very specific topography [2]. An illustrative example is Denmark, which has currently the largest share of electricity delivered from fluctuating wind power (50.5% in 2017) [3]. However, the potential of Denmark of storing such energy by pumped hydro storage installations is negligible due to extremely flat topographic characteristics. In contrast, Spain and Germany have the largest number of pumped hydro storage plants. Nevertheless, they still have problems through because of high penetration of wind energy to the grid in some regions, e.g. in the wind state of Saxony-Anhalt (62% in 2014) [4]. With respect to Spain, wind farms have been punctually disconnected overnight due to low demand since 2008 [5]. These examples reveal that massive electricity storage will be a critical issue for further penetration of renewable power on the road to meet national targets.

In this context, Power-to-Gas strategy aims to interconnect the power grid with the gas grid by converting power excesses to a gas compatible with the current infrastructure. Power-to-Gas as massive storage technology can increase the share of renewable sources supply. The most mature technology is based on a two-step process, hydrogen production through water splitting and conversion of the electrolytic hydrogen with carbon dioxide by means of catalytic methanation [6,7]. The gas obtained is methane, with some remaining hydrogen and carbon dioxide, which is referred to as synthetic/substitute natural gas (SNG). The potential of storing electricity by means of the current gas infrastructure is 3600 TWh, 30-times higher than that from water pumping [8].

The conversion of carbon dioxide with hydrogen is a well-known exothermic reaction, which is typically carried out at moderate temperatures (250–350 °C) and pressures (5–25 bar g) through heterogeneous catalysis (Eq. (1)). Reactor engineering is critical in order to achieve a proper heat evacuation and optimum temperature profile due to the exothermicity of the reaction [9–11]. A proper temperature control can prevent catalyst sintering and undesired secondary reactions. In addition, since the reaction is reversible, the temperature

* Corresponding author.

E-mail address: jguilera@irec.cat (J. Guilera).

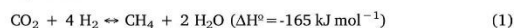
<https://doi.org/10.1016/j.jcou.2019.01.003>

Received 22 October 2018; Received in revised form 3 January 2019; Accepted 7 January 2019

Available online 10 January 2019

2212-9820/© 2019 Elsevier Ltd. All rights reserved.

profile is a key factor to obtain a gas with enough methane content to be injected to the grid, typically about 95–96 vol.% of CH₄. In this sense, the superior heat transfer capacity of micro-structured reactors favours an efficient temperature control within the reactor, so that they are considered suitable alternatives to classical reactors for CO₂ methanation. The fabrication of micro-channel reactors by means of welding technologies is already at demonstration scale and very close to industrial application. Micro-reactors technology for CO₂ methanation is already commercialized by the companies Atmostat, Inerotec and Velocys [12].



According to thermodynamics, the injectable gas composition cannot be achieved at high reaction temperatures. Thus, mild temperatures are needed to achieve the desired quality without an unnecessary increase of pressure ($T \leq 300^\circ\text{C}$, $P \leq 10 \text{ bar}$) [7]. At these conditions, catalyst design plays a determinant role to overcome kinetic limitations and achieve acceptable reaction rates and low reactor volumes. These reaction rates can be obtained by using nickel as available and economic active material [13]. In terms of selectivity, high values (> 99%) are easily achieved on nickel catalysts, so that secondary products were not even detected in some published works [14–16].

The most used methanation catalyst is based on two economic materials, nickel as active phase and γ -alumina as support, which is used to disperse the active phase and confer stability to the whole catalyst [17]. Besides γ -alumina, it is well-known that alternative supports such as Y₂O₃, Sm₂O₃, ZrO₂ and CeO₂ provide better properties to nickel-based catalysts, which consequently exhibit higher catalytic activity [18,19]. In this direction, Muroyama et al. studied the effect of these supports on 10 wt.% wet impregnated nickel. The authors related the catalytic enhancement to the presence of moderate basic sites [20]. Westermann et al. reported that hydrogen reacts with weak adsorbed CO₂ or carbonates as a prior step to form methane. Besides, they observed that methane formation was controlled by the concentration of adsorbed species [21].

Unfortunately, the aforementioned supports are not as abundant as alumina. Indeed, Y, Sm, Ce and La are considered rare-earth elements and this is reflected in their international prices. For industrialization, the proposed catalyst should show a good compromise between the material costs and the catalytic improvement, as well as the desired shape for their implementation in catalytic reactors. Consequently, some researchers proposed that these rare elements can be used effectively as promoters instead of bulk support in similar reactions [22–24]. As regards to CO₂ methanation reaction, Liu et al. observed that the addition of 2 wt.% CeO₂ on Ni/Al₂O₃ system led to an interesting increase of the initial activity but also of the stability [25]. In another study, the addition of La₂O₃ as promoter also showed significant enhancement of the CO₂ methanation catalytic activity [26]. Besides, the use of ternary or quaternary mixed oxides allow to decrease the temperature for CO₂ methanation [27]. Therefore, it seems that promoters are crucial to increase the activity and the stability of the materials.

Those promoted Ni-based catalysts that are reported in the literature were prepared in powder form, not suitable for their commercial application. Turning promising laboratory catalysts into industrial catalyst implies the shaping of powders into macroscopic form or metal incorporation to shaped supports [28–30]. Industrial methanation catalysts are typically manufactured in pellet, extrudates and ring shapes of 4–6 mm of diameter, not suitable for innovative submillimetre-sized reactors [31]. A dimension reduction of an order of magnitude is required for efficient and uniform packing in micro-channel reactor configuration.

In the present work, we evaluate the influence of using various metal oxides at high loading level as promoters on Ni/Al₂O₃ micro-size catalysts. These materials can be considered technical catalysts as they are designed according to their commercial application on micro-

reactor technology and no further treatment or modification is necessary before implementation [28]. Metal oxides were used as promoters, instead of bulk support, for economical purposes. The promoted catalysts were developed for CO₂ conversion to synthetic natural gas in industrial applications with some tolerance to H₂S traces. The promoting effect of CeO₂, La₂O₃, Sm₂O₃, Y₂O₃ and ZrO₂ is examined at different temperatures (200–350 °C) at 5 bar g. Then, the most promising catalysts were tested with and without the presence of H₂S traces for 170 h, in order to predict their behaviour in an industrial environment. Besides, the series of manufactured catalysts was compared with a reference industrial catalyst to evaluate the benefits of the proposed strategy on catalyst development.

2. Experimental

2.1. Catalyst preparation

The series of catalysts were prepared by wet impregnation method. Nickel and one promoter (CeO₂, La₂O₃, Sm₂O₃, Y₂O₃, ZrO₂) were incorporated to γ -Al₂O₃ micro-spheres ($d_p = 400\text{--}500 \mu\text{m}$, Saint-Gobain NorPro). In addition, a nickel catalyst without promoter was prepared for comparison purposes. The following nitrates were used as precursors in the manufacturing of the catalysts: nickel (II) nitrate hexahydrate [Ni(NO₃)₂·6H₂O] (98%, Alfa Aesar), cerium (III) nitrate hexahydrate [Ce(NO₃)₃·6H₂O] (99.5%, Alfa Aesar), yttrium (III) nitrate hexahydrate [Y(NO₃)₃·6H₂O] (99.8%, Aldrich), samarium (III) nitrate hexahydrate [Sm(NO₃)₃·6H₂O] (99.9%, Aldrich), zirconium (IV) oxynitrate hydrate [ZrO(NO₃)₂·xH₂O] (99.0%, Aldrich) and lanthanum (III) nitrate hexahydrate [La(NO₃)₃·6H₂O] (99.999%, Aldrich). Meth[®] 134 catalyst (Clariant) was crushed, sieved ($d_p = 400\text{--}500 \mu\text{m}$) and used as industrial reference.

In a typical synthesis, 5 g of catalyst was prepared per batch. The nitrate precursors (nickel + promoter) were dissolved together in pure water at room temperature for 1 h. Alumina support was pre-dried at 105 °C overnight, weighed and added into the aqueous solution. Then, the mixture was kept on a bath at 80 °C under slow stirring until complete evaporation, typically after 4 h. The impregnated material was kept at 105 °C in an atmospheric oven overnight. Then, the catalysts were calcined at 450 °C for 30 min (heating ramp 1 °C·min⁻¹). Nominal nickel loading amount was fixed at 25 wt% and the metal oxide promoter at 15 wt%.

2.2. Catalyst characterization

Catalyst bulk density (ρ_b) was measured by means of the mass of particles divided by the occupied volume (5 mL). This measurement includes the space between the intra-particles and it is representative of the actual density in a fixed-bed reactor. Topology and elemental analysis of the catalysts were studied by scanning electron microscopy (SEM, Zeiss Auriga 60) equipped with an energy dispersive x-ray spectrometer (EDX, Oxford Inca Energy). Prior to the elemental analysis, samples were crushed to study the average composition of the sample and not only the external particle layer. The presented chemical composition is an average of ten individual measurements of powder sample. Elemental data obtained from EDX technique can be consistent with the exact composition determined by Inductively coupled plasma mass spectrometry (ICP-MS) results [32]. However, it should be pointed out the measured amount of metals by EDX can also lead to over-estimation given metal accumulation on the surface, even though the catalysts were previously crushed.

Textural properties of the catalysts were determined by N₂-physorption (TriStar II 3020-Micromeritics). Prior to the measurements, the samples were degassed at 90 °C for 1 h, and then at 250 °C for 4 h. Brunauer-Emmett-Teller (BET) method was used to calculate the BET surface area for a relative pressure (P/P_0) range between 0.05–0.30. Barrett-Joyner-Halenda (BJH) method was applied to desorption

branch of the isotherm to determinate the pore volume and size.

Structural properties were studied by powder X-ray Diffraction (XRD, Bruker D8 Advance A25). The wide-angles data were obtained using a Cu K α radiation ($\lambda = 1.5406 \text{ \AA}$), a voltage of 40 kV, a current of 40 mA and a step size of 0.05° (3 s per step). The diffraction acquisitions were done in a range from 20 to 80° . Crystalline phase were identified by using International Centre for Diffraction Data. The average nickel¹ crystallite sizes (d_{Ni}) of pre-reduced and used samples were estimated by the Scherrer equation at 44.8° [33].

Reducibility of the calcined catalysts was studied by temperature programmed reduction (H₂-TPR, Autochem Micromeritics). H₂-TPR were conducted using 12 vol.% H₂/Ar at flow of 50 N mL·min⁻¹ in the temperature range of 35–800 °C at a heating ramp of 10 °C·min⁻¹. The amount of H₂ uptake was measured with a thermal conductivity detector. Metal dispersion and metallic surface area were determined by pulsed CO chemisorption (Autochem Micromeritics). Prior to adsorption measurements, each sample (50 mg) was reduced in 12 vol.% H₂/Ar flow at 500 °C for 3 h.

CO uptake was measured by injecting CO pulses through a calibrated on-line sampling valve until saturation was attained. Nickel metal surface area, dispersion and particle size were calculated assuming the stoichiometric factor for CO to Ni as one, atomic weight of 58.71, atomic cross-sectional area of 0.0649 nm² and density of 8.90 g·cm⁻³. Note that CO adsorption on nickel is a complex process; the stoichiometry can vary with metal dispersion, metal loading, temperature, preparation method and it can form volatile complexes. However, it can be used for screening purposes [34].

The amount and heat of CO₂ adsorption was studied by coupled thermogravimetric analysis and differential scanning calorimetry with CO₂ pulses (TGA-DSC, Setaram Evo). The samples (50 mg) were placed at 90 °C for 30 min in Ar flow (50 N mL·min⁻¹) to remove water. Then, samples were reduced using 12% H₂/Ar at flow of 10 N mL·min⁻¹. The temperature was increased up to 500 °C for 3 h with a heating ramp of 5 °C·min⁻¹, then cooled down to a representative temperature of reaction (300 °C). Finally, the 12% H₂/Ar flow was replaced with a 10% CO₂/Ar flow (10 N mL·min⁻¹) to measure the CO₂ adsorbed mass amount and the heat of adsorption at 300 °C.

The species adsorbed on the catalyst during reaction were characterized by temperature programmed oxidation (TPO) using a thermogravimetric analyser (TGA-DSC, Setaram Evo). Analysis of the gaseous burn off products was on-line performed by mass spectroscopy (Pfeiffer). The samples (15 mg) were oxidised using air at flow of 20 N mL·min⁻¹ from 35 to 700 °C at a heating rate of 5 °C·min⁻¹, and kept at 700 °C for 3 h.

2.3. Catalyst activity

Catalyst activity, selectivity and stability was tested in a fully automated laboratory scale fixed-bed catalytic reactor (Microactivity Reference, PID Eng&Tech). Experiments were conducted using 300 mg of dry catalyst particles, sieved to $d_p = 400\text{--}500 \mu\text{m}$. Catalyst was diluted with 3 g of silicon carbide 46 grit (Cymit) of similar particle sizes ($d_p = 355 \mu\text{m}$) to assure isothermal behaviour through the catalyst bed. Prior to reaction, catalyst was reduced in-situ under H₂ flow (100 N mL·min⁻¹) at 500 °C (ramp 5 °C·min⁻¹) for 3 h. Higher in-situ reduction temperatures (> 500 °C) cannot be reached in some micro-reactor devices. After reduction, temperature was decreased to 200 °C, reactants H₂ (99.999%, Linde) and CO₂ (99.9993%, Linde) were adjusted and the reaction started. Long runs were conducted by additionally introducing 20 N mL·min⁻¹ of N₂ for 24 h (99.999%, Linde), which then was switched to 20 N mL·min⁻¹ of H₂S/N₂ (0.4 ppm H₂S, Linde) to approach the industrial case. Experiments were conducted using H₂/CO₂ stoichiometric molar ratio of 4.0 and pressure of 5.0 bar g. Catalyst screening was performed isothermally at intervals of 50 °C in the temperature range of 200–350 °C, started at the lowest temperature and waited until steady state was attained. Long

experiments were conducted at 300 °C. Reaction temperature was monitored using a K-type thermocouple placed in the middle of the diluted catalyst bed.

After reaction, the product stream passed through a cold trap (5 °C, 5 bar g), where water was collected, and then through a mass flow meter (Bronkhorst). The composition (CH₄, H₂, CO and CO₂) of the dry gas was measured by an on-line gas micro-chromatograph (490 microGC, Agilent Technologies). Samples were analysed every 2.5 min in the screening experiments and hourly during long experiments. CO₂ conversion and CH₄ selectivity were calculated as follows. Catalyst activity experiments were replicated to assure reproducibility. Data shown in this study has a relative error in the range 1–15%. Carbon mass balance between inlet and outlet was accomplished within an accuracy of $\pm 6\%$.

$$X_{\text{CO}_2} = 1 - \frac{F_{\text{CO}_2,\text{out}}}{F_{\text{CO}_2,\text{in}}} \cdot 100 \quad (2)$$

$$S_{\text{CH}_4} = \frac{F_{\text{CH}_4,\text{out}}}{F_{\text{CH}_4,\text{out}} + F_{\text{COout}}} \cdot 100 \quad (3)$$

3. Results and discussion

3.1. Catalyst properties

A total of six nickel-based catalysts were prepared by wet impregnation on high porous γ -Al₂O₃ microspheres. Sample names indicate the presence of nickel as active phase and a second metal-oxide as reaction promoter. As shown in Table 1, the apparent bulk density of Al₂O₃ is 0.55 g mL⁻¹, very low compared to that of dense powder alumina (3.65 g mL⁻¹). The apparent bulk density was increased to 0.73 g mL⁻¹ after nickel deposition, whereas the addition of the promoter provoked a further increase to 0.84–0.87 g mL⁻¹, except sample Ni-ZrO₂. As regards to the commercial Meth[®] 134 catalyst, the bulk density of crushed and sieved catalyst was slightly lower than the ones prepared in this study (0.76 g mL⁻¹). This density value is in the range of other commercial Ni-based catalysts; however, comparison is complex due to changes in the geometrical shape [9,10]. At the same particle form, low bulk density positively increase the surface area of the catalyst but lowers the amount of material in weight that can be introduced in a fixed reactor volume.

The average chemical composition of catalyst was determined by EDX. The amount of observed nickel was close to the nominal one (25 wt.%), with small divergences of $\pm 3\%$. Likewise, the amount of promoter was close to the nominal (15 wt.%), except for Ni-ZrO₂ (9 wt.%) and Meth[®] 134 (2 wt.%). The behaviour of ZrO₂ can be a consequence of the lower solubility of zirconium precursor (zirconium (IV) oxynitrate hydrate). Therefore, the amount of ZrO₂ and CaO as promoter is lower respect to the others, as indicated by the bulk density measurement, and its effect on the catalytic properties is not directly

Table 1
Catalysts used in this study.

Sample	metal content [wt.%] ^a		ρ_b [g mL ⁻¹]
	nickel	promoter	
Support	–	–	0.55
Ni	25 \pm 2	–	0.73
Ni-CeO ₂	23 \pm 1	16 \pm 1	0.84
Ni-La ₂ O ₃	28 \pm 2	14 \pm 1	0.85
Ni-Sm ₂ O ₃	28 \pm 1	16 \pm 1	0.87
Ni-Y ₂ O ₃	23 \pm 1	15 \pm 1	0.86
Ni-ZrO ₂	27 \pm 2	9 \pm 1	0.72
Meth [®] 134	22 \pm 1	2 \pm 1	0.76

^a Elemental composition from EDX analysis. Promoter amount is expressed as metal (Ce, La, Sm, Y, Zr, Ca).

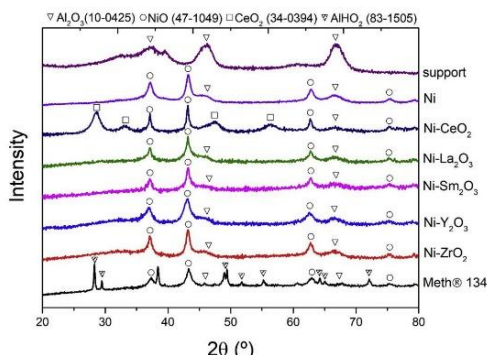


Fig. 1. XRD patterns of calcined samples.

comparable.

The XRD patterns of the catalysts as prepared are reported in Fig. 1. NiO and γ -Al₂O₃ patterns were detected in all the samples. As for the promoters, CeO₂ crystals were clearly observed, while La₂O₃, Sm₂O₃, Y₂O₃ and ZrO₂ crystals were not detected. The diffuse pattern of γ -Al₂O₃ in comparison to other supports may hinder the detection of the promoter. Another plausible option is that some promoters remained in amorphous phase as a result of the mild calcination temperatures (450 °C). Likewise, CaO pattern was not detected in Meth[®] 134 sample. However, it was noticed the presence of boehmite pattern that were not transformed into well-crystallized γ -Al₂O₃, most probably due to low calcination temperature [35].

Nitrogen physisorption isotherms showed a type IV profile in all samples, characteristic of mesoporous materials with uniform cylindrical pores (IUPAC classification). As representative example, Fig. 2 illustrates the pore size distributions of the support, Ni and Ni-La₂O₃ samples. It is clearly observed that the pore volume was significantly reduced by the incorporation of Ni to the support and it was further reduced by the incorporation of a promoter, in this case by La₂O₃. In addition, the pore size distribution was shifted to smaller diameters by the incorporation of metals. BET surface area, pore volume and pore diameter of all samples, obtained from N₂ physisorption results, are listed in Table 2. The γ -Al₂O₃ support used in this study exhibited high surface area (> 250 m² g⁻¹) and the main pore diameter tailored to 10 nm, which confirmed the mesoporous character of this material (2–50 nm, IUPAC classification). At first sight, it is inferred that the

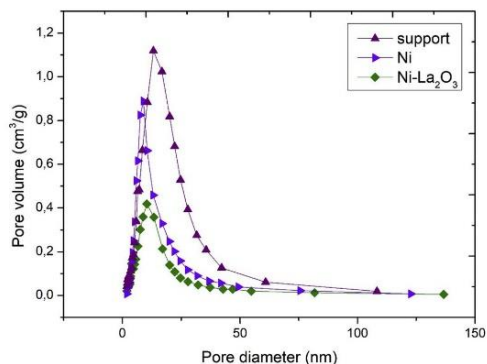


Fig. 2. Pore size distribution of support, Ni and Ni-La₂O₃ samples.

Table 2

Catalyst characterization from N₂-physorption.

Sample	BET surface area [m ² ·g ⁻¹]	pore volume [cm ³ ·g ⁻¹]	pore size [nm]
support	267	0.67	10
Ni	196	0.42	8.8
Ni-CeO ₂	144	0.26	7.2
Ni-La ₂ O ₃	116	0.23	8.1
Ni-Sm ₂ O ₃	105	0.23	8.7
Ni-Y ₂ O ₃	120	0.22	7.5
Ni-ZrO ₂	134	0.29	8.6
Meth [®] 134	63	0.07	4.8

proposed ternary catalysts have 105–144 m² g⁻¹ surface area, 0.22–0.29 cm³ g⁻¹ pore volume and 7.2–8.7 nm pore diameter, indicating much higher porosity than the commercial reference Meth[®] 134.

As a general trend, the addition of 25 wt.% nickel to the support decreased proportionally 25% the surface area of the sample. The addition of 15 wt.% of promoter decreased a further 25% of surface area. On the whole, the high-loading catalysts exhibited half surface area respect to the support, slightly higher reduction than the corresponding decrease of Al₂O₃ support amount (60 wt.%). In comparison with the surface area behaviour, the decrease of pore diameter was less intense, from 10 to 8 nm. This behaviour is attributed to the partial blocking of some γ -Al₂O₃ pores by the metal incorporation but not the modification of these ones. On the other hand, it is revealed that the main consequence of the addition both metals, active phase and promoter on the textural properties was a severe reduction on pore volume (up to 67%). The differences among pore volume and surface area behaviour were attributed to the fact that metal particles contributed with some additional surface area but not with additional pore volume.

The H₂-TPR profiles of the nickel catalysts are displayed in Fig. 3. The species present in the catalysts were reduced in the range of 200–600 °C. This reduction is attributed to the reduction of NiO to Ni⁰ and not to the reduction of alumina support or metal oxide promoters [20]. The peaks located in the low temperature region (200–350 °C) are typically assigned to α -type NiO species, corresponding to free nickel oxides that showed weak interaction with alumina support [36,37]. Interestingly, these species are only formed by the addition of promoter and they were not significantly formed on the Ni catalyst and the commercial reference. Most nickel remains in the form of β -type NiO (350–600 °C) without the presence of promoter but for Ni-ZrO₂. These species have stronger interaction with alumina and, at first sight, are less active for CO₂ methanation. The last nickel species were assigned to γ -type NiO, related to stable Ni-Al phase with spinel structure. In the case of commercial catalyst, the last peak observed is attributed to the interaction of Ni with some additional compounds such as Ca. Overall,

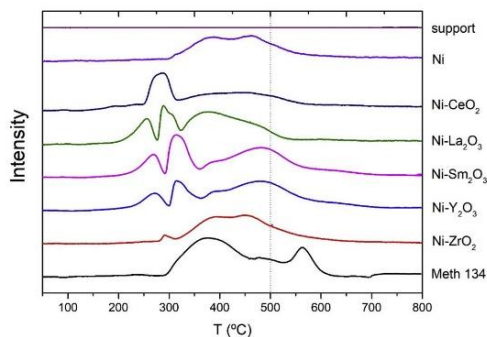


Fig. 3. H₂-TPR profiles of samples. TCD signal is normalised by sample weight.

Table 3
CO chemisorption measurements at 35 °C.

sample	adsorbed CO	metal dispersion	metallic surface area	
	[cm ³ /g]		[m ² /g _{cat}]	^a [m ² /m _{cat} ²] ^a ·10 ⁴
Ni	2.42	2.53	4.22	22
Ni-CeO ₂	2.16	2.26	3.77	26
Ni-La ₂ O ₃	2.20	2.31	3.84	33
Ni-Sm ₂ O ₃	1.77	1.85	3.08	29
Ni-Y ₂ O ₃	1.30	1.36	2.26	19
Ni-ZrO ₂	1.47	1.54	2.56	19
Meth [†] 134	0.71	0.93	1.24	20

^a BET surface area was used for calculation.

the introduction of promoters Ce, La, Sm, Y or Zr, improved greatly the reducibility of the materials. In this sense, 91% of the total hydrogen uptake took place below 500 °C on Ni-La₂O₃, followed by 84% on Ni-CeO₂ and 71–78% on the other promoted catalysts. On the contrary, the catalyst without promoter (Ni) only consumed 65% of the total hydrogen below this temperature. H₂-TPR results revealed that the promoters favoured the reduction of NiO, probably because they weaken the interaction between Ni and the support [36].

Table 3 shows the results of metal dispersion by CO chemisorption measurements. The highest nickel dispersion (2.53%) and metallic surface area was exhibited by the unpromoted catalyst (Ni). In this sample, nickel was dispersed in 75 wt.% γ-Al₂O₃ support, which means that there were more porosity available for nickel to be dispersed. The promoted samples showed lower dispersion of nickel due to the less availability of support (60 wt.%). Among promoted samples, the highest nickel dispersion was achieved when La₂O₃ was introduced (2.31%), followed closely by CeO₂ (2.26%). In terms of nickel area per surface area, nickel was more dispersed in LaO₃ and CeO₂ than the unpromoted one, 54 and 22% higher, respectively. Therefore, it is confirmed that La₂O₃ and CeO₂ favoured the nickel dispersion, thus providing more active sites for reaction. Ni-Sm₂O₃, Ni-ZrO₂, Ni-Y₂O₃ presented lower nickel dispersion values (1.36–1.85%) but far superior than the commercial reference (0.93%). All synthesized catalysts showed higher nickel surface areas (9–17 m²g_{Ni}⁻¹) than the commercial reference (6 m²g_{Ni}⁻¹) as a result of higher nickel dispersion but also higher nickel loading.

The amount of CO₂ adsorbed and heat of adsorption are direct measures of CO₂ interaction with the catalyst carried out by micro-calorimetry. Table 4 shows that nickel catalyst without promoter (Ni) exhibited the lowest amount of CO₂ adsorbed (71 μmol g_{cat}⁻¹). The addition of a promoter clearly increased the amount of CO₂ adsorbed (117–178 μmol g_{cat}⁻¹) per mass of sample, while this positive effect was negligible for Ni-ZrO₂ sample (62 μmol g_{cat}⁻¹). Nonetheless, all promoted samples adsorbed higher amount of CO₂ per surface unit (0.46–1.52 μmol/m_{cat}²) than the unpromoted one (0.36 μmol/m_{cat}²). Regarding the heat of adsorption, all values fell in the chemisorption region (> 80 kJ mol⁻¹) [38], necessary for the CO₂ activation step in

Table 4
CO₂ adsorption data at 300 °C by TGA-DSC analysis.

sample	CO ₂ adsorbed		heat of adsorption
	[μmol/g _{cat}]	[μmol/m _{cat} ²] ^a	
Ni	71	0.36	242
Ni-CeO ₂	117	0.81	182
Ni-La ₂ O ₃	147	1.27	168
Ni-Sm ₂ O ₃	160	1.52	131
Ni-Y ₂ O ₃	178	1.48	124
Ni-ZrO ₂	62	0.46	312
Meth [†] 134	345	5.48	132

^a BET surface area were considered.

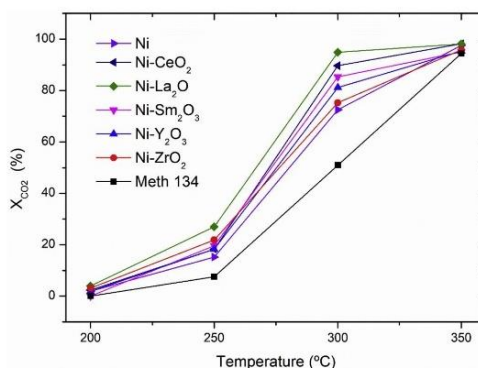


Fig. 4. Effect of the promoter on CO₂ conversion at different temperatures. Reaction conditions H₂:CO₂ = 4 (mol), P = 5 barg, m_{cat} = 0.3 g, F = 200 N mL·min⁻¹.

heterogeneous catalysis. CO₂ adsorption measurements revealed a relation between heat of adsorption and adsorbed amount data. Samples with higher amount of CO₂ adsorbed showed the weakest adsorption bonds – lowest heats of adsorption – and vice versa. In this sense, the weakest chemical bonds were found in Ni-Y₂O₃ and Ni-Sm₂O₃ samples, while the strongest bonds were found in samples Ni and Ni-ZrO₂. In the midst of them, Ni-La₂O₃ and Ni-CeO₂ exhibited moderate heat of adsorption and amount of CO₂ adsorbed.

3.2. Catalyst activity

CO₂ methanation reaction over nickel based catalysts was analysed at 5 barg in the temperature range of 200–350 °C, representative of industrial methanation conditions. As illustrated in Fig. 4, CO₂ conversion always increased with the temperature. Selectivity to CH₄ was in all cases ≥ 99%, and only traces of CO were observed. At this flow conditions (29,000–35,000 h⁻¹), reaction kinetics controlled the catalytic behaviour at T ≤ 300 °C and catalytic differences between materials were observed. At 350 °C, reaction approached to equilibrium conditions (X_{CO2} = 95%) and conversion was independent of the catalyst. On the one hand, all the synthesized catalysts in this work (25 wt.% nickel) were more active than the commercial reference (22 wt.% nickel), which can be related to the higher metallic surface area and, above this, the higher nickel reducibility observed by H₂-TPR profiles. On the other hand, ternary catalysts (nickel, promoter and γ-Al₂O₃) were more active than the binary one. Therefore, the strategy of adding promoter led to catalytic benefits. The activity enhancement was led by La₂O₃ and CeO₂, whereas the least positive effect was shown by Sm₂O₃ and ZrO₂.

Experiments were carried out in terms of a fixed volume flow (200 N mL·min⁻¹) and catalyst mass (300 mg). However, the bulk density of promoted catalysts was higher, and less volume of catalyst were accordingly loaded in each run. In this sense, the benefits of adding a promoter were even more noticeable in terms of volumetric space time. For instance, the space time used for Ni-La₂O₃ was 16% higher than that without promoter. Accordingly, more amount of catalyst can be potentially loaded in a conventional fixed-bed reactor, where the amount of catalyst is limited by the volume of the fixed-bed, and not by the mass.

The differences on catalytic performance between promoters can be related to the characterization measurements. The two most active catalysts, Ni-La₂O₃ and Ni-CeO₂, showed similar properties. Both presented the highest nickel i) reducibility (84–91% at 500 °C), ii) dispersion (2.3%) and iii) surface area (15 m²g_{Ni}⁻¹). Therefore, more

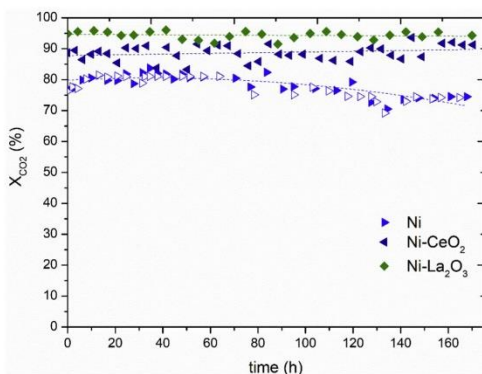


Fig. 5. Catalytic performance along time. Reaction conditions H₂:CO₂ = 4 (mol), P = 5 barg, m_{cat} = 0.3 g, F = 200 N mL·min⁻¹. Closed symbols: H₂S concentration of 50 ppb. Open symbol: H₂S-free.

amount of Ni⁰ active sites were available for CO₂ methanation. Furthermore, some general tendencies were observed by the interaction between CO₂ and the promoter/support material. Strong basic sites adsorb CO₂ irreversibly, less available for CH₄ formation. As Muroyama reported, strongly-adsorbed CO₂ can inhibit the formation of CH₄ and moderate basic sites are the most effective for CO₂ methanation [20]. The same tendency was observed in this work, and moderate adsorption of CO₂ onto the promoter seems beneficial. Thus, the existence of moderate basic sites in Ni-CeO₂ and Ni-La₂O₃ favour the conversion of CO₂. In parallel, it is worth noting that neither the crystallinity (XRD) nor the total surface area (N₂-physisorption) of the present samples were key factors to predict catalytic performance.

3.3. Catalyst stability

Additional long runs were performed on the two most promising catalysts in terms of initial activity, Ni-CeO₂ and Ni-La₂O₃. Long-term experiments were running for 24 h to evaluate at first the catalyst stability without impurities, and then a gas feed with 0.4 ppm of H₂S were added to the reactant mixture during 146 h. Fig. 5 plots CO₂ conversion at T = 300 °C and P = 5 barg as a function of time-on-stream. The highest catalytic activity was again achieved over Ni-La₂O₃, being this value constant during the whole experiment (X_{CO₂} = 95%). In the same way, no differences in performance over time were found in Ni-CeO₂ catalyst, at CO₂ conversion level of X_{CO₂} = 89%. It should be pointed out that slight catalyst deactivation could be masked over Ni-La₂O₃ due to activity close to the equilibrium (X_{CO₂} = 97%) but not in the case of Ni-CeO₂.

On the contrary, the catalytic activity of sample Ni was not constant during the long test. Initially, the conversion was X_{CO₂} = 77% and then it increased up to a maximum of X_{CO₂} = 84% after 30–35 h reaction. This activity enhancement suggested that not all the Ni was activated during the reduction step and it was further reduced during methanation reaction step (reducing atmosphere). As shown in H₂-TPR profiles, unpromoted nickel catalyst was much more difficult to reduce than Ni-La₂O₃ or Ni-CeO₂, so that the initial activation process was not completed at T = 500 °C for 3 h. After reaching this conversion maximum, it was observed a steady decrease of conversion to X_{CO₂} = 74% at 170 h. This behaviour was not related to catalyst poisoning by H₂S as identical results were observed in the equivalent H₂S-free experiment. Therefore, it is possible to conclude that the addition of industrial-level H₂S traces (50 ppb) did not show any impact on the catalytic performance of the tested catalysts. This fact discloses that catalysts are stable below the

detection limit of most commercial H₂S analysers, at least during one week of continuous H₂S injection.

Characterization of spent samples was performed to elucidate the reasons why the activity of Ni catalyst changed during the stability test. Used samples were removed from the experimental setup for characterization by EDX, XRD and TPO. Results were compared with fresh samples (see supporting information). As previously mentioned, sulphur poisoning did not infer in catalytic performance because identical results were obtained either with or without feed impurities. In agreement, sulphur compounds were not detected TPO analyses. Likewise, elemental sulphur was not identified in EDX measurements of spent samples. On the other hand, the chemical composition of spent catalysts was very similar to that of fresh ones and always within the experimental error. Accordingly, metal leaching was not relevant as components remained in the catalyst during operation. It is therefore reasonable to expect that catalyst fouling due to carbonaceous species formation or nickel particle sintering by metal migration could lead to the slight activity decay on Ni [39]. Results of Ni crystal size, measured by the Scherrer equation taking into account the accuracy of XRD (Table S2), suggested that nickel sintering was the responsible for Ni slight activity decay. The value of used sample (8.6 nm) was higher than that of the fresh one (7.8 nm). In contrast, nickel crystal size of fresh and used promoted samples was not increased, which was consistent with XRD results on dry reforming reaction [40]. Therefore, the role of La and Ce as promoters was also to prevent Ni from sintering and lengthen the catalyst lifetime.

4. Conclusions

The influence of using various metal oxides as promoters for CO₂ methanation reaction was studied at T = 200–350 °C and P = 5 barg. CeO₂, La₂O₃, Sm₂O₃, Y₂O₃ and ZrO₂ were incorporated together with nickel to γ-Al₂O₃ micro-spheres by wet impregnation method. The addition of metal oxide promoters was beneficial in all cases. Characterization results revealed that their role was to enhance the interaction between CO₂ and the catalyst. In this sense, the amount of CO₂ adsorbed on the promoted samples was clearly higher than that of the unpromoted one. Among them, the catalytic performance was led by the catalyst with La₂O₃ and CeO₂, while the least positive effect was shown by Sm₂O₃ and ZrO₂. The highest catalytic performance of Ni-La₂O₃ and Ni-CeO₂ was related to the significant increase of nickel reducibility and dispersion, so that more nickel active sites were available for reaction. Besides, both catalysts exhibited an intermediate heat of CO₂ adsorption (-168–182 kJ mol⁻¹). This fact strengthens the idea that moderate CO₂ chemisorption had a positive effect on the catalytic performance for CO₂ methanation.

Ni-CeO₂ and Ni-La₂O₃ samples were tested with the presence of almost undetectable, industrial-level H₂S traces for 170 h. The continuous addition of 50 ppb sulphur impurities did not show any influence on their catalytic performance as identical results were obtained without feed impurities. This fact discloses that the studied catalysts are stable below the detection limit of most commercial H₂S analysers, at least during one week of continuous H₂S injection. Accordingly, the strategy of adding metal oxide promoters was beneficial in terms of superior initial activity and, even more important, catalyst stability, as they prevented Ni from deactivation by sintering. The best performance was achieved by Ni-La₂O₃, which can be potentially used in biogas micro-structured methanation reactors as they show much higher catalytic performance than the commercial reference used in this study.

Acknowledgements

Authors thank Generalitat de Catalunya for financial support through the CERCA Programme, M2E (2017SGR1246) and XaRMAE network. IREC also gratefully acknowledge the funding of this work by the CoSin project (COMRDI15-1-0037), funded by ACCIÓ and the

European Regional Development Fund (ERDF) under the framework of RIS3CAT Energy Community. Andreina is grateful to Escuela Superior Politécnica del Litoral (ESPOL) for the support during her postgraduate studies (“Walter Valdano Raffo” Program, First edition). The authors thank Saint-Gobain NorPro for kindly providing γ -Al₂O₃ Accu spheres. Authors kindly thank Dr. Marco Argudo for the characterization of materials.

Appendix A. Supplementary data

Supplementary material related to this article can be found, in the online version, at doi:<https://doi.org/10.1016/j.jcou.2019.01.003>.

References

- [1] International Renewable Energy Agency (IRENA), Renewable Capacity Statistics 2018, (2018).
- [2] S. Rehman, L.M. Al-Hadhrani, M.M. Alam, Pumped hydro energy storage system: a technological review, *Renew. Sustain. Energy Rev.* 44 (2015) 586–598, <https://doi.org/10.1016/j.rser.2014.12.040>.
- [3] International Energy Agency, Monthly Electricity Statistics, (2018).
- [4] The Economic Development Agency of the German Federal State of Saxony-Anhalt, Invest in Saxony-Anhalt, (2018) www.invest-in-saxony-anhalt.com.
- [5] WIP Renewable Energies, Store Project, (2015) <http://www.store-project.eu/>.
- [6] J. Guilera, J. Ramon Morante, T. Andreu, Economic viability of SNG production from power and CO₂, *Energy Convers. Manage.* 162 (2018) 218–224, <https://doi.org/10.1016/j.enconman.2018.02.037>.
- [7] J. Witte, J. Settino, S.M.A. Biollaz, T.J. Schildhauer, Direct catalytic methanation of biogas – part I: new insights into biomethane production using rate-based modelling and detailed process analysis, *Energy Convers. Manage.* 171 (2018) 750–768, <https://doi.org/10.1016/j.enconman.2018.05.056>.
- [8] M. Götz, J. Lefebvre, F. Mörs, A. McDaniel Koch, F. Graf, S. Bajohr, R. Reimert, T. Kolb, Renewable Power-to-Gas: a technological and economic review, *Renew. Energy* 85 (2016) 1371–1390, <https://doi.org/10.1016/j.renene.2015.07.066>.
- [9] M. Martínez Molina, C. Kern, A. Jess, Catalytic hydrogenation of carbon dioxide to methane in wall-cooled fixed-bed reactors, *Chem. Eng. Technol.* 39 (2016) 2404–2415, <https://doi.org/10.1002/ceat.201500614>.
- [10] J. Ducamp, A. Bengouzer, P. Baurens, Modelling and experimental validation of a CO₂ methanation annular cooled fixed-bed reactor exchanger, *Can. J. Chem. Eng.* 95 (2017) 241–252, <https://doi.org/10.1002/cjce.22706>.
- [11] A. Alarcón, J. Guilera, T. Andreu, CO₂ conversion to synthetic natural gas: reactor design over Ni-Ce/Al₂O₃ catalyst, *Chem. Eng. Res. Des.* 140 (December) (2018) 155–165, <https://doi.org/10.1016/j.cherd.2018.10.017>.
- [12] M. Neubert, A. Hauser, B. Pourhossein, M. Dillig, J. Karl, Experimental evaluation of a heat pipe cooled structured reactor as part of a two-stage catalytic methanation process in Power-to-Gas applications, *Appl. Energy* 229 (2018) 289–298, <https://doi.org/10.1016/j.apenergy.2018.08.002>.
- [13] S. Abelló, C. Berruaco, D. Montané, High-loaded nickel–alumina catalyst for direct CO₂ hydrogenation into synthetic natural gas (SNG), *Fuel* 113 (2013) 598–609, <https://doi.org/10.1016/j.fuel.2013.06.012>.
- [14] S. Rönisch, J. Schneider, S. Matthischke, M. Schlüter, M. Götz, J. Lefebvre, P. Prabhakaran, S. Bajohr, Review on methanation – from fundamentals to current projects, *Fuel* 166 (2016) 276–296, <https://doi.org/10.1016/j.fuel.2015.10.111>.
- [15] M.A.A. Aziz, A.A. Jalil, S. Triwahyono, A. Ahmad, CO₂ methanation over heterogeneous catalysts: recent progress and future prospects, *Green Chem.* 17 (2015) 2647–2663, <https://doi.org/10.1039/C5G000119F>.
- [16] X. Su, J. Xu, B. Liang, H. Duan, B. Hou, Y. Huang, Catalytic carbon dioxide hydrogenation to methane: a review of recent studies, *J. Energy Chem.* 25 (2016) 553–565, <https://doi.org/10.1016/j.jechem.2016.03.009>.
- [17] E.Z. Golosman, V.N. Eremov, Industrial catalysts for the hydrogenation of carbon oxides, *Catal. Use Indium* 4 (2012) 267–283, <https://doi.org/10.1134/S2070050412040071>.
- [18] S. Tada, T. Shimizu, H. Kameyama, T. Haneda, R. Kikuchi, Ni/CeO₂ catalysts with high CO₂ methanation activity and high CH₄ selectivity at low temperatures, *Int. J. Hydrogen Energy* 37 (2012) 5527–5531, <https://doi.org/10.1016/j.ijhydene.2011.12.122>.
- [19] L. Atzori, M.G. Cutrufello, D. Meloni, C. Cannas, D. Gazzoli, R. Monaci, M.F. Sini, E. Rombi, Highly active NiO-CeO₂ catalysts for synthetic natural gas production by CO₂ methanation, *Catal. Today* 299 (2018) 183–192, <https://doi.org/10.1016/j.cattod.2017.05.065>.
- [20] H. Muroyama, Y. Tsuda, T. Asakoshi, H. Masitah, T. Okanishi, T. Matsui, K. Eguchi, Carbon dioxide methanation over Ni catalysts supported on various metal oxides, *J. Catal.* 343 (2016) 178–184, <https://doi.org/10.1016/j.jcat.2016.07.018>.
- [21] A. Westermann, B. Azambre, M.C. Bacariza, I. Graça, M.F. Ribeiro, J.M. Lopes, C. Henriques, Insight into CO₂ methanation mechanism over NiUSY zeolites: an operando IR study, *Appl. Catal. B Environ.* 174–175 (2015) 120–125, <https://doi.org/10.1016/j.apcatb.2015.02.026>.
- [22] A. Beuls, C. Swalus, M. Jacquemin, G. Heyen, A. Karelavic, P. Ruiz, Methanation of CO₂: Further insight into the mechanism over Rh/ γ -Al₂O₃ catalyst, *Appl. Catal. B Environ.* 113–114 (2012) 2–10, <https://doi.org/10.1016/j.apcatb.2011.02.033>.
- [23] A. Zhao, W. Ying, H. Zhang, H. Ma, D. Fang, La and Mn promotion of Ni/Al₂O₃ catalysts for syngas methanation, *Energy Sour. Part A Recov. Util. Environ. Eff.* 36 (2014) 1049–1056, <https://doi.org/10.1080/15567036.2012.666621>.
- [24] P. Reñones, F. Fresno, J.L.G. Fierro, V.A. de la Peña O’Shea, Effect of La as promoter in the photoreduction of CO₂ over TiO₂ catalysts, *Top. Catal.* 60 (2017) 1119–1128, <https://doi.org/10.1007/s11244-017-0797-x>.
- [25] H. Liu, X. Zou, X. Wang, X. Lu, W. Ding, Effect of CeO₂ addition on Ni/Al₂O₃ catalysts for methanation of carbon dioxide with hydrogen, *J. Nat. Gas Chem.* 21 (2012) 703–707, [https://doi.org/10.1016/S1003-9953\(11\)60422-2](https://doi.org/10.1016/S1003-9953(11)60422-2).
- [26] S. Rahmani, F. Meshkini, M. Rezaei, Preparation of Ni-M (M: La, Co, Ce, and Fe) catalysts supported on mesoporous nanocrystalline γ -Al₂O₃ for CO₂ methanation, *Environ. Prog. Sustain. Energy* (2018), <https://doi.org/10.1002/ep.13040>.
- [27] C. Mebrahtu, S. Abate, S. Perathoner, S. Chen, G. Centi, CO₂ methanation over Ni catalysts based on ternary and quaternary mixed oxide: a comparison and analysis of the structure-activity relationships, *Catal. Today* 304 (April) (2017) 181–189, <https://doi.org/10.1016/j.cattod.2017.08.060>.
- [28] S. Mitchell, N.-L. Michels, J. Pérez-Ramírez, From powder to technical body: the undervalued science of catalyst scale up, *Chem. Soc. Rev.* 42 (2013) 6094–6112.
- [29] G.M. Lari, A.B.L. de Moura, L. Weimann, S. Mitchell, C. Mondelli, J. Pérez-Ramírez, Design of a technical Mg–Al mixed oxide catalyst for the continuous manufacture of glycerol carbonate, *J. Mater. Chem. A* 5 (2017) 16200–16211, <https://doi.org/10.1039/C7TA02061A>.
- [30] M. Seo, S.Y. Kim, Y.D. Kim, E.D. Park, S. Uhm, Highly stable barium zirconate supported nickel oxide catalyst for dry reforming of methane: From powders toward shaped catalysts, *Int. J. Hydrogen Energy* 43 (2018) 11355–11362, <https://doi.org/10.1016/j.ijhydene.2018.03.181>.
- [31] A. Bengouzer, J. Ducamp, I. Champon, R. Try, Performance evaluation of fixed-bed, millistructured, and metallic foam reactor channels for CO₂ methanation, *Can. J. Chem. Eng.* 96 (2018) 1937–1945, <https://doi.org/10.1002/cjce.23140>.
- [32] X. Yang, F. Cheng, J. Liang, Z. Tao, J. Chen, Pt/Ni – x nanoparticles as catalysts for hydrogen generation from hydrolysis of ammonia borane, *Int. J. Hydrogen Energy* 34 (2009) 8785–8791, <https://doi.org/10.1016/j.ijhydene.2009.08.075>.
- [33] H.P. Klug, L.E. Alexander, Harold P. Klug, Leroy E. Alexander (Eds.), X-Ray Diffraction Procedures: for Polycrystalline and Amorphous Materials, X-Ray Diff. Proced. Polycryst. Amorph. Mater. 2nd ed., Wiley-VCH, 1974, p. 992 Pp. 992. ISBN 0-471-49369-4. May 1974.
- [34] C.H. Bartholomew, R.B. Pannell, The stoichiometry of hydrogen and carbon monoxide chemisorption on alumina- and silica-supported nickel, *J. Catal.* 65 (1980) 390–401, [https://doi.org/10.1016/0021-9517\(80\)90316-4](https://doi.org/10.1016/0021-9517(80)90316-4).
- [35] Q. Liu, A. Wang, X. Wang, P. Gao, X. Wang, T. Zhang, Synthesis, characterization and catalytic applications of mesoporous γ -alumina from boehmite sol, *Microporous Mesoporous Mater.* 111 (2008) 323–333, <https://doi.org/10.1016/j.micromeso.2007.08.007>.
- [36] Z. He, X. Wang, R. Liu, S. Gao, T. Xiao, Performances of different additives on NiO/ γ -Al₂O₃ catalyst in CO methanation, *Appl. Petrochem. Res.* 6 (2016) 235–241, <https://doi.org/10.1007/s13203-016-0160-3>.
- [37] C.H. Bartholomew, R.J. Farrauto, Chemistry of nickel-alumina catalysts, *J. Catal.* 45 (1976) 41–53, [https://doi.org/10.1016/0021-9517\(76\)90054-3](https://doi.org/10.1016/0021-9517(76)90054-3).
- [38] M.E. Davis, R.J. Davis, Fundamentals of chemical reaction engineering, *Courier Corporation* 45 (1) (2012) 41–53 October 1976.
- [39] S. Ewald, M. Kolbeck, T. Kratky, M. Wolf, O. Hinrichsen, On the deactivation of Ni-Al catalysts in CO₂ methanation, *Appl. Catal. A Gen.* 570 (January) (2018) 376–386, <https://doi.org/10.1016/j.apcata.2018.10.033>.
- [40] N. Wang, W. Qian, W. Chu, F. Wei, Crystal-plane effect of nanoscale CeO₂ on the catalytic performance of Ni/CeO₂ catalysts for methane dry reforming, *Catal. Sci. Technol.* 6 (2016) 3594–3605, <https://doi.org/10.1039/C5CY01790D>.



Contents lists available at ScienceDirect

Fuel Processing Technology

journal homepage: www.elsevier.com/locate/fuproc

Research article

Optimization of nickel and ceria catalyst content for synthetic natural gas production through CO₂ methanationAndreina Alarcón^{a,b}, Jordi Guilera^{a,*}, José Antonio Díaz^{a,c}, Teresa Andreu^a^a Catalonia Institute for Energy Research (IREC), Jardins de les Dones de Negre 1, 08930 Sant Adrià de Besòs, Spain^b Escuela Superior Politécnica del Litoral, ESPOL, Facultad de Ingeniería en Ciencias de la Tierra, Campus Gustavo Galindo Km.30.5 Vía Perimetral, P.O. Box 09-01-5863, Guayaquil, Ecuador^c Department of Mechanical, Chemical and Industrial Design Engineering, ETSIDI, Universidad Politécnica de Madrid (UPM), 28012 Madrid, Spain

ARTICLE INFO

Keywords:

Power-to-Gas
Synthetic natural gas
Carbon dioxide conversion
Micro-catalyst
Formulation
Catalytic activity

ABSTRACT

Manufacturing of catalysts with high reaction rates at mild conditions is important for an efficient production of synthetic natural gas through the CO₂ methanation process. In this work, the design of a technical catalyst based on an optimal content of Ni as active phase, CeO₂ as promoter and γ -Al₂O₃ micro-spheres as support ($d_p = 400\text{--}500\ \mu\text{m}$) is evaluated. The systematic optimization of Ni, CeO₂ and γ -Al₂O₃ content revealed that a proper balance of the positive effects that each component provided individually, was found at 25 wt% Ni, 20 wt% CeO₂ and 55 wt% γ -Al₂O₃ content. This catalyst was stable for 120 h at 300 °C. The high loading of CeO₂ is far from the classical definition of promoter and it covers the gap between the addition in a low amount as promoter and its uncompetitive use as bulk support. The highest catalytic activity was attributed to high metallic surface area (5 m²g⁻¹), high nickel reducibility (79% at 500 °C) and the formation of moderate basic sites that can adsorb CO₂ (−65 kJ·mol_{CO₂}⁻¹). In comparison with similar research catalysts and a commercial reference, the optimum formation showed higher activity for synthetic natural gas production. Therefore, the micro-catalyst can be implemented in the micro-structured reactors that are available in the market.

1. Introduction

The implementation of renewable energies, such as solar and wind, into national energy mixes reduce drastically CO₂ emissions in the atmosphere respect to fossil fuels [1,2]. One of the major challenges of these low-carbon technologies is the ability to match the unscheduled intermittent production with consumer demand, i.e. reliable electricity supply. As already experienced in some countries, grid balancing is becoming a major issue leading to temporary shutdowns of wind turbines. One long-term solution for power balancing can be the implementation of Power-to-Gas technologies, especially in countries where there is already a significant investment in wind and solar energy sources [3]. These technologies convert the surpluses of electrical energy coming from unpredictable energy sources into storable renewable hydrogen through water electrolysis. Besides, they can also incorporate CO₂ as a source of carbon for the production of synthetic natural gas (SNG) [4,5]. In this sense, Power-to-Gas reduce the CO₂ content in the atmosphere by supporting the continuous implementation of wind and solar sources into electricity mix but also by converting CO₂ to useful energy products as SNG [6,7].

At present, natural gas constitutes 40% of the fuel mix to satisfy the heating and cooling services across EU. This represents one of the main reasons to support SNG in the future as a low carbon alternative [8]. However, SNG is not economically competitive with respect to fossil natural gas [9]. ENEA consulting concluded that the competitiveness of SNG for grid injection requires, at least, reducing capital expenditures by a factor of two [10]. Among the total costs, the capital expenditures of the catalytic methanation unit significantly contribute to the SNG cost [11,12]. As the CO₂ methanation is not a mature technology, gains on capital expenditures are possible driven by R&D efforts.

The catalytic CO₂ methanation is a thermochemical process carried out through the Sabatier reaction (Eq. (1)), in which one molecule of CO₂ is combined with four molecules of H₂ over a suitable catalyst to form CH₄ and H₂O. According to thermodynamics, this reaction is favourable ($\Delta G_{298\text{K}} = -130.8\ \text{kJ}\cdot\text{mol}^{-1}$) at low temperatures ($\leq 300\ \text{°C}$) [13,14]. Nevertheless, kinetic limitations appear at low temperature, since it requires an eight-electron process to reduce the fully oxidized carbon to methane. Therefore, the design and development of highly active catalysts is necessary to obtain reasonable reaction rates of SNG production at the aforementioned conditions. These active catalysts

* Corresponding author.

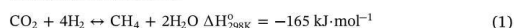
E-mail address: jguilera@irec.cat (J. Guilera).<https://doi.org/10.1016/j.fuproc.2019.05.008>

Received 8 February 2019; Received in revised form 7 May 2019; Accepted 7 May 2019

Available online 18 May 2019

0378-3820/ © 2019 Elsevier B.V. All rights reserved.

should be manufactured according to reactor design application [15]. In recent years, the concept of modular compact reactors has been proposed, typically in the form of micro-channels below 1 mm [16–21]. Therefore, catalyst particle dimensions should also be adapted to technological advances.



Catalysts based on noble- and transition-metal materials (Ru, Rh, Pd and Ni) supported on metal oxides (Al_2O_3 , CeO_2 , ZrO_2 , TiO_2 , SiO_2 , La_2O_3) are usually applied for the CO_2 methanation process [22,23]. Among them, Ni-based catalysts, usually supported on $\gamma\text{-Al}_2\text{O}_3$ are the most widely investigated for industrial purposes, as they combine reasonable activity and low cost. However, sintering of Ni nanoparticles and carbon deposition on the surface of Ni/ $\gamma\text{-Al}_2\text{O}_3$ catalysts can lead to rapid deactivation [24,25]. To overcome these issues, modification of the support through addition of promoters has gained interest, since it can play an important role on the metal-support interaction, as well as on the bonding and reactivity of chemisorbed species [26]. Promoter oxides such as CeO_2 , La_2O_3 , Pr_2O_3 , Eu_2O_3 , Gd_2O_3 , ZrO_2 , MnO_2 and MgO have been recently studied [27–31]. Among them, CeO_2 has been extensively studied as interesting support, alone or with its combination with ZrO_2 (Ce-ZrO_2 mixed oxides) in heterogeneous catalysis [32–36].

For economic purposes, some researchers proposed that CeO_2 could be effectively used as promoter (≤ 3 wt%) instead of bulk support (≥ 50 wt%). In those cases, alumina is employed as inexpensive support. Recently, Liu et al. [37] optimized CeO_2 content on a 15 wt% Ni/ $\gamma\text{-Al}_2\text{O}_3$ catalyst. They found that the addition of 2 wt% CeO_2 gave the optimum catalytic performance. In another study, Zhou et al. [38] reported that the addition of 2.5 wt% CeO_2 to 10 wt% Ni highly improve the catalytic performance in comparison to unpromoted Ni/ $\gamma\text{-Al}_2\text{O}_3$. Nie et al. [39] concluded that the presence of 3 wt% CeO_2 on a highly loaded 20 wt% Ni/ $\gamma\text{-Al}_2\text{O}_3$ exhibits optimal catalytic properties in terms superior CH_4 activity and selectivity. In these reported works, the effect of ceria addition as promoter has been studied based on a fixed amount of Ni; 15 wt%, 10 wt% and 20 wt%, respectively.

The innovative aspect of the present work is the simultaneous optimization of the amount of Ni, CeO_2 and $\gamma\text{-Al}_2\text{O}_3$ to obtain the global optimum of catalytic performance on Ni-CeO₂/ $\gamma\text{-Al}_2\text{O}_3$ formulations. This is in contrast to local optimums found in previous works, where the amount of the active phase was already fixed. The proposed catalysts have been synthesized with a proper particle size ($d_p = 400\text{--}500 \mu\text{m}$) to be directly implemented in the micro-structured reactors that are now available in the market [40]. In particular, optimal formulation will be applied in the context of the CoSin project, an industrial action led by Naturgy aiming to demonstrate the technical and economic viability of SNG production at a sewage treatment plant in Catalonia [41]. In the present work, the catalytic performance was evaluated in a lab-scale reactor at 250–350 °C, $P = 0\text{--}5$ barg and gas hourly space velocities (GHSV) = 4,500–54,000 h^{-1} , by feeding the stoichiometric $\text{H}_2\text{:CO}_2$ molar ratio = 4. In addition, the catalytic stability of the most promising catalyst was evaluated for 120 h and compared with a commercial reference.

2. Experimental

2.1. Catalyst preparation

A series of Ni-CeO₂/ $\gamma\text{-Al}_2\text{O}_3$ catalysts were prepared by the wet impregnation method. The content of Ni and CeO_2 was varied simultaneously in a range from 0 to 30 wt%. Accordingly, the content of $\gamma\text{-Al}_2\text{O}_3$ was in the range of 40–100 wt%. The systematic experimental design led to the preparation of the eight samples with different composition.

Materials used for catalyst synthesis were commercial $\gamma\text{-Al}_2\text{O}_3$ microspheres with particle diameters of $d_p = 450\text{--}500 \mu\text{m}$ (Saint-Gobain NorPro), and salt precursors of nickel (II), nitrate hexahydrate [Ni

(NO₃)₂6H₂O] (98% purity, Alfa Aesar), and cerium (III), nitrate hexahydrate [Ce(NO₃)₃6H₂O] (99% purity, Fluka). Furthermore, METH® 134 catalyst (Clariant) with a Ni content of 22 wt% was crushed, sieved ($d_p = 400\text{--}500 \mu\text{m}$) and used as commercial reference.

Prior to the synthesis, $\gamma\text{-Al}_2\text{O}_3$ support was pre-dried at 105 °C overnight. Successively, an aqueous solution was prepared with the appropriate amount of distilled water (weight ratio $\text{H}_2\text{O}:\gamma\text{-Al}_2\text{O}_3 = 5$) and the salt precursors of nickel and cerium. Then, $\gamma\text{-Al}_2\text{O}_3$ support was added to the aqueous solution and mixed in a rotary vacuum evaporator with constant stirring (25 rpm) at room temperature for 1 h. The mixture was evaporated out in the same equipment at $T = 85 \text{ }^\circ\text{C}$ and $P = 0.8$ bar during 6 h. The recovered material was then dried at 105 °C in an atmospheric oven overnight. Lastly, the catalysts were calcined at 450 °C for 30 min with a heating ramp of 1 °C·min⁻¹.

2.2. Catalyst characterization

Microscope images and elemental analysis of the catalysts were studied by scanning electron microscopy (SEM, Zeiss Auriga 60) equipped with an energy dispersive X-ray spectrometer (EDX, Oxford Inca Energy). Textural properties were determined from N₂-physorption (adsorption/desorption) isotherms recorded by a TriStar II 3020-Micromeritics sorption analyser. Prior to the measurements, the samples were degassed at 90 °C for 1 h, and then at 250 °C for 4 h on a FlowPrep 060-Micromeritics. Brunauer-Emmett-Teller (BET) method was used to calculate the BET surface area for a relative pressure (P/P_0) range between 0.05 and 0.30. Furthermore, Barrett-Joyner-Halenda (BJH) method applied to desorption branch of the isotherm was used to determinate the mesopore volume.

Structural properties were studied by powder X-ray Diffraction (XRD). The wide-angles data were obtained on a Bruker type XRD D8 Advance A25 diffractometer using a Cu K α radiation ($\lambda = 1.5406$ nm), a voltage of 40 kV, a current of 40 mA and a step size of 0.05° (with 3 s duration at each step). The acquisitions were done in a range from 20 to 80°. The software XPert HighScorePlus was used to identify the crystalline phase using the standard powder XRD files published by the International Centre for Diffraction Data (ICDD). The average crystal size was calculated using the Scherer's equation: $d_{\text{Ni}} = (K\lambda/\beta\cos\theta)$, where λ is the X-ray wavelength, β is the full width of the diffraction line at half maximum (FWHM), and θ is the Bragg angle.

Reducibility of the catalysts was analysed by temperature programmed reduction method (H_2 -TPR) on an Autochem (Micromeritics). In each run, 70 mg of fresh calcined catalyst were used for the analysis. The H_2 -TPR measurements were conducted using 12 vol% H_2/Ar at a flow of 50 $\text{NmL}\cdot\text{min}^{-1}$ in the temperature range of 35 to 800 °C and a heating ramp of 10 °C·min⁻¹. The amount of reduced NiO to Ni⁰ was calculated by integrating the reduction peaks in the H_2 -TPR profiles and expressed as a percentage of consumption to reduce the Ni species in the catalysts.

Metal dispersion and metallic surface area were measured by CO chemisorption with the Autochem (Micromeritics) apparatus. In this case, 50 mg of catalyst were reduced using 50 $\text{NmL}\cdot\text{min}^{-1}$ in a 12 vol% H_2/Ar flow at 500 °C for 3 h with a heating ramp of 5 °C·min⁻¹. Then, CO chemisorption was performed at 35 °C under a 10 vol% CO/He flow. CO pulses were introduced for several times until saturation was reached. Nickel metal surface area and dispersion were calculated assuming the stoichiometric factor for CO to Ni as one.

The amount and heat of CO₂ adsorption was studied by coupled thermogravimetric analysis and differential scanning calorimetry with CO₂ pulses (TGA-DSC, Setaram Evo). The samples (50 mg) were placed at 90 °C for 30 min in a Ar flow (50 $\text{NmL}\cdot\text{min}^{-1}$) to remove water. Then, samples were reduced using 12 vol% H_2/Ar at a flow of 10 $\text{NmL}\cdot\text{min}^{-1}$. The temperature was increased up to 500 °C for 3 h with a heating ramp of 5 °C·min⁻¹, then cooled down to room temperature. Finally, the 12 vol% H_2/Ar flow was replaced with a 10 vol% CO₂/Ar flow (10 $\text{NmL}\cdot\text{min}^{-1}$) to measure the CO₂ adsorbed mass amount and the heat of

adsorption at 35 °C.

2.3. Catalytic activity

The catalytic activity of the samples was tested in a fixed-bed laboratory reactor with internal diameter of 13 mm and 305 mm length (Microactivity Reference, PID Eng&Tech). Experiments were conducted using 0.3 g of catalyst mass diluted with 3 g of silicon carbide 46 grit (Cymit) of similar particle sizes ($d_p = 355 \mu\text{m}$) to assure isothermal behaviour through the catalyst bed [42]. The reaction temperature was monitored using a K-type thermocouple placed in the middle of the catalyst bed. The reactants were continuously controller via mass flow rates (MFC, Bronkhorst) and introduced as feed mixture at $200 \text{ NmL}\cdot\text{min}^{-1}$ with a stoichiometric $\text{H}_2\text{:CO}_2$ molar ratio of 4 (99.999% and 99.9993%, respectively; Linde). After reaction, the products passed through a cold liquid-gas separator (5 °C) where water was trapped, and then the dry flow was measured by using a mass flow meter (MF, Bronkhorst). The composition of the dry gas (CH_4 , H_2 , CO , CO_2) was determined with an on-line gas micro-chromatograph (490 microGC, Agilent Technologies) and automatically analysed every 2.5 min along the screening experiments, and hourly during the stability test.

The experimental procedure is described below. Prior to reaction, the catalysts were in-situ reduced under H_2 (99.999%, Linde) flow ($100 \text{ NmL}\cdot\text{min}^{-1}$) at 500 °C for 3 h with a heating ramp of $5 \text{ °C}\cdot\text{min}^{-1}$, then cooling down to room temperature with the same ramp. The systematic Ni-CeO₂/γ-Al₂O₃ catalyst screening was carried out isothermally at atmospheric pressure with intervals of 50 °C in the temperature range of 250–350 °C. In each run, the experiment started at the lowest temperature, with a holding time of 30 min at each temperature (at this time steady state was always attained) and increasing to the following value at $10 \text{ °C}\cdot\text{min}^{-1}$. In addition, the catalytic activity of the most promising Ni-CeO₂ catalyst was studied at 300 °C, a pressure range of 0–10 barg and GHSVs of 4500–54,000 h⁻¹. Finally, the catalytic stability was also evaluated and compared with a commercial catalyst for 120 h at 5 barg, 300 °C and using a GHSV of 36,000 h⁻¹.

GHSV was calculated as the ratio of inlet flow rate in standard conditions to the volume of the catalyst. Volumetric flow rate (F) was varied in a range of 25 to 300 mL·min⁻¹, whereas the catalyst mass was kept constant ($m_{\text{cat.}} = 0.3 \text{ g}$). The bulk density of each catalyst (ρ_{bulk}) can be found in Table S1. GHSV (Eq. (2)) as well as CO₂ conversion (Eq. (3)), CH₄ selectivity (Eq. (4)) and CO selectivity (Eq. (5)) were determined using the following equations:

$$\text{GHSV} = \frac{F}{\frac{m_{\text{cat.}}}{\rho_{\text{bulk}}}} \quad (2)$$

$$X_{\text{CO}_2} = \left(1 - \frac{F_{\text{CO}_2,\text{out}}}{F_{\text{CO}_2,\text{in}}}\right) \cdot 100 \quad (3)$$

$$S_{\text{CH}_4} = \left(\frac{F_{\text{CH}_4,\text{out}}}{F_{\text{CH}_4,\text{out}} + F_{\text{CO}_2,\text{out}}}\right) \cdot 100 \quad (4)$$

$$S_{\text{CO}} = \left(\frac{F_{\text{CO}_2,\text{out}}}{F_{\text{CO}_2,\text{out}} + F_{\text{CH}_4,\text{out}}}\right) \cdot 100 \quad (5)$$

where $[F_x]$ ($x = \text{CO}_2$, CH_4 and CO) represents the molar flow rate of the species in the inlet and outlet gas. Similar conversion values were obtained from CO₂ than from H₂ (standard deviation of ± 2%).

3. Results and discussion

3.1. Metal content optimization

A total of eight samples were prepared by varying simultaneously the Ni and CeO₂ content, to cover the range of 0–30 wt%. Preliminary results indicated that the highest catalytic activity can be found within

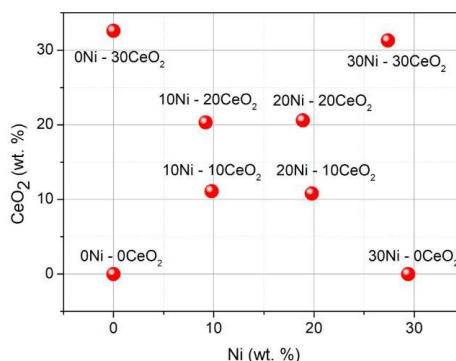


Fig. 1. Elemental composition by EDX analysis.

this metal range. The elemental composition of the crushed catalysts was obtained by EDX analyses, displayed in Fig. 1. The experimental metal contents were very close to the nominal ones (0–30 wt%), with an absolute error of ± 1 wt% for the samples with 10 and 20 wt% of Ni and CeO₂ content and ± 3 wt% for the samples with 30 wt% Ni and CeO₂ content. After metal impregnation, it was observed by SEM images that the geometric shape of the samples was very similar to the initial γ-Al₂O₃ support, i.e. micro-spheres with proper sizes between 400 and 500 μm. As an example, Fig. 2 shows the geometric shape and particle diameter (approximately 468 μm) for the 10Ni-10CeO₂ sample.

Textural properties were studied by N₂-physiosorption. All isotherms were of type IV with H₁ shaped hysteresis loops (see Fig. S1), which are associated to uniform mesoporous spheres in fairly regular array [43]. In this study, the γ-Al₂O₃ support (0Ni-0CeO₂ catalyst) exhibited the largest BET surface area ($S_{\text{BET}} = 267 \text{ m}^2\cdot\text{g}^{-1}$) and pore volume ($V_{\text{pore}} = 0.41 \text{ cm}^3\cdot\text{g}^{-1}$). A significant reduction in these properties was observed once Ni and CeO₂ were introduced and the amount of support was accordingly reduced. The progressive reduction of BET surface area (from 267 to 120 m²·g⁻¹) is shown in Fig. 3. An analogous trend was observed regarding the pore volume of the samples (from 0.41 to 0.11 cm³·g⁻¹), illustrated in Fig. S2. Results indicate that Ni and CeO₂ cause a similar pore blocking effect on the support.

The XRD patterns of all calcined materials exhibited comparable structures (see Fig. S3). On one hand, characteristic peaks associated to cubic gamma alumina (ICDD file # 010-0425) were identified in all samples around 37.12, 46.07 and 66.98°. After the metal impregnation, the corresponding samples also exhibited characteristic reflections of cubic NiO phase (ICDD file # 047-1049) at 37.29, 43.45, 62.95 and 75.52°, and the cubic CeO₂ phase [44] (ICDD file # 034-0394) at 28.71,

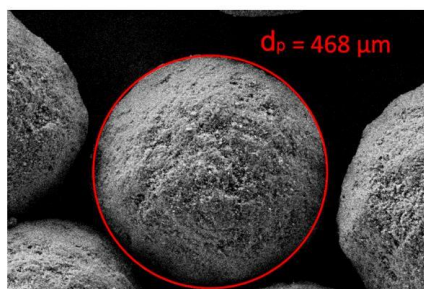


Fig. 2. Representative SEM image of a 10Ni-10CeO₂ sample.

A. Alarcón, et al.

Fuel Processing Technology 193 (2019) 114–122

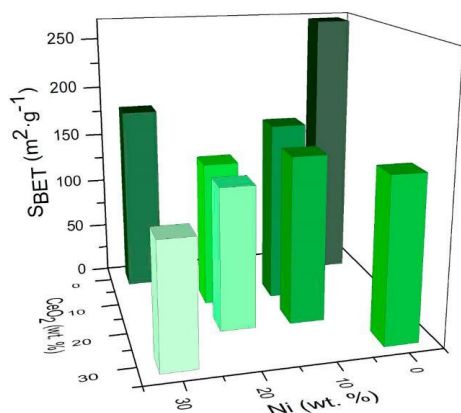


Fig. 3. S_{BET} ($m^2 \cdot g^{-1}$) from N_2 -physorption.

33.26, 47.49, 56.53 and 77.21°. The diffraction peaks associated to NiO were clearly recognized in all Ni-based samples. At a low content of Ni (10 wt%), only a diffraction peak of NiO was detected at 37.3°. In contrast, the diffraction peaks of NiO were remarked into the four aforementioned angles at higher contents of Ni (≥ 20 wt%).

In addition, XRD measurements were carried out in the reduced samples. Ni was detected in all the XRD profiles. As it can be seen in Fig. 4, the most intense diffraction peaks associated to metallic Ni phase (ICDD file # 004-0850) were identified at $2\theta = 44.51$, 51.84 and 76.37°. These peaks were especially recognized in the samples with a high Ni content (≥ 20 wt%). The crystallite sizes of Ni (d_{Ni}) were estimated by the Scherrer's equation at $2\theta = 44.51^\circ$ (see Fig. S4). The Ni particle sizes were found in the nanometer range (≤ 23.30 nm). Particle diameter can be related to the Ni content; higher nickel amount, higher particle diameter.

The reducibility of Ni-based materials was studied by H_2 -TPR technique. The most representative H_2 -TPR profiles, 0Ni-0CeO₂, 0Ni-30CeO₂, 30Ni-0CeO₂ and 30Ni-30CeO₂, are displayed in Fig. 5. For the sake of clarity, other profiles can be found in Fig. S5. The similar pattern of 0Ni-0CeO₂ and 0Ni-30CeO₂ confirm that neither the γ -Al₂O₃ support nor the CeO₂ promoter was reduced within the explored

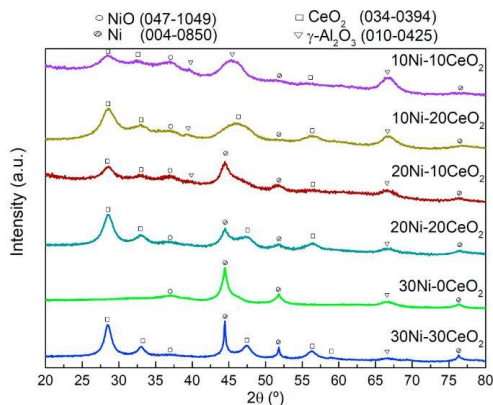


Fig. 4. XRD patterns of reduced catalysts.

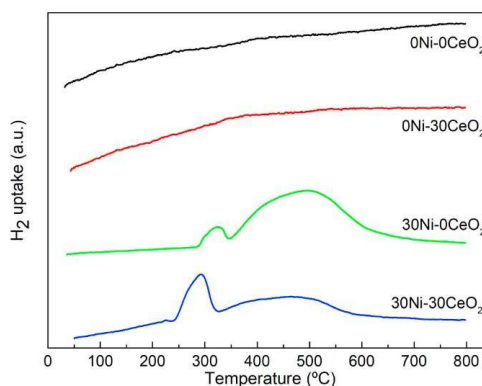


Fig. 5. H_2 -TPR profiles of 0Ni-0CeO₂, 0Ni-30CeO₂, 30Ni-0CeO₂ and 30Ni-30CeO₂ catalysts.

temperature range ($T < 800^\circ C$). Thus, H_2 -TPR measurements indicated that all peaks were generated because of the reduction of NiO to Ni⁰.

According to previous works [45,46], the reducible NiO species could be divided into three types: α , β and γ . Interestingly, α -type NiO species (200–350 °C), which corresponded to species with weak or even no interaction with γ -Al₂O₃ support, were only predominantly formed when CeO₂ was added as promoter. The mild-temperature peaks represent β -type NiO species (350–600 °C), which showed stronger interaction with the γ -Al₂O₃ support. It is worth noting that the 30Ni-30CeO₂ catalyst exhibited a large fraction of NiO that interacts weakly with the support, leading to reduction peaks at 225, 291 and 465 °C. In contrast, stronger-interacting NiO species were observed in the non-promoted 30Ni-0CeO₂ catalyst, by showing reduction peaks at 320 and 500 °C. Finally, high-temperature peaks are typically assigned to γ -type NiO species (600–800 °C), which are ascribed to the stable nickel aluminate phase with the spinel structure. No γ -type NiO species were observed in any sample, most probably due to the low calcination temperature used in the present work (450 °C).

The amount of H_2 consumed was estimated from the H_2 -TPR measurements (see Fig. S6). In the studied temperature range ($T = 35$ –800 °C), the obtained H_2 uptake was in the range of 0.071–0.165 mmol_{g_{cat}}⁻¹. As concerns to the effect of the promoter, the introduction of CeO₂ clearly improved the catalyst reducibility. The degree of reduction of most Ni-CeO₂ catalysts at 500 °C, compared to the total uptake value at $T = 800^\circ C$, was between 59 and 69%. These results were in agreement with XRD measurements, where diffraction peaks associated to NiO phase were also identified in the reduced catalysts. In the case of the high-loaded 30Ni-0CeO₂ sample, only 56% of the H_2 was consumed at 500 °C. On the contrary, the addition of CeO₂ greatly enhanced this percentage to 78% for 30Ni-30CeO₂. Accordingly, the availability of active nickel after sample reduction at 500 °C is much higher in the case of CeO₂-promoted samples.

Ni-CeO₂/ γ -Al₂O₃ samples were evaluated on the production of SNG by CO₂ methanation reaction. The reaction was carried out isothermally in a temperature range of 250–350 °C, at atmospheric pressure and 200 NmL_{min}⁻¹ of reactants (stoichiometric mixture). Catalytic performances were evaluated by means of CO₂ conversion and CH₄ selectivity. Besides CH₄ as the main product, only CO was observed as reaction by-product ($S_{CO} \leq 3\%$). In all experiments, higher CO₂ conversions (from 3.53 to 79.90%) and CH₄ selectivities (from 97 to 100%) were obtained as temperature increased up to 350 °C. Fig. 6 shows CO₂ conversion as function of reaction temperature over the catalysts at the boundary limits of the systematic experimental design,

A. Alarcón, et al.

Fuel Processing Technology 193 (2019) 114–122

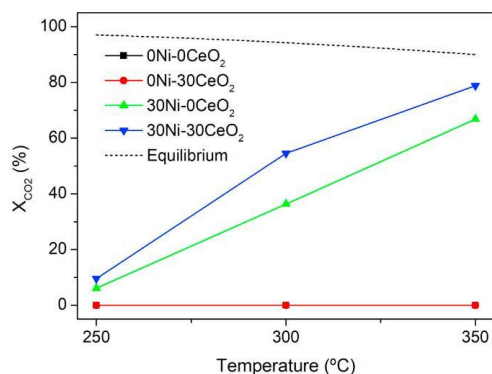


Fig. 6. CO₂ conversion (%) of 0Ni-0CeO₂, 0Ni-30CeO₂, 30Ni-0CeO₂ and 30Ni-30CeO₂ catalysts as function of reaction temperature. Reaction conditions: P = 0 barg, F = 200 NmLmin⁻¹, m_{cat.} = 0.3 g and H₂:CO₂ molar ratio = 4. Note: the obtained results for the 0Ni-30CeO₂ and 0Ni-0CeO₂ catalysts are overlapped.

0Ni-0CeO₂, 0Ni-30CeO₂, 30Ni-0CeO₂ and 30Ni-30CeO₂ catalysts. No conversion was observed on 0Ni-0CeO₂ and 0Ni-30CeO₂ samples and experimental results are overlapped in the graph. Therefore, it can be concluded that the catalytic activity of γ -Al₂O₃ and CeO₂ for SNG production is negligible and they both need the presence of Ni as the active phase. In this sense, 30Ni-0CeO₂, 30Ni-30CeO₂ catalysts, and the rest of Ni-based catalysts (shown in Fig. S7) exhibited significant catalytic activities. Among Ni-based samples, 30Ni-30CeO₂ catalyst was clearly more active than 30Ni-0CeO₂. Thus, the presence of CeO₂ as promoter was clearly beneficial for the reaction.

The whole series of catalyst screening results are displayed in Fig. 7 as surface response form. It is clearly inferred that the presence of Ni and CeO₂ improves the catalytic activity, in such a way that highly loaded catalysts led to higher catalytic performances. However, the catalyst with highest metal loading, 30Ni-30CeO₂, was not the most active and a maximum in catalytic performance was observed within the limits explored. Therefore, the systematic experimental design proposed in this study allowed to obtain a mathematical maximum region of catalytic activity, in particular around 22–28 wt% of Ni and

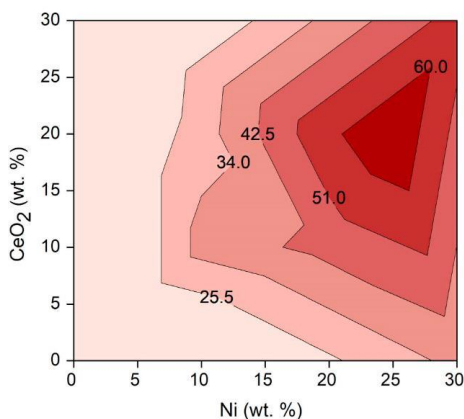


Fig. 7. CO₂ Conversion (%) trend of the tested Ni-CeO₂ catalysts at 300 °C.

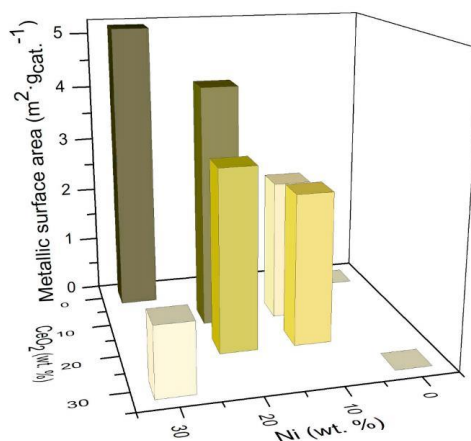


Fig. 8. Metallic surface area (m²·g_{cat.}⁻¹) from CO-chemisorption.

15–25 wt% of CeO₂.

For a better understanding of the maximum region of catalytic activity, samples were further evaluated by CO chemisorption measurements. As a rule, the increase of Ni content showed two opposite effects. On one hand, it led to lower metal dispersion (Fig. S8). On the other hand, the total metallic surface area was increased (Fig. 8) in such a way that nickel was poorly dispersed at high-loading levels. Still, these samples presented higher metallic surface area than low-loaded counterparts did. In principle, the availability of Ni active sites for methanation reaction is increasing with the total metallic surface area. However, the addition of CeO₂ revealed an interesting effect on Ni dispersion. At low loading-level, it favoured the dispersion of the active phase (Ni). Indeed, the highest Ni dispersion was achieved by 10Ni-10CeO₂ (4.05%). However, at medium- and high-loading levels of promoter, the dispersion was reduced due to the substitution of some γ -Al₂O₃ for CeO₂. At high CeO₂ level, less surface area is available for nickel to be dispersed. As an example, 30Ni-0CeO₂ is composed by 70% of porous γ -Al₂O₃ (S_{BET} = 160 m²·g⁻¹), while the amount of support in 30Ni-30CeO₂ sample was reduced to 40% (S_{BET} = 120 m²·g⁻¹).

In parallel, microcalorimetry studies were carried out to quantify the amount of CO₂ adsorbed at 35 °C, as an indirect indicator of sample basicity. The amount of CO₂ adsorbed is shown in Fig. 9. From the results, it was inferred that the amount of CO₂ adsorbed on CeO₂ was higher than that on γ -Al₂O₃, statistically about 2.5 times more on the promoter than on the micro-sphere support. At the far end, the amount of CO₂ adsorbed at 35 °C by Ni was negligible. Concerning the heat of adsorption, similar contributions were observed between promoter, support and active phase (see Fig. S9). Microcalorimetry results suggested that the role of CeO₂ is to increase the basicity of the catalyst surface. According to Muroyama et al. [47], moderate basic sites are one of the desired properties of Ni-CeO₂ catalysts for the CH₄ production from CO₂ methanation. Overall, the range of heat of adsorption was at the moderate range of (–56.51)–(–64.80) kJ·mol_{CO₂}⁻¹. Other factors, as hydrophobicity of the support, could be responsible for significant enhancement on the catalytic performance. However, Bacariza et al. found similar water interaction on Ce-promoted methanation catalysts than non-promoted ones [48].

Catalytic results reported so far, together with catalyst characterization, revealed that a compromise between Ni, CeO₂ and γ -Al₂O₃ content allows obtaining a suitable catalyst for the CO₂ methanation. Firstly, Ni dispersion was higher at low loading levels. However, the catalysts with higher Ni content presented higher metallic area, even

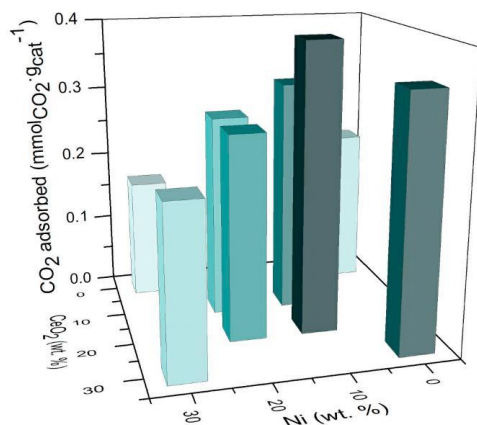


Fig. 9. CO₂ adsorbed (mmol_{CO₂}%_{cat}⁻¹) from TGA-DSC.

though Ni dispersion level was lower. As Ni is the active phase for reaction, higher metallic area was expected to enhance the catalytic performance. On the other hand, the presence of CeO₂ in the system as reaction promoter allows to enhance the reducibility of the catalyst, as well as to increase the amount of CO₂ molecules adsorbed on the catalyst. Finally, the presence of γ -Al₂O₃ support on this system is favourable in terms of increasing the surface area and pore volume of samples. An optimum balance between these effects seems to be found around 25Ni-20CeO₂.

3.2. Optimal formulation

Based on the previous results, the 25Ni-20CeO₂ catalyst was prepared and its catalytic performance was evaluated. Table 1 lists the CO₂ conversion of 25Ni-20CeO₂ at 300 °C and samples with similar composition, namely 20Ni-20CeO₂ and 30Ni-30CeO₂. Selectivity to methane resulted to be 100% in these samples. Catalytic performance as a function of the temperature can be found in Fig. S10. Results confirmed the catalytic performance predicted from the surface area response. 25Ni-20CeO₂ catalyst exhibited higher catalytic activity ($X_{\text{CO}_2} = 67.94\%$ with $S_{\text{CH}_4} = 100\%$) than samples with slightly higher or lower metal loading, and much higher activity than the rest of prepared catalysts for the catalytic screening. The classic definition of a promoter in catalysis is a substance that is added in small amounts to improve its properties; for instance, activity, selectivity and/or stability. In this sense, previous studies reported the use of CeO₂ as promoter with 2–3 wt% [37–39]. Therefore, the optimal formulation found in this work (20 wt% of CeO₂ as promoter) highly contrasts with those previously reported and the classic definition. In any case, the catalytic improvement should balance out the higher material costs.

Table 1
Catalytic activity of 20Ni-20CeO₂, 25Ni-20CeO₂ and 30Ni-30CeO₂ catalysts: Reaction conditions: T = 300 °C, P = 0 barg, F = 200 NmL·min⁻¹, m_{cat} = 0.3 g and H₂:CO₂ molar ratio = 4.

catalyst	X_{CO_2} (%)
20Ni-20CeO ₂	58.04
25Ni-20CeO ₂	67.94
30Ni-30CeO ₂	54.52

Analogously, the benefits of using CeO₂ as porous support in 50–90 wt %, instead of γ -Al₂O₃, should counterweight the economic impact on the material manufacturing [32,35].

The highest catalytic activity of 25Ni-20CeO₂ was attributed to the synergistic effects achieved when the content of all species is optimized. In this sense, 25Ni-20CeO₂ exhibited the highest values of metallic surface area, and similar degree of reduction and CO₂ adsorbed (see Table 2). As for CO₂ adsorbed, counterintuitive results were observed. Although 30Ni-30CeO₂ was the sample with the highest CeO₂ content, it presented less basicity – less CO₂ adsorbed and heat of adsorption. This behaviour may be caused by two effects: on the one hand, CeO₂ dispersion and metallic surface area may behave like Ni, showed a maximum of the latter. On the other hand, CO₂ adsorption on γ -Al₂O₃ is much higher than that of Ni, whose content decreased sharply as the content of Ni and CeO₂ increased to 30 wt%. In general, a high metallic surface area is beneficial for the reaction. This property is achieved by an optimum balance between the presence of support and metal species (Ni and CeO₂). At high metal loading, Ni is poorly dispersed, as no support is available. At low loading, Ni is appropriately dispersed but there is lower Ni amount. On the other hand, the presence of CeO₂ in the system as reaction promoter enhances the reducibility of the catalyst and improves the interaction of CO₂ molecules with the catalyst.

In order to compare the catalytic results of the optimal formulation with literature values, the influence of the pressure, GHSV and time-on-stream was tested on 25Ni-20CeO₂ catalyst. The effect of the pressure was evaluated up to 10 barg, at a isothermal temperature of 300 °C, a GHSV of 36,000 h⁻¹ and using a stoichiometric H₂:CO₂ molar ratio of 4. Fig. 10 shows the effect of the pressure on CO₂ conversion and selectivity over 25Ni-20CeO₂ catalyst. Within the tested pressure range, CH₄ selectivity was close to 100%, whereas CO₂ conversion was increased from 68 to 94% by the effect of the pressure. This fact was a consequence of both favourable kinetics and thermodynamics at higher pressure. However, the increasing effect was more pronounced at low pressures than higher ones. CO₂ conversion was only increased by 2% from 5 to 10 barg. This slight improvement on the conversion cannot justify the capital and operational cost to double the pressure of the whole methanation plant. Accordingly, 5 barg was further considered as reaction pressure by the proposed catalyst.

The promising 25Ni-20CeO₂ catalyst was additionally tested in the range of GHSV = 4500–54,000 h⁻¹ and P = 0–5 barg, at T = 300 °C, and a H₂:CO₂ molar ratio = 4. Experiments at different pressure and GHSV favour the comparison of the proposed Ni-CeO₂ catalyst with literature values. At these conditions, CH₄ selectivity was always equal to 100%. As expected, CO₂ conversion decreased with the increase of the GHSV. For industrial applications, the catalyst mass and the reactants flow should be carefully adjusted to obtain the desired conversion.

As it can be observed in Fig. 11, the activity of the proposed 25Ni-20CeO₂ catalyst seems superior than most of reported values of Ni-CeO₂ catalysts at similar reaction conditions (T = 300–400 °C, H₂:CO₂ molar ratio = 3.5–4, GHSV = 4,000–43,000 h⁻¹ and P = 1–30 barg). At atmospheric pressure, similar results were obtained by 20Ni-3CeO₂/ γ -Al₂O₃ and by 10Ni/CeO₂ samples. Tada et al. [32] proposed a system in which the porosity is induced by 90 wt% of CeO₂, which is more expensive than γ -Al₂O₃. From an economic point of view, the advantage of the 20Ni-3CeO₂ proposed by Nie et al. [39] is the significant reduction of metal amount. They achieved uniformly dispersed Ni nanoparticles by co-impregnation with citric acid. However, it is important to note that these two interesting research catalysts were prepared in powder form and they cannot be used directly on industrial applications. In contrast, the system proposed in this study is ready to be used in micro-structured reactors. Lastly, under moderate pressure, the Ni-Ce-Zr material [35] exhibited lower activity than the material proposed in this work at 5 barg, and it showed signs of deactivation at 150 h of reaction. Overall, the optimal catalyst formulation presented in this work outstands among those reported in the literature.

Table 2
Characterization data of the mesoporous 20Ni-20CeO₂, 25Ni-20CeO₂ and 30Ni-30CeO₂ catalysts.

Catalyst	Composition (wt%)		S _{BET} (m ² ·g ⁻¹)	Metallic surface area (m ² ·g ⁻¹)	Degree of reduction (%)	CO ₂ adsorbed mmol CO ₂ ·g _{cat.} ⁻¹	Heat of adsorption -kJ·mol _{CO₂} ⁻¹
	Ni	CeO ₂					
20Ni-20CeO ₂	18.9	20.6	139	3.24	62.87	0.28	64.80
25Ni-20CeO ₂	26.1	20.8	131	5.13	78.90	0.29	65.34
30Ni-30CeO ₂	27.4	31.3	120	1.23	78.18	0.23	56.51

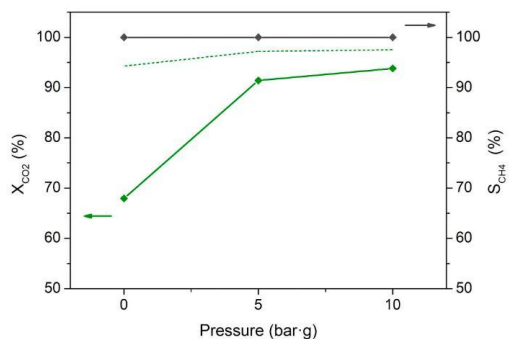


Fig. 10. Effect of the pressure on the CO₂ conversion (%) and CH₄ selectivity (%) for the 25Ni-20CeO₂ catalyst. Reaction conditions: T = 300 °C, P = 0–10 bar.g, GHSV = 36,000 h⁻¹, m_{cat.} = 0.3 g, ρ_{cat.} = 0.9 g·mL⁻¹ and H₂:CO₂ molar ratio = 4. Short dash line (—): Equilibrium.

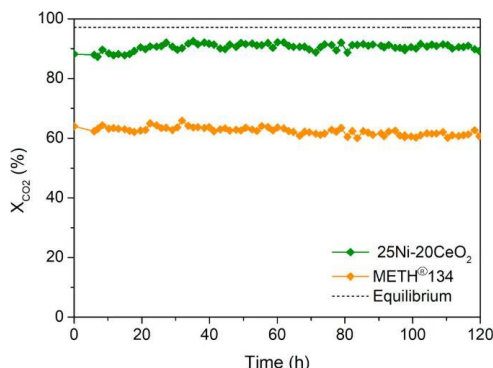


Fig. 12. Lifetime testing comparison of 25Ni-20CeO₂ and METH® 134 catalysts. Reaction conditions: T = 300 °C, P = 5 bar.g; GHSV = 36,000 h⁻¹, m_{cat.} = 0.3 g, ρ_{cat.} = 0.9 g·mL⁻¹ and H₂:CO₂ molar ratio = 4.

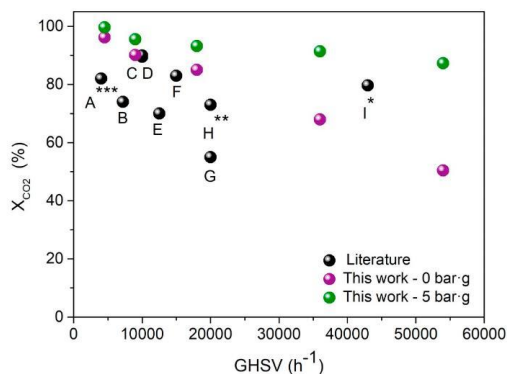


Fig. 11. Comparison of catalytic activity for the CO₂ methanation over Ni-CeO₂ based catalysts. Reported catalysts at 1 atm, 5 atm^{*}, 3 MPa^{**}, and 5 bar.g^{***}: A^{***})20Ni/55γ-Al₂O₃-15ZrO₂-15TiO₂-15CeO₂ [32], B)10Ni-2.5CeO₂/γ-Al₂O₃ [38], C)20Ni-3CeO₂/γ-Al₂O₃ [39], D)10Ni/CeO₂ [32], E)15Ni-3Co/CeO₂ZrO₂ [33], F)15Ni-2CeO₂/γ-Al₂O₃ [37], G)10Ni/CeO₂-ZrO₂ [34], H^{**})10Ni/Ce_{0.5}Zr_{0.5}O₂ [36] and I^{*})5Ni/CeZr(60-40) [35].

The stability of the optimized 25Ni-20CeO₂ catalyst was evaluated at 300 °C and 5 barg. The same test was also carried out using a commercial reference catalyst (METH® 134). Fig. 12 shows the CO₂ conversions as a function of time-on-stream during 120 h. At first sight, it can be inferred that the activity of 25Ni-20CeO₂ was much higher (90.5%) than the commercial reference (64%). As concerns to the catalyst stability, both systems were stable within the explored time interval. However, in the case of the commercial reference, a slightly reduction of 3% activity after 3 days of reaction was observed. No

activity loss was observed in the case of the 25Ni-20CeO₂ catalyst. Furthermore, the proposed 25Ni-20CeO₂ catalyst exhibited a higher productivity (reaction rate) by nominal Ni content (6.46 mol_{CO₂conv.}·h⁻¹·g_{Ni}⁻¹) than the commercial catalyst (5.19 mol_{CO₂conv.}·h⁻¹·g_{Ni}⁻¹), indicating an improvement of approximately 25% for this catalyst at the same conditions that can be attributed to the presence of high amounts of CeO₂.

The spent catalysts were further evaluated through SEM-EDX and XRD measurements. Characterization data was summarized in Table 3. No relevant changes in the elemental composition after reaction were observed, with respect to reduced catalysts. However, new diffraction peaks were noticed in the XRD profiles (see Fig. S11) of the used catalysts. A characteristic peak linked to CeAlO₃ phase was identified for the used 25Ni-20CeO₂ and some new peaks related to CaO and CaCO₃ phases were recognized for the used commercial catalyst. In addition, XRD measurements revealed that the average Ni crystallite size of the used catalysts increased by 8.3% and 38.9% for Ni-CeO₂ and commercial, respectively. Therefore, the slightly activity decay of the commercial catalyst can be related with sintering of Ni particles.

Table 3
Characterization data of used catalysts.

Sample	State	Elemental composition [wt%]			d _{Ni} [nm] 2θ = 44.51°
		Ni	CeO ₂	Ca	
25Ni-20CeO ₂	Fresh ^a	26 ± 1	21 ± 1	–	22
	Used ^b	26 ± 1	21 ± 1	–	24
METH® 134	Fresh ^a	21 ± 1	–	4 ± 1	11
	Used ^b	21 ± 1	–	5 ± 1	18

^a In reduced form.

^b After 120 h of reaction.

4. Conclusions

A series of ternary catalytic systems based on different contents of Ni as active phase, CeO₂ as promoter and γ -Al₂O₃ micro-spheres as support was systematically studied in order to obtain the optimal composition for the CO₂ methanation reaction. A proper compromise between the positive effects of each component of this ternary system is found when 25 wt% of Ni and 20 wt% of CeO₂ were impregnated on γ -Al₂O₃. The presence of the optimal content of γ -Al₂O₃ support in this system is favourable in terms of surface area, pore volume and therefore availability for proper metal dispersion. As Ni is the active phase for reaction, high metallic surface area enhances the reactivity. On the other hand, the presence of optimal CeO₂ content in the system as reaction promoter enhances the reducibility of the catalyst and improves the interaction of CO₂ molecules with the catalyst. In summary, the optimal catalytic activity of the 25Ni-20CeO₂ is mainly attributed to the metallic surface area, nickel reducibility and the formation of moderate basic sites for CO₂ adsorption.

The proposed optimum content covers the gap between the classic definition of promoter addition in low amounts and its use as bulk support. In comparison with literature values of similar Ni-CeO₂ catalytic systems, the catalyst proposed in this study exhibits higher initial activity for SNG production. Therefore, the use of CeO₂ as bulk support seems unnecessary due to its higher costs. In addition, the stability of the catalyst is not altered with time on-stream, at least up to 120 h. In contrast with reported Ni-Ce systems, the catalyst is synthesized with the proper particle size and it can be directly implemented in compact micro-structured reactors that are now available on the market. Therefore, the optimum formulation presented in this work is a competitive, active and ready-to-use catalyst in the methanation of CO₂.

Abbreviations and symbols

Symbol	Unit	Denotation
d_p	[μm]	Particle diameter catalyst
$\Delta G_{298\text{K}}$	[$\text{kJ}\cdot\text{mol}^{-1}$]	Gibbs free energy of methanation
$\Delta H_{298\text{K}}$	[$\text{kJ}\cdot\text{mol}^{-1}$]	Enthalpy of methanation
P	[bar(g)]	Pressure
T	[$^{\circ}\text{C}$]	Temperature
GHSV	[h^{-1}]	Gas hourly space velocity
m_{cat}	[g]	Catalyst mass
ρ_{cat}	[$\text{g}\cdot\text{mL}^{-1}$]	Apparent bulk density
F	[$\text{NmL}\cdot\text{min}^{-1}$]	Volumetric flow rate
d_{Ni}	[nm]	Ni particle size
λ	[nm]	X-ray wavelength
θ	[$^{\circ}$]	Bragg angle
X_{CO_2}	[%]	CO ₂ conversion
$F_{\text{CO}_2, \text{in}}$	[$\text{mol}\cdot\text{min}^{-1}$]	Molar flow rate of CO ₂ at the reactor inlet
$F_{\text{CO}_2, \text{out}}$	[$\text{mol}\cdot\text{min}^{-1}$]	Molar flow rate of CO ₂ at the reactor outlet
S_{CH_4}	[%]	CH ₄ selectivity
$F_{\text{CH}_4, \text{in}}$	[$\text{mol}\cdot\text{min}^{-1}$]	Molar flow rate of CH ₄ at the reactor inlet
$F_{\text{CH}_4, \text{out}}$	[$\text{mol}\cdot\text{min}^{-1}$]	Molar flow rate of CH ₄ at the reactor outlet
$F_{\text{CO}, \text{out}}$	[$\text{mol}\cdot\text{min}^{-1}$]	Molar flow rate of CO at the reactor outlet
S_{BET}	[$\text{m}^2\cdot\text{g}^{-1}$]	BET surface area
V_{pore}	[$\text{cm}^3\cdot\text{g}^{-1}$]	Pore volume
α , β and γ	[–]	Reducible NiO species types
β	[–]	The full width of the diffraction line at half maximum (FWHM)
Abbreviation	Denotation	
SNG	Synthetic natural gas	
SEM	Scanning electron microscopy	
EDX	Energy dispersive X-ray spectrometer	
BET	Brunauer-Emmett-Teller	
BJH	Barrett-Joyner-Halenda	
XRD	X-ray diffraction	
ICDD	International centre for diffraction data	
TCD	Thermal conductivity detector	
H ₂ -TPR	Hydrogen-Temperature programmed reduction	
TGA-DSC	Thermogravimetric analysis and differential scanning calorimetry	

Acknowledgements

Authors thank Generalitat de Catalunya for financial support through the CERCA Programme, M2E (2017SGR1246) and XaRMAE network. IREC also gratefully acknowledge the funding of this work by the CoSin project (COMRD115-1-0037), funded by ACCIÓ and the European Regional Development Fund (ERDF) under the framework of RIS3CAT Energy Community. Andreina Alarcón is grateful to Escuela Superior Politécnica del Litoral (ESPOL) for the support during her postgraduate studies (“Walter Valdano Raffo” Program, First edition). The authors thank Saint-Gobain NorPro for kindly providing γ -Al₂O₃ Accu*spheres. Authors are grateful to Marco Argudo for sample characterization.

Appendix A. Supplementary data

Supplementary data to this article can be found online at <https://doi.org/10.1016/j.fuproc.2019.05.008>.

References

- N.L. Panwar, S.C. Kaushik, S. Kothari, Role of renewable energy sources in environmental protection: a review, *Renew. Sust. Energ. Rev.* 15 (2011) 1513–1524, <https://doi.org/10.1016/j.rser.2010.11.037>.
- W. Zappa, M. Jungling, M. van den Broek, Is a 100% renewable European power system feasible by 2050? *Appl. Energy* 233–234 (2019) 1027–1050, <https://doi.org/10.1016/j.apenergy.2018.08.109>.
- M. Jentsch, T. Trost, M. Sterner, Optimal use of Power-to-Gas energy storage systems in an 85% renewable energy scenario, *Energy Procedia*, The Authors, 2014, pp. 254–261, <https://doi.org/10.1016/j.egypro.2014.01.180>.
- M. Bailera, B. Peña, P. Lisbona, L.M. Romeo, Decision-making methodology for managing photovoltaic surplus electricity through Power to Gas: Combined heat and power in urban buildings, *Appl. Energy* 228 (2018) 1032–1045, <https://doi.org/10.1016/j.apenergy.2018.06.128>.
- S. Rönsch, J. Schneider, S. Matthieschke, M. Schlüter, M. Götz, J. Lefebvre, P. Prabhakaran, S. Bajohr, Review on methanation - from fundamentals to current projects, *Fuel* 166 (2016) 276–296, <https://doi.org/10.1016/j.fuel.2015.10.111>.
- S. Garmsiri, M. Rosen, G. Smith, Integration of wind energy, hydrogen and natural gas pipeline systems to meet community and transportation energy needs: a parametric study, *Sustainability* 6 (2014) 2506–2526, <https://doi.org/10.3390/su6052506>.
- T. Schaaf, J. Grünig, M.R. Schuster, T. Rothenfluh, A. Orth, Methanation of CO₂ - storage of renewable energy in a gas distribution system, *Energy. Sustain. Soc.* 4 (2014) 1–14, <https://doi.org/10.1186/s13705-014-0029-1>.
- H. Blanco, W. Nijs, J. Ruf, A. Faaij, Potential of Power-to-Methane in the EU energy transition to a low carbon system using cost optimization, *Appl. Energy* 232 (2018) 323–340, <https://doi.org/10.1016/j.apenergy.2018.08.027>.
- M. Götz, J. Lefebvre, F. Mörs, A. McDaniel Koch, F. Graf, S. Bajohr, R. Reimert, T. Kolb, Renewable Power-to-Gas: a technological and economic review, *Renew. Energy* 85 (2016) 1371–1390, <https://doi.org/10.1016/j.renene.2015.07.066>.
- E. Consulting, *The Potential of Power-to-Gas*, (2016).
- J. Guiler, J. Ramon Morante, T. Andreu, Economic viability of SNG production from power and CO₂, *Energy Convers. Manag.* 162 (2018) 218–224, <https://doi.org/10.1016/j.enconman.2018.02.037>.
- A. Hassan, M.K. Patel, D. Parra, An assessment of the impacts of renewable and conventional electricity supply on the cost and value of power-to-gas, *Int. J. Hydrog. Energy* 44 (2019) 9577–9593, <https://doi.org/10.1016/j.ijhydene.2018.10.026>.
- J. Gao, Y. Wang, Y. Ping, D. Hu, G. Xu, F. Gu, F. Su, A thermodynamic analysis of methanation reactions of carbon oxides for the production of synthetic natural gas, *RSC Adv.* 2 (2012) 2358, <https://doi.org/10.1039/c2ra00632d>.
- K. Stangeland, D. Kalai, H. Li, Z. Yu, CO₂ methanation: the effect of catalysts and reaction conditions, *Energy Procedia* (2017) 2022–2027, <https://doi.org/10.1016/j.egypro.2017.03.577>.
- M. Gruber, P. Weinbrecht, L. Biffar, S. Harth, D. Trimis, J. Brabandt, O. Posdziech, R. Blumentritt, Power-to-Gas through thermal integration of high-temperature steam electrolysis and carbon dioxide methanation - experimental results, *Fuel Process. Technol.* 181 (2018) 61–74, <https://doi.org/10.1016/j.fuproc.2018.09.003>.
- M. Martínez Molina, C. Kern, A. Jess, Catalytic hydrogenation of carbon dioxide to methane in wall-cooled fixed-bed reactors \ddagger , *Chem. Eng. Technol.* 39 (2016) 2404–2415, <https://doi.org/10.1002/ceat.201500614>.
- F.P. Bernardo, P.M. Saraiva, A conceptual model for chemical product design, *Am. Inst. Chem. Eng. J.* 61 (2014) 1–15, <https://doi.org/10.1002/aic>.
- A. Alarcón, J. Guiler, T. Andreu, CO₂ conversion to synthetic natural gas: reactor design over Ni-Ce/Al₂O₃ catalyst, *Chem. Eng. Res. Des.* (2018), <https://doi.org/10.1016/j.cherd.2018.10.017>.
- R. Dittmeyer, T. Boeltken, P. Piermartini, M. Selinsek, M. Loewert, F. Dallmann, H. Kreuder, M. Cholewa, A. Wunsch, M. Belimov, S. Farsi, P. Pfeifer, Micro and

micro membrane reactors for advanced applications in chemical energy conversion, *Curr. Opin. Chem. Eng.* 17 (2017) 108–125, <https://doi.org/10.1016/j.coche.2017.08.001>.

[20] J. Ducamp, A. Bengaouer, P. Burens, Modelling and experimental validation of a CO₂ methanation annular cooled fixed-bed reactor exchanger, *Can. J. Chem. Eng.* 95 (2017) 241–252, <https://doi.org/10.1002/cjce.22706>.

[21] S. Pérez, J.J. Aragón, I. Peciña, E.J. García-Suarez, Enhanced CO₂ methanation by new microstructured reactor concept and design, *Top. Catal.* (2019), <https://doi.org/10.1007/s11244-019-01139-4>.

[22] P. Frontera, A. Macario, M. Ferraro, P. Antonucci, Supported catalysts for CO₂ methanation: a review, *Catalysts* 7 (2017) 59, <https://doi.org/10.3390/catal7020059>.

[23] W. Wang, J. Gong, Methanation of carbon dioxide: an overview, *Front. Chem. Eng. China* 5 (2011) 2–10, <https://doi.org/10.1007/s11705-010-0528-3>.

[24] J. Gao, Q. Liu, F. Gu, B. Liu, Z. Zhong, F. Su, Recent advances in methanation catalysts for the production of synthetic natural gas, *RSC Adv.* 5 (2015) 22759–22776, <https://doi.org/10.1039/c4ra16114a>.

[25] S.-S. Liu, Y.-Y. Jin, Y. Han, J. Zhao, J. Ren, Highly stable and coking resistant Ce promoted Ni/SiC catalyst towards high temperature CO methanation, *Fuel Process. Technol.* 177 (2018) 266–274, <https://doi.org/10.1016/j.fuproc.2018.04.029>.

[26] M.A.A. Aziz, A.A. Jalil, S. Triwahyono, A. Ahmad, CO₂ methanation over heterogeneous catalysts: recent progress and future prospects, *Green Chem.* 17 (2015) 2647–2663, <https://doi.org/10.1039/C5GC00119F>.

[27] W. Ahmad, M.N. Younis, R. Shawabkeh, S. Ahmed, Synthesis of lanthanide series (La, Ce, Pr, Eu & Gd) promoted Ni/T-Al₂O₃ catalysts for methanation of CO₂ at low temperature under atmospheric pressure, *Catal. Commun.* 100 (2017) 121–126, <https://doi.org/10.1016/j.catcom.2017.06.044>.

[28] J. Liu, W. Shen, D. Cui, J. Yu, F. Su, G. Xu, Syngas methanation for substitute natural gas over Ni-Mg/Al₂O₃ catalyst in fixed and fluidized bed reactors, *Catal. Commun.* 38 (2013) 35–39, <https://doi.org/10.1016/j.catcom.2013.04.014>.

[29] A. Zhao, W. Ying, H. Zhang, H. Ma, D. Fang, La and Mn promotion of Ni/Al₂O₃ catalysts for syngas methanation, *Energy Sources, Part A* 36 (2014) 1049–1056, <https://doi.org/10.1080/15567036.2012.666621>.

[30] J. Guilera, J. del Valle, A. Alarcón, J.A. Díaz, T. Andreu, Metal-oxide promoted Ni/Al₂O₃ as CO₂ methanation micro-size catalysts, *J. CO₂ Util.* 30 (2019) 11–17, <https://doi.org/10.1016/j.jcou.2019.01.003>.

[31] G. Garbarino, C. Wang, T. Cavattoni, E. Finocchio, P. Riani, M. Flytzani-Stephanopoulos, G. Busca, A study of Ni/La-Al₂O₃ catalysts: a competitive system for CO₂ methanation, *Appl. Catal. B Environ.* (2018), <https://doi.org/10.1016/j.apcath.2018.12.063>.

[32] S. Tada, T. Shimizu, H. Kameyama, T. Haneda, R. Kikuchi, Ni/CeO₂ catalysts with high CO₂ methanation activity and high CH₄ selectivity at low temperatures, *Int. J. Hydrog. Energy* 37 (2012) 5527–5531, <https://doi.org/10.1016/j.ijhydene.2011.12.122>.

[33] L. Pastor-Pérez, E. Le Saché, C. Jones, S. Gu, H. Arellano-García, T.R. Reina, Synthetic natural gas production from CO₂ over Ni-x/CeO₂-ZrO₂(x = Fe, Co) catalysts: Influence of promoters and space velocity, *Catal. Today* 2 (2017) 10–15, <https://doi.org/10.1016/j.cattod.2017.11.035>.

[34] J. Ashok, M.L. Ang, S. Kawi, Enhanced activity of CO₂ methanation over Ni/CeO₂-ZrO₂ catalysts: influence of preparation methods, *Catal. Today* 281 (2017) 304–311, <https://doi.org/10.1016/j.cattod.2016.07.020>.

[35] F. Ocampo, B. Louis, A. Kiennemann, A.C. Roger, CO₂ methanation over Ni-Ceria-Zirconia catalysts: effect of preparation and operating conditions, *IOP Conf. Ser. Mater. Sci. Eng.* 19 (2011), <https://doi.org/10.1088/1757-899X/19/1/012007>.

[36] S. Wang, Q. Pan, J. Peng, T. Sun, D. Gao, S. Wang, CO₂ methanation on Ni/Ce_{0.5}Zr_{0.5}O₂ catalysts for the production of synthetic natural gas, *Fuel Process. Technol.* 123 (2014) 166–171, <https://doi.org/10.1016/j.fuproc.2014.01.004>.

[37] H. Liu, X. Zou, X. Wang, X. Lu, W. Ding, Effect of CeO₂ addition on Ni/Al₂O₃ catalysts for methanation of carbon dioxide with hydrogen, *J. Nat. Gas Chem.* 21 (2012) 703–707, [https://doi.org/10.1016/S1003-9953\(11\)60422-2](https://doi.org/10.1016/S1003-9953(11)60422-2).

[38] L. Zhou, Q. Wang, L. Ma, J. Chen, J. Ma, Z. Zi, CeO₂ promoted mesoporous Ni/γ-Al₂O₃ catalyst and its reaction conditions for CO₂ methanation, *Catal. Lett.* 145 (2015) 612–619, <https://doi.org/10.1007/s10562-014-1426-y>.

[39] W. Nie, X. Zou, X. Shang, X. Wang, W. Ding, X. Lu, CeO₂-assisted Ni nanocatalysts supported on mesoporous γ-Al₂O₃ for the production of synthetic natural gas, *Fuel* 202 (2017) 135–143, <https://doi.org/10.1016/j.fuel.2017.04.026>.

[40] P. Pfeifer, P. Piermartini, A. Wenka, Microstructure reactor for carrying out exothermic heterogeneously-catalysed reactions with efficient evaporative cooling, U.S. Patent Application No 10/150,093, 2018.

[41] Naturgy, Gas Natural Fenosa launches pilot project to produce renewable gas in Catalonia, <http://prensa.naturgy.com/en/gas-natural-fenosa-launches-pilot-project-to-produce-renewable-gas-in-catalonia/>, (2018).

[42] R.A. van S.J.A. Mouljin, P.W.N.M. van Leeuwen, An Integrated Approach to Homogeneous, Heterogeneous and Industrial Catalysis, (1993).

[43] K.S.W. Sing, D.H. Everett, R.A.W. Haul, L. Moscou, R.S. Pierotti, J. Rouquerol, T. Stemienniewska, International Union of Pure Commission on Colloid and Surface Chemistry Including Catalysis-Reporting physisorption data for gas/solid systems with special reference to the determination of surface area and porosity, *Pure Appl. Chem.* 57 (1985) 603–619, <https://doi.org/10.1351/pac198557040603>.

[44] W. Ahmed, A.E. Awadallah, A.A. Aboul-Enein, Ni/CeO₂-Al₂O₃ catalysts for methane thermo-catalytic decomposition to CO_x-free H₂ production, *Int. J. Hydrog. Energy* 41 (2016) 18484–18493, <https://doi.org/10.1016/j.ijhydene.2016.08.177>.

[45] J. Gao, C. Jia, J. Li, M. Zhang, F. Gu, G. Xu, Z. Zhong, F. Su, Ni/Al₂O₃ catalysts for CO methanation: effect of Al₂O₃ supports calcined at different temperatures, *J. Energy Chem.* 22 (2013) 919–927, [https://doi.org/10.1016/S2095-4956\(14\)60273-4](https://doi.org/10.1016/S2095-4956(14)60273-4).

[46] S. Rahmani, M. Rezaei, F. Meshkini, Preparation of highly active nickel catalysts supported on mesoporous nanocrystalline γ-Al₂O₃ for CO₂ methanation, *J. Ind. Eng. Chem.* 20 (2014) 1346–1352, <https://doi.org/10.1016/j.jiec.2013.07.017>.

[47] A. Westermann, B. Azambre, M.C. Bacariza, I. Graça, M.F. Ribeiro, J.M. Lopes, C. Henriques, Insight into CO₂ methanation mechanism over NiUSY zeolites: an operando IR study, *Appl. Catal. B Environ.* 174–175 (2015) 120–125, <https://doi.org/10.1016/j.apcath.2015.02.026>.

[48] M.C. Bacariza, M. Biset-Peiró, I. Graça, J. Guilera, J. Morante, J.M. Lopes, T. Andreu, C. Henriques, DBD plasma-assisted CO₂ methanation using zeolite-based catalysts: structure composition-reactivity approach and effect of Ce as promoter, *J. CO₂ Util.* 26 (2018) 202–211, <https://doi.org/10.1016/j.jcou.2018.05.013>.

Chapter

*Evaluation of the catalyst
in relevant industrial environment*

In the previous chapter, an optimized ternary catalytic system composed by 25 wt.% of Ni as active phase, 20 wt.% of CeO₂ as promoter and 55 wt.% of micro-sized γ -Al₂O₃ spheres as support was proposed for the production of synthetic natural gas. As it was revealed, the synergic effects produced between the optimum Ni, CeO₂ and γ -Al₂O₃ contents allowed that the CeO₂ promoted Ni/ γ -Al₂O₃ catalyst achieved a high catalytic performance (X_{CO_2} >90% and S_{CH_4} =100%) with high stability during the 120 h of the experimental test. Despite promising results at the tested moderate reaction conditions ($T=300$ °C, $P=5$ bar-g, $\text{GHSV}=36,000$ h⁻¹, and H_2/CO_2 molar ratio=4), special attention in the deactivation of the optimized catalyst in a more real environment is required for its technical implementation.

As it was discussed in Chapter 1 section 1.1.5 and 1.3, reactor technologies available to carry out CO₂ methanation process in industrial power-to-gas applications are operated under adiabatic, isothermal, and polytropic (non-isothermal) conditions with temperature profiles up to 500 °C. These high temperatures not only limit the equilibrium conversion during the process but also lead to thermal degradation of the metallic particles, causing a decrease of the catalyst activity. This physical deactivation process is also known as sintering and represents the loss of the active surface area of Ni-based catalysts as a result of the agglomeration of smaller particles to form larger crystals.

In addition to thermal degradation caused by high temperatures, Ni-based catalysts can be easily deactivated by poisoning if the industrial CO₂ methanation processes are fed by CO₂-impurities derived from carbon sources, such as cement industry, biogas from waste or simply captured from air. Most CO₂ feedstocks contain traces of impurities of O₂, N₂, siloxanes, VOCs and H₂S. The latter is considered as the most severe nickel poison for because sulfur compounds are strongly chemisorbed on the metal surface.

The lifetime of active CO₂ methanation catalysts may be reduced to only a few months or weeks because of high temperatures and small ppm quantities of sulfur contaminants. Therefore, further research on the deactivation by sulfur poisoning of CeO₂ promoted Ni/ γ -Al₂O₃ catalysts at relevant industrial environments is necessary.

In this chapter, two papers are presented, which are focused on:

- The catalytic stability evaluation of the catalyst using high temperature and H₂S impurities in order to identify the role and effects of CeO₂ on governing the poisoning mechanism.
- The scale-up of the micro-sized Ni-CeO₂/ γ -Al₂O₃ catalyst and its catalytic performance evaluation at pilot plant scale to demonstrate its technical implementation on advanced microstructured reactors.

3.1. Higher tolerance to sulfur poisoning in CO₂ methanation by the presence of CeO₂

The aim of this work was to identify the role of CeO₂ into the poisoning mechanism of the optimized Ni-CeO₂/γ-Al₂O₃ catalyst. High temperatures (T=500 °C) and the presence of H₂S impurities (<1-5 ppm) were selected to evaluate its catalytic performance at harsh conditions, representative of the initial position of the catalyst inside the reactor.

The catalyst preparation of the optimum proposed formulation (25 wt.% Ni, 20 wt.% CeO₂ and 55 wt.% γ-Al₂O₃) was scaled-up to a batch of 50 g. As in previous work, the simple and cost-effective wet impregnation method was used for the catalyst synthesis. In this case, a weight ratio H₂O:Al₂O₃=3 was used to guarantee the reproductivity of the optimized Ce promoted Ni/γ-Al₂O₃ catalyst. With the aim of assessing the specific effect of the promoter, a non-promoted Ni catalyst with similar active phase content (25 wt.% Ni) was also synthesized.

The catalytic activity of both catalysts was tested for 142 h under a systematic procedure to verify their catalyst deactivation (see Figure 3.1). At the high temperature of 500 °C, the promoted catalyst, named as Ni-CeO₂, showed excellent stability (close to 100%) with respect to non-promoted Ni catalyst (close to 40%). On the contrary, the addition of 1 ppm of H₂S caused the deactivation of both catalysts. However, the activity of the Ni-CeO₂ catalyst (close to 25%) was higher than the Ni catalyst (close to 10%).

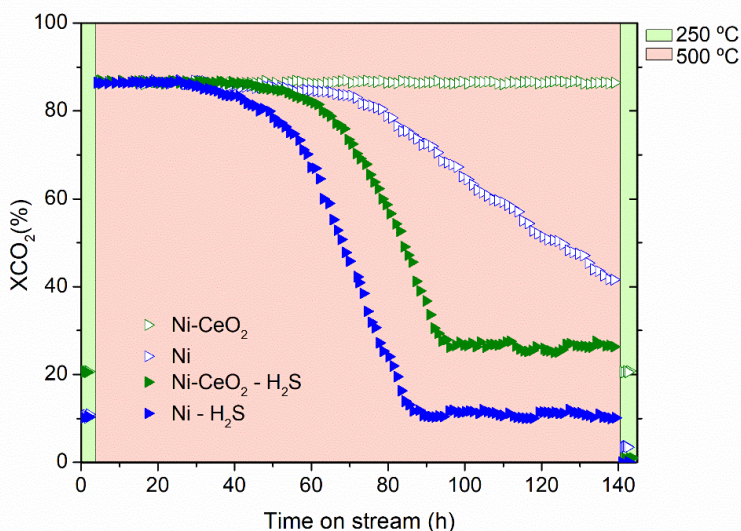


Figure 3.1. CO₂ conversion (%) vs. 142 h time on stream at 250 and 500 °C, 5 bar-g, F=200 mL·min⁻¹, H₂/CO₂ molar ratio=4 and 1 ppm of H₂S.

To analyse the structure-activity relationships, the characterization of the catalysts in their three states: fresh, used and used after H₂S poisoning was performed. EDX analysis revealed the presence of sulfur impurities in the catalysts. XRD, TEM and CO-chemisorption analysis evidenced that the unaltered stability of the Ni-CeO₂ catalyst was due to the strong metal-promoter interaction. The favourable formation of nanocomposite between Ni and CeO₂ particles was detected. In contrast, the rapid deactivation of Ni catalyst was associated with the thermal degradation of Ni particles (sintering), since nickel leaching and carbon deposition were negligible, as confirmed by SEM and TPO. The modification of textural properties detected by N₂-physisorption for both used catalysts was associated with thermal degradation of either CeO₂ for Ni-CeO₂ catalyst or Ni particles in Ni catalyst.

The formation of sulfide species in both U-H₂S catalysts were identified through the crystallographic planes from HRTEM images. For Ni catalyst, its deactivation in presence of H₂S impurities was associated with the formation of nickel sulfide (NiS). In contrast, the higher catalytic activity achieved for the CeO₂ promoted catalyst can be explained by the favourable formation of cerium oxy-sulfide (Ce₂O₂S), as it can be observed in Figure 3.2. This sulfide specie restricted the formation of nickel sulfide, helping thereby to maintain the catalyst stability. These results allowed to confirm the role of CeO₂ for increasing the sulfur tolerance by the formation of species that counteract the poisoning of Ni active sites.

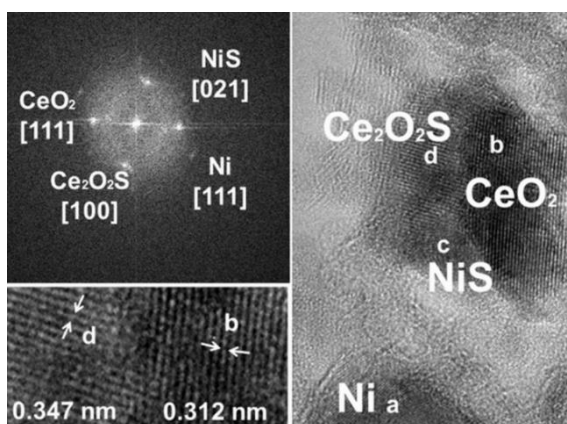


Figure 3.2. HRTEM: Lattice-fringe analysis and Fourier Transform (FT) imaging of the Ni-CeO₂ (U-H₂S) catalyst.

The previous findings were further confirmed by DRIFTS measurements. On the basis of these results, a reaction mechanism scheme under H₂S poisoning for the Ni-CeO₂/γ-Al₂O₃ was also proposed. It was detected that the methane production at the high temperature of 500 °C proceeds preferentially via formate dissociation followed by hydrogenation of the adsorbed CO on the available Ni sites, which were prevented by the favourable formation of Ce₂O₂S.

3.2. Pushing the limits of SNG process intensification: High GHSV operation at pilot scale

In the second work, the aim was to evaluate the technical implementation of the micro-sized catalyst on an advanced microstructured reactor technology at pilot plant scale, in which H₂S impurities could be present as industrial biogas was used.

The scale-up of micro-sized catalyst was performed using the same catalyst preparation procedure of the previous work, i.e. 50 g of catalyst was manufactured by batch for its implementation. The SNG production over the optimized catalyst formulation was carried out using renewable H₂ produced from an alkaline electrolysis (37 kWh_e) of tap water and two different carbon sources, such as biogas (46% CO₂ and 54% CH₄) from an anaerobic digester and CO₂ (99% CO₂ and 1% CH₄) released by the upgrading unit. Sulfur impurities were removed and undetectable, but not negligible (H₂S < 0.1 mg·Nm⁻³), during the whole experimental campaign.

The methanation pilot plant shown in Figure 3.3 was designed for a net SNG production of 1.5 Nm³·h⁻¹ at mild pressure conditions (≤10 atm). The thermocatalytic process consisted of a 2-step synthesis unit, including gas pre-heating, catalytic reaction and water condensation. A total catalyst amount of 105 g was implemented on the microstructured reactors developed by KIT and delivered by INERATEC. The first reactor was filled with 60 g of the optimized catalyst, while the second with 45 g. In both reactors, silicon carbide with similar size particles was used to dilute the catalyst. The used catalyst amount was adjusted in accordance with the obtained results of the experimental study previously performed at KIT, using a lab-scale microstructured reactor.

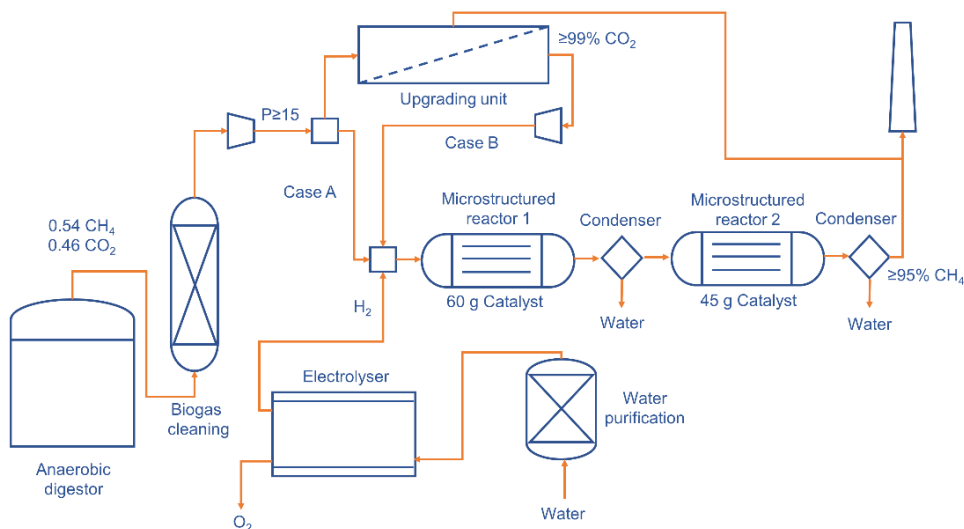


Figure 3.3. Process flow diagram of the methanation pilot plant.

The experimental campaigns were focused on the evaluation of the pressure ($P=1-10$ bar·g), gas hour space velocity ($GHSV=19,442-37,500$ h⁻¹) and carbon feedstock (upgraded CO₂ or biogas) effect on the product gas composition. The results revealed that pressure, GHSV and carbon feedstock have a relevant impact on product gas composition. The desired gas quality ($CH_4 \geq 92.5\%$, $H_2 \leq 5\%$ and $CO_2 \leq 2.5\%$) in the 2-step process using the upgraded CO₂ stream can be obtained at the maximum plant capacity ($37,500$ h⁻¹), with moderate pressure ($P=7$ bar·g) and decreasing temperature profiles ($T=450-275$ °C), as it can be observed in Figure 3.4. In contrast, very low pressures (≤ 3 bar·g) were not positive for SNG production ($CH_4 \leq 92.5\%$). CH₄ selectivity of 100% was achieved in all the experiments.

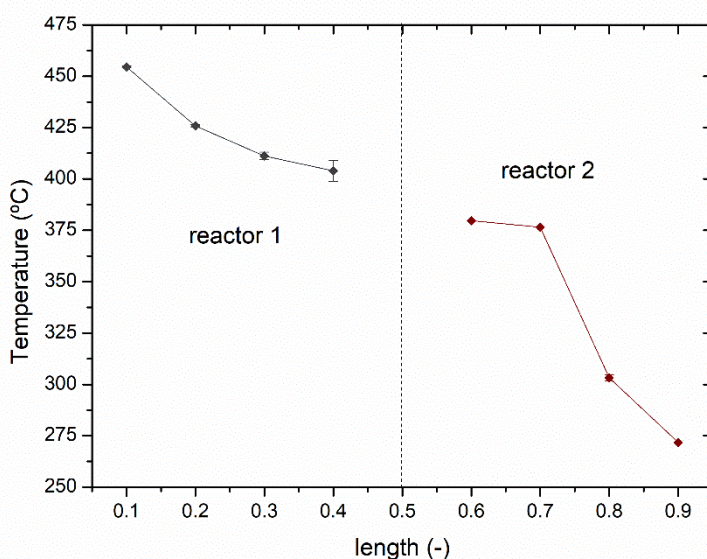


Figure 3.4. Temperature profile along the reactors during CO₂ methanation at $GHSV=37,500$ h⁻¹ and $P=5$ bar·g.

On the other hand, GHSV and carbon feedstock effects (see Figure 3.5) suggested that the proposed process can be operated at GHSV values as high as $31,500$ h⁻¹ using almost pure CO₂ and $37,500$ h⁻¹ using biogas as carbon source. In both cases, 5 bar·g was selected since it is the minimum pressure for direct gas grid injection purposes. Methanation of biogas is beneficial in terms of process intensification as lower reactor volume is required. Compared to commercial process of reference (Audi e-gas plant), this represents a reduction of 4 times the volume.

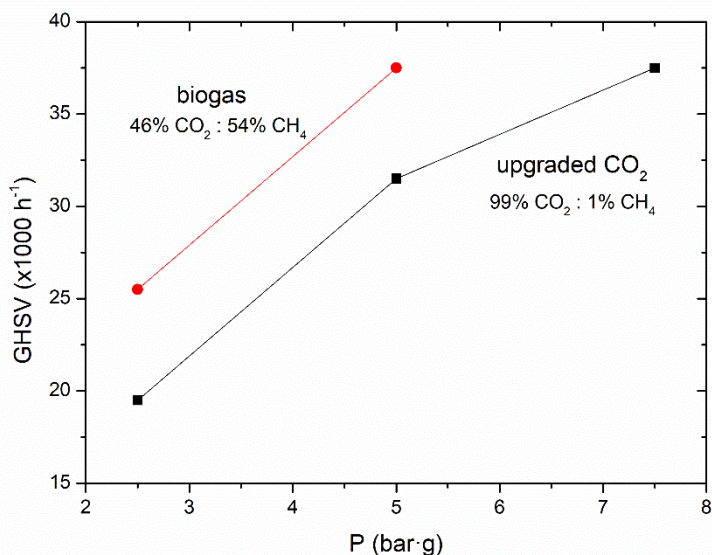


Figure 3.5. Maximum GHSV values to meet gas grid requirements as a function of the pressure and the carbon dioxide stream.

Catalyst deactivation by a displacement of the position of the maximum temperature toward the reactor outlet or by a decrease of the CH₄ content at the reactor outlet were not evidenced during the 2000 h of experimentation. According to the post-mortem catalyst analysis, negligible changes in the elemental composition between the fresh and spent catalyst were detected by EDX. Therefore, the implementation of the micro-sized catalyst on the industrial-scale two-stage microstructured reactor system was demonstrated.



Higher tolerance to sulfur poisoning in CO₂ methanation by the presence of CeO₂



Andreina Alarcón^{a,b}, Jordi Guilera^{a,*}, Rodrigo Soto^c, Teresa Andreu^a

^a Catalonia Institute for Energy Research (IREC), Jardins de les Dones de Negre 1, 08930 Sant Adrià de Besòs, Spain

^b Escuela Superior Politécnica del Litoral (ESPOL), Facultad de Ingeniería en Ciencias de la Tierra, Campus Gustavo Galindo Km.30.5 Vía Perimetral, P.O. Box 09-01-5863, Guayaquil, Ecuador

^c Synthesis and Solid State Pharmaceutical Centre (SSPC), Bernal Institute, Department of Chemical and Environmental Science, University of Limerick, Limerick V94 TPXX, Ireland

ARTICLE INFO

Keywords:

Synthetic natural gas
CO₂ methanation
Thermal stability
H₂S poisoning mechanism
Ce₂O₃ phase

ABSTRACT

This study investigates the deactivation mechanism of CeO₂-promoted catalyst for the CO₂ methanation reaction. The catalytic performance was evaluated at high temperature (T = 500 °C, P = 5 barg) and under the presence of unfavourable H₂S impurities (1–5 ppm). The thermal stability of the CeO₂-promoted catalyst was excellent, while the non-promoted sample suffered from nickel sintering. In contrast, the presence of H₂S was detrimental for both catalysts. The tolerance to H₂S of CeO₂-promoted sample was higher; keeping one third of the initial catalytic activity under continuous addition of H₂S. The identification of crystallographic planes associated with Ce₂O₃ phase (HRSTEM) evidenced that the addition of CeO₂ to nickel catalyst minimized the formation of non-active NiS sites. This finding was further confirmed through DRIFT spectroscopy since for the Ni-CeO₂/γ-Al₂O₃, methane formation derived from formate dissociation was followed by hydrogenation of the adsorbed CO on the remaining available active sites.

1. Introduction

The implementation of innovative storage technologies that integrate the electricity excess derived from unpredictable renewable energy along with CO₂ exploitation have attracted increasing attention in recent years. Apart from being a greenhouse gas, CO₂ is also an abundant and inexpensive chemical feedstock. Its valorization is crucial for enhancing flexibility in future energy systems and for progressing toward a low-carbon-emission society able to counteract the climate change effects. A potential route for absorbing renewable electricity at times of excess supply and to provide backup energy at times of excess demand is the Power to Gas concept [1]. The first step in the process is the production of hydrogen (H₂) from renewable power through water electrolysis. The second stage is the catalytic reaction between renewable H₂ and CO₂ to produce methane (CH₄), the so-called CO₂ methanation process [2–4]. The atmosphere, cement industry or biogas plants are feasible carbon dioxide sources for its exploitation. The produced renewable methane can be injected into the natural gas pipeline network or directly applied in the principal sectors where fossil fuels are still in use [5].

The catalytic Sabatier reaction (Eq. 1) is highly exothermic and

hence thermodynamically favorable at low temperatures (< 300–350 °C), under high pressure (> 10–20 barg), and using a stoichiometric ratio of H₂/CO₂ = 4 [6,7]. Since CO₂ methanation process is often considered a combination between endothermic reverse water gas shift (RWGS) reaction (Eq. 2) and exothermic CO methanation reaction (Eq. 3), its operation at high temperatures is not recommended because RWGS reaction reduces CH₄ selectivity in favour of carbon monoxide (CO) [7]. Nevertheless, the main limitations involved at low temperatures are related to the reaction kinetics, making the design of active catalysts essential for its competent implementation and for the process intensification. Heterogeneous catalytic systems based on Ru, Pd or Ni supported on Al₂O₃ [8–10], SiO₂ [11], CeO₂ [12,13], TiO₂ [14], ZrO₂ [15], MCM-4 [16], Co₃O₄ [17], La₂O₃ [18], Y- and BETA-Zeolites [19], core-shell Ni-Al@Al₂O₃ [20], or a combination of them [21], are the most widely studied for this reaction. Among them, Ni-based catalyst supported on Al₂O₃ are the most common at industrial scale due to their valuable catalytic activity per unit cost [22]. However, the main drawback of such catalysts is the initial loss of activity and even deactivation due to the aggregation of catalytic Ni particles produced by the exothermic nature of Sabatier reaction (unpredictable formation of hot spots).

* Corresponding author.

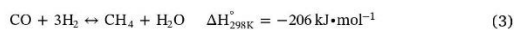
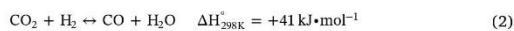
E-mail address: jguilera@irec.cat (J. Guilera).

<https://doi.org/10.1016/j.apcatb.2019.118346>

Received 12 August 2019; Received in revised form 23 October 2019; Accepted 26 October 2019

Available online 04 November 2019

0926-3373/ © 2019 Elsevier B.V. All rights reserved.



Sintering generally occurs at high temperatures (> 500 °C) by migration of metal atoms that eventually grow to metal crystallites, which affects detrimentally the metal particle size distribution and the active catalytic surface area. Such undesired phenomenon is known to be boosted by the presence of water vapor [23]. Hence, the catalytic performance of Ni-based catalysts is strongly influenced by the size of catalytic particles and their structure since the loss of activity can occur by physical aspects associated with the thermal degradation of the active metallic particles [24,25]. A similar conclusion has been claimed in a recent CO₂ methanation study over co-precipitated Ni-Al samples, where the main causes of deactivation were the Ni sintering and the decrease of medium basic sites. The depletion of CO₂ adsorption capacity was induced by structural changes and a loss of BET surface area [26].

Besides, deactivation by poisoning is another great challenge since Ni-based catalysts are very sensitive to impurities inherently present in the CO₂ stream, e.g. biogas, flue gas or atmosphere [27]. As reported by Muller et al. [28], the most significant deactivation of a Ni/SiO₂ catalyst occurs when sulfur impurities are present in the feedstream. Other compounds such as oxygen or nitrogen show less negative or negligible effect on the catalyst stability. Another study [29] concluded that catalyst poisoning can be caused even by traces of H₂S as all sulfur introduced to the reactor is retained by the Ni catalyst. Recently, Wolf et al. [30] inferred that the stability of nickel catalysts against sulfur poisoning (H₂S or SO₂) depends on the available Ni surface atoms. Accordingly, the key factor to increase sulfur tolerance – the activity of the catalyst at saturation coverage of poison – is to maintain the nickel surface area.

The addition of promoters to Ni-based catalysts is considered a plausible alternative to prevent physicochemical deactivation. It is well-reported that the presence of CeO₂ can enhance the catalytic performance as a result of the presence of moderate basic sites and due to its redox properties [31]. CeO₂ promoted Ni catalysts have shown significantly improved sintering and coking-resistance for CO methanation [32] and dry reforming [33–36]. Properly designed Ni-CeO₂/Al₂O₃ catalysts can prevent sintering because CeO₂ acts as physical barrier to restrain the growth of nickel particles. In addition, CeO₂ presence inhibits coke formation by increasing the supply of active oxygen species on the nickel surface. Recent findings on solid oxide fuel cells [37–40] revealed that the presence of CeO₂ also improves the sulfur resistance of the Ni/YSZ anodes. With regards to CO₂ methanation, we recently reported that, at low temperature (T = 300 °C) and under 0.4 ppm of H₂S, the addition of rare earth oxide promoters (as CeO₂ and La₂O₃) leads to prevention of typical Ni catalyst deactivation by sintering and sulfur poisoning [41]. Besides, Gac et al. [42] also reported that ceria improves sulfur tolerance at high temperature (T = 475 °C) since it may facilitate transformation of CO₂ to suitable intermediates and change the course of catalysts deactivation. However, to the best of our knowledge, the specific role of CeO₂ on sulfur tolerance of catalysts applied to CO₂ methanation process has not been elucidated yet from a mechanistic point of view. Studies on the desulfurization of biogas using solid oxide fuel cells [43] suggest that CeO₂ acts as an oxygen storage in desulfurization by the formation of CeO_xS_y phases. This scenario might be altered by the presence of Ni, Al₂O₃, and other CO₂ methanation involved species due to synergic effects and to the formation of other intermediates. Therefore, further research on the deactivation by sulfur poisoning of CeO₂ promoted Ni-catalysts applied to the CO₂ methanation at high temperature, especially at industrially relevant conditions, is necessary.

In this context, the aim of this work is to study the role and effects of

CeO₂ on governing the poisoning mechanism of an optimized Ni-CeO₂/γ-Al₂O₃ catalyst for the CO₂ methanation process. The catalytic activity is explored at high temperature (T = 500 °C) in absence and presence of H₂S impurities (1 ppm) for 142 h and compared to a Ni-based non-promoted catalyst. The relations between structure and catalytic activity are assessed and linked by detailed characterization studies. In light of the results obtained, a sulfur poisoning mechanism over the Ni-CeO₂/γ-Al₂O₃ catalyst is proposed.

2. Experimental

2.1. Catalyst preparation

Catalysts were prepared by wet impregnation method using γ-Al₂O₃ commercial support in shape of microspheres with particle diameters d_p = 450–500 μm (Saint-Gobain NorPro); and salt precursors of nickel (II) nitrate hexahydrate [Ni(NO₃)₂·6H₂O] (98% purity, Alfa Aesar), and cerium (III) nitrate hexahydrate [Ce(NO₃)₃·6H₂O] (99% purity, Fluka).

In the impregnation of 50 g-batch, an aqueous solution was firstly prepared with the respective salt precursors and distilled water. A weight ratio H₂O:γ-Al₂O₃ = 3 was used to guarantee the total dissolution of the salt precursors at room temperature. Secondly, γ-Al₂O₃ support pre-dried at 105 °C overnight was incorporated to the aqueous solution and mixed in a rotary vacuum evaporator at constant stirring (25 rpm) and room temperature for 1 h. Afterwards, most of the liquid-phase was evaporated in the same equipment at T = 85 °C and P = 0.8 bar during 6 h. The recovered material was then dried at 105 °C in an atmospheric oven overnight. Lastly, the catalysts were calcined at 450 °C for 30 min using a heating ramp of 1 °C·min⁻¹.

The catalyst composition was selected according to our previous study [44] on the optimum formulation: 25 wt. % of Ni as active phase, 20 wt. % of CeO₂ as promoter and 55 wt.% of γ-Al₂O₃ as support. In addition, a non-promoted catalyst was synthesized with analogous Ni content (25 wt. %) for comparison purposes. Hereinafter, the terms Ni-CeO₂ and Ni will be used to refer to these catalysts. Characterization of the catalyst samples was carried out before reaction referred as fresh, and after reaction, referred as used (U) or (U-H₂S) when H₂S impurities were introduced in the feed.

2.2. Catalyst characterization

Hydrogen temperature programmed reduction (H₂-TPR) experiments were conducted in an automated chemisorption analyzer (Autochem HP-Micromeritics). A total calcined catalyst mass of 70 mg was loaded in a quartz tube and kept under constant flow of 50 N mL·min⁻¹ of 12 vol.% H₂ in Ar. The temperature increased from 35 to 800 °C using a heating ramp of 10 °C·min⁻¹. The H₂ consumption was measured with a thermal conductivity detector (TCD). Before the detector, the gas flow was passed through a cold trap (composed of ice and NaCl) to condense the water generated during the experiment. The amount of reduced NiO to Ni⁰ was calculated by integrating the reduction peaks in the H₂-TPR profiles and expressed as percentage of consumption to reduce the Ni species in the catalysts.

N₂-physisorption (adsorption/desorption) measurements were determined at liquid nitrogen temperature using an automated TriStar II 3020-Micromeritics analyzer. Prior to measurements, fresh, U and U-H₂S samples were degassed at 90 °C for 1 h, and then at 250 °C for 4 h in a FlowPrep 060-Micromeritics. Brunauer-Emmett-Teller (BET) method was used to calculate the BET surface area for a relative pressure (P/P₀) range of 0.05–0.30. Furthermore, Barrett-Joyner-Halenda (BJH) method was applied to desorption branch of the isotherms to determine the average pore size and the total pore volume, which was calculated from the maximum adsorption value at P/P₀ = 0.999.

SEM micrographs and elemental composition analysis of the fresh, U and U-H₂S samples were obtained using a scanning electron microscopy (SEM, Zeiss Auriga 60) equipped with energy dispersive X-rays

spectroscopy (EDX, Oxford Inca Energy). Prior to EDX analysis, catalysts were crushed and fixed over a holder using carbon tape. The chemical composition was expressed as the average over ten measurements on individual particles for each powder sample. The elemental analysis was restricted to Ni, Al, Ce, O and S to avoid inconsistent results. Transmission electron microscopy (TEM) and high-resolution scanning transmission electron microscopy (HRSTEM) analysis were conducted using a 200 kV JEOL JEM-2100 F field emission microscope equipped with a Gatan Ultrascan CCD camera and EDAX Genesis EDS detector. The powder samples were dispersed by ultrasound in isopropanol. Suspension drops were deposited on a holey carbon-coated copper grid of 300 mesh (Agar Scientific Ltd., Essex, UK) and then dried in air. The particle size distribution of metallic supported particles on Al₂O₃ was obtained by individual image analysis of approximately 800 particles for each solid sample using the software Gatan Digital Micrograph.

X-ray diffraction (XRD) patterns were collected within the 2θ range 20–80° in a Bruker type XRD D8 Advance A25 diffractometer using a Cu Kα radiation (λ = 1.5406 Å), a voltage of 40 kV, a current of 40 mA and a step size of 0.05° (with 3 s duration at each step). The average crystal sizes of the metallic nickel (Ni⁰) and cerium oxide (CeO₂) were estimated using the Scherrer's equation at 2θ = 44.50° for Ni (111) and 47.36° for CeO₂ (220): D = (Kλ/βCosθ), where λ is the X-ray wavelength, β is the full width of the diffraction line at half maximum (FWHM), and θ is the Bragg angle.

CO-Chemisorption was performed on the same chemisorption analyzer (Autochem HP-Micromeritics) used for H₂-TPR. Before measurements, the fresh, U, and U-H₂S catalysts (ca. 50 mg) were reduced using 50 N mL·min⁻¹ in a 12 vol.% H₂/Ar flow at 500 °C for 3 h and a heating ramp of 1 °C·min⁻¹. Then, CO-Chemisorption was measured at 35 °C under a 10 vol.% CO/He flow. CO pulses were periodically introduced until saturation was reached. Nickel metal surface area and dispersion were calculated assuming the stoichiometric factor for CO to Ni equal to unity [41], atomic weight of 58.71, atomic cross-sectional area of 0.0649 nm² and density of 8.90 g·cm⁻³.

Temperature programmed oxidation (TPO) analysis of the fresh, U and U-H₂S catalysts for evaluation of carbon deposition were carried out in a thermal analyzer (Sensys evo TG-DSC, Seratan). Approximately, 30 mg of sample was placed at 35 °C for 30 min in N₂ flow (20 N mL·min⁻¹) to remove water. Then, the N₂ flow was switched to Air and the temperature was increased to 700 °C using a heating ramp of 5 °C·min⁻¹, and kept for 3 h.

In-situ diffuse reflectance infrared Fourier transform (DRIFT) spectroscopy was used to evaluate the nature of the species formed on the surface of fresh and U-H₂S catalysts. Measurements were conducted on a Bruker-Vertex70 equipped with a nitrogen cooled MCT detector and a high-temperature stainless steel reaction cell (Harrick Praying Mantis) with ZnSe windows. Prior to DRIFT measurements, samples were reduced at 500 °C for 3 h under a 5 vol.% H₂/Ar flow of 100 N mL·min⁻¹ and using a heating ramp of 1 °C·min⁻¹, followed by a purge with Ar for 30 min to remove residual H₂, and then cooled to a desired temperature. CO₂ methanation reaction was carried out from 100 to 500 °C using 20 mL·min⁻¹ of gas mixture (75% of stoichiometric mixture (H₂/CO₂ ratio = 4) and 25% of Ar gas). Stepwise heating and cooling with an increment from 50 up to 500 °C was applied. The temperature was held for 30 min at each step. Before methanation experiments, a background spectrum was collected at Ar atmosphere at each temperature. The product stream was analyzed continuously in a thermal analyzer ThermoStart by following the main molecular weights (*m/z* ratios) of CH₄ (15 and 16), H₂O (17 and 18) and CO₂ (12, 28 and 44).

The experimental uncertainties of textural properties associated with N₂-physisorption, CO chemisorption, XRD and TEM measures presented in this study was 7, 12 and 4%, in terms of the relative error.

2.3. Catalytic activity

CO₂ methanation reaction was tested in a fixed-bed laboratory reactor with internal diameter of 13 mm and 305 mm length (Microactivity Reference, PID Eng&Tech). Experiments were conducted using 0.3 g of catalyst mass diluted with 3 g of silicon carbide 46 grit (Cymit) of similar particle sizes (d_p = 355 μm). A mass dilution ratio m_{SiC}/m_{cat} = 10 was used aiming to keep isothermal behavior through the catalyst bed [45]. Reaction temperature was monitored continuously by a K-type thermocouple placed in the middle of the diluted catalyst bed. Mass flow meter controllers (MFC, Bronkhorst) were used to regulate the reactant gases H₂ (99.999%, Linde) and CO₂ (99.999%, Linde) at the reactor inlet. After reaction, the gas products passed through a cold liquid-gas separator (5 °C) where water was trapped, and then the dry gas flow was measured by a mass flow meter (MF, Bronkhorst). The dry gas composition (CH₄, H₂, CO, CO₂) was determined periodically (1 h) by an on-line gas micro-chromatograph (490 microGC, Agilent Technologies).

Catalysts were reduced in-situ under H₂ (99.999%, Linde) flow (100 N mL·min⁻¹) at 500 °C for 3 h at a heating ramp of 1 °C·min⁻¹, and then cooled to room temperature with the same ramp rate. Long-term activity tests were carried out under a flow rate of 200 N mL·min⁻¹ (GHSV = 40,000 N mL·g⁻¹·h⁻¹) and at a stoichiometric H₂:CO₂ molar ratio of 4. Catalyst stability was examined using the following procedure: 2 h at 250 °C, followed by 138 h at 500 °C, and finally, 2 h at 250 °C to check for deactivation. Additional runs were carried out by feeding H₂S flows of 20–100 N mL·min⁻¹ (1–5 ppm, Linde) to the H₂:CO₂ mixture.

Experimental conditions selected aimed to mimic the industrial adverse conditions to which methanation catalysts can be exposed by both the exothermicity of involved reaction and the presence of impurities derived from carbon sources as biogas. At industrial scale, methanation reactors may operate under adiabatic, isothermal or non-isothermal conditions with temperature profiles up to 500 °C [46]. In the latter scenario, the highest temperatures are typically found at the beginning of the reactor along with the most noticeable presence of H₂S. Under the explored experimental conditions, the contribution of internal mass transfer may be significant and diffusional limitations are expected to occur, as estimated for the Ni-CeO₂ catalyst using the Weisz-Prater criterion (N_{w,p} = 7.7). However, this fact does not interfere with the objectives of this work or with the conclusions that can be drawn from the results presented.

The CO₂ conversion (Eq. 4), CH₄ selectivity (Eq. 5) and CO selectivity (Eq. 6) were determined using the following equations:

$$X_{CO_2} = \left(1 - \frac{F_{CO_2,out}}{F_{CO_2,in}}\right) \cdot 100 \quad (4)$$

$$S_{CH_4} = \left(\frac{F_{CH_4,out}}{F_{CH_4,out} + F_{CO,out}}\right) \cdot 100 \quad (5)$$

$$S_{CO} = \left(\frac{F_{CO,out}}{F_{CO,out} + F_{CH_4,out}}\right) \cdot 100 \quad (6)$$

where *F_j* represents the molar flow rate of species *j* (*j* = CO₂, CH₄ and CO) in the inlet and outlet gas. Similar conversion values were obtained in terms of H₂ (standard deviation of ± 2%).

3. Results and discussion

3.1. Catalytic activity

The catalytic stability tests of the fresh catalysts were evaluated for 142 h at P = 5 barg, GHSV = 40,000 mL·g⁻¹·h⁻¹, T = 250 °C and 500 °C, in both the absence and presence of H₂S. Fig. 1 shows the CO₂ conversion (%) evolution over the course of long-term experiments for both Ni and Ni-CeO₂ catalysts. At the selected reaction conditions, the

A. Alarcón, et al.

Applied Catalysis B: Environmental 263 (2020) 118346

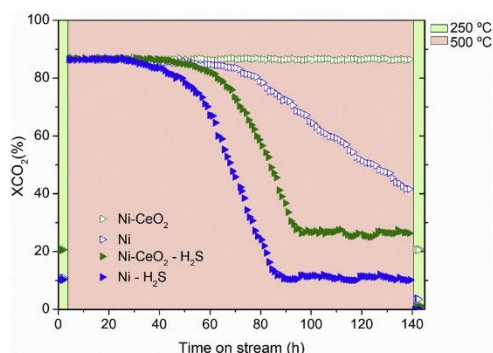


Fig. 1. CO₂ conversion (%) vs. 142 h time on stream at 250 and 500 °C, bag, 200 mL·min⁻¹, H₂/CO₂ molar ratio = 4 and 1 ppm of H₂S.

formation of byproducts was never detected, being the selectivity toward CH₄ equal to 100% for both catalysts during all runs. On one hand, the catalytic performance at low temperature (T = 250 °C) during 2 h confirmed that promoted Ni-CeO₂ catalyst (X_{CO₂} = 21%) was more active than the non-promoted one (X_{CO₂} = 10%). On the other hand, the evaluation at T = 500 °C revealed that the catalytic performance of the Ni-CeO₂ was completely stable for 138 h. This behavior pinpoints Ni-CeO₂ as an excellent candidate for CO₂ methanation at high temperature. Conversely, the activity of non-promoted catalyst at high temperature was stable for about 50 h and decreased by 48% after 138 h time-on-stream. The final evaluation at 250 °C also proved its permanent loss of activity (X_{CO₂} = 3%).

In the presence of H₂S impurities, both catalysts exhibited signs of poisoning during the time on stream evaluated at high temperature. Deactivation pattern of both catalysts followed three main stages. Initially, both catalysts were stable, Ni during 32 h and Ni-CeO₂ during 45 h. Then, both samples were rapidly deactivated over a period time of approximately 54 h. Finally, a steady catalytic activity was achieved until the test was completed. In this latter stage, the tolerance to H₂S was higher for Ni-CeO₂ since its catalytic activity (X_{CO₂} = 25%) was much higher than that of Ni catalyst (X_{CO₂} = 10%). Thus, the final total loss of catalytic activity was about 69% for Ni-CeO₂ and about 88% for the non-promoted catalyst. Furthermore, deactivation by poisoning was also verified at low temperature (250 °C) for both catalysts (X_{CO₂} < 1%).

Fig. S1 depicts the effect of H₂S impurities partial pressure on the activity of Ni-CeO₂ catalyst. At high H₂S concentration (5 ppm), the Ni-CeO₂ first stable period was notably shorter. Afterwards, the activity decay period was fast and the final steady catalytic activity was slightly lower (X_{CO₂} = 19%) in the presence of high H₂S concentration. This suggests a positive kinetic order in the deactivation kinetics with respect to the poison concentration and sheds light to the fact that high levels of H₂S impurities can shorten the lifespan of Ni-CeO₂ catalysts dramatically.

Based on these results, the relations between catalysts structure and activity were studied aiming to clearly understand the poisoning deactivation causes of Ni and Ni-CeO₂ catalysts. Several characterization techniques were applied to the catalysts in their three states (fresh, used and used-H₂S) to elucidate the main effects of poisoning on physico-chemical properties and to better understand the mechanism of deactivation. The results are presented and discussed in detail in next section.

3.2. Catalyst characterization

Elemental compositions obtained from EDX analysis for Ni and Ni-CeO₂ catalysts in their three experimental states are summarized in Table S1. For fresh samples, the experimental contents related to active phase (26 wt.% Ni ± 1) and promoter (21 wt.% CeO₂ ± 1) were very close to nominal ones. Moreover, EDX elemental mapping images displayed in Fig. S2 (a–b) evidenced a notably high and even distribution in the impregnation of the main components (Ni, Ce, Al, O) over both fresh catalysts. This speaks for the appropriateness of the method followed in the catalysts preparation. After reaction, the elemental composition of U and U-H₂S samples did not differ significantly. However, the presence of H₂S impurities were clearly identified in the two U-H₂S catalysts. Sulfur content was 0.51 wt.% ± 0.05 for Ni, while for Ni-CeO₂ was 0.54 wt.% ± 0.05. According to representative SEM images illustrated in Fig. 2, after 142 h of reaction under low/high temperature, high pressure and H₂S impurities, the geometric shape of both Ni and Ni-CeO₂ micro-spheres remained unaltered, confirming the proficient attrition/crushing resistance of prepared catalysts.

Textural properties such as BET specific surface area, pore volume and pore size distribution measured by N₂-physisorption for the three experimental states of Ni and Ni-CeO₂ catalysts are listed in Table 1. Fig. S3 (a–b) illustrates the corresponding adsorption/desorption isotherms. All the catalysts show characteristic plots of the reversible type IV isotherm with well-defined cylindrical pore channels (type H1 loops), according to IUPA classification [47]. Concerning to BET specific surface areas after contact with sulfur in relation to fresh catalysts, a decrease from 150 to 112 m²·g⁻¹ and from 120 to 87 m²·g⁻¹ were obtained for Ni and Ni-CeO₂ samples, respectively. The analogous reduction of BET specific surface areas for both U samples after reaction at high temperature was similar (23%). Because of the addition of H₂S impurities, further BET specific surface area reduction was observed for Ni (U-H₂S) (+2%) and Ni-Ce (U-H₂S) (+5%) catalysts. In contrast to the effect on BET surface area, the pore size of Ni and Ni-CeO₂ catalysts in their both U and U-H₂S states increased from 9 to 13 nm. Probably, the pore size increase was due to the agglomeration of metallic particles originated by the high temperature. In concordance with J. Richardson et al. [48], small metallic particles sintering result in the blockage of smaller pore sizes. This phenomenon leading to the increase of pore sizes can also be the main cause of loss of BET surface area in both U catalysts. On the other hand, a pore volume reduction was noticeable for the U-H₂S catalysts; about 22% for Ni (U-H₂S) and about 14% for Ni-CeO₂ (U-H₂S). The lower pore volume decrease of Ni-CeO₂ (U-H₂S) suggests that the addition of CeO₂ to Ni-based catalysts promotes the modification of textural properties at high temperature in the presence of H₂S impurities.

Possible carbon deposition on the Ni and Ni-CeO₂ catalysts was studied by measuring the weight loss during its temperature programmed oxidation under air gas flow. The thermogravimetric and mass spectrometric (TG-MS) analysis of both catalysts in their different experimental states are displayed in Fig. 3, S4 and S5. At temperature below 220 °C, U and U-H₂S catalysts showed a weight loss related to the vaporization of surface water and volatile species as reactants, products and reaction intermediates. From 220–370 °C, a noticeable weight increase was observed for both U and U-H₂S catalysts, being attributed to the oxidation of Ni to NiO. It must be noted that the formation of SO₂ that would lead to a weight decrease was not detected by MS (see Fig. S5). For temperatures above 370 °C, U and U-H₂S catalysts lost some weight in the air stream (0.36–0.71%), which can be ascribed to the oxidation of carbon species [49,50], as confirmed by the CO₂ detected by TG-MS in Fig. S4. However, these carbon species were not identified by SEM micrographs (Fig. S6).

XRD of Ni and Ni-CeO₂ catalysts in fresh, U and U-H₂S states were measured to evaluate their structural properties. The main peaks detected in the diffractograms of all samples were associated with phases of Ni, NiO, γ-Al₂O₃ and CeO₂, as detailed in Appendix A (Supporting

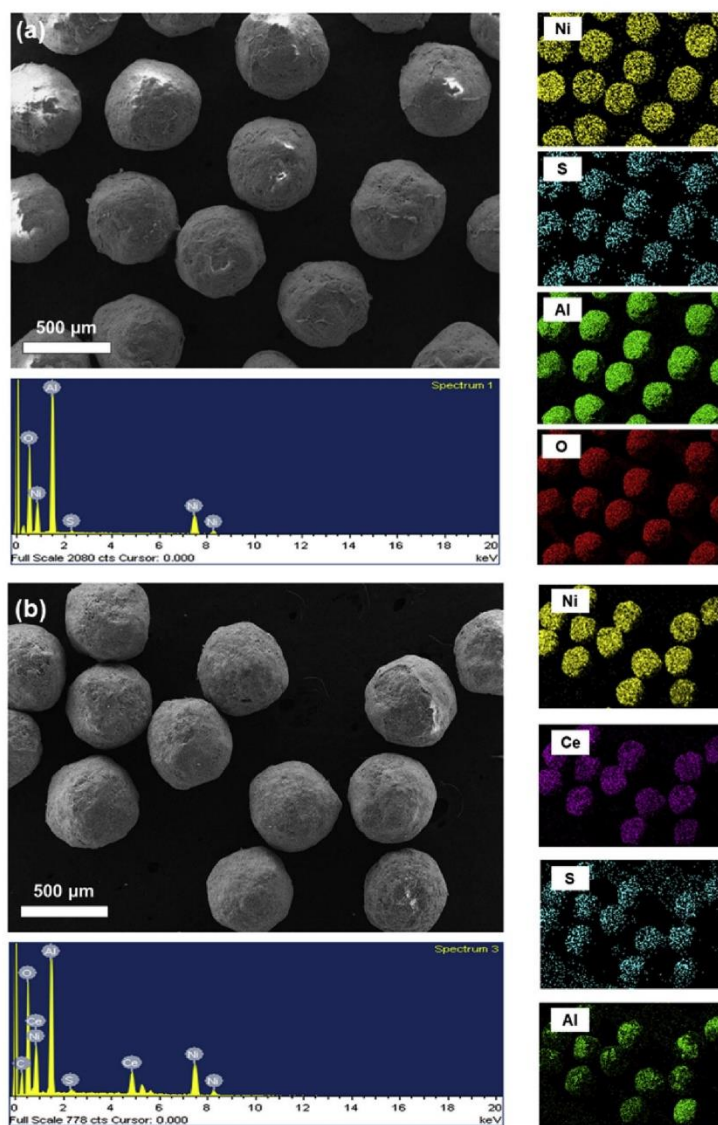


Fig. 2. EDX elemental mapping images of the used-H₂S micro-spheres catalysts: a) Ni and b) Ni-CeO₂.

Information). Table 1 summarizes the average Ni and CeO₂ crystallite sizes estimated by Scherrer's equation. For fresh Ni and Ni-CeO₂ catalysts, the average Ni crystallite size was 12.41 nm and 13.44 nm, respectively. For Ni-CeO₂, the corresponding average CeO₂ crystallite size was 4.14 nm. An increase of the average Ni and CeO₂ crystallite sizes was determined for U samples. This can be attributed to the catalysts thermal degradation (sintering) that produces the growth of impregnated metal nanoparticles on the support by either Ostwald ripening or particle migration and coalescence mechanisms [51].

Compared to fresh Ni-CeO₂, interesting effects on Ni and CeO₂ crystallite sizes were observed in Ni-CeO₂ (U) sample. On one hand, the Ni particle size reduced by 20%, while on the other, the CeO₂ particle size increased by 51%. On the contrary, Ni particle size of Ni (U) increased by 19%. This growth of metallic Ni particles induced by temperature, i.e. sintering, is most likely to be the main cause of deactivation of Ni (U) catalyst, as previously observed for co-precipitated Ni-Al samples [26]. A major conclusion is that sintering of Ni particles is less noticeable in the catalyst promoted with Ce, where sintering preferentially

Table 1
Physicochemical properties of Ni and Ni-CeO₂ catalysts.

Sample	State	BET ^a [m ² g ⁻¹]	Pore ^a volume [cm ³ g ⁻¹]	Pore ^a size [nm]	d _{Ni} ^b [nm]	d _{CeO₂} ^b [nm]	d _{Ni} ^c [nm]	Ni ^d dispersion[%]	Metallic ^d surface area [m ² g _{Ni} ⁻¹]
Ni	fresh	150	0.36	9	12.41	–	14.48	1.21	8.08
	used	116	0.34	13	14.73	–	20.76	0.64	4.25
	used-H ₂ S	112	0.28	13	13.91	–	15.11	0.17	1.15
Ni-CeO ₂	fresh	120	0.21	9	13.44	4.14	14.88	1.29	8.58
	used	92	0.22	13	10.74	8.45	25.73	0.60	4.02
	used-H ₂ S	87	0.18	13	13.21	4.16	15.66	0.28	1.88

^a Calculated from N₂-Physisorption data.

^b Calculated from XRD data.

^c Derived from TEM particle size distribution.

^d Calculated from CO-Chemisorption data.

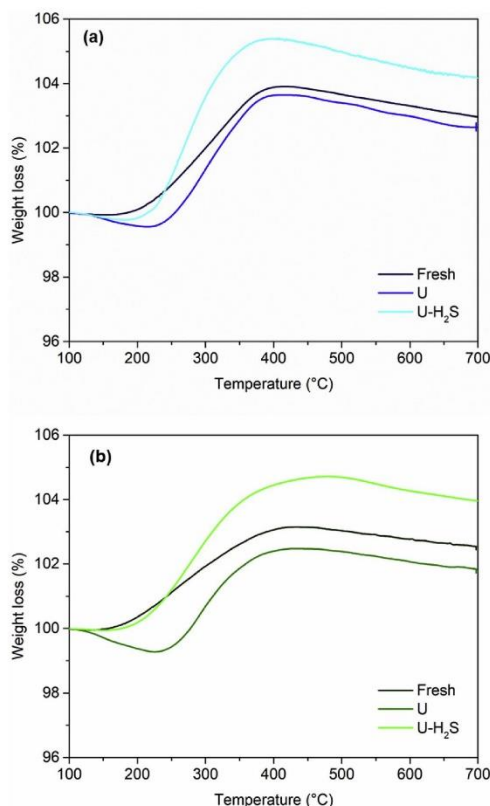


Fig. 3. TGA profiles corresponding to the temperature programmed oxidation of the a) Ni and b) Ni-CeO₂ catalysts.

affect CeO₂ particles. This in agreement with the enhanced thermal degradation of the promoted catalyst observed in the activity tests.

At the tested reaction conditions, the sintering behaviour of CeO₂ particles can be related to the structural conversion of non-stoichiometric CeO_{2-x} caused by the redox reaction between Ce³⁺ and Ce⁴⁺ [52], whereas the inhibition of Ni particles sintering can be induced by the strong metal-promoter bonding between Ni and CeO₂ nanoparticles [53], which is generated by incorporation of Ni²⁺ species into lattices of CeO₂ particles [54] or the migration of partial reduced CeO_{2-x}

to Ni nanoparticles [55]. This structural behaviour can explain the stable activity of the Ni-CeO₂ (U) and also be the origin of the changes of textural properties previously estimated for this sample by N₂-physisorption. Regarding the Ni-CeO₂ (U-H₂S) catalyst, the estimated decrease of Ni crystallite size (1%) and increase of CeO₂ crystallite size (0.5%) were both less significant. At the same conditions, the increase of Ni crystallite size of Ni (U-H₂S) was also less pronounced (12%). This is an interesting finding revealing that the observed sintering of U-samples is inhibited by the presence of H₂S impurities. Indeed, T. Yoneima et al. [56] reported that excess sulfur beyond the solubility limit in nickel contributed to the formation of nickel sulfide phases that prevent grain growth.

Ni dispersion and metallic surface areas of Ni and Ni-CeO₂ catalysts in their three experimental states were estimated from CO-chemisorption data. The results, listed in Table 1, revealed that Ni dispersion and metallic surface area were higher for fresh Ni-CeO₂ catalyst (1.29% and 8.58 m²g_{Ni}⁻¹) than for fresh Ni catalyst (1.21% and 8.08 m²g_{Ni}⁻¹). The better structural properties achieved in Ni-CeO₂ are also in concordance with its Ni reducibility (83.22%), as estimated by TPR measurements (Appendix B, Supporting Information). Furthermore, Ni dispersions and metallic surface areas for both U samples decreased by 45% due to the aggregation of Ni particles in Ni (U) or of CeO₂ particles in Ni-CeO₂ (U) catalyst. This is somewhat in discrepancy with the decrease of d_{Ni} estimated for Ni-CeO₂ (U) catalyst by XRD in Table 1 but in coherence with overall TEM results. The difference in Ni crystallite size between XRD and TEM can be explained on the basis that XRD allows for estimating the crystallite sizes whereas TEM is used to determine particle sizes of particles that often can be an agglomerate of crystallites.

In any case, reduction of these properties was more noticeable in presence of H₂S, which was linked to the formation of nickel sulfur. The corresponding reductions were about 86% for Ni (U-H₂S) and 78% for Ni-CeO₂ (U-H₂S). Therefore, textural properties can be modified by both thermal degradation of supported metallic particles and the formation of NiS species. The higher metallic surface area and Ni dispersion determined for Ni-CeO₂ (U-H₂S) is also in agreement with the superior activity achieved in the tests for the promoted catalyst. The reported values for U-H₂S samples are in contrast to a recent study [30], where only negligible amounts of H₂ were adsorbed on co-precipitated Ni-Al catalysts after H₂S and SO₂ poisoning. In that case, CH₄ yield after sulfur poisoning was negligible.

TEM analysis was used to provide reliable information about the size of supported metallic particles. Fig. 4 illustrates representative TEM images of the three states of Ni and Ni-CeO₂ catalysts. From different TEM images of several catalyst particles, approximately 800 supported metallic particles were measured for each sample. This allowed for a proper characterization with statistically significant particle size distributions (PSD), see Fig. S7. The mean Ni particle size of fresh Ni was 14.48 ± 0.38 nm, whereas a mean spotty particle size of 14.88 ± 0.66 nm was estimated for the fresh Ni-CeO₂ catalyst. According to the literature [57], the assembly of CeO₂ particles can lead to

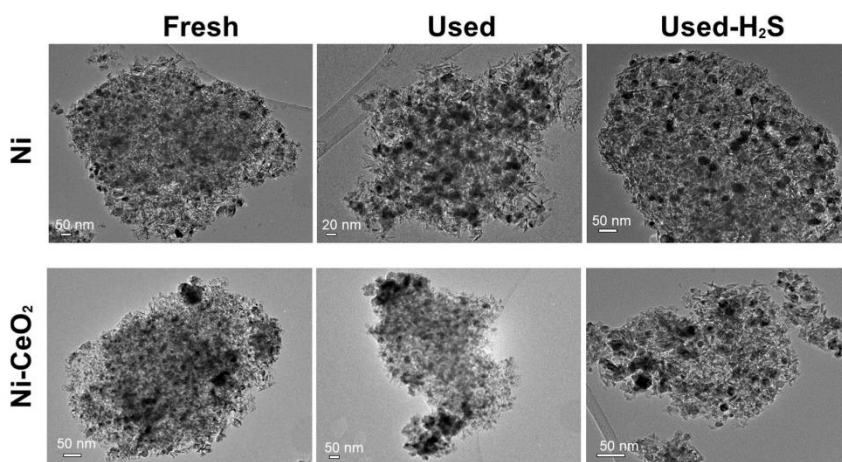


Fig. 4. TEM images of Ni and Ni-CeO₂ catalysts using a scale between 20–50 nm.

the formation of spotty particles in the CeO₂ promoted Ni catalysts. The formation of nanocomposite enables large interface of Ni-CeO₂ [58]. After reaction at 500 °C, there is significant broadening of the PSD for both U samples, which results in a larger mean particle size of Ni (20.76 ± 0.36 nm) and nanocomposite (25.73 ± 1.16 nm). This is another evidence of sintering along with XRD and BET results. Based on XRD results, the growth of CeO₂ particles can be attributed to the increase of nanocomposites in Ni-CeO₂ (U) that can even contain Ni particles smaller than those in fresh Ni-CeO₂. Apart from that, the main particle and nanocomposite size increase observed for the catalysts working in the presence of H₂S impurities was inferior than that of U samples. The mean Ni particle size of Ni (U-H₂S) was 15.11 ± 0.35 nm and the mean nanocomposite particle size of Ni-CeO₂ (U-H₂S) was 15.66 ± 0.37 nm. This lesser significant growth of metallic particles (~5%) can be attributed to the formation of new phases originated by the addition of hydrogen sulfide impurities.

HRSTEM (Fig. 5) was used to identify the main crystallographic planes of the experimental states studied for Ni and NiCeO₂ catalysts. Lattice-fringe analysis and Fourier Transform (FT) imaging revealed spots at 2.04, 1.76 and 1.25 Å in the particle named “a”, which are ascribed to (111), (200) and (220) crystallographic planes of metallic Ni. Besides, in the Ni-CeO₂ samples, the particle named “b” exhibited lattice fringes of 3.12, 2.71, 1.91, 1.63, 1.56, and 1.35 Å that were linked to CeO₂ (111), (200), (220), (311), (222) and (400) planes. The assumption about nanocomposites formation can be verified in the three HRSTEM images of Ni-CeO₂ catalysts. Furthermore, we identified the formation of the sulfide species in both U-H₂S samples. For the Ni (U-H₂S) sample, nickel sulfides were distinguished with lattice fringes of 2.41 and 2.51 Å in the particle named “c”, in turn related to crystallographic planes (220) and (021). The most striking result to emerge from the data is that in addition to NiS, the formation of cerium oxy-sulfide (particle named “d”) was identified over Ni-CeO₂ (U-H₂S). The crystallographic plane of Ce₂O₂S (100) was ascribed to lattice fringes of 3.47 Å. These results provide extremely valuable insight into the governing poisoning deactivation mechanisms. To the best of our knowledge, the precise role of CeO₂ in deactivation by sulfur poisoning has never been reported and the reasons why CeO₂ promoted Ni-based catalysts exhibit improved tolerance are still unclear. The oxygen vacancies at ceria surface involve the presence of Ce⁴⁺/Ce³⁺ coupling [59]. Considering the Gibbs free energy of cerium sulfides and nickel (see Fig. S8), the formation of Ce₂O₂S (s) is thermodynamically more

favorable and spontaneous than that of NiS (s) in the whole range of reaction temperatures [60,61]. At the tested temperature of 500 °C, ΔH_{solid}⁰ values of Ce₂O₂S and NiS are -548 kJ·mol⁻¹ and -129 kJ·mol⁻¹, respectively. Therefore, the higher catalytic activity achieved for the CeO₂ promoted catalyst can be explained by the favorable formation of Ce₂O₂S, that restricted the formation of nickel sulfide [40], helping thereby to maintain the catalyst stability.

Linking activity and characterization results, the findings of this study indicate that under the selected CO₂ methanation conditions, the unaltered catalytic activity of Ni-CeO₂ catalyst was due to the formation of nanocomposites, which positively promote a larger interface between the particles of metallic Ni and CeO_{2-x}. Through this structural effect, CeO_{2-x} can act as an active site of the CO₂ activation and the active metal Ni surface acts a supplier of atomic hydrogen yielding stable catalytic activity. On the contrary, the rapid activity decay of Ni sample was attributed to the aggregation of metallic Ni since leaching and carbon deposition were negligible for both U samples as confirmed by SEM and O₂-TPO. For both Ni and Ni-CeO₂ catalysts, XRD and TEM results suggest that the modification of textural properties after reaction is associated with thermal degradation of either CeO₂ particles in Ni-CeO₂ or Ni particles in Ni catalyst.

Two main conclusions can be drawn in light of TEM-HRSTEM results: i) the identification of crystallographic planes allowed for confirming the presence of Ce₂O₂S, and ii) the effect of sintering is far less noticeable for the samples exposed to H₂S. On one hand, inference i) is of paramount importance since it confirms the role of Ce for increasing the sulfur tolerance by the formation of species that counteract the poisoning of Ni active sites. This is in agreement with the large metallic surface area determined by CO-chemisorption. The supported Ce metallic particles act as sacrificial functional groups that eventually make the catalyst lifespan longer lasting. On the other, ii) confirms that the interaction of sulfur with Ni leads to the production of NiS that prevent the growth of Ni particles at high temperature. Such statements reveal a complex situation where two deactivation mechanisms, poisoning and sintering, are at play simultaneously. The understanding of the underlying overall poisoning mechanism is therefore essential to mitigate the observed deactivation effects and towards the design of catalysts with improved efficiency. Accordingly, DRIFTS experiments were performed over fresh and U-H₂S catalysts aiming to obtain useful information for elucidating a plausible mechanism.

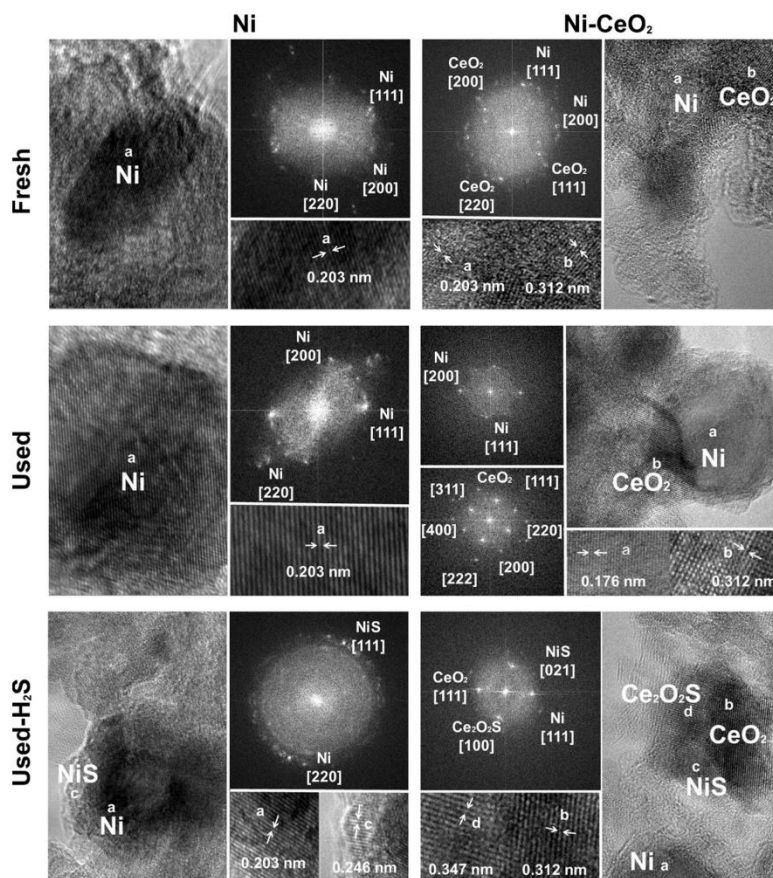


Fig. 5. HRSTEM images of Ni and Ni-CeO₂ catalysts at a scale between 1–5 nm.

3.3. Poisoning mechanism

Fig. 6 shows the DRIFTS measurements collected in the course of CO₂ methanation conditions over fresh Ni and Ni-CeO₂ catalysts at increasing temperature range from 100 to 500 °C. The interaction of the reactive mixture over fresh Ni sample (Fig. 6a) at 100 °C lead to the formation of species associated with the hydrogen carbonate (HCO₃⁻) (1656, 1437 and 1228 cm⁻¹) and monodentate carbonate (m-CO₃²⁻) (1532 and 1384 cm⁻¹) [62]. At the same temperature, U(OH) vibration of OH species were identified in the range 3730-3589 cm⁻¹. With increasing temperature, the bands intensity and position changed. At 150 °C, the transformation of carbonate species (CO₂²⁻) to bidentate formate species (b-HCOO⁻) was observed. The bands linked to these species were identified at 1549, 1391, 1372 cm⁻¹. Besides formates, carbonyl species adsorbing on metallic Ni sites, such as tri-carbonyl (2058 cm⁻¹), bi-(2035), mono-(2010) and bridged carbonyls (1910 and 1819 cm⁻¹) were recognized, in agreement with literature [63,64]. The symmetric evolutions between carbonyl group and formates evidenced that CO can be arisen from formates [65]. Further increase in temperature generated the formation of new bands at 1305, 2906 and 3016 cm⁻¹, assigned to vibration modes of methane gas δ(CH), surface

bidentate formates (Ua(CO₂) + δ(CH)) and methane gas (U(CH)). Above 250 °C, the intensity of the bands associated with carbonyl group increased, specially bridged carbonyl, whereas the characteristic bands of formate species decreased appreciably. Above 450 °C, the thermodynamic effects on Ni catalyst were distinguished, causing a depletion of the methane production.

Fig. 6b illustrates the species formed over fresh Ni-CeO₂ catalyst surface. At 100 °C, bands assigned to U(OH) (3730-3589 cm⁻¹), HCO₃⁻ (1652, 1437, 1228 cm⁻¹), bridged carbonate (1395 cm⁻¹), m-CO₃²⁻ (1375 cm⁻¹) and b-HCOO⁻ (1594 cm⁻¹) were identified [66-69]. At this low temperature, CO derived from formate species was subsequently adsorbed on metallic Ni sites. Such carbonyl species were revealed at the absorption bands of 2064, 1910 and 1824 cm⁻¹, respectively. The carbonyl band at 2064 cm⁻¹ can be formed over the dispersed small nickel oxide particles, while bridged carbonate can be originated from new active sites related to Ce⁺³ sites [70,71]. With increasing temperature, HCO₃⁻ and CO₂²⁻ bands were shifted to b-HCO₂²⁻, while the bands associated with CO adsorbed on Ni sites were substituted by di- (2041 cm⁻¹) and mono-(2010 cm⁻¹) carbonyls. Above 200 °C, new peaks appeared at 1305 and 1316 cm⁻¹ that were assigned to the δ(CH) and U(CH) vibration modes, respectively. In

A. Alarcón, et al.

Applied Catalysis B: Environmental 263 (2020) 118346

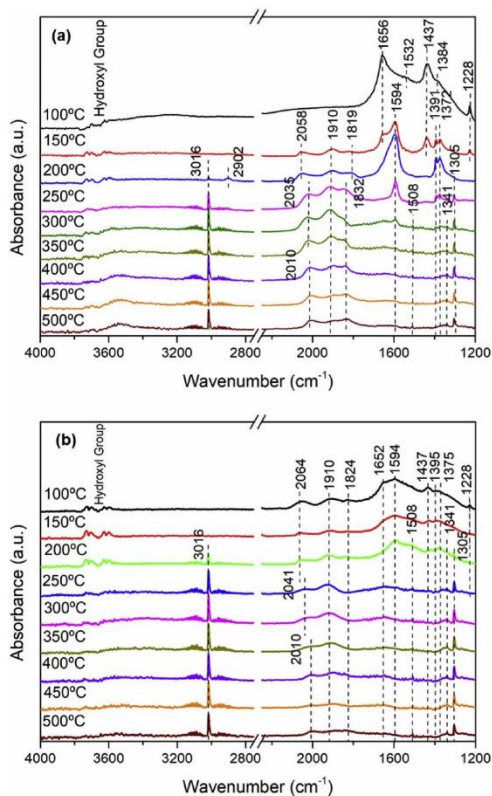


Fig. 6. In-situ DRIFTS spectra during CO₂ methanation reaction over fresh a) Ni and b) Ni-CeO₂ catalysts at the temperature range 100–500 °C.

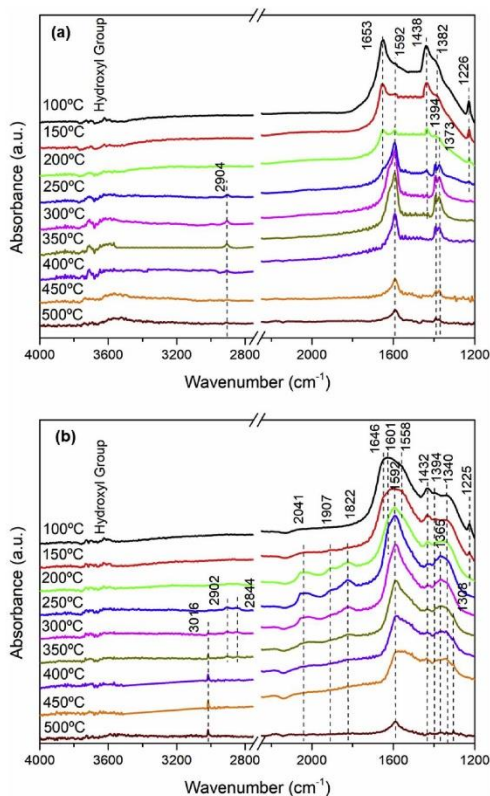


Fig. 7. In-situ DRIFTS spectra during CO₂ methanation reaction over used-H₂S a) Ni and b) Ni-CeO₂ catalysts at the temperature range 100–500 °C.

agreement with activity test, the high intensity observed for the peak of methane confirmed the higher activity of Ni-CeO₂ compared to Ni catalyst at low temperature. According to the behavior of U(CH) band along with formates and carbonyl species, the main limitation of CH₄ production apparently was the dissociation/hydrogenation of CO. Similar to Ni catalyst, the thermodynamic effects on Ni-CeO₂ were distinguished at temperatures above 450 °C.

DRIFT experiments were also conducted with Al₂O₃ and CeO₂/Al₂O₃ samples at different temperatures, see Supporting Information Fig. S9. Only the vibration modes assigned to carbonates, CO₂ and surface bidentate formates (Ua(CO₂)+δ(CH)) at < 3000 cm⁻¹ were observed confirming the selective adsorption of CO on Ni⁰ phase and that methane production is unattainable in absence of Ni⁰.

In order to examine the poisoning reaction pathway at high temperature, both Ni and Ni-CeO₂ U-H₂S catalysts were evaluated using DRIFTS under CO₂ methanation conditions in the temperature range of 100–500 °C, see Fig. 7. As can be observed, similar carbonate species were recognized over Ni (U-H₂S) at 100 °C yet with a slight shift (± 2 cm⁻¹) in their positions, which can be attributed to the sulfur poisoning. Hence, the bands identified at 1653, 1438, 1228 and 1382 cm⁻¹ were also related with the HCO₂⁻ and m-CO₃²⁻ species. In this poisoned sample, the formation of bidentate formate species (1592, 1394 and 1373 cm⁻¹) increased with temperature. However, carbonyl species recognized in the Ni catalyst above 150 °C were not detected in

the Ni (U-H₂S) indicating that methane gas band was not formed. Based on TEM and CO-chemisorption analysis, the methane production by the dissociation/ hydrogenation of CO is unattainable owing to the unfavorable formation of nickel sulphides.

Fig. 7b shows the corresponding DRIFTS spectra of Ni-CeO₂ (U-H₂S) catalyst. Compared to fresh Ni-CeO₂, in addition to HCO₃⁻ (1432, 1225 cm⁻¹), bridged carbonate (1394 cm⁻¹) and m-CO₃²⁻ (1340 cm⁻¹), three new bands were observed at 1643, 1601 and 1588 cm⁻¹. These bands probably arise from formate species produced via the reaction of adsorbed CO and surface OH groups [66,72]. With increasing temperature, the formation of formate species was very similar to those over Ni-CeO₂ catalyst. It is noteworthy that carbonyl species derived from the CO adsorbed on Ni sites (di- (2041 cm⁻¹) and bridged carbonyl (1019 1832 and 1822 cm⁻¹)) were clearly detected above 150 °C. This phenomenon was not identified over Ni (U-H₂S) catalyst and strengthens our conviction that the higher production of methane over Ni-CeO₂ is due to the formation of Ce₂O₃. The presence of carbonyl and CH₄ bands in the Ni-CeO₂ (U-H₂S) catalyst confirms that the catalyst preserved free active sites for methane formation at saturation coverage. This reveals that the main role of Ce₂O₃ is to restrict the formation of NiS species increasing thereby the tolerance to sulfur poisoning.

In light of DRIFTS results and the catalytic behavior-structure evidences collected for Ni-CeO₂ catalyst, a poisoning deactivation mechanism for CO₂ methanation is proposed (Fig. 8). At low temperature,

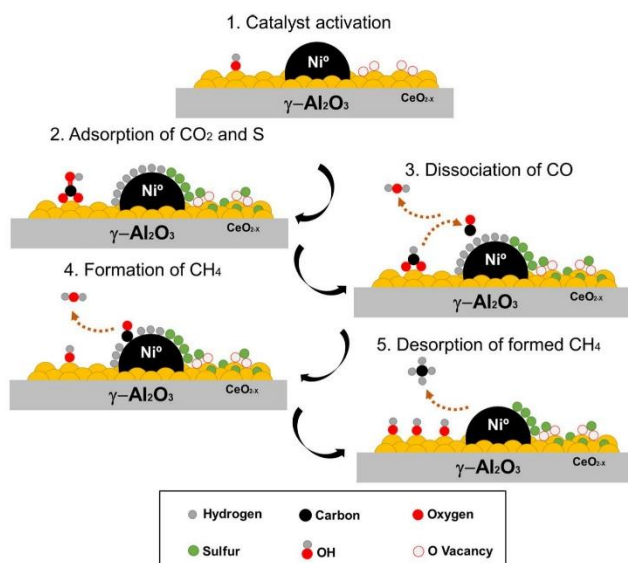
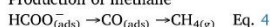


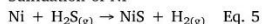
Fig. 8. Schematic representation of the proposed reaction mechanism of CO_2 methanation under H_2S poisoning for Ni- CeO_2 catalyst.

hydrogen carbonate and monodentate carbonate are hydrogenated to form bidentate and monodentate formate species. The interaction between formate species and carbonyl group suggests that CO adsorbed on Ni sites arises from formate species. At the high temperature of 500 °C, the CH_4 production proceeds preferentially via formate dissociation followed by hydrogenation of adsorbed CO (Eq. 4). Sulfur poisoning on the Ni sites (Eq. 5) was prevented by the favorable formation of $\text{Ce}_2\text{O}_2\text{S}$ (Eq. 7). Accordingly, the higher activity of Ni- CeO_2 catalyst can be attributed to its larger metallic surface area.

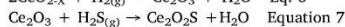
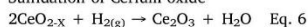
Production of methane



Sulfidation of Ni



Sulfidation of Cerium oxide



4. Conclusion

The performance over time on non-promoted Ni and promoted Ni- CeO_2 catalysts is studied under accelerated aging conditions at high temperature (500 °C) in the absence and presence of H_2S impurities (1–5 ppm). The Ni- CeO_2 catalyst achieves excellent thermal stability over more than 138 h of operation, while the non-promoted Ni sample suffers from nickel sintering. Interestingly, sintering mechanism is inhibited by the presence of H_2S impurities due to the formation of nickel sulfide that prevents grain growth. The presence of H_2S leads to deactivation of both catalysts by sulfur poisoning. However, Ni- CeO_2 exhibits higher final steady activity ($X_{\text{CO}_2} = 25\%$), and therefore, higher tolerance to H_2S poisoning in comparison with non-promoted Ni ($X_{\text{CO}_2} = 10\%$). The higher tolerance is derived from the thermodynamically favorable formation of $\text{Ce}_2\text{O}_2\text{S}$ phase that restricts the formation of nickel sulfide, as evidenced by HRSTEM. The reaction mechanism under H_2S poisoning for Ni- CeO_2 catalyst is hereby proposed. CH_4 production preferentially proceeds via formate dissociation followed by hydrogenation of the adsorbed CO on non-poisoned active

sites. Accordingly, the presence of CeO_2 in nickel-based catalysts for CO_2 methanation is beneficial since it enhances initial activity, thermal resistance and tolerance to H_2S impurities. The latest finding is of utmost relevance for its implementation in biogas industrial applications.

Declaration of Competing Interest

The authors declare that they have no known competing financial interests or personal relationships that could have appeared to influence the work reported in this paper.

Acknowledgements

Authors thank Generalitat de Catalunya for financial support through the CERCA Programme, M2E (2017SGR1246) and XaRMAE network. IREC also gratefully acknowledge the funding of this work by the CoSin project (COMRD115-1-0037), funded by ACCIÓ and the European Regional Development Fund (ERDF) under the framework of RIS3CAT Energy Community. Andreina Alarcón is grateful to Escuela Superior Politécnica del Litoral (ESPOL) for the support during her postgraduate studies (“Walter Valdano Raffo” Program, First edition). Authors gratefully acknowledge Dr. Marco Argudo (IREC) for sample characterization and Dr. Alan Harvey (University of Limerick) for his assistance with HRSTEM.

Appendix A. Supplementary data

Supplementary material related to this article can be found, in the online version, at doi:<https://doi.org/10.1016/j.apcatb.2019.118346>.

References

- [1] C.J. Quarton, S. Samsatli, Power-to-gas for injection into the gas grid: what can we learn from real-life projects, economic assessments and systems modelling? *Renewable Sustainable Energy Rev.* 98 (2018) 302–316, <https://doi.org/10.1016/j.rser.2018.09.007>.
- [2] J. Lefebvre, M. Friedemann, G. Manuel, F. Graf, S. Bajohr, R. Reimert, T. Kolb,

A. Alarcón, et al.

Applied Catalysis B: Environmental 263 (2020) 118346

Renewable Power-to-Gas : A technological and economic review 85 (2016), <https://doi.org/10.1016/j.renene.2015.07.066>.

[3] A. Buttler, H. Spliethoff, Current status of water electrolysis for energy storage, grid balancing and sector coupling via power-to-gas and power-to-liquids: a review, *Renewable Sustainable Energy Rev.* 82 (2018) 2440–2454, <https://doi.org/10.1016/j.rser.2017.09.003>.

[4] J. Guílera, J. Ramon Morante, T. Andreu, Economic viability of SNG production from power and CO₂, *Energy Convers. Manage.* 162 (2018) 218–224, <https://doi.org/10.1016/j.enconman.2018.02.037>.

[5] S.F. Ferreira, L.S. Buller, M. Berni, T. Forster-Carneiro, Environmental impact assessment of end-uses of biomethane, *J. Clean. Prod.* 230 (2019) 613–621, <https://doi.org/10.1016/j.jclepro.2019.05.034>.

[6] C. Mebrahtu, F. Krebs, S. Abate, S. Perathoner, G. Centi, R. Palkovits, CO₂ Methanation: Principles and Challenges, 1st ed., Elsevier B.V., 2019, <https://doi.org/10.1016/B978-0-444-64127-4.00005-7>.

[7] A. Alarcón, J. Guílera, T. Andreu, CO₂ conversion to synthetic natural gas: reactor design over Ni-Ce/Al₂O₃ catalyst, *Chem. Eng. Res. Des.* (2018), <https://doi.org/10.1016/j.cherd.2018.10.017>.

[8] S. Tada, O. James, R. Kikuchi, Promotion of CO₂ methanation activity and CH₄ selectivity at low temperatures over Ru/CeO₂/Al₂O₃ catalysts, *Int. J. Hydrogen Energy* 39 (2014) 10990–10100, <https://doi.org/10.1016/j.ijhydene.2014.04.133>.

[9] T.A. Le, M.S. Kim, S.H. Lee, T.W. Kim, E.D. Park, CO and CO₂ methanation over supported Ni catalysts, *Catal. Today* 293–294 (2017) 89–96, <https://doi.org/10.1016/j.cattod.2016.12.036>.

[10] S. Natalia, M. Martín, Catalytic hydrogenation of CO₂ to methane over supported Pd, Rh and Ni catalysts (2017), <https://doi.org/10.1039/c6cy02536f>.

[11] J. Gao, Q. Liu, F. Gu, B. Liu, Z. Zhong, F. Su, Recent advances in methanation catalysts for the production of synthetic natural gas, *RSC Adv.* 5 (2015) 22759–22776, <https://doi.org/10.1039/c4ra16114a>.

[12] S. Tada, T. Shimizu, H. Kameyama, T. Haneda, R. Kikuchi, Ni/CeO₂ catalysts with high CO₂ methanation activity and high CH₄ selectivity at low temperatures, *Int. J. Hydrogen Energy* 37 (2012) 5527–5531, <https://doi.org/10.1016/j.ijhydene.2011.12.122>.

[13] M.V. Konishcheva, D.I. Potemkin, S.D. Badmaev, P.V. Snytnikov, On the Mechanism of CO and CO₂ Methanation Over Ni / CeO₂ Catalysts (2016) 1424–1430, <https://doi.org/10.1007/s11244-016-0650-7>.

[14] J. Xu, Q. Lin, X. Su, H. Duan, H. Geng, Y. Huang, CO₂ methanation over TiO₂-Al₂O₃ binary oxides supported Ru catalysts, *CJCHE* 24 (2016) 140–145, <https://doi.org/10.1016/j.cjche.2015.07.002>.

[15] J. Ashok, M.L. Ang, S. Kawi, Enhanced activity of CO₂ methanation over Ni/CeO₂-ZrO₂ catalysts: influence of preparation methods, *Catal. Today* 281 (2017) 304–311, <https://doi.org/10.1016/j.cattod.2016.07.020>.

[16] X. Wang, L. Zhu, Y. Liu, S. Wang, CO₂ methanation on the catalyst of Ni/MCM-41 promoted with CeO₂, *Sci. Total Environ.* 625 (2018) 686–695, <https://doi.org/10.1016/j.scitotenv.2017.12.308>.

[17] Q. Liu, B. Bian, J. Fan, J. Yang, Cobalt doped Ni based ordered mesoporous catalysts for CO₂ methanation with enhanced catalytic performance, *Int. J. Hydrogen Energy* 43 (2018) 4893–4901, <https://doi.org/10.1016/j.ijhydene.2018.01.132>.

[18] G. Garbarino, C. Wang, T. Cavatoni, E. Finocchio, P. Riani, M. Flytzani-Stephanopoulos, G. Busca, A study of Ni/La-Al₂O₃ catalysts: a competitive system for CO₂ methanation, *Appl. Catal. B* 248 (2019) 286–297, <https://doi.org/10.1016/j.apcatb.2018.12.063>.

[19] A. Quindimil, U. De-la-torre, B. Pereda-ayo, J.A. González-marcos, J.R. González-velasco, Environmental Ni catalysts with La as promoter supported over Y- and BETA- zeolites for CO₂ methanation, *Appl. Catal. B* 238 (2018) 393–403, <https://doi.org/10.1016/j.apcatb.2018.07.034>.

[20] T.A. Le, J.K. Kang, S.H. Lee, E.D. Park, CO and CO₂ methanation over Ni/Al₂O₃ core-shell catalyst, *J. Nanosci. Nanotechnol.* 19 (2019) 3252–3262, <https://doi.org/10.1166/jnn.2019.16585>.

[21] S. Abate, C. Mebrahtu, E. Giglio, F. Deorsola, S. Bensaid, S. Perathoner, R. Pirone, G. Centi, Catalytic performance of γ-Al₂O₃-ZrO₂-TiO₂-CeO₂ composite oxide supported Ni-based catalysts for CO₂ methanation, *Ind. Eng. Chem. Res.* 55 (2016) 4451–4460, <https://doi.org/10.1021/acs.iecr.6b00134>.

[22] E.Z. Golosman, V.N. Efremon, Industrial catalysts for the hydrogenation of carbon oxides, *Catal. Int. J.* 4 (2012) 267–283, <https://doi.org/10.1134/S2070050412040071>.

[23] M. Argyle, C. Bartholomew, Heterogeneous catalyst deactivation and regeneration: a review, *Catalysts* 5 (2015) 145–269, <https://doi.org/10.3390/catal5010145>.

[24] J.R. Rostrup-Nielsen, K. Pedersen, J. Sehested, High temperature methanation. Sintering and structure sensitivity, *Appl. Catal. A Gen.* 330 (2007) 134–138, <https://doi.org/10.1016/j.apcata.2007.07.015>.

[25] P. Forzatti, Catalyst deactivation, *Catal. Today* 52 (2002) 165–181, [https://doi.org/10.1016/S0920-5861\(99\)00074-7](https://doi.org/10.1016/S0920-5861(99)00074-7).

[26] S. Ewald, M. Kolbeck, T. Kratky, M. Wolf, O. Hinrichsen, On the deactivation of Ni-Al catalysts in CO₂ methanation, *Appl. Catal. A Gen.* 570 (2019) 376–386, <https://doi.org/10.1016/j.apcata.2018.10.033>.

[27] M. Younas, L. Loong Kong, M.K.J. Bashir, H. Nadeem, A. Shehzad, S. Sethupathi, Recent advancements, fundamental challenges, and opportunities in catalytic methanation of CO₂, *Energy Fuels* 30 (2016) 8815–8831, <https://doi.org/10.1021/acs.energyfuels.6b01723>.

[28] K. Müller, M. Fleige, F. Rachow, D. Schmelzer, Sabatier based CO₂-methanation of flue gas emitted by conventional power plants, *Energy Procedia* 40 (2013) 240–248, <https://doi.org/10.1016/j.egypro.2013.08.028>.

[29] B. Legras, V.V. Ordomsky, C. Dujardin, M. Virginie, A.Y. Khodakov, Impact and detailed action of sulfur in syngas on methane synthesis on ni/γ-Al₂O₃ catalyst, *ACS Catal.* 4 (2014) 2785–2791, <https://doi.org/10.1021/cs500436f>.

[30] M. Wolf, C. Schüller, O. Hinrichsen, Sulfur poisoning of co-precipitated Ni-Al catalysts for the methanation of CO₂, *J. Co₂ Util.* 32 (2019) 80–91, <https://doi.org/10.1016/j.jcou.2019.03.003>.

[31] D.R. Mullins, The surface chemistry of cerium oxide, *Surf. Sci. Rep.* 70 (2015) 42–85, <https://doi.org/10.1016/j.surfrep.2014.12.001>.

[32] Q. Liu, J. Gao, M. Zhang, H. Li, F. Gu, G. Xu, Z. Zhong, F. Su, Highly active and stable Ni/γ-Al₂O₃ catalysts selectively deposited with CeO₂ for CO methanation, *RSC Adv.* 4 (2014) 16094–16103, <https://doi.org/10.1039/c4ra00746h>.

[33] S. Wang, G.Q. Lu, Role of CeO₂ in Ni/CeO₂-Al₂O₃ catalysts for carbon dioxide reforming of methane, *Appl. Catal. B* 19 (1998) 267–277, [https://doi.org/10.1016/S0926-3373\(98\)00081-2](https://doi.org/10.1016/S0926-3373(98)00081-2).

[34] G. Xu, K. Shi, Y. Gao, H. Xu, Y. Wei, Studies of reforming natural gas with carbon dioxide to produce synthesis gas. X. The role of CeO₂ and MgO promoters, *J. Mol. Catal. A Chem.* 147 (1999) 47–54, [https://doi.org/10.1016/S1381-1169\(99\)00127-2](https://doi.org/10.1016/S1381-1169(99)00127-2).

[35] W. Chen, G. Zhao, Q. Xue, L. Chen, Y. Lu, High carbon-resistance Ni/CeAlO₃-Al₂O₃ catalyst for CH₄/CO₂ reforming, *Appl. Catal. B* 136–137 (2013) 260–268, <https://doi.org/10.1016/j.apcatb.2013.01.044>.

[36] I. Luisetto, S. Tuti, C. Battocchio, S. Lo Mastro, A. Sodo, Ni/CeO₂-Al₂O₃ catalysts for the dry reforming of methane: the effect of CeAlO₃ content and nickel crystallite size on catalytic activity and coke resistance, *Appl. Catal. A Gen.* 500 (2015) 12–22, <https://doi.org/10.1016/j.apcata.2015.05.004>.

[37] N. Laosiripojana, W. Suttisriropok, S. Assabunrungrat, Synthesis gas production from dry reforming of methane over CeO₂ doped Ni/Al₂O₃: influence of the doping ceria on the resistance toward carbon formation, *Chem. Eng. J.* 112 (2005) 13–22, <https://doi.org/10.1016/j.cej.2005.06.003>.

[38] A. Lima Da Silva, N.C. Heck, Oxide incorporation into Ni-based solid oxide fuel cell anodes for enhanced sulfur tolerance during operation on hydrogen or biogas fuels: A comprehensive thermodynamic study, *Int. J. Hydrogen Energy* 40 (2015) 2334–2353, <https://doi.org/10.1016/j.ijhydene.2014.12.037>.

[39] J.W. Yun, S.P. Yoon, J. Han, S. Park, H.S. Kim, S.W. Nam, Ceria coatings effect on H₂S poisoning of Ni/YSZ anodes for solid oxide fuel cells, *J. Electrochem. Soc.* 157 (2010) B1825, <https://doi.org/10.1149/1.3499221>.

[40] C.J. Laycock, J.Z. Staniforth, R.M. Ormerod, Biogas as a fuel for solid oxide fuel cells and synthesis gas production: effects of ceria-doping and hydrogen sulfide on the performance of nickel-based anode materials, *J. Chem. Soc. Dalton Trans.* 40 (2011) 5494–5504, <https://doi.org/10.1039/c0dt01373k>.

[41] J. Guílera, J. del Valle, A. Alarcón, J.A. Díaz, T. Andreu, Metal-oxide promoted Ni/Al₂O₃ as CO₂ methanation micro-size catalysts, *J. Co₂ Util.* 30 (2019) 11–17, <https://doi.org/10.1016/j.jcou.2019.01.003>.

[42] W. Gac, W. Zawadzki, M. Rotko, G. Slowik, M. Greluk, CO₂ methanation in the presence of Ce-promoted alumina supported nickel catalysts: H₂S deactivation studies, *Top. Catal.* (2019), <https://doi.org/10.1007/s11244-019-01148-3>.

[43] R.S. Kempegowda, N. Laosiripojana, S. Assabunrungrat, High temperature desulfurization over nano-scale high surface area ceria for application in SOFC 25 (2008) 223–230.

[44] A. Alarcón, J. Guílera, T. Andreu, J.A. Díaz, Optimization of nickel and ceria content for CO₂ methanation catalyst supported on γ-Al₂O₃ micro-spheres, *Fuel Process. Technol.* 193 (2019) 114–122, <https://doi.org/10.1016/j.fuproc.2019.05.008>.

[45] J.A. Moulijn, P.W.N.M. van Leeuwen, R.A. van Santen, Catalysis: an integrated approach to homogeneous, Heterogeneous and Industrial Catalyst (1993).

[46] J. Guílera, T. Andreu, N. Basset, T. Boeltken, F. Timm, L. Mallol, J.R. Morante, Synthetic natural gas production from biogas in a waste water treatment plant, *Renew. Energy* 146 (2020) 1301–1308, <https://doi.org/10.1016/j.renene.2019.07.044>.

[47] K.S.W. Sing, D.H. Everett, R.A.W. Haul, I. Moscou, R.S. Pierotti, J. Rouquerol, T. Siemieniewska, Reporting physisorption data for gas/solid systems with special reference to the determination of surface area and porosity, *Pure Appl. Chem.* 57 (1985) 603–619, <https://doi.org/10.1351/pac198557040603>.

[48] J.T. Richardson, J.L. Propp, Pore size effects on sintering of NiAl₂O₃ catalysts, *J. Catal.* 98 (1986) 457–467, [https://doi.org/10.1016/0021-9517\(86\)90333-7](https://doi.org/10.1016/0021-9517(86)90333-7).

[49] V.R. Sunil Joshi, Industrial Catalytic Processes for Fine and Specialty, John Fedor, 2016.

[50] R. Yang, C. Xing, C. Lv, L. Shi, N. Tsubaki, Promotional effect of La₂O₃ and CeO₂ on Ni/γ-Al₂O₃ catalysts for CO₂ reforming of CH₄, *Appl. Catal. A Gen.* 385 (2010) 92–100, <https://doi.org/10.1016/j.apcata.2010.06.050>.

[51] T.W. Hansen, A.T. Delariva, S.R. Challa, A.K. Datye, Sintering of catalytic nanoparticles: particle migration or Ostwald ripening? *Acc. Chem. Res.* 46 (2013) 1720–1730, <https://doi.org/10.1021/ar3002427>.

[52] M. Ozawa, Effect of oxygen release on the sintering of fine CeO₂ powder at low temperature, *Scr. Mater.* 50 (2004) 61–64, <https://doi.org/10.1016/j.scriptamat.2003.09.040>.

[53] J.A. Farmer, C.T. Campbell, Ceria maintains smaller metal catalyst particles by strong metal-support bonding, *Science* 329 (2010) 933–936, <https://doi.org/10.1126/science.1191778>.

[54] N. Wang, W. Qian, W. Chu, F. Wei, Crystal-plane effect of nanoscale CeO₂ on the catalytic performance of Ni/CeO₂ catalysts for methane dry reforming, *Catal. Sci. Technol.* 6 (2016) 3594–3605, <https://doi.org/10.1039/c5cy01790d>.

[55] M. Li, H. Amari, A.C. van Veen, Metal-oxide interaction enhanced CO₂ activation in methanation over ceria supported nickel nanocrystallites, *Appl. Catal. B* 239 (2018) 27–35, <https://doi.org/10.1016/j.apcatb.2018.07.074>.

[56] T. Yonezima, K. Fukushima, N. Saito, K. Nakashima, Effect of sulfur on the sintering of nickel particles, *Mater. Trans.* 57 (2016) 1374–1377, <https://doi.org/10.2320/matertrans.m2015464>.

[57] T. Kimura, T. Miyazawa, J. Nishikawa, S. Kado, K. Okumura, T. Miyao, S. Naito,

- K. Kunimori, K. Tomishige, Development of Ni catalysts for tar removal by steam gasification of biomass, *Appl. Catal. B* 68 (2006) 160–170, <https://doi.org/10.1016/j.apcatb.2006.08.007>.
- [58] D. Li, Y. Nakagawa, K. Tomishige, Development of Ni-based catalysts for steam reforming of tar derived from biomass pyrolysis, *Chinese J. Catal.* 33 (2012) 583–594, [https://doi.org/10.1016/s1872-2067\(11\)60359-8](https://doi.org/10.1016/s1872-2067(11)60359-8).
- [59] J. Paier, C. Penschke, J. Sauer, Oxygen defects and surface chemistry of ceria: quantum chemical studies compared to experiment, *Chem. Rev.* 113 (2013) 3949–3985, <https://doi.org/10.1021/cr3004949>.
- [60] F. Pan, J. Zhang, H.-L. Chen, Y.-H. Su, Y.-H. Su, W.-S. Hwang, Thermodynamic calculation among cerium, oxygen, and sulfur in liquid Iron, *Sci. Rep.* 6 (2016) 35843, <https://doi.org/10.1038/srep35843>.
- [61] NIST, NIST Database, National Institute of Standards and Technology, 2018.
- [62] Q. Pan, J. Peng, T. Sun, S. Wang, S. Wang, Insight into the reaction route of CO₂ methanation: Promotion effect of medium basic sites, *CATCOM.* 45 (2014) 74–78, <https://doi.org/10.1016/j.catcom.2013.10.034>.
- [63] P.A.U. Aldana, F. Ocampo, K. Kobl, B. Louis, F. Thibault-Starzyk, M. Daturi, P. Bazin, S. Thomas, A.C. Roger, Catalytic CO₂ valorization into CH₄ on Ni-based ceria-zirconia. Reaction mechanism by operando IR spectroscopy, *Catal. Today* 215 (2013) 201–207, <https://doi.org/10.1016/j.cattod.2013.02.019>.
- [64] H. Muroyama, Y. Tsuda, T. Asakoshi, H. Masitah, T. Okanishi, T. Matsui, K. Eguchi, Carbon dioxide methanation over Ni catalysts supported on various metal oxides, *J. Catal.* 343 (2016) 178–184, <https://doi.org/10.1016/j.jcat.2016.07.018>.
- [65] A. Westermann, B. Azambre, M.C. Bacariza, I. Graça, M.F. Ribeiro, J.M. Lopes, C. Henriques, Insight into CO₂ methanation mechanism over NIUSY zeolites: an operando IR study, *Appl. Catal. B* 174–175 (2015) 120–125, <https://doi.org/10.1016/j.apcatb.2015.02.026>.
- [66] C. Li, Y. Sakata, T. Arai, K. Domen, K. Maruya, T. Onishi, Carbon monoxide and carbon dioxide adsorption on cerium oxide studied by Fourier-transform infrared spectroscopy. Part 1. - Formation of carbonate species on dehydroxylated CeO₂ at room temperature, *Journal of the Chemical Society, Faraday Transactions 1: Physical Chemistry in Condensed Phases* 85 (1989) 929–943, <https://doi.org/10.1039/F19898500929>.
- [67] E.T. Saw, U. Oemar, M.L. Ang, H. Kus, S. Kawi, High-temperature water gas shift reaction on Ni-Cu/CeO₂ catalysts: effect of ceria nanocrystal size on carboxylate formation, *Catal. Sci. Technol.* 6 (2016) 5336–5349, <https://doi.org/10.1039/c5cy01932j>.
- [68] G.N. Vayssilov, M. Mihaylov, P.S. Petkov, K.I. Hadjiivanov, K.M. Neyman, Reassignment of the vibrational spectra of carbonates, formates, and related surface species on ceria: a combined density functional and infrared spectroscopy investigation, *J. Phys. Chem. C* 115 (2011) 23435–23454, <https://doi.org/10.1021/jp208050a>.
- [69] C. Binet, M. Daturi, J.C. Lavalley, IR study of polycrystalline ceria properties in oxidised and reduced states, *Catal. Today* 50 (1999) 207–225, [https://doi.org/10.1016/S0920-5861\(98\)00504-5](https://doi.org/10.1016/S0920-5861(98)00504-5).
- [70] P. Bera, A. Lo, A. Horne, A. Marti, Comparative in situ DRIFTS-MS study of 12CO- and 13CO-TPR on CuO/CeO₂ catalyst, *J. Phys. Chem. C* 113 (2009) 10689–10695, <https://doi.org/10.1021/jp9020504>.
- [71] S. Lee, Y.H. Lee, D.H. Moon, J.Y. Ahn, D.D. Nguyen, S.W. Chang, S. Kim, Reaction mechanism and catalytic impact of Ni/CeO₂-X catalyst for low temperature CO₂ methanation, *Ind. Eng. Chem. Res.* 58 (2019), <https://doi.org/10.1021/acs.iecr.9b00983> acs.iecr.9b00983.
- [72] S. Wang, Q. Pan, J. Peng, S. Wang, In situ FTIR spectroscopic study of the CO₂ methanation mechanism on Ni/Ce_{0.5}Zr_{0.5}O₂, *Catal. Sci. Technol.* 4 (2014) 502–509, <https://doi.org/10.1039/c3cy00868a>.

Pushing the Limits of SNG Process Intensification: High GHSV Operation at Pilot Scale

Jordi Guilera,* Tim Boeltken, Friedemann Timm, Ignasi Mallo, Andreina Alarcón, and Teresa Andreu



Cite This: *ACS Sustainable Chem. Eng.* 2020, 8, 8409–8418



Read Online

ACCESS |



Metrics & More



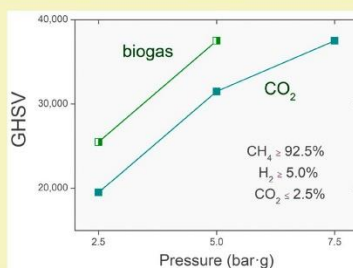
Article Recommendations



Supporting Information

ABSTRACT: Process intensification leads to a substantially smaller process technology. In this work, we present a combination of an active microsize catalyst and an effective microstructured reactor technology for CO₂ methanation. The product of the reaction is renewable synthetic natural gas which can be injected into the existing gas infrastructure. The designed process was evaluated at pilot scale (37 kW electrolyzer) in a relevant environment using sewage biogas and a CO₂ waste stream as carbon sources. The desired gas quality was obtained in a 2-step synthesis process at moderate pressure using a decreasing temperature profile ($T = 275\text{--}475\text{ }^{\circ}\text{C}$) and water sequestration. Temperature profiles were adjusted by vaporizing water, compressed air, and heating cartridges. It was observed that pressure, carbon feedstock, and GHSV had an impact on the product gas quality. At the minimum pressure ($P = 5\text{ bar-g}$) for direct gas grid injection purposes, the process worked successfully at $31\,500\text{ h}^{-1}$ using upgraded CO₂ and $37\,500\text{ h}^{-1}$ using biogas. This represents a reduction of 4 times the volume of the commercial reference. Accordingly, the limits of CO₂ methanation process intensification were clearly crossed by the combination of reactor and catalyst miniaturization.

KEYWORDS: Power-to-gas, Renewable gas, Synthetic natural gas, Microstructured reactor, Microsize catalyst



INTRODUCTION

The CO₂ methanation reaction has recently gained increasing interest in the context of Power-to-Gas to store intermittently renewable energy in the form of green methane.^{1–10} The process allows, through the Sabatier reaction, converting CO₂ emissions to a useful fuel. The reaction is exothermic and reversible. Thermodynamic equilibrium conversion is favored at low temperature, where the chemical reaction is kinetically limited.^{11–13} Accordingly, a compromise between favorable kinetics and equilibrium, as well as catalyst thermal deactivation should be considered.

The main challenge in the design of CO₂ methanation reactor is to properly control the reaction temperature. There are several approaches to overcome this issue, each with their own advantages and disadvantages. The simplest heat management approach is via adiabatic reactors. However, several methanation stages are required to achieve a reasonable conversion level, which is why this concept is not applicable for decentralized applications. Moreover, the high temperature reached in the first reactor, up to 700 °C, can lead to catalyst thermal degradation.^{14,15} Relatively easy temperature control can be obtained by using isothermal fluidized-bed and trickle-bed reactors,^{9,16} which are typically used in methanation bioreactors.^{17–20} Nonetheless, isothermal operation requires high residence times causing high reactor volumes.

Process intensification is an engineering approach that leads to a substantially smaller, cleaner, safer, and more energy-efficient process technology. Optimal temperature profiles along the catalyst bed enable smaller equipment volumes and thus intensification of the CO₂ methanation process.²¹ These temperature profiles can only be achieved by applying polytropic reactors, where the required heat to sustain the process remains in the reaction medium, and the excess of heat is taken away from the system using molten salt, water, air, or thermal oil^{22–24} as cooling media. In brief, a polytropic reactor includes heat transfer systems, while adiabatic reactors do not. Among them, cooled fixed-bed reactors benefit from high performance, simple manufacturing, and high level of maturity.^{25–31} Moioli et al.³² proposed an interesting reactor design for small-scale applications, which is divided into three zones: reaction activation, removal of excess heat, and the approach of the thermodynamic equilibrium. Nevertheless, channel geometry at the macroscopic level limits the process intensification due to undesired radial temperature profiles.

Received: April 7, 2020

Published: May 29, 2020



This aspect can be overcome by reducing the lateral dimensions to microscopic scale, i.e., below 1 mm.

In this direction, microreactor technology seems to be the most appropriate for CO₂ methanation process intensification.^{33–38} This technology can also be referred to as a milli- or microstructured reactor.^{39–41} Presently, the fabrication of microstructured reactors by means of structuring and welding technologies is already an established process.⁴² The reactors are manufactured by several stacking sequences of catalytic foils, enabling microbeds for the catalyst and cooling foils. Short distances combined with high surface to volume ratios are the key to excellent temperature control. Besides, the modular technology offers great chances for mass manufacturing.⁴³

The most suitable metric to evaluate the reactor intensification is by comparing the Gas Hourly Space Velocity (GHSV), which is defined as the time necessary to process one reactor volume of fluid. Less reactor volume is required as the GHSV increases. At one end, biological trickle-bed reactors operate at really low GHSVs of 1–10 h⁻¹, at most 100 h⁻¹. Adiabatic fixed-bed reactors can operate in the range of 2000–5000 h⁻¹.⁴⁴ Higher values can easily be achieved in cooled reactors. The DWE methanation multichannel reactor operates at 9000 h⁻¹.²⁵ At the other end, microstructured reactors can operate at very high GHSVs of 15 000–30 000 h⁻¹ as they can effectively overcome heat transfer limitations.^{30,40} Note that higher GHSV values can be easily achieved in laboratory tests compared to the aforementioned technical plants, as they typically work only in the kinetic regime.^{45,46}

Most heat and mass transfer limitations can be suppressed using microstructured reactor technology. As soon as the process is free of mass-energy transfer resistances, reaction kinetic rate limitations appear. Accordingly, a highly active methanation catalyst is especially utilized within microstructured reactors. Unfortunately, most commercial methanation catalysts cannot be directly used in microreactors because of its macroscopic dimensions ($d_p = 3–6$ mm).^{47–49} Alternatively, powder form methanation catalysts (<200 μm)³⁶ or as submillimeter-sized catalysts (300–500 μm)^{30,33,50} can be implemented. As an alternative, the active material can be deposited by a wash-coating process on the microstructure surface,³⁵ but challenges arise when maintenance catalyst exchange tasks are required. Therefore, catalyst formulations with an easy replacement procedure are preferred.

The composition of the synthetic gas produced through the CO₂ methanation reaction is of similar quality as natural gas and therefore referred to as synthetic natural gas (SNG). This gas benefits from potential injection, transportation, and distribution through the existing gas infrastructure. The technical specifications for accommodating SNG in the gas network are not yet harmonized, and they vary from country to country; namely, Wobbe index, gross calorific value, density, composition, and tolerance to impurities.^{51,52} The key parameters for the produced SNG are CH₄, H₂, and CO₂ content limits. In the present work, the current Spanish gas regulations were considered (CH₄ ≥ 92.5%, H₂ ≤ 5% and CO₂ ≤ 2.5%^{53,54}), which is quite representative of the European regulatory framework.

The combination of an active microsize catalyst⁵⁵ and an effective microstructured reactor technology⁵³ for CO₂ methanation process intensification purposes is hereby studied at an industrially relevant environment. The aim of the CO₂

methanation process is to produce an SNG that meets the legislation requirements for its injection into the existing gas infrastructure. In this sense, the limits between process intensification and SNG technical specifications are discussed in this work using sewage biogas or the waste stream of a biogas membrane upgrading plant as the CO₂ sources.

EXPERIMENTAL SECTION

The methanation pilot plant was located at a municipal sewage treatment plant (EDAR Riu Sec, Sabadell). The sewage plant has two anaerobic digesters (100 N m³·h⁻¹) and a biogas membrane upgrading plant in operation. A detailed description of the overall plant can be found in a preliminary work.⁵⁶ The main impurities of the biogas produced from the anaerobic digestion consisted of H₂S (11–31 mg/Nm³), VOCs (1–32 mg/Nm³), NH₃ (0–11 mg/Nm³), BTEX (0–9 mg/Nm³), and siloxanes (0.6–1.5 mg/Nm³).

Raw biogas was dried using a water–glycol mixture at 5 °C, cleaned through two active carbon filters (Prodeal) and compressed up to 10–15 bar. At that point, most biogas (50 N m³·h⁻¹) was directed toward the biogas upgrading unit, while some biogas (4.25 N m³·h⁻¹) was directed to the methanation unit. After the carbon filtration, the biogas was clean enough for biogas upgrading purposes (VOCs < 20 mg/Nm³, H₂S < 14 mg/Nm³, siloxanes < 1 mg/Nm³). Two additional filters were installed before the methanation pilot plant: the first filter was based on active carbon (Bioconservacion) and the second was filled with ZnO based adsorbent (ActiSorbS2, Clariant) which operates at 250 °C. Before methanation, sulfur impurities were undetectable (H₂S < 0.1 mg/Nm³) during the whole experimental campaign.

The methanation unit worked with two carbon sources alternatively. Dry, clean, and compressed biogas (46% CO₂ and 54% CH₄) and the carbon dioxide (99% CO₂ and 1% CH₄) released from the membrane upgrading unit. Biogas was delivered at medium pressure and no further pressurization was required, while the carbon dioxide released from the upgrading unit was further compressed by an air-driven piston compressor (Maximator). The carbon feed, biogas, or carbon dioxide was mixed with on-site produced hydrogen (99.5% H₂, 0.5% O₂, and 2000 ppm of H₂O) at the pressure of ≤12 bar-g. A commercial 37 kW alkaline electrolyzer (G10, Erredue) was installed to supply the stoichiometric hydrogen for CO₂ methanation (eq 1).



The methanation pilot unit, which is shown in Figure 1, was designed for a net production of 1.5 N m³·h⁻¹ of synthetic natural gas at mild pressure conditions (<10 bar-g). The process consisted of a 2-step synthesis unit, both including gas preheating, catalytic reaction,



Figure 1. Image of the methanation setup.

and water condensation. The gas preheating was carried out in microstructured heat exchangers ($45 \times 40 \times 25 \text{ mm}^3$), while the methanation reaction was conducted in microstructured reactors developed at KIT⁵³ and delivered by INERATEC. The microstructured reactors were made up by several stacking sequences of catalytic microbeds and cooling foils. Details, claims, and drawings of the microreactor for methanation invention can be found in WO2017211864A1.⁵⁷ In the present system, the reaction volume of each reactor was 100 mL, formed by 10 diffusion bonded reaction foils containing micropillars of 10 cm length. Temperature control was ensured by structured foils, which were stacked in between the reaction slits and where the cooling fluid was pumped through. The cooling channels were aligned parallel to the direction of the reactants flow. The reversal direction of the cooling fluid was essential for maintaining the temperature in the reactor as the cooling fluid was then heated more slowly.

A greater amount of heat was released in the first reactor than in the second one. In this direction, the first reactor was cooled down by vaporizing boiling water at high pressures ($P \leq 29 \text{ bar-g}$), while the second one was cooled down by compressed air. In the first reactor, the temperature of the cooling water was kept close to the vaporizing temperature at the selected pressure. Accordingly, the temperature of the water was controlled by the pressure of the cooling system, which was adjusted by auxiliary pressurized nitrogen. Reaction temperature profiles of the first reactor were controlled by two control loops, a first one that adjusted the total water flow and a second one that directed the water flow to the initial or latest zone of the reactor. In contrast, the temperature profile of the second reactor was controlled only by the total amount of the supplied air. Besides the cooling system, heating cartridges were installed in four independent zones to enable a well-controlled start-up, shutdown, catalyst reduction, and even the modification of the temperature profile along the reactor axis.⁵⁴ Both reactors presented identical external dimensions ($295 \times 150 \times 335 \text{ mm}^3$). Each one was placed in an aluminum box and surrounded by insulation material (Liapor sand) to avoid heat losses to the environment. In order to follow the catalytic process, temperature was monitored along the length of each reactor. A total of 10 thermocouples were placed in the first reactor and 5 thermocouples in the second one. An overpressure of $\Delta P \geq 0.75 \text{ bar}$ was applied in the supply of carbon dioxide and hydrogen to overcome the pressure drop through the entire process. With respect to the pressure drop through each catalyst bed, $0.1\text{--}0.4 \text{ bar}\cdot\text{m}^{-1}$ is expected in similar micro packed-bed reactors.⁵⁸

The CO_2 methanation catalyst used in this work was composed by 25% of Ni, 20% of CeO_2 , and 55% of $\gamma\text{-Al}_2\text{O}_3$ (wt). Catalyst design and formulation were optimized at the lab scale.⁵⁵ The catalyst was prepared by the conventional wet impregnation method. During the catalyst synthesis, nitrate precursors (98% nickel(II) nitrate hexahydrate and 99% cerium(III) nitrate hexahydrate, Alfa Aesar) were first dissolved in water. Then, alumina microspheres ($d_p = 450\text{--}500 \mu\text{m}$, Saint-Gobain Norpro) were added to the precursor mixture. The aqueous solvent was evaporated in a rotary vacuum evaporator at $85 \text{ }^\circ\text{C}$ and $P = 0.8 \text{ bar}$ under slow stirring. The catalyst was calcined at $450 \text{ }^\circ\text{C}$ for 30 min (heating ramp $1 \text{ }^\circ\text{C}\cdot\text{min}^{-1}$). 50 g of catalyst were prepared per batch for its implementation at the pilot scale. Detailed material characterization was presented in earlier works.^{50,55} The first reactor was filled with 45 g of catalyst, and the second reactor with 60 g of catalyst ($400\text{--}500 \mu\text{m}$), diluted with 75 and 50 g of silicon carbide ($300\text{--}400 \mu\text{m}$), respectively. Dilution ratio ($m_{\text{SiC}}/m_{\text{catalyst}}$) was 1.67 in the first reactor and 0.83 in the second reactor. The amount of loaded catalyst was adjusted according to previous experimentation at KIT laboratory facilities. Details of the preliminary experiments can be found in the Supporting Information (SI) Preliminary experiments.

Before experimentation, the catalyst was reduced in situ with diluted hydrogen (5% H_2/Ar , Linde). The activation procedure was started by a heating ramp ($0.02 \text{ }^\circ\text{C}\cdot\text{s}^{-1}$, $800 \text{ NL}\cdot\text{h}^{-1}$) up to $480 \text{ }^\circ\text{C}$. Afterward, the temperature was kept constant for 3 h ($1200 \text{ NL}\cdot\text{h}^{-1}$) and was then decreased to $320 \text{ }^\circ\text{C}$ ($0.10 \text{ }^\circ\text{C}\cdot\text{s}^{-1}$, $800 \text{ NL}\cdot\text{h}^{-1}$). The reduction process lasted about 10 h. During catalyst activation, the

pressure was set at $P = 5 \text{ bar-g}$, and the total gas consumption was about 9000 NL.

The experimental campaign lasted 6 months, June to November 2019. All the experiments presented in this study were performed using the same catalyst load. A total of 2000 h of experimentation were carried out. Catalyst deactivation could be expressed by a displacement of the position of maximum temperature toward the reactor outlet or by a decrease of the CH_4 content at the reactor outlet.⁵⁹ None of these experimental evidences of catalyst deactivation were observed during this experimental campaign. Besides, no relevant changes in the elemental composition were observed between the fresh and the spent catalyst (SI post-mortem analysis of catalyst composition). Thus, catalyst deactivation was not considered during the results hereby presented.

CO_2 methanation reaction gases were analyzed by an online gas microchromatograph (490 Agilent Technologies), consisting of a dual channel cabinet including a 10 m MSSA plot column (molecular sieve 5 A) with Ar as carrier gas and a 10 m Poraplot-U column with He as carrier gas. A multiport valve was integrated for gas sampling after the first reactor and the second one. Analytic results of the inlet and outlet gas were confirmed by external gas analysis (Ingeniería Analítica S.L.).

Experiments were carried out by feeding the stoichiometric H_2/CO_2 molar ratio = 4 of Sabatier reaction (eq 1). GHSV was calculated as the ratio of inlet flow rate of reactants ($\text{CO}_2 + \text{H}_2$) in standard conditions to the total reactor volume (eq 2). The methane introduced at the inlet when biogas was used was not considered for GHSV calculations. Experiments were carried out in the GHSV range of $19\ 442\text{--}37\ 500 \text{ h}^{-1}$ by varying the inlet gas flow rate.

$$\text{GHSV} = \frac{F_{\text{reactants at the inlet}}}{V_{\text{reactor},1} + V_{\text{reactor},2}} \quad (2)$$

RESULTS

CO_2 Methanation. CO_2 methanation was conducted in a 2-step reaction process using a stoichiometric mixture of $\text{H}_2/\text{CO}_2 = 4$. As displayed in Figure 2, the desired composition ($\text{CH}_4 \geq 92.5\%$) was obtained after 8–30 min from the CO_2 methanation process start-up. The required time to achieve the steady-state conditions was related to the initial conditions of the methanation reactors. The fastest start-up was achieved by setting the temperature of both reactors already at the optimum temperature profile by means of the internal heating

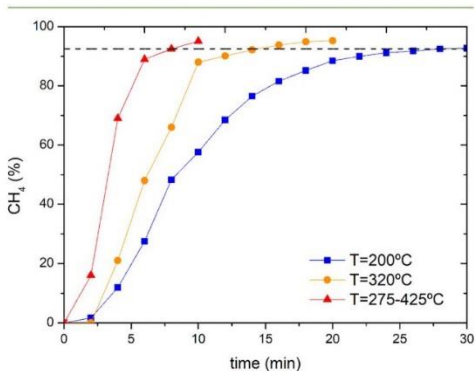


Figure 2. Representative example of CH_4 content at the process outlet along time during plant start-up. $\text{GHSV} = 19\ 442 \text{ h}^{-1}$ and $P = 5 \text{ bar-g}$. $T = 200 \text{ }^\circ\text{C}$ (isothermally), $T = 320 \text{ }^\circ\text{C}$ (isothermally), $T = 275\text{--}425 \text{ }^\circ\text{C}$ (temperature profile); reactor 1 $T = 425, 400, 340, 325 \text{ }^\circ\text{C}$; reactor 2 $T = 375, 325, 300, 275 \text{ }^\circ\text{C}$.

cartridges. In that case, the desired composition and thus successful reaction start-up was achieved in just 8 min. Under those initial conditions, carbon dioxide and hydrogen was fed to the system, heat from the exothermic reaction was released, and temperature was progressively increased. At that point, the heating cartridges of the first reactor were switched-off, and the temperature was controlled by the pressurized water. In the second reactor, the heating cartridges maintained the temperature of the initial zone of the reactor at 375 °C. As soon as the optimum temperature profiles were reached, steady state conditions were maintained. Alternatively, the process start-up was slower when the reactors were kept at constant temperature ($T = 200$ °C or $T = 320$ °C), and the lower the temperature, the more time-consuming the process. In conclusion, a fast CO₂ methanation start-up can be achieved by the present reactor configuration that allows us to keep the reactors at the optimal temperature profile using heating cartridges. An alternative strategy of fast heating through thermal cartridges was avoided to minimize thermal stress within catalyst particles.⁶⁰

Fast start-up of the overall CO₂ methanation process is relevant for managing the continuous penetration of renewable intermittent power sources; such as photovoltaics and eolics.⁶¹ Comparison with competing technologies is difficult as experimental results on CO₂ methanation start-up procedures at full-scale pilot plant are scarce, and most information is based on mathematical approaches.^{62,63} In any case, the flexibility of the Power-to-Gas to overcome renewable power surpluses is essentially provided by the electrical response of the electrolyzer.⁶⁴ In general, an electrolyzer has a response time of minutes, while the pumped hydropower is in seconds, and the electrochemical batteries are in the millisecond range.⁶⁵

During steady-state operation, both reactors operated nonisothermally in decreasing temperature profile from the beginning to the end of the reaction volume. Temperature was always limited to $T \leq 500$ °C to avoid reaction runaway, catalyst sintering, and to preserve reactor integrity. The temperature profiles were adjusted using (i) vaporizing pressurized water for cooling the first reactor ($P = 15$ bar), (ii) compressed air for cooling the latest zone of the second reactor ($P = 6$ bar), and (iii) heating cartridges for reaction ignition in the second reactor. As an illustrative example, Figure 3 shows the temperature profiles ($T = 475$ –275 °C) of both reactors at 5 bar-g at full plant capacity. The first reactor always operated at higher temperatures to favor reaction kinetics ($T \geq 400$ °C), whereas the second reactor operated at lower temperatures ($T \leq 375$ °C) to achieve a suitable gas quality for the injection into the gas grid.

As mentioned, the temperature profile of the first reactor was adjusted by the volume flow and the pressure of water. The profile of the first reactor was impacted by the GHSV. Figure 4 shows that higher temperatures were reached by increasing the GHSV. At high gas flow rates, higher amounts of CO₂ moles were converted to CH₄. Consequently, more heat was released from the reaction (-165 kJ·mol⁻¹). The GHSV limits of the process are caused by two effects: (1) the capacity of the microstructured reactor to take away the heat from the reaction microchannels, and (2) the capacity of the catalyst to carry out the reaction at low contact times. In contrast, the temperature of the second reactor was kept constant in all experimental conditions.

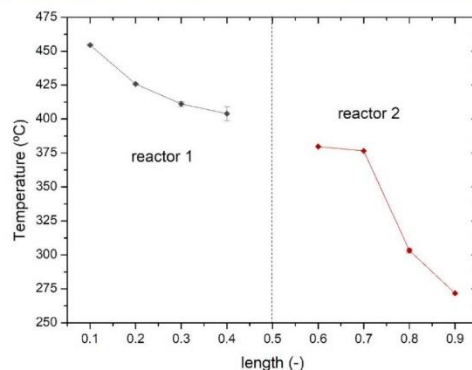


Figure 3. Temperature profile along the reactors during CO₂ methanation at GHSV = 37 500 h⁻¹ and $P = 5$ bar-g.

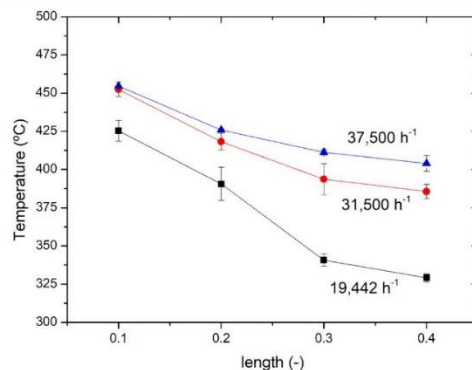


Figure 4. Temperature profiles of the first reactor on CO₂ methanation at different GHSV values and $P = 5$ bar-g.

The experimental campaign was focused on the evaluation of both GHSV and pressure effects on the product gas composition. Detailed experimental data can be found in the SI Detailed experimental data. Figure 5 presents the effect of the pressure on the gas composition after each reactor. As can be seen, pressure has a severe impact on product composition. After the first methanation stage, CH₄ composition ranged between 47% and 71%. After the first reactor, the CH₄ content was far from the desired gas quality for grid injection purposes, regardless of the applied pressure. Therefore, the use of a second reactor stage was necessary to meet the legislation requirements at mild pressure conditions. After the second methanation stage, the CH₄ content increased to 79–95%. The rest of the mixture consisted of unreacted CO₂ (0.3–3.8%) and H₂ (4.5–17.3%). Selectivity to CH₄ was 100% in all experiments. Those runs also revealed that a pressure of ≥ 7 bar-g was necessary to satisfy gas grid requirements using a highly concentrated industrial CO₂ stream. Very low pressures (≤ 3 bar-g) were clearly negative for process intensification.

These results highlight that pressure favors both kinetics (reactor 1) and equilibrium conversion (reactor 2) of the CO₂ methanation reaction. In summary, it was proven that the

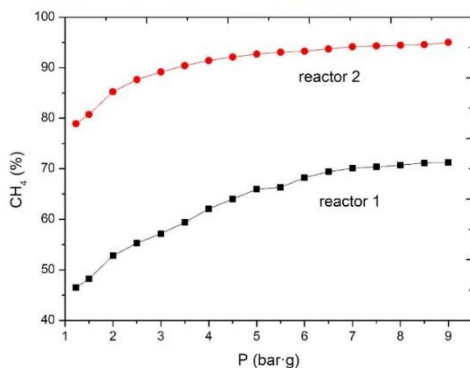


Figure 5. CH₄ content as a function of the pressure during CO₂ methanation at GHSV = 37 500 h⁻¹.

desired gas quality can be obtained at the maximum plant capacity (GHSV = 37 500 h⁻¹), with a pressure of 7 bar-g. However, as the operation pressure rises, investment and operational costs increase as the CO₂ stream from the biogas membrane permeation are typically delivered at low pressures. In this aspect, process intensification cannot be exclusively related to miniaturization of equipment size. Transformation of traditional chemical reactors to advanced microstructured reactors should also lead to more energy-efficient processes.⁶⁶ With this objective, the process pressure should be kept to the lowest value by adjusting the process GHSV at zero energy cost. Interestingly, the high dependence of the pressure and the process behavior suggest that this parameter can be adjusted during operation to the needs; for instance, if catalyst activity declines after long-time operation.

Following this approach, the next series of experiments were performed at 5 bar-g and varying GHSV. This pressure was selected as the minimum process pressure for gas grid injection into the distribution grid ($P \geq 4$ bar-g). Figure 6 highlights the influence of the GHSV on the product gas composition of the first reaction stage. A high GHSV decreases the CH₄ content

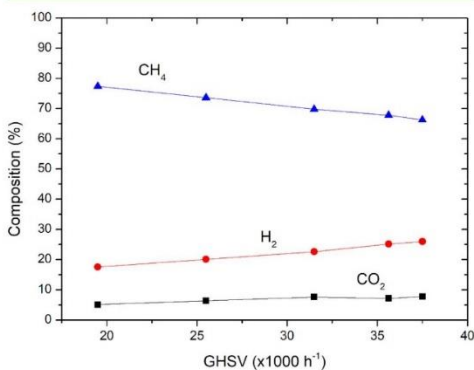


Figure 6. Gas composition after the first CO₂ methanation stage at P = 5 bar-g.

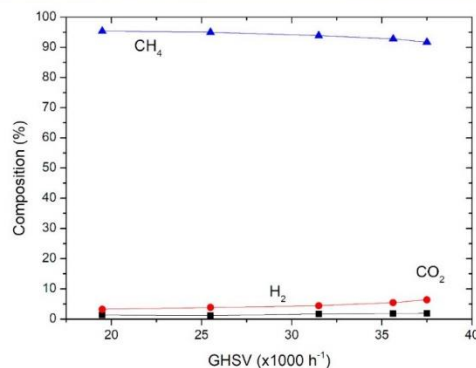


Figure 7. Gas composition after the second CO₂ methanation stage at P = 5 bar-g.

to 66%, and lowering the GHSV increases the CH₄ content to a maximum of 77%. Figure 7 displays the composition after the second reactor. In this case, CH₄ values reached 92–95%. At 5 bar-g, gas quality requirements (CH₄ = 93.85%, H₂ = 4.44% and CO₂ = 1.71%) were met at GHSV ≤ 31 500 h⁻¹. Under these conditions, the outlet composition of the first reactor was ≥69.79% CH₄, ≤22.61% H₂, and ≤7.61% CO₂. Note that this GHSV is still 6 times higher than commercial processes using a multitubular reactor.²⁵ In conclusion, the overall performance of the combination of the microsize catalyst and the microstructured reactor technology is superior over conventional catalysts and reactors. Alternatively, these requirements can also be achieved at lower GHSV and lower pressure, or else, at higher GHSV and higher pressure. Specifically, the desired composition was obtained using GHSV ≤ 19 500 h⁻¹ at 2.5 bar-g and GHSV ≥ 37 500 h⁻¹ at 7.5 bar-g (see SI Detailed experimental data).

Biogas Methanation. Alternatively to the use of pure CO₂, biogas is an interesting carbon feedstream for the production of synthetic natural gas as the main byproduct of biogas, CH₄, matches the reaction product. In this sense, any additional process unit dealing with CO₂ capture or upgrading can be avoided. In the present case, a sewage biogas stream with 46% CO₂ and 54% CH₄ was used for methanation. As in the previous section, a series of experiments were carried out using different GHSV by adjusting the gas flow rates. Figure 8 shows that more pronounced temperature profiles were obtained at low flow rates. Using biogas as feedstock at 37 500 h⁻¹, the highest temperature was not obtained at the beginning of the reactor. Thus, the optimum temperature profile was not obtained at full capacity even when electrical preheaters were used at the initial reactor zone. This is due to low contact times between gas and catalyst at the first part of the reactor resulting in higher amounts of unreacted CO₂ and CH₄ reaching the second part of the reactor. These findings indicate that the amount of loaded catalyst in the first reactor should be adjusted to the carbon source (membrane permeate or biogas) in future works or using additional gas preheating power. The difference in the temperature profile behavior between methanation of upgraded CO₂ and biogas is a consequence of the heat adsorption by the inert CH₄ present in the biogas.

Table 1. Summary of Selected Process Intensification Indicators^b

		F_m (Nm ³ ·h ⁻¹)	GHSV (h ⁻¹)	CH ₄ (%)	heat removed (kW)	specific heat removal (kW·m ⁻³)
CO ₂	reactor 1	6.30	63 000 ^a	69.79	-2.66	-180
	reactor 2	1.76	17 533 ^a	93.85	-0.33	-22
	global		31 500		-2.99	-202
biogas	reactor 1	10.29	75 000 ^a	72.66	-2.88	-194
	reactor 2	4.77	19 857 ^a	93.48	-0.61	-41
	global		37 500		-3.49	-235

^aPartial GHSV values of each reactor. ^bReactor 1 = 50 mL catalyst, reactor 2 = 67 mL catalyst.

driven by a reduction of the process complexity using a single-stage methanation unit.⁴⁰ Within this alternative strategy, lower GHSV values are necessary, although they operate at higher pressure; otherwise, the gas quality does not meet the grid injection requirements.^{39,67}

In the present case, the potential gas injection point was set at $P = 3$ bar-g, which is representative of the gas distribution grid. Therefore, no further compression of the produced gas would be required for injection purposes as the plant operates at 5 bar-g. Under these conditions, only 0.37% of the energy delivered in the final product is lost during compression. In the case of biogas methanation, energy consumption is proportionally increased to 0.56%, because of compression of the CH₄ already present in the biogas. Energy and economic considerations for the compression unit can be found in the SI Compression costs. Note that hydrogen compression was not considered at it is already delivered at high pressure by the electrolyzer without the need for a compressor. Accordingly, the proposed CO₂ methanation process benefits from operating close to the pressure of the injection point, in terms of energy efficiency. With respect to the costs, the impact of carbon source compression is estimated to <1% of the overall process (electrolysis and methanation).² Thus, the reduction of the process pressure is positive for the energy efficiency of the process, while it is not a key factor for the economics of SNG.

With regard to the heat transfer, the first reactor removed -2.66–2.88 kW by vaporizing boiling water at $P = 15$ bar-g. The temperature of the cooling water increased from 50 °C at the inlet to about 325 °C at the vapor outlet. The heat removed from the second reactor was much lower -0.33–0.61 kW. In this case, compressed air at 50 °C was used for cooling in this device. Considering the whole reactor dimensions, heat exchange is in the range of 180–194 kW·m⁻³ in the first and 22–41 kW·m⁻³ in the second reactor. Cooling requirements in the case of biogas were higher due to the cooling of the methane coming from the biogas. A minor disadvantage of using biogas instead of pure CO₂ is the higher amount of gas to be compressed, preheated, and cooled. However, the biogas methanation process benefits from the much higher amount of SNG produced; in the present case, 2.5 higher (3.44 versus 1.35 N m³/h).

As a representative example, the process proposed in this work would be able to convert all the carbon dioxide coming from the current anaerobic digesters of EDAR Riu Sec plant, which processes the municipal wastewater from 200 000 equivalent inhabitants, in 0.54 m³ of reaction volume. Therefore, the process intensification by catalyst and reactor miniaturization strategy for decentralized Power-to-Gas systems seems plausible in future plants. Nevertheless, the SNG plant designer must consider the cost when selecting the appropriate reactor technology. At present, mass production of

microstructured reactor technology and microsize catalyst is feasible and especially the reactor technology is competitive to conventional reactor technology. Last but not least, legislation is required for the implementation of commercial projects for CO₂ utilization. Unfortunately, heat management was not considered in the present work. Thermal integration of the 2-step methanation process (preheating, reactor cooling, and water condensation) would be beneficial in terms of overall energy efficiency. Finally, integration of the heat released by the methanation process with other units seems necessary to relevantly improve the overall energy efficiency of the SNG process.^{68–70}

CONCLUSIONS

In the present work, a 2-stage SNG production process was evaluated at pilot scale in an industrial environment. The combination of microsize catalysts and microstructured reactor technology were explored for process intensification. Optimal reaction conditions are achieved using a continuously decreasing temperature profile ($T = 275$ – 475 °C) under patented coflow conditions. At these conditions, gas quality requirements for grid injection can be successfully achieved after the second methanation step ($\geq 92.5\%$ CH₄, $\leq 5\%$ H₂, and $\leq 2.5\%$ CO₂). Pressure, GHSV, and carbon feedstock have a relevant impact on product gas composition. At 5 bar-g, the proposed process can operate at overall GHSV values as high as 31 500 h⁻¹ using almost pure CO₂ and 37 500 h⁻¹ using biogas as the carbon source. Therefore, methanation of biogas is beneficial in terms of process intensification as lower reactor volume is required. To the best of our knowledge, successful operation at these extremely low residence times at a technical scale with a two-stage microreactor systems has not been previously reported. The intensification of the process by the combination of microstructured reactor technology, microsize catalysts, and optimized process conditions was successfully achieved.

ASSOCIATED CONTENT

Supporting Information

The Supporting Information is available free of charge at <https://pubs.acs.org/doi/10.1021/acssuschemeng.0c02642>.

Detailed information on the laboratory CO₂ methanation experiments to adjust the amount of catalyst mass (section 1, Preliminary experiments, Figure S1, Table S1); detailed experimental data on the evaluation of GHSV, pressure, and gas composition of the experimental campaign (section 2, Detailed experimental data, Tables S2–S9); elemental analysis of the fresh and spent catalyst (section 3, Post-mortem analysis of catalyst composition, Tables S10); and energy and economic

considerations for CO₂ and biogas compression (section 4, Compression costs, Tables S11–S13) (PDF)

AUTHOR INFORMATION

Corresponding Author

Jordi Guilera – Catalonia Institute for Energy Research (IREC), 08930 Sant Adrià de Besòs, Spain; orcid.org/0000-0002-7184-6404; Email: jguilera@irec.cat

Authors

Tim Boeltken – INERATEC GmbH, 76187 Karlsruhe, Germany

Friedemann Timm – INERATEC GmbH, 76187 Karlsruhe, Germany

Ignasi Mallol – Naturgy, 08003 Barcelona, Spain

Andreina Alarcón – Catalonia Institute for Energy Research (IREC), 08930 Sant Adrià de Besòs, Spain; Escuela Superior Politécnica del Litoral, ESPOL, Facultad de Ingeniería en Ciencias de la Tierra, Guayaquil EC090112, Ecuador

Teresa Andreu – Catalonia Institute for Energy Research (IREC), 08930 Sant Adrià de Besòs, Spain; orcid.org/0000-0002-2804-4545

Complete contact information is available at:

<https://pubs.acs.org/10.1021/acssuschemeng.0c02642>

Notes

The authors declare no competing financial interest.

ACKNOWLEDGMENTS

The authors acknowledge the support of this work by the CoSin project (COMRD115-1-003) of the RIS3CAT Energy Community, which has been cofounded by ACCIO and the European Regional Development Fund under the FEDER Operational Program of Catalonia 2014-2020. Preliminary experiments were supported by LLAV-2018-00066 project, which has been cofinanced by the EU through FEDER funds and with the support of the Department of Business and Knowledge of the Generalitat de Catalunya. We thank the water treatment operator Ajuntament de Sabadell and Companyia d'Aigües de Sabadell (CASSA) for giving us the space and the biogas for the realization of this project. We are also thankful for the partnership of Cetaqua, especially Núria Basset, Adriana Romero, and Paula Gómez, for the supply of the carbon dioxide stream to the methanation plant and their unconditional help during this project. A.A. is grateful to Escuela Superior Politécnica del Litoral (ESPOL) for the support during her postgraduate studies ("Walter Valdano Raffo" Program, First edition). Last but not least, we want to thank the Institute of Micro Process Engineering at Karlsruhe Institute of Technology for the scientific collaboration.

REFERENCES

- Ghaib, K.; Ben-Fares, F.-Z. Power-to-Methane: A State-of-the-Art Review. *Renewable Sustainable Energy Rev.* **2018**, *81*, 433–446.
- Guilera, J.; Ramon Morante, J.; Andreu, T. Economic Viability of SNG Production from Power and CO₂. *Energy Convers. Manage.* **2018**, *162*, 218–224.
- Thema, M.; Bauer, F.; Sterner, M. Power-to-Gas: Electrolysis and Methanation Status Review. *Renewable Sustainable Energy Rev.* **2019**, *112*, 775–787.
- Bassano, C.; Deiana, P.; Lietti, L.; Visconti, C. G. P2G Movable Modular Plant Operation on Synthetic Methane Production from CO₂ and Hydrogen from Renewables Sources. *Fuel* **2019**, *253*, 1071–1079.
- Gutiérrez-Martín, F.; Rodríguez-Antón, L. M. Power-to-SNG Technologies by Hydrogenation of CO₂ and Biomass Resources: A Comparative Chemical Engineering Process Analysis. *Int. J. Hydrogen Energy* **2019**, *44*, 12544.
- Blanco, H.; Nijs, W.; Ruf, J.; Faaij, A. Potential of Power-to-Methane in the EU Energy Transition to a Low Carbon System Using Cost Optimization. *Appl. Energy* **2018**, *232*, 323–340.
- Meylan, F. D.; Piguet, F.-P.; Erkman, S. Power-to-Gas through CO₂ Methanation: Assessment of the Carbon Balance Regarding EU Directives. *J. Energy Storage* **2017**, *11*, 16–24.
- Galadima, A.; Muraza, O. Catalytic Thermal Conversion of CO₂ into Fuels: Perspective and Challenges. *Renewable Sustainable Energy Rev.* **2019**, *115*, 109333.
- Witte, J.; Calbry-Muzzyka, A.; Wieseler, T.; Hottinger, P.; Biollaz, S. M. A.; Schildhauer, T. J. Demonstrating Direct Methanation of Real Biogas in a Fluidised Bed Reactor. *Appl. Energy* **2019**, *240*, 359–371.
- Peters, R.; Baltruweit, M.; Grube, T.; Samsun, R. C.; Stolten, D. A Techno Economic Analysis of the Power to Gas Route. *J. CO₂ Util.* **2019**, *34*, 616–634.
- Champon, L.; Bengaouer, A.; Chaise, A.; Thomas, S.; Roger, A.-C. Carbon Dioxide Methanation Kinetic Model on a Commercial Ni/Al₂O₃ Catalyst. *J. CO₂ Util.* **2019**, *34*, 256–265.
- Koschany, F.; Schlereth, D.; Hinrichsen, O. On the Kinetics of the Methanation of Carbon Dioxide on Coprecipitated NiAl(O)_x. *Appl. Catal., B* **2016**, *181*, 504–516.
- Gao, J.; Wang, Y.; Ping, Y.; Hu, D.; Xu, G.; Gu, F.; Su, F. A Thermodynamic Analysis of Methanation Reactions of Carbon Oxides for the Production of Synthetic Natural Gas. *RSC Adv.* **2012**, *2* (6), 2358–2368.
- Nguyen, T. T. M.; Wissing, L.; Skjøth-Rasmussen, M. S. High Temperature Methanation: Catalyst Considerations. *Catal. Today* **2013**, *215*, 233–238.
- Nguyen, T. Topsoe's Synthesis Technology for SNG with Focus on Methanation in General and BioSNG in Particular. In *Conference Proceedings 1st International Conference on Renewable Energy Gas Technology*; 2014; pp 51–54. <https://regatec.org/home/conference-proceedings/> (Accessed 13 May 2020).
- Martin, J. W. Liquid-Phase Methanation/Shift Process Development—Final Technical Report; 1982 DOI: 10.2172/5276671.
- Burkhardt, M.; Koschack, T.; Busch, G. Biocatalytic Methanation of Hydrogen and Carbon Dioxide in an Anaerobic Three-Phase System. *Bioresour. Technol.* **2015**, *178*, 330–333.
- Strübing, D.; Huber, B.; Leubuh, M.; Drewes, J. E.; Koch, K. High Performance Biological Methanation in a Thermophilic Anaerobic Trickle Bed Reactor. *Bioresour. Technol.* **2017**, *245*, 1176–1183.
- Alitalo, A.; Niskanen, M.; Aura, E. Biocatalytic Methanation of Hydrogen and Carbon Dioxide in a Fixed Bed Bioreactor. *Bioresour. Technol.* **2015**, *196*, 600–605.
- Ullrich, T.; Lemmer, A. Performance Enhancement of Biological Methanation with Trickle Bed Reactors by Liquid Flow Modulation. *GCB Bioenergy* **2019**, *11* (1), 63–71.
- Reay, D.; Ramshaw, C.; Harvey, A. *Process Intensification: Engineering for Efficiency, Sustainability and Flexibility*; Butterworth-Heinemann, 2013 DOI: 10.1016/C2012-0-00253-0.
- Coker, A. K. *Modeling of Chemical Kinetics and Reactor Design*; Gulf Professional Publishing, 2001.
- Neubert, M.; Widzowski, J.; Rönsch, S.; Treiber, P.; Dillig, M.; Karl, J. Simulation-Based Evaluation of a Two-Stage Small-Scale Methanation Unit for Decentralized Applications. *Energy Fuels* **2017**, *31* (2), 2076–2086.
- Currie, R.; Mottaghi-Tabar, S.; Zhuang, Y.; Simakov, D. S. A. Design of an Air-Cooled Sabatier Reactor for Thermocatalytic Hydrogenation of CO₂: Experimental Proof-of-Concept and Model-Based Feasibility Analysis. *Ind. Eng. Chem. Res.* **2019**, *58* (29), 12964–12980.

- (25) MAN Energy Solutions SE. Methanation Reactors [https://dwe.man-es.com/chemical-reactors/tubular-reactors-with-air-oil-boiling-and-pressure-water-cooling/methanation-reactors-\(sng\)](https://dwe.man-es.com/chemical-reactors/tubular-reactors-with-air-oil-boiling-and-pressure-water-cooling/methanation-reactors-(sng)). (Accessed 13 May 2020).
- (26) Neubert, M.; Hauser, A.; Pourhossein, B.; Dillig, M.; Karl, J. Experimental Evaluation of a Heat Pipe Cooled Structured Reactor as Part of a Two-Stage Catalytic Methanation Process in Power-to-Gas Applications. *Appl. Energy* **2018**, *229*, 289–298.
- (27) Schlereth, D.; Hinrichsen, O. A Fixed-Bed Reactor Modeling Study on the Methanation of CO₂. *Chem. Eng. Res. Des.* **2014**, *92* (4), 702–712.
- (28) Alarcón, A.; Guílera, J.; Andreu, T. CO₂ Conversion to Synthetic Natural Gas: Reactor Design over Ni–Ce/Al₂O₃ Catalyst. *Chem. Eng. Res. Des.* **2018**, *140*, 155.
- (29) Martínez Molina, M.; Kern, C.; Jess, A. Catalytic Hydrogenation of Carbon Dioxide to Methane in Wall-Cooled Fixed-Bed Reactors. *Chem. Eng. Technol.* **2016**, *39* (12), 2404–2415.
- (30) Ducamp, J.; Bengaouer, A.; Baurens, P. Modelling and Experimental Validation of a CO₂Methanation Annular Cooled Fixed-Bed Reactor Exchanger. *Can. J. Chem. Eng.* **2017**, *95* (2), 241–252.
- (31) Kiewidt, L.; Thöming, J. Predicting Optimal Temperature Profiles in Single-Stage Fixed-Bed Reactors for CO₂-Methanation. *Chem. Eng. Sci.* **2015**, *132*, 59–71.
- (32) Moioi, E.; Gallandat, N.; Züttel, A. Model Based Determination of the Optimal Reactor Concept for Sabatier Reaction in Small-Scale Applications over Ru/Al₂O₃. *Chem. Eng. J.* **2019**, *375*, 121954.
- (33) Belimov, M.; Metzger, D.; Pfeifer, P. On the Temperature Control in a Microstructured Packed Bed Reactor for Methanation of CO/CO₂Mixtures. *AIChE J.* **2017**, *63* (1), 120–129.
- (34) Dittmeyer, R.; Boeltken, T.; Piernartini, P.; Selinsek, M.; Loewert, M.; Dallmann, F.; Kreuder, H.; Cholewa, M.; Wunsch, A.; Belimov, M.; et al. Micro and Micro Membrane Reactors for Advanced Applications in Chemical Energy Conversion. *Curr. Opin. Chem. Eng.* **2017**, *17*, 108–125.
- (35) Neuberger, S.; Pennemann, H.; Shanmugam, V.; Thiermann, R.; Zapf, R.; Gac, W.; Greluk, M.; Zawadzki, W.; Kolb, G. CO₂ Methanation in Microstructured Reactors—Catalyst Development and Process Design. *Chem. Eng. Technol.* DOI: 10.1002/ceat.201900132.
- (36) Brooks, K. P.; Hu, J.; Zhu, H.; Kee, R. J. Methanation of Carbon Dioxide by Hydrogen Reduction Using the Sabatier Process in Microchannel Reactors. *Chem. Eng. Sci.* **2007**, *62* (4), 1161–1170.
- (37) Ducamp, J. *Conception et Optimisation d'un Reacteur-Echangeur Structuré Pour l'hydrogénation Du Dioxyde de Carbone En Méthane de Synthèse Dédié à La Filière de Stockage d'énergie Électrique Renouvelable*; Université de Strasbourg, 2015. <https://tel.archives-ouvertes.fr/tel-01303724>. (Accessed 13 May 2020).
- (38) Raghu, A. K.; Kaisare, N. S. Analysis of the Autothermal Operability of the Sabatier Reaction in a Heat-Recirculating Microreactor Using CFD. *React. Chem. Eng.* **2019**, *4*, 1823.
- (39) Bengaouer, A.; Ducamp, J.; Champon, I.; Try, R. Performance Evaluation of Fixed-Bed, Millistructured, and Metallic Foam Reactor Channels for CO₂Methanation. *Can. J. Chem. Eng.* **2018**, *96* (9), 1937–1945.
- (40) Pérez, S.; Aragón, J. J.; Peciña, I.; García-Suarez, E. J. Enhanced CO₂Methanation by New Microstructured Reactor Concept and Design. *Top. Catal.* **2019**, *62*, 518.
- (41) Pérez, S.; Del Molino, E.; Barrio, V. L. Modeling and Testing of a Milli-Structured Reactor for Carbon Dioxide Methanation. *Int. J. Chem. React. Eng.* **2019**1711 DOI: 10.1515/ijcre-2018-0238
- (42) Pfeifer, P.; Piernartini, P.; Wenka, A. Microstructure Reactor for Carrying out Exothermic Heterogeneously-Catalysed Reactions with Efficient Evaporative Cooling. Google Patents 2018. <https://patents.google.com/patent/WO2017013003A1/en> (Accessed 13 May 2020).
- (43) Mills, P. L.; Quiram, D. J.; Ryley, J. F. Microreactor Technology and Process Miniaturization for Catalytic Reactions—A Perspective on Recent Developments and Emerging Technologies. *Chem. Eng. Sci.* **2007**, *62* (24), 6992–7010.
- (44) Götz, M.; Lefebvre, J.; Mörs, F.; McDaniel Koch, A.; Graf, F.; Bajohr, S.; Reimert, R.; Kolb, T. Renewable Power-to-Gas: A Technological and Economic Review. *Renewable Energy* **2016**, *85*, 1371–1390.
- (45) Abelló, S.; Berruoco, C.; Montané, D. High-Loaded Nickel–Alumina Catalyst for Direct CO₂ Hydrogenation into Synthetic Natural Gas (SNG). *Fuel* **2013**, *113* (0), 598–609.
- (46) Li, W.; Zhang, A.; Jiang, X.; Chen, C.; Liu, Z.; Song, C.; Guo, X. Low Temperature CO₂Methanation: ZIF-67-Derived Co-Based Porous Carbon Catalysts with Controlled Crystal Morphology and Size. *ACS Sustainable Chem. Eng.* **2017**, *5* (9), 7824–7831.
- (47) Golosman, E. Z.; Efremov, V. N. Industrial Catalysts for the Hydrogenation of Carbon Oxides. *Catal. Ind.* **2012**, *4* (4), 267–283.
- (48) Haldor Topsoe. SNG Methanation—Catalysts <https://www.topsoe.com/processes/sng/methanation>. (Accessed 13 May 2020).
- (49) Türks, D.; Mena, H.; Armbruster, U.; Martin, A. Methanation of CO₂ on Ni/Al₂O₃ in a Structured Fixed-Bed Reactor—A Scale-Up Study. *Catalysts* **2017**, *7* (5), 152.
- (50) Guílera, J.; del Valle, J.; Alarcón, A.; Díaz, J. A.; Andreu, T. Metal-Oxide Promoted Ni/Al₂O₃ as CO₂Methanation Micro-Size Catalysts. *J. CO₂ Util.* **2019**, *30*, 11–17.
- (51) Kreeft, G. Legislative and Regulatory Framework for Power-to-Gas in Germany, Italy and Switzerland; 2018. https://www.storeandgo.info/fileadmin/downloads/publications/Kreeft_G.J._2018_-_Legislative_and_Regulatory_Framework_for_Power-to-Gas_in_Italy_Germany_and_Switzerland.pdf (Accessed 13 May 2020).
- (52) European Commission. Impact of the Use of the Biomethane and Hydrogen Potential on Trans-European Infrastructure; 2019. https://ec.europa.eu/energy/studies/impact-use-biomethane-and-hydrogen-potential-trans-european-infrastructure_en (Accessed 13 May 2020).
- (53) BOE-A-2013–185. 2013; pp 889–892. https://www.boe.es/diario_boe/txt.php?id=BOE-A-2013-185 (Accessed 13 May 2020).
- (54) BOE-A-2018–14557; 2018. pp 102917–102950 https://www.boe.es/diario_boe/txt.php?id=BOE-A-2018-14557 Accessed 13 May 2020).
- (55) Alarcón, A.; Guílera, J.; Díaz, J. A.; Andreu, T. Optimization of Nickel and Ceria Catalyst Content for Synthetic Natural Gas Production through CO₂Methanation. *Fuel Process. Technol.* **2019**, *193*, 114–122.
- (56) Guílera, J.; Andreu, T.; Basset, N.; Boeltken, T.; Timm, F.; Mallof, I.; Morante, J. R. Synthetic Natural Gas Production from Biogas in a Waste Water Treatment Plant. *Renewable Energy* **2020**, *146*, 1301–1308.
- (57) Pfeifer, P.; Belimov, M. WO2017211864(A1) Micro-Reactor and Method Implementation for Methanation, 2017. <https://patentscope.wipo.int/search/en/detail.jsf?docId=WO2017211864> (Accessed 13 May 2020).
- (58) Knobloch, C.; Güttel, R.; Turek, T. Holdup and Pressure Drop in Micro Packed-Bed Reactors for Fischer–Tropsch Synthesis. *Chem. Ing. Tech.* **2013**, *85* (4), 455–460.
- (59) Wolf, M.; Schüller, C.; Hinrichsen, O. Sulfur Poisoning of Co-Precipitated Ni–Al Catalysts for the Methanation of CO₂. *J. CO₂ Util.* **2019**, *32*, 80–91.
- (60) Bartholomew, C. H. Mechanisms of Catalyst Deactivation. *Appl. Catal., A* **2001**, *212* (1), 17–60.
- (61) Lisbona, P.; Frate, G. F.; Bailera, M.; Desideri, U. Power-to-Gas: Analysis of Potential Decarbonization of Spanish Electrical System in Long-Term Prospective. *Energy* **2018**, *159*, 656–668.
- (62) Matthischke, S.; Roensch, S.; Güttel, R. Start-up Time and Load Range for the Methanation of Carbon Dioxide in a Fixed-Bed Recycle Reactor. *Ind. Eng. Chem. Res.* **2018**, *57* (18), 6391–6400.
- (63) Kreitz, B.; Wehinger, G. D.; Turek, T. Dynamic Simulation of the CO₂Methanation in a Micro-Structured Fixed-Bed Reactor. *Chem. Eng. Sci.* **2019**, *195*, 541–552.

(64) Mazza, A.; Bompard, E.; Chicco, G. Applications of Power to Gas Technologies in Emerging Electrical Systems. *Renewable Sustainable Energy Rev.* **2018**, *92*, 794–806.

(65) Institute, G. Which Energy Storage Technology Can Meet My Needs?, 2020. https://www.imperial.ac.uk/media/imperial-college/grantham-institute/public/publications/GICJ3998_EnergyStorage_final.pdf (Accessed 13 May 2020).

(66) Stankiewicz, A. I.; Moulijn, J. A. Process Intensification: Transforming Chemical Engineering. *Chem. Eng. Prog.* **2000**, *96* (1), 22–34. <https://www.rvo.nl/sites/default/files/2013/10/Process%20Intensification%20Transforming%20Chemical%20Engineering.pdf> (Accessed 13 May 2020).

(67) Sveinbjörnsson, D.; Münster, E. Upgrading of Biogas to Biomethane with the Addition of Hydrogen from Electrolysis; 2017 https://futuregas.dk/wp-content/uploads/2018/06/FutureGas-WP1-Deliverable-1.1.1.-Technologies-and-status-of-methanation-of-biogas-2017_Final.pdf (Accessed 13 May 2020).

(68) Luo, Y.; Wu, X.; Shi, Y.; Ghoniem, A. F.; Cai, N. Exergy Analysis of an Integrated Solid Oxide Electrolysis Cell-Methanation Reactor for Renewable Energy Storage. *Appl. Energy* **2018**, *215*, 371–383.

(69) Lorenzi, G.; Lanzini, A.; Santarelli, M.; Martin, A. Exergo-Economic Analysis of a Direct Biogas Upgrading Process to Synthetic Natural Gas via Integrated High-Temperature Electrolysis and Methanation. *Energy* **2017**, *141*, 1524–1537.

(70) Ancona, M. A.; Antonucci, V.; Branchini, L.; Catena, F.; De Pascale, A.; Di Blasi, A.; Ferraro, M.; Italiano, C.; Melino, F.; Vita, A. Thermal Integration of a High-Temperature Co-Electrolyzer and Experimental Methanator for Power-to-Gas Energy Storage System. *Energy Convers. Manage.* **2019**, *186*, 140–155.

Chapter

*Reactor design and modelling
for SNG production*

This chapter is devoted to the design of fixed-bed reactors for a cost-effective application in real environments. Currently, fixed-bed reactors represent the useful and available design for commercial large-size SNG production in P2G applications. In particular, multitubular fixed-bed heat-exchanger reactors operated under polytropic conditions are attractive to carry out CO₂ methanation process due to its cost-effective design.

The use of multitubular fixed-bed heat-exchanger reactor is particularly of interest for decentralized applications in which a low-cost reactor design is required for mid-size SNG production. In this reactor approach, the heat of the reaction is transferred from the reactive tube to a coolant. Besides, its configuration is simple, flexible and easy to scale-up. However, reaching its optimum temperature profile remains as a technological challenge since the formed high temperatures influence on both thermodynamics and kinetics of the reaction. Understanding the design aspects and reaction conditions can be essential to achieve an optimum temperature profile, and thus propose this reactor approach for mid-size SNG production (50-250 Nm³·h⁻¹).

On the other hand, biogenic carbon dioxide can be released in a very dispersed way, in contrast to large refineries. An illustrative example is biogas from small anaerobic digesters. In these, small-size SNG plants require a reduced engineering complexity of the overall process to keep the investment costs at a reasonable level. For those cases, a novel reactor design should be proposed. A free convection heat transfer to the surroundings for the reactor cooling can be a technological alternative for lowering the investment costs of the reactor and the corresponding cooling auxiliaries. This concept is based on the fact that the produced heat of the Sabatier process can be controlled by some reaction parameters and naturally released to the environment without the implementation of intensive cooling systems.

The two reactor approaches can be designed by three-dimensional (3D) mathematical models based on experimental kinetic data through computational fluid dynamics (CFD). This is a computer-based tool for simulating the behaviour of systems involving fluid flow, heat and mass transfer, chemical reactions and other phenomena. It works by solving the equations of fluid flow (in a special form) over a region of interest, with specified (known) conditions on the boundary of that region. An advantage of using 3D CFD mathematical models to design industrial-size reactors is that these can eliminate subjective experience and empiricism, and lead to better-designed, more-efficient units.

In this context, the following two works shown in this section are focused on:

- The development of a 3D CFD model based on kinetic data to simulate and optimize temperature profile of an multitubular fixed-bed reactor design for mid-scale SNG production.

- The evaluation of a novel heat-management concept based on free convection by means of 3D mathematical model to propose a new small-scale CO₂ methanation reactor design.

4.1. CO₂ conversion to synthetic natural gas: Reactor design over Ni-Ce/Al₂O₃ catalyst

In this first approach, the implementation of a nickel-ceria-alumina catalyst on a multitubular fixed-bed exchanger reactor was evaluated. The goal was to propose an optimum reactor design for industrial mid-scale synthetic natural gas production. The biogas (100 Nm³·h⁻¹, 65% CH₄) derived from two anaerobic digestors of a wastewater treatment plant was considered as the industrial representative case. With this aim, a 3D CFD model was developed using Ansys® Fluent software.

As part of reactor modelling, an experimental kinetic study was carried out over nickel-ceria-alumina catalyst to determinate the intrinsic reaction kinetics of methane formation. Experimental kinetic data was obtained at differential conditions ($X_{\text{CO}_2} \leq 15\%$) using different temperatures (473-673 K), CO₂/H₂/Ar concentrations (25-100%) and catalyst mass (0.008-0.120 g). Simple power rate expressions for forward and backward Sabatier reaction were proposed, which were able to predict successfully the reaction rates. The main kinetic parameters for forward reaction were determined by adjusting the experimental data, while for the backward reaction were calculated as from NIST equilibrium database mathematical fit.

CFD simulations carried out at a proposed base case ($T_{\text{inlet}}=573$ K, $T_{\text{wall}}=573$ K, $P=1$ atm, $\text{GHSV}=3600$ h⁻¹) evidenced that the gas mixture interacted from the very beginning of the reactor, and as a result, reactants (H₂+CO₂) were converted to the products (CH₄+H₂O). Furthermore, it was detected a non-isothermal temperature profile with temperatures up to 733 K. The higher temperature was formed on the first 5 mm of total tube length. With this temperature behaviour, the CO₂ conversion achieved was restricted to 71%.

In order to further increase CO₂ conversions, a sensitive analysis was additionally performed for reactor optimization. Among all evaluated variables, the inlet temperature, the wall temperature, the pressure, the inlet velocity and the tube inner diameter were identified as the key parameters to obtain the optimum temperature profile with highest CO₂ conversion. In particular, the formation of the maximum temperatures was identified to be significantly decreased when the internal diameter is reduced, as it can be observed in Figure 4.1.

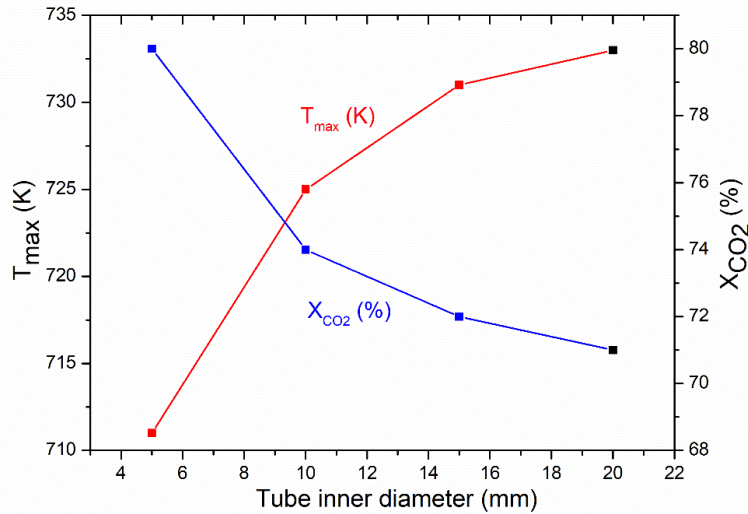


Figure 4.1. T_{max} (K) and CO_2 conversion (%) at different tube inner diameter (mm). $T_{inlet}=573$ K, $T_{wall}=573$ K, $P=1$ atm and $L=250$ mm. Black square indicates the base case.

The reactor design proposal is shown in Figure 4.2 (a-b). This was found using a reactor tube of 9.25 mm internal diameter and 250 mm length, which operate with an inlet temperature of 473 K, a lower wall temperature of 373 K, pressure of 5 atm and GHSV of $14,400\text{ h}^{-1}$. At these conditions, the temperatures formed inside of the tube reactor were lower than 673 K, and as a result, it was achieved highest CO_2 conversion ($X_{CO_2}=99\%$). According to the proposed tube reactor dimensions, a total of 1000 tubes are required for the CO_2 methanation of $100\text{ Nm}^3\cdot\text{h}^{-1}$ biogas.

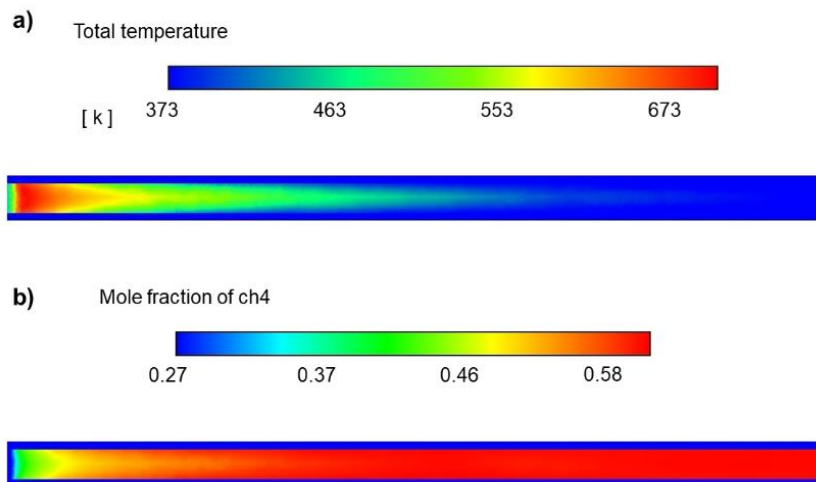


Figure 4.2. a) Temperature profile and b) CH_4 molar fraction profile as from design proposal. $T_{inlet}=473$ K, $T_{wall}=373$ K, $GHSV=14400\text{ h}^{-1}$, $P=5$ atm, $di=9.25$ mm and $L=250$ mm.

4.2. An insight into the heat management for the CO₂ methanation based on free convection

In the second approach, the final goal was to propose a low-cost reactor design with a novel heat-management approach based on the free convection for small-scale CO₂ methanation applications. With this aim, a combined study based on experimentation and CFD simulation was performed. Furthermore, the small-scale SNG production of 1 Nm³·h⁻¹ was selected as the representative case to evaluate the scale-up of proposal reactor.

In the first part of this study, a single reactor channel (inner diameter of 4.6 mm and length of 250 mm) was built and experimentally evaluated using a methanation set-up at lab-scale. The dimensions were selected to facilitate the heat transfer to the environment, as it is highly promoted when the inner diameter is reduced from 10 mm. CO₂ methanation tests to evaluate reactor channel were conducted by varying the gas flow rate in a range from of GHSV=3,039-18,235 h⁻¹ at atmospheric pressure and T_{inlet}=573 K. The optimized Ni-CeO₂-Al₂O₃ catalyst formulation was implemented as the catalytic material to carry out Sabatier reaction.

A first set of experiments revealed that higher temperatures (T_{max}=673-806 K) along the reactor were obtained at higher GHSV values (3,039-18,235 h⁻¹). As it can be observed in Figure 4.3, non-isothermal temperature profiles with CO₂ conversions between 82 and 79% were achieved by increasing GHSV. These results allowed to confirm that a simple way to control the temperature profile in a free convection heat-management reactor configuration is by adjusting the inlet gas flowrate. In such a way that the reactor can be heated up by increasing the gas flowrate and cooled down by lowering it.

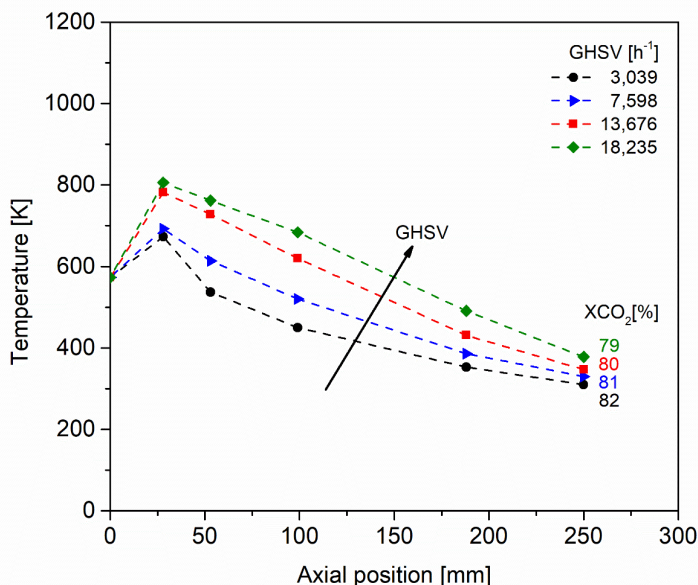


Figure 4.3. Experimental temperature profiles by varying GHSV at $P=1$ atm and $T_{inlet}=573$ K.

However, the achieved level of conversions was still too low for industrial applications, and out of the scope of our work ($\geq 90\%$). Thus, a second set of experiments, using the same reaction conditions and adjusting the temperatures by addition of external heat to the last zone of the reactor, was performed to achieve conversions close to the equilibrium (91-84%). With this experimental alternative, the most favourable conditions were obtained when the lowest temperature was higher than 573 K. Therefore, optimal conditions to achieve a CO_2 methanation based on free convection cannot be only obtained by simply adjusting the inlet flowrate.

On the basis of the experience gained during the experimentation and considering that the computational fluid dynamics (CFD) simulation is a potential tool, CFD was used to obtain the optimum reaction conditions able to achieve a higher conversion level. In the second part of this study, a 3D mathematical model to simulate Sabatier reaction on the lab-scale fixed-bed reactor design was built by means of Ansys® Fluent software. The CFD model was first validated using an experimental case and then was used to optimize through sensitive analysis the main reaction parameters (Pressure, inlet temperature, GHSV, air temperature) of the proposed reactor design.

The sensitive analysis proved that the operation of the free convection heat-management reactor configuration is feasible through a compromise between three operation parameters. A GHSV of $11,520 \text{ h}^{-1}$, an inlet temperature of 503 K, a pressure of 5 atm, and an air temperature of 298 K were found as the optimal

conditions to guarantee high CO₂ conversion without the need of external heating or cooling units. The simulation and experimental validation shown in Figure 4.4. proved the feasibility of this reactor approach. An interesting level of CO₂ conversion (93%) and a decreasing temperature profile along the reactor (T=830 to 495 K) were successfully achieved. According to the proposed reactor dimensions, 23 channels will be required to achieve the industrial small-scale production of 1 Nm³·h⁻¹ of synthetic natural gas.

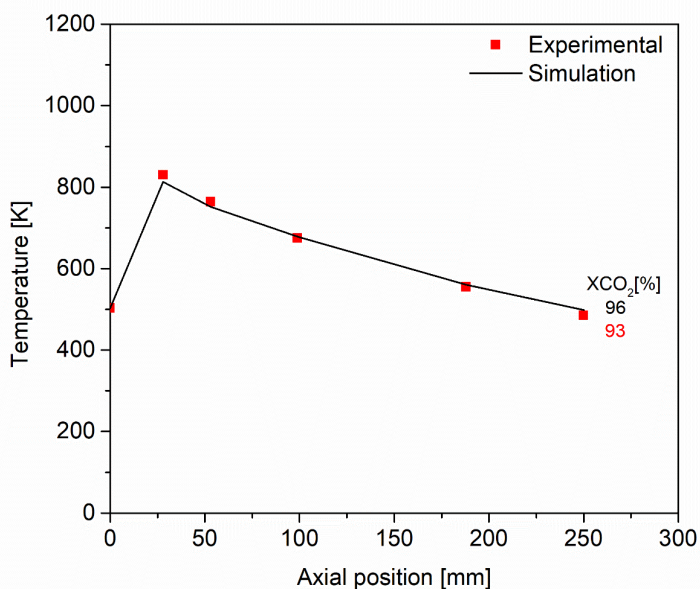


Figure 4.4. Experimental and simulation comparison of the proposed reactor conditions. GHSV=11,520 h⁻¹, T_{inlet}=503 K, T_{air}= 298 K, P=5 atm and H₂/CO₂ molar ratio=4.



Contents lists available at ScienceDirect

Chemical Engineering Research and Design

journal homepage: www.elsevier.com/locate/cherdIChemE ADVANCING
TECHNICAL
ENGINEERING
WORKFORCE

CO₂ conversion to synthetic natural gas: Reactor design over Ni–Ce/Al₂O₃ catalyst

Andreina Alarcón^{a,b}, Jordi Guilera^{a,*}, Teresa Andreu^a

^a Catalonia Institute for Energy Research (IREC), Jardins de les Dones de Negre 1, 08930 Sant Adrià de Besòs, Spain

^b Escuela Superior Politécnica del Litoral, ESPOL, Facultad de Ingeniería en Ciencias de la Tierra, Campus Gustavo Galindo Km.30.5 Vía Perimetral, P.O. Box 09-01-5863, Guayaquil, Ecuador

ARTICLE INFO

Article history:

Received 13 April 2018

Received in revised form 19

September 2018

Accepted 11 October 2018

Available online 18 October 2018

Keywords:

Power-to-Gas

CO₂ methanation

Synthetic natural gas

Reactor design

CFD model

Nickel–ceria–alumina catalyst

ABSTRACT

Within the Power-to-Gas concept, the catalytic conversion of renewable hydrogen and carbon dioxide to methane for injection to the gas grid has recently attracted much attention. In the present work, the implementation of a nickel–ceria–alumina catalyst on a multitubular reactor for CO₂ methanation was studied. The reaction kinetics were experimentally obtained and considered for a CFD model by means of Ansys® Fluent software, to evaluate the behaviour of a multitubular heat-exchange reactor. The simulations showed that most reaction occurs at the beginning of the reactor tube and the temperature raises rapidly. At the kinetic regime zone, a proper control of the temperature is required to avoid excessive hot-spots. In contrast, the final reactor volume is mainly controlled by the reaction thermodynamics. In this zone, the reaction is shifted toward products by using a cooling medium at low temperature. The effect of several design variables on the final methane yield and on the temperature profile was carried out, and finally, a reactor able to convert the CO₂ present in the biogas to synthetic natural gas is proposed. The modelling showed that the proposed reactor tube (d_i = 9 mm and L = 250 mm) should be able to obtain a high methane content (>95%), at high GHSV (14,400 h⁻¹), and keeping the hot-spots at minimum (Δ100 K). Within this reactor design approach, almost 1000 of tubes are necessary for the methanation of a medium-size biogas plant.

© 2018 Institution of Chemical Engineers. Published by Elsevier B.V. All rights reserved.

1. Introduction

The contribution of renewable energies in the electricity mix is expected to be very high in the near future. A high share of green electricity generated by unpredictable resources, such as sun and wind, into the national energy mix cannot guarantee a reliable and continuous power supply to the costumers (Garmsiri et al., 2014; Granovskii et al., 2007). Thus, the implementation of grid storage systems is required. The conversion of electrical energy into chemicals, in the form of gas, liquid or even solid, has recently induced great study and application interest as a large-scale solution for the electricity storage (Jentsch et al., 2014; Varone and Ferrari, 2015). As concerns to Power-to-Gas (PtG), the strategy relies on the transformation of the excesses of electrical energy coming from unpredictable energy sources into renewable

hydrogen through water electrolysis process (Gassner and Maréchal, 2008; Kroposki et al., 2006). At present, the hydrogen infrastructure readiness is very limited, i.e. pipelines, buffers, refuelling stations, stationary fuel cells or hydrogen-powered vehicles. A further conversion of the renewable hydrogen to methane exhibits some practical benefits. Methane is the primary component of natural gas (≈94%), together with other alkanes as ethane. Hence, renewable methane can be mixed, stored and delivered through the already existing natural gas infrastructure (Guilera et al., 2018; Schaaf et al., 2014; Götz et al., 2016).

The methane obtained through a PtG plant, referred to as synthetic natural gas, can be formed by the combination of renewable hydrogen with CO₂ as carbon source (captured from the atmosphere, biogas or flue gas) (Barbarossa et al., 2014). Among different routes, the catalytic CO₂ methanation can be a viable option for the production of renew-

* Corresponding author.

E-mail address: jguilera@irec.cat (J. Guilera).

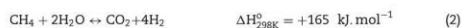
<https://doi.org/10.1016/j.cherd.2018.10.017>

0263-8762/© 2018 Institution of Chemical Engineers. Published by Elsevier B.V. All rights reserved.

able methane (Guilera et al., 2018; Götz et al., 2014). The methanation of CO₂ is a thermochemical process carried out through the Sabatier reaction (Eq. (1)) (Wang and Gong, 2011), in which CO₂ is combined with four molecules of H₂ over a suitable catalyst to form CH₄ and H₂O. This reaction is reversible, highly exothermic and it has an important decreasing volume. Therefore, according to the Le Chatelier principle, the methanation reaction is favourable at low temperature and high pressure.



At elevated temperatures, the endothermic reactions are promoted and the equilibrium is shifted toward the reactants (Eq. (2)). Besides, the reverse water gas shift is enhanced (Eq. (3)). Both endothermic reactions are undesired because they reduce the final yield of methane, the former by limiting the conversion and the latter by lowering the methane selectivity (Gao et al., 2012). From a thermodynamic point of view, the reaction should be carried out at the lowest possible temperature. Nevertheless, high reactor volumes and large amounts of catalyst are then required due to kinetic limitations at low temperatures (<573 K). To overcome those difficulties, the catalytic CO₂ methanation process requires of an active catalyst at low temperatures.



The supported catalysts composed by non-noble nickel metal, or noble ruthenium and rhodium, are the most applicable in the Sabatier reaction as the active phase (Stangeland et al., 2017; Golosman and Efmov, 2012). Among them, nickel based systems are in principle less costly. The most studied nickel-based supports are those formed by titania, silica, alumina, ceria, zirconia, lanthanum oxide or a combination of them (Abate et al., 2016; Feng et al., 2014; Zhao et al., 2012). In particular, nickel supported on ceria exhibits excellent methanation activity at low temperatures and high methane selectivity (Tada et al., 2012; Atzori et al., 2018). The activity, selectivity and effectiveness of the catalyst are also influenced by the nature and preparation method of the support, as well as the incorporation of promoting substances. The addition of promoters can enhance the initial activity and reduce its deactivation as a result of reaction hot-spots that promote sintering or formation of coke.

A proper control of the temperature on the chemical reactor is mandatory to obtain efficient production of synthetic natural gas. Industrial reactors dealing with exothermic reactions, as Sabatier, are typically adiabatic fixed-bed reactors arranged in series or parallel with intermediate cooling systems and gas recycling. Adiabatic reactors have a simple design and low cost; however, the global process requires a high complex configuration, not applicable for decentralized applications such as biogas conversion to synthetic natural gas (Rönsch et al., 2016; Chein et al., 2016).

Conversely, exothermic reactions can be performed through heat transfer systems, with the aim of maintaining the reactor temperature within a specific narrow range. This concept is often described as “isothermal fixed-bed reactor”. Simple heat transfer reactors can be constructed analogously as conventional shell and tube heat exchangers by a multitubular design (Eigenberger, 1992). In real conditions, the reaction exothermicity is so high that the reactor operates with some temperature profile. A controlled increase of the temperature inside the reactor is not necessarily negative and it can decrease the total volume of the reactor, compared to completely isothermal reactors (Belimov et al., 2017).

A suitable reactor design is the key factor to obtain an optimal temperature profile. A proper understanding of relevant design aspects is essential to optimize this profile. In the open literature, some useful mathematical models have been proposed by coupling the methanation reaction kinetics with heat and mass transport parameters. The models were based on the optimization of the reactor thermal management using commercial methanation catalysts. Numerical simulations

can be found in 1D and 2D on pseudo-homogenous models (Martínez Molina et al., 2016; Sun and Simakov, 2017), and in 2D on heterogeneous model (Ducamp et al., 2017).

In the present work, the implementation of a nickel–ceria–alumina catalyst on a multitubular heat exchange reactor is evaluated. The goal of this study is to propose a reactor with a simple design for optimal synthetic natural gas production at industrial scale. In line with some national legislations regarding gas grid injection, it was considered that the reactor outlet should contain, at least, 95% of CH₄. As a representative case, the biogas produced by two anaerobic digesters of a waste water treatment plant was considered (100 Nm³ h⁻¹, 65% CH₄). For that purpose, a kinetic study was carried out in a laboratory scale reactor over the nickel–ceria–alumina catalyst. Then, a 3D mathematical model based on computational fluid dynamics (CFD) through Ansys[®] Fluent software was developed. The influence of the design parameters on the reactor temperature profile were evaluated, and finally, a multitubular reactor is proposed for the case study.

2. Materials and methods

2.1. Catalyst

The catalyst prepared for this study was composed by 15 wt.% nickel as active phase with 10 wt.% of ceria as a promoter. Alumina was used as non-expensive support since it has a large surface area and pore volumes. The influence of the ceria content on the methane yield was previously evaluated experimentally. The ternary catalyst system 15Ni–10Ce/Al₂O₃ was facilely synthesized via one-pot, evaporation-induced, self-assembly (EISA) strategy adapted from a previous work (Camacho, 2017).

In a typical synthesis procedure, approximately 5 g of P123 Pluronic triblock copolymer ((EO)₂₀(PO)₇₀(EO)₂₀) was dissolved at room temperature in 100 mL of ethanol under vigorous stirring. Then, 15 mL of nitric acid was added, together with 15 g of aluminium isopropoxide (C₉H₂₁AlO₃), 3.71 g of nickel nitrate hexahydrate (Ni(NO₃)₂·6H₂O) and 1.26 g cerium (III) nitrate hexahydrate (Ce(NO₃)₃·6H₂O). The resulting mixture was covered with a polyethylene film, continuously stirred for 6 h until complete dissolution. Then, the mixture was placed in a digital auto-regulator water-bath at 333 K to undergo slow evaporation of the ethanol and the acid. Eventually, the obtained green xerogels were calcined slowly in air at 723 K for 5 h (heating rate 0.5 K min⁻¹).

2.2. Experimental setup

A laboratory-scale reactor was used for the kinetic experiments. The reactor consisted on a quartz tube with internal diameter of 20 mm and 250 mm length. The catalyst was placed in the middle of the reactor length, supported on quartz wool. The gases were fed by a multiple gas supply unit with four mass flow controllers for: the reacting mixture (20% CO₂–80% H₂), argon as diluting agent, H₂ for catalyst activation (5% H₂–95% Ar) and the last for micro-GC calibration purposes. The reactor was electrically heated up (473–723 K) and the furnace produced a 150 mm isothermal zone. The reaction temperature was monitored using a thermocouple placed in the middle of the catalyst bed. After reaction, the gases were flowed through a water condenser (278 K) to remove the water produced in the reaction, a volumetric flow meter to measure the decrease of flowrates, and finally, introduced to the micro-GC to determine the dry gas composition (CH₄, H₂, CO, CO₂). Typically, composition was constant after 15 min of operation.

2.3. Experimental procedure

Prior to reaction, the catalyst was loaded into the reactor and reduced in situ by flowing 170 mL min⁻¹ of 5% H₂ at 723 K for 3 h. A series of methanation reaction experiments were carried out at different temperatures (473–673 K) and CO₂/H₂ concentrations (Ar dilutions 25–100%). The total flow rate was kept constant (200 mL min⁻¹). The working pressure was atmospheric. The catalyst mass was adjusted (0.008–0.120 g) to avoid CO₂ conversions over 15% and therefore to ensure differential regime conditions. A total number of 45 kinetic experiments were carried out to cover the maximum conditions range.

Experimental reaction rates of methane formation were calculated as follows (Eq. (4)):

$$r_{CH_4, experimental} = \dot{n}_{CH_4, out} \cdot m_{cat}^{-1} \cdot \rho_{cat}^{-1} \quad (4)$$

The molar flowrate of methane at the outlet was determined by the outlet composition and flowrate (Eq. (5))

$$\dot{n}_{CH_4, out} = F_{out} \cdot C_{CH_4} \quad (5)$$

3. Reactor modelling methodology

Fig. 1 illustrates the prototype design of a multitubular fixed-bed exchanger reactor. The catalyst packaging is arranged inside the tubes, while the heat transfer medium is flowed around the tube bundle. The temperature of the cooling liquid is adjusted by an external heat exchanger. The flow regime is axial, which allows the fluid to flow through the free space between the catalyst particles, with a flow model very close to the piston type (block progression) (Ducamp, 2015).

3.1. CFD model

A CFD model was developed through Ansys® Fluent software in order to evaluate the temperature behaviour and the methane formation of the multitubular fixed-bed exchange reactor.

3.1.1. Geometry model

The geometry defined for the study consisted on half reactor tube using computer aided design. With this approach, it was assumed that the temperature behaviour depends only

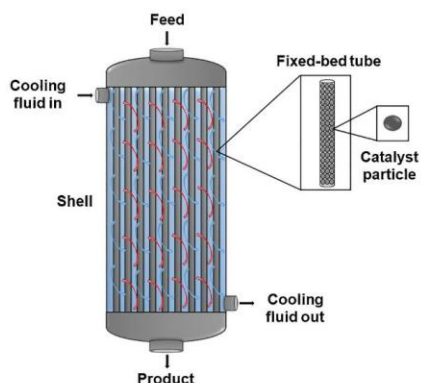


Fig. 1 – Multitubular fixed-bed exchanger reactor.

on the species interaction formed inside of each tube and that the cooling fluid remained at constant temperature. The reactor tube was plotted in the XY plane and the reacting mixture flowed along the Z positive axis. The reactor tube was divided in two symmetrically in order to visually assess the parameters at the centre of the tube, where the highest temperatures and reaction rates were expected.

Five principal zones were defined as boundary conditions: gas inlet mixture, gas outlet mixture, symmetry, tube and interface. Then, a dynamic meshing design was created to characterize the homogenous phase of the reactive zone. The number of nodes was 96,391 and the number of elements was 32,176. They were divided into the reactive zone and the solid zone. The meshing design was optimized to generate a mesh with the minimum number of nodes, in which the numerical solution did not depend on the number of discrete cells. The selected mesh was non-uniform and a higher number of nodes were defined at the initial reacting volume. The discretized 3D computational geometry used for the simulations is shown in Fig. 2.

3.1.2. Model assumptions and governing equations

The mathematical model established for this study was constituted by a set of five partial differential equations formed

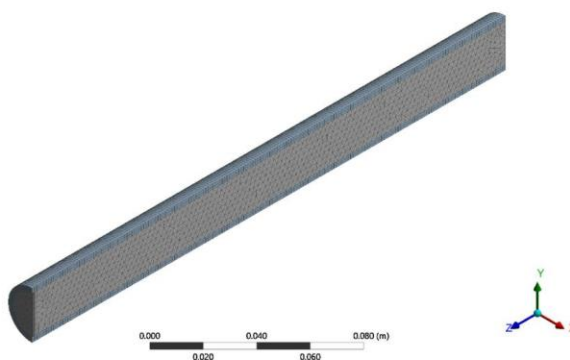


Fig. 2 – Discretized model geometry used for CFD modelling.

Table 1 – Governing equation used on the CFD model.

Energy balance	
Conservation equation	$\frac{\partial}{\partial t}(\rho Y_i) + \nabla \cdot (\rho \vec{v} Y_i) = -\nabla \cdot \vec{J}_i + R_i$
Diffusion flux of species	$\vec{J}_i = -\left(\rho D_{i,m} + \frac{\mu_t}{Sc_t}\right) \nabla Y_i - D_{T,i} \frac{\nabla T}{T}$
Species transport	
Net rate of production of species by chemical reaction	$R_i = M_{w,i} \sum_{r=1}^{N_R} \tilde{R}_{i,r}$
	Viscous model (standard k-ε 2 equations)
Turbulence kinetic energy (k)	$\frac{\partial (k)}{\partial t} + \frac{\partial}{\partial x_j}(\rho u_j k) = \frac{\partial}{\partial x_j} \left[\left(\mu + \frac{\mu_t}{\sigma_k} \right) \frac{\partial k}{\partial x_j} \right] + G_k + G_b - \rho \epsilon - Y_M + S_k$
Dissipation rate (ε)	$\frac{\partial (\epsilon)}{\partial t} + \frac{\partial}{\partial x_j}(\rho u_j \epsilon) = \frac{\partial}{\partial x_j} \left[\left(\mu + \frac{\mu_t}{\sigma_\epsilon} \right) \frac{\partial \epsilon}{\partial x_j} \right] + \frac{\epsilon}{k} C_{1\epsilon} (G_k + C_{3\epsilon} G_b) - C_{2\epsilon} \rho \frac{\epsilon^2}{k} + S_\epsilon$
The μ_t turbulence viscosity is linked to the turbulence kinetic energy and dissipation	$\mu_t = C_\mu \rho \frac{k^2}{\epsilon}$
Constant values (Jones and Launder, 1973)	$C_{1\epsilon} = 1.44$ $C_{2\epsilon} = 1.92$ $C_\mu = 0.09$ $\sigma_\epsilon = 1.3$ $\sigma_k = 1.0$

from the strategic integration of three sub-models. The first sub-model was the mass and energy model to predict mass conservation of the species and heat transfer during the process. The second sub-model was the species transport inside the reacting tube. This volume was treated as a homogeneous porous medium composed by catalytic particles and gas mixture. The porosity of the reactive zone considered was 58%, this value was obtained experimentally. The volumetric reaction model was defined to evaluate the species consumption and formation. Besides, a finite-rate model was nominated for the reacting flows assuming in this way that the chemical reaction was the rate-limiting step. The third sub-model was the viscous model (standard k-ε 2 equations), it was incorporated to the set of equations, considering that the flow rate was axial with an ideal piston type model with turbulent movement. The fundamental assumption of this model is that the turbulent viscosity is isotropic. In addition, it was considered that mean deformation's rate and the ratio between Reynolds stress is the same in all directions. Table 1 shows the set of partial equations configured on the model CFD.

In this sense, the following assumptions were made for simplify purposes:

- The reactor operates at steady-state.
- The wall temperature of the reactor tube is isothermal due to that the cooling fluid temperature is constant along of its length.
- The model includes two zones: reactive zone (catalyst and species) and solid zone (steel reactor tube).

3.2. Reactions kinetics

The net rate of production of species by chemical reaction were obtained experimentally. The reaction kinetic expressions introduced on the model were adapted to the species transport model used by Ansys® Fluent. The formation or consumption of each species R_i (Eq. (6)) were computed as the sum of N_R reactions that each species participates in:

$$R_i = M_{w,i} \sum_{r=1}^{N_R} \tilde{R}_{i,r} \quad (6)$$

where, $M_{w,i}$ is the molecular weight of species, i and $\tilde{R}_{i,r}$ (Eq. (7)) is the molar rate of creation/destruction of species i in reaction r .

$$\tilde{R}_{i,r} = \left(k_{f,r} \prod_{j=1}^{N_i} [C_{j,r}]^{n_{j,r}'} - k_{b,r} \prod_{j=1}^{N_i} [C_{j,r}]^{n_{j,r}''} \right) \quad (7)$$

The kinetic parameters $k_{f,r}$ and $n_{j,r}'$ of the forward reaction were determined through the experimental kinetic study (Eq. (8)), by the minimization of the sum of absolute squared errors between the proposed power law rate expression and experimental data.

$$r_{CH_4, \text{experimental}} = k_{f,r} \cdot C_{CO_2}^{n'} \cdot C_{H_2}^{4n'} \quad (8)$$

The study was carried out at differential conditions ($X_{CO_2} < 15\%$) and it was considered that the concentrations of reactants were constant over the entire bed length. The pre-exponential factor (A_r') and the activation energy (E_r') were related to the rate constant by the Eq. (9).

$$k_{f,r} = A_r' T^{B_r} e^{-E_r'/RT} \quad (9)$$

As the Sabatier reactions is a reversible reaction, the kinetic parameters of the backward reaction ($k_{b,r}$) was also taken into consideration. The K_{eq} was obtained from the NIST equilibrium database (NIST, 2018). Then, the pre-exponential factor (A_r'') and the activation energy (E_r'') of the backward reaction were obtained by a mathematical fit. The $n_{j,r}''$ values were obtained from the equilibrium relation.

3.3. Simulation

Once the physical model was defined, the boundary conditions were specified. In this sense, the governing equations are solved subject to some initial and boundary conditions. In the present CFD model, both external and internal boundaries were specified. As concerns to the gas mixture, a preheated gas (T_{inlet}) with a uniform velocity was considered (V_{inlet}). The species were introduced with stoichiometric molar ratio of H_2 and CO_2 . At the tube outlet, the pressure was defined accord-

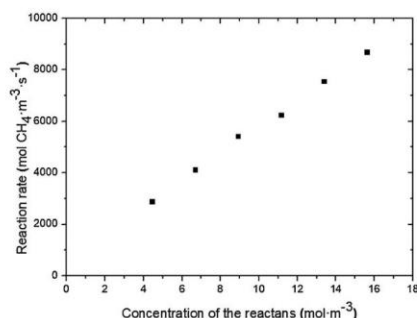


Fig. 3 – Relation between the rate of CH₄ formation with the concentration of the reactants at 673 K.

ing to the operational pressure for each specific condition. The heat released by the reaction was evacuated through the steel wall by means of the specification of a wall temperature (T_{wall}). Lastly, the symmetry boundary condition was applied at the center-plane to impose zero normal gradients at the velocity, pressure, temperature, and species mole fraction.

The simulations were solved by a standard initialization method with a number of iterations equal to 1000. The results were considered valid when the equation solving had no fluctuations and the error range was less than 10^{-4} for all the parameters and for the energy less than 10^{-6} . The reactor behaviour was evaluated by the temperature, velocity and molar fraction of each species through the reactor tube. Finally, the CO₂ conversion at the outlet was obtained by the CO₂ consumption during the reaction by Eq. (10).

$$X_{\text{CO}_2} = \frac{\dot{n}_{\text{CO}_2,\text{in}} - \dot{n}_{\text{CO}_2,\text{out}}}{\dot{n}_{\text{CO}_2,\text{in}}} \times 100\% \quad (10)$$

4. Results and discussion

4.1. Reaction kinetics

The reaction kinetics of methane formation over 15Ni–10Ce/Al₂O₃ were obtained from experimental rate data. The experiments were carried out using stoichiometric reactant ratio ($R_{\text{H}_2/\text{CO}_2} = 4$), together with Ar mixtures, at the temperature range of 473–673 K. The catalyst mass was varied to assure differential conditions. The dependence of the reaction rates on the temperature was really high, in such a way that, the amount of catalyst at the lowest temperature (473 K) was about 25 times lower than at the highest one (673 K). Complete experimental rate data can be found in Supporting Information (Table S1).

Besides the temperature, the reaction rates were influenced by the reactant concentration. As an example, Fig. 3 shows the dependence of the reaction rates on the concentration of the reactants at 673 K. It can be observed that there is a clear relation between the CH₄ formation rate with the reactant concentration, in such a way that the highest reaction rates were observed with pure reactant and they decrease with dilution. The dependence of reaction rates with reactant concentration was practically linear, indicating the global reaction order was low ($n \approx 1$). In reaction systems with low reaction orders, such as in the present case, the ideal reactor configuration is a tubular one (Levenspiel, 1999).

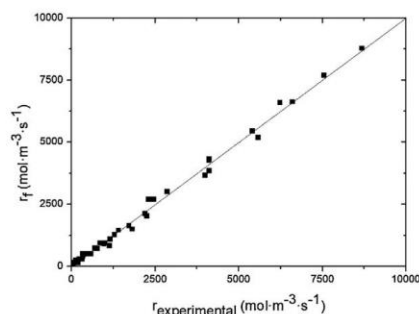


Fig. 4 – Comparison between experimental rate data and the proposed expression.

The kinetic parameters were determined by adjusting the experimental data to the proposed power law rate expression by Ansys® Fluent. The most suitable kinetic expression found was (Eq. (11)):

$$r_f \text{ (mol} \cdot \text{m}^{-3} \cdot \text{s}^{-1}) = 8.38 \cdot 10^7 \cdot \exp\left(\frac{-6.20 \cdot 10^7}{RT}\right) (\text{CO}_2)^{0.171} \cdot (\text{H}_2)^{0.683} \quad (11)$$

Regardless its simplicity, the proposed kinetic model was able to predict successfully the experimental data obtained in the whole range of explored conditions, as displayed in Fig. 4. In addition, residuals of the fitted equations were randomly distributed. The partial reaction order was 0.171 for CO₂ and it was 0.683 for H₂, while the obtained global reaction order was 0.854. The pre-exponential factor (A_f) and the activation energy (E_f) were found to be 8.38×10^7 and 6.20×10^7 J Kg mol⁻¹, respectively. In comparison with literature values, the obtained activation energy was slightly lower than reported by Cai et al. (7.7 J Kg mol⁻¹) (Cai et al., 2011), where the kinetic study was conducted over 12Ni/γ-Al₂O₃ catalyst. On the other hand, the kinetic parameters of backward reaction were calculated as from NIST equilibrium database mathematical fit. The backward reaction order obtained was -0.829 and -3.316 for CO₂ and H₂, respectively. The values found were 8.78×10^{17} for the pre-exponential factor (A_r) and 2.33×10^8 J Kg mol⁻¹ for the activation energy (E_r). Accordingly, the obtained kinetic expression was (Eq. (12)):

$$r_b \text{ (mol} \cdot \text{m}^{-3} \cdot \text{s}^{-1}) = 8.78 \cdot 10^{17} \cdot \exp\left(\frac{-2.33 \cdot 10^8}{RT}\right) (\text{CO}_2)^{-0.829} \cdot (\text{H}_2)^{-3.316} \quad (12)$$

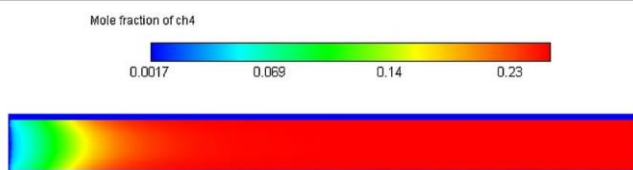
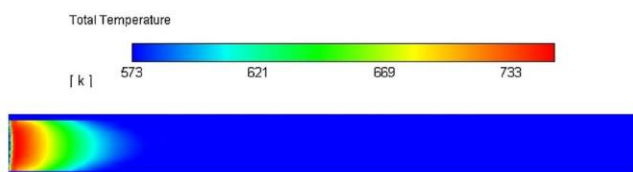
4.2. Reactor modelling

4.2.1. Base case

The implementation of the 15Ni–10Ce/Al₂O₃ catalyst on a multitubular heat exchange reactor was evaluated through the CFD model developed in this study. Table 2 summarizes the parameters used for the base case. It was considered a tube diameter of 20 mm and a length of 250 mm and the GHSV was set at 3600 h⁻¹. The gases were preheated at 573 K and introduced to the reactor at atmospheric pressure with the

Table 2 – Parameters used in the simulation for the base case.

Parameters		Values
Molar fraction CO ₂	20	[%]
Molar fraction H ₂	80	[%]
Pressure, P _{inlet}	1	[atm]
Reactor tube inner diameter, d _i	20	[mm]
Reactor tube length, L	250	[mm]
Forward reaction order, n	0.854	–
Pre-exponential factor of the forward reaction, A _f	8.38 × 10 ⁷	–
Activation energy of the forward reaction, E _f	6.20 × 10 ⁷	[J Kg mol ⁻¹]
Pre-exponential factor of the backward reaction, A _b	8.78 × 10 ¹⁷	–
Activation energy of the backward reaction, E _b	2.33 × 10 ⁸	[J Kg mol ⁻¹]
Specific heat of the reactive zone, C _{prz}	5754	[J kg ⁻¹ K ⁻¹]
Thermal conductivity of the reactive zone, λ _{rz}	0.53	[W m ⁻¹ K ⁻¹]
Temperature of the gas mixture, T _{inlet}	573	[K]
Velocity of the gas mixture, V _{inlet}	0.25	[m s ⁻¹]
Gases hourly space velocity, GHSV	3600	[h ⁻¹]
Temperature of tube wall, T _{wall}	573	[K]

**Fig. 5 – CH₄ molar fraction profile for the base case (T_{inlet}=573 K, T_{wall}=573 K, GHSV=3600 h⁻¹, P_{inlet}=1 atm, d_i=20 mm and L=250 mm).****Fig. 6 – Temperature profile for the base case (T_{inlet}=573 K, T_{wall}=573 K, GHSV=3600 h⁻¹, P_{inlet}=1 atm, d_i=20 mm and L=250 mm).**

stoichiometric molar ratio (H₂/CO₂ = 4). In this model, the heat was released by external cooling at the constant temperature of 573 K, to keep at minimum the temperature profiles in the reactor (see Fig. 1). At these conditions, it was observed that the gas mixture interacted from the very beginning of the reactor, and as a result, CO₂ and H₂ were converted to the products CH₄ and water. The progressive conversion of CO₂ and H₂ to CH₄ is illustrated in Fig. 5. It is seen that the reaction was fast and the largest amount of methane was formed at the initial zone of the reactor.

The conversion of carbon dioxide to methane produced an increase of temperature inside the tube, due to the exothermicity of the reaction. The temperature profile of the reactor tube is shown in Fig. 6. It is seen that the maximum temperature registered in the reaction zone was T_{max} = 733 K. Thus, the exothermicity of the reaction led to a temperature profile of Δ160 K. The temperature raise was mainly registered on the first 5 mm of the total tube length (250 mm). After this initial raise of temperature, the exothermicity of the reaction was balanced by the heat exchange with the wall. At the end of the reactor, the temperature decreased again to reach the wall temperature. Therefore, the reactor showed a pronounced internal temperature profile at the beginning of the

reactor, while the inlet and the outlet were at the same temperature. A controlled temperature profile can be beneficial to enhance the reaction rates at the kinetic reaction regime. Unfortunately, the CO₂ conversion achieved by this reactor design was restricted to 71%. Consequently, further reactor optimization is required. With this aim, a sensitivity analysis was carried out to identify the most relevant variables that influence the behaviour of the reacting mixture temperature and the CO₂ conversion.

4.2.2. Sensitive analysis: reaction conditions

A sensitive analysis was conducted in order to find the key parameters for obtaining higher CO₂ conversions than the base case. In parallel, the observed increase of the temperature (Δ160 K) is not desirable as it can damage the catalyst. These finding will be useful to propose an optimal design reactor for the CO₂ methanation process. The first variables studied on the sensitive analysis were mainly linked to the working conditions of the process (T_{inlet}, T_{wall}, P_{inlet} and GHSV). Additionally, the dilution of reactants by the introduction of CH₄ at the gas inlet mixture was also considered as a possibility, as biogas is considered an interesting CO₂ source.

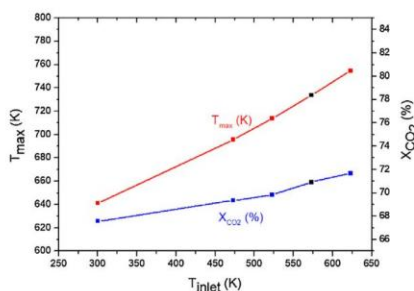


Fig. 7 – T_{max} (K) and CO₂ conversion (%) at different T_{inlet} (K). T_{wall} = 573 K, GHSV = 3600 h⁻¹, P_{inlet} = 1 atm, d_i = 20 mm and L = 250 mm. Black square indicates the base case.

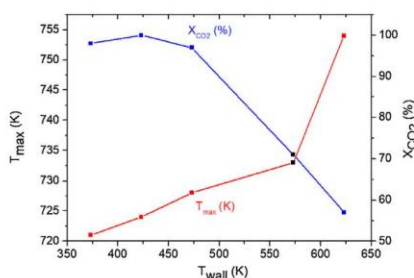


Fig. 8 – T_{max} (K) and CO₂ conversion (%) at different T_{wall} (K). T_{inlet} = 573 K, GHSV = 3600 h⁻¹, P_{inlet} = 1 atm, d_i = 20 mm and L = 250 mm. Black square indicates the base case.

In the next section, the reactor dimensions are evaluated (tube inner diameter and length).

The temperature of the gas preheating (T_{inlet}) were varied in the range of temperatures between 300–623 K. The T_{inlet} effects on T_{max} and CO₂ conversion are illustrated in Fig. 7. As shown, a decrease of the reactor hot spots can be achieved by the reduction of the inlet temperature; however, at expenses of lower CO₂ conversion. On this regard, the lowest hot spot (T_{max} = 641 K) and the lowest CO₂ conversion (69%) were obtained at the lowest inlet temperature considered (T_{inlet} = 300 K). As for T_{inlet} between 523–623 K, CO₂ conversions above 70% were achieved. However, the maximum CO₂ conversion achieved was only 72%, at the highest inlet temperature considered (T_{inlet} = 623 K). The reduction of CO₂ conversion at low inlet temperatures is due to kinetic restrictions to induce the Sabatier reaction. Therefore, the decrease of the inlet temperature, reduces positively the formation of hot spots but it negatively reduces the CO₂ conversion.

In contrast, Fig. 8 shows that the reactor hot spots can be decreased by the reduction of the wall temperature without lowering the final CO₂ conversion. The lowest T_{max} (721 K) was obtained at the minimum T_{wall} (373 K). In parallel, a positive increase in CO₂ conversion was also observed with decreasing T_{wall}. In this line, almost complete CO₂ conversion was obtained at T_{wall} (423 K) and 40% decrease in conversion was observed at T_{inlet} between 473–623 K. Accordingly, a decrease of wall temperature favours the thermodynamics at the end of the tube displacing the reaction toward products, while the potential negative effect of decreasing the kinetics at the ini-

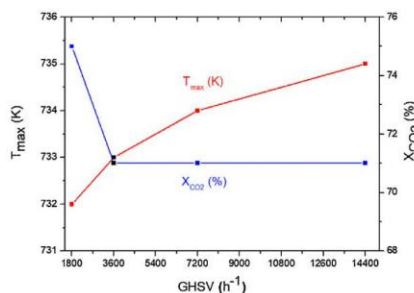


Fig. 9 – T_{max} (K) and CO₂ conversion (%) at different GHSV (h⁻¹). T_{inlet} = 573 K, T_{wall} = 573 K, P_{inlet} = 1 atm, d_i = 20 mm and L = 250 mm. Black square indicates the base case.

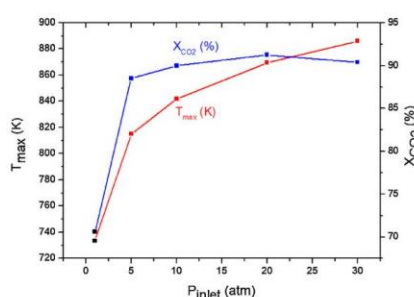


Fig. 10 – T_{max} (K) and CO₂ conversion (%) at different P_{inlet} (atm). T_{inlet} = 573 K, T_{wall} = 573 K, GHSV = 3600 h⁻¹, d_i = 20 mm and L = 250 mm. Black square indicates the base case.

tial zone were less pronounced. Thus, a decrease of the cooling fluid temperature seems beneficial for the multitubular reactor behaviour.

Another really important parameter on the reactor design is the selection of the GHSV. Reactors able to work at higher space velocities requires less reactor volume and catalyst amount. The V_{inlet} range selected for the analysis was between 0.1–1 m s⁻¹, representing for this tube dimension 1800 h⁻¹ and 14,400 h⁻¹. Fig. 9 shows that reactor hot spots clearly increase with flow velocity. At high flowrates, more reactant moles were introduced to the reactor and more methane moles were formed. Accordingly, the total release of heat was also enhanced. On the other hand, the species have less contact time with the catalyst at high flow velocities and conversion should be significantly reduced in isothermal conditions. However, in the present case study, high GHSV also led to an increase of temperature. This behaviour minimized the typical conversion drop.

A possible way to increase the conversion, without working at low flowrates, is by changing the pressure inside the tube. The P_{inlet} effects on T_{max} and CO₂ conversion were evaluated from 1 up to 30 atm. In Fig. 10 is illustrated that the reactor hot spots increased, together with CO₂ conversion, with the increment of the pressure. The conversion was increased from 71 to 91% at P_{inlet} = 20 atm. At higher pressures, the pressure effects on the conversion were negligible. The Sabatier reaction has an important decreasing of volume. Then, it is more

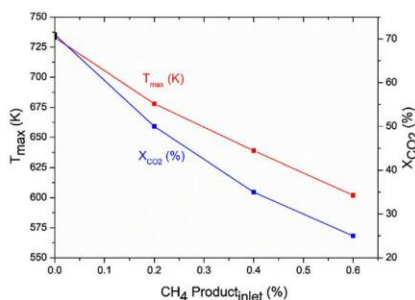


Fig. 11 – T_{max} (K) and CO₂ conversion (%) at different Product_iinlet (%). $T_{inlet} = 573$ K, $T_{wall} = 573$ K, GHSV = 3600 h⁻¹, $P_{inlet} = 1$ atm, $d_i = 20$ mm and $L = 250$ mm. Black square indicates the base case.

favourable to operate at higher pressures, both from kinetic and thermodynamic point of view. However, it is worth mentioning that the increase of the pressure has some technical and economic implications on the process, since higher capital and operational costs are required. An inlet pressure of 5 atm can be economically achieved by the incorporation of a CO₂ compressing unit instead of a blower. Hydrogen pressure is given inside the electrolyzer and thus an external hydrogen electrolyzer is not necessary (Gahleitner, 2013).

From an industrial point of view, biogas (mixture of CO₂ and CH₄) is an interesting CO₂ source for SNG production (Martinez Molina et al., 2016). Thus, the introduction of CH₄ together with CO₂ is considered in the sensitive analysis. The effect on T_{max} and on CO₂ conversion by the CH₄ addition is illustrated in Fig. 11. The reactor hot spots visibly decrease with the CH₄ addition, as well as CO₂ conversion. At high product addition percentages (0.6), it was observed a large decrease of the maximum temperature (602 K). Therefore, it was revealed that the presence of CH₄ at the inlet can decrease the reaction hot spots considerably; however, at expenses of the final yield. Accordingly, a reduction of the conversion and the hot-spots should be taken into account when methanation of biogas, instead of pure CO₂, is considered.

4.2.3. Sensitive analysis: tube dimensions

Proper tube sizing is relevant to achieve high methane contents. In this sensitive analysis, it was studied the tube inner diameter range of 5–20 mm and tube length of 125–1000 mm. As expected, reactor hot spots decreased with the reduction of the tube inner diameter (Fig. 12). At higher surface to volume ratio of reactor, the heat release was clearly favoured. In contrast, it should be pointed out that the decrease of the tube inner diameter implies the construction of a reactor with larger number of reactor tubes, thus adding complexity to the reactor manufacturing process. The increase of CO₂ conversion using thin tubes is also due to the temperature behaviour. At low tube diameter, the temperature at the center of the tube was lower compared to large tubes. According to the Le Chatelier principle, the methanation reaction is shifted to products at low temperatures.

Fig. 13 shows that the CO₂ conversion increase with the increment of the tube length up to 250 mm because the contact time between the reactants and the catalyst is higher. Accordingly, it is inferred that a tube length of 250 mm is sufficient for this case and a longer length would not contribute to the

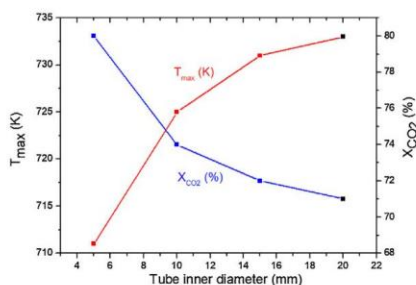


Fig. 12 – T_{max} (K) and CO₂ conversion (%) at different tube inner diameter (mm). $T_{inlet} = 573$ K, $T_{wall} = 573$ K, $P_{inlet} = 1$ atm and $L = 250$ mm. Black square indicates the base case.

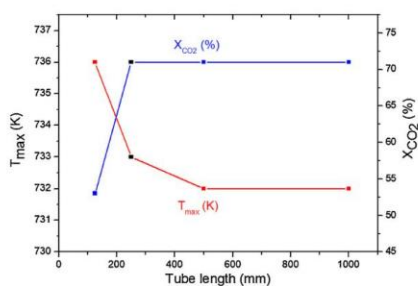


Fig. 13 – T_{max} (K) and CO₂ conversion (%) at different tube length (mm). $T_{inlet} = 573$ K, $T_{wall} = 573$ K, $P_{inlet} = 1$ atm and $d_i = 20$ mm. Black square indicates the base case.

formation of more CH₄ moles. This indicates that the reactor operates at a chemical equilibrium regime at the end of the tube. Finally, the influence of the tube length on the temperature is almost negligible ($\Delta 5$ K). The maximum temperature appeared at the initial zones of the reactor and not at the end of the reactor.

4.3. Reactor proposal

The inlet temperature, the wall temperature, the inlet pressure, the inlet velocity and the tube inner diameter were identified as the key parameters to have an optimum temperature profile in the reactor. Unfortunately, the modification of the inlet temperature, pressure, velocity and production addition led to reduction of hot spots but they also to a negative reduction of the CO₂ conversion. On the contrary, hot spots can be reduced by an optimum reactor geometry and the temperature of the cooling system. Therefore, based on these results, decisions were made with the aim of present a reactor proposal.

The optimum design should ease an efficient temperature control during the process of CO₂ methanation. As mentioned, an excessive preheating induces hot spots. Thus, the inlet temperature was kept at minimum. According to this study, reaction rates were really low below 473 K. Thus, it is proposed a reactor in which the gases are introduced at this temperature, after a preheating step. Wall temperature was also kept at minimum of the range explored ($T_{wall} = 373$ K) due

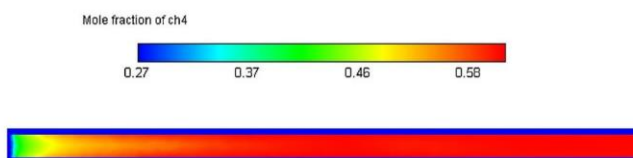


Fig. 14 – CH₄ molar fraction profile as from design proposal. $T_{inlet} = 473\text{ K}$, $T_{wall} = 373\text{ K}$, $GHSV = 14400\text{ h}^{-1}$, $P_{inlet} = 5\text{ atm}$, $d_i = 9.25\text{ mm}$ and $L = 250\text{ mm}$.

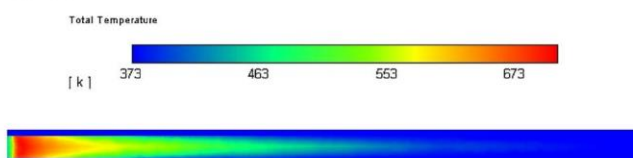


Fig. 15 – Temperature profile as from design proposal. $T_{inlet} = 473\text{ K}$, $T_{wall} = 373\text{ K}$, $GHSV = 14,400\text{ h}^{-1}$, $P_{inlet} = 5\text{ atm}$, $d_i = 9.25\text{ mm}$ and $L = 250\text{ mm}$.

Table 3 – Design proposal for the optimization of the reactor.

Operational conditions	Value	
Temperature of the gas mixture, T_{inlet}	473	[K]
Temperature of the reactor tube wall, T_{wall}	373	[K]
Velocity of the gas mixture, V_{inlet}	1	[m s ⁻¹]
Gases hourly space velocity, GHSV	14,400	[h ⁻¹]
Pressure, P_{inlet}	5	[atm]
Reactor tube inner diameter, d_i	9.25	[mm]
Reactor tube length, L	250	[mm]

to the beneficial effects both in temperature control and in final methane content.

Since a proper transfer of heat to the cooling medium was achieved by optimizing the dimensions of the reactor, a tube with an inner diameter of 9.25 mm (adapted to standard pipe diameter) and a length of 250 mm are proposed to achieve an efficient temperature control in the reactor. It was considered that further reduction of the tube involves an excessive number of tubes. In addition to the heat management, the operation pressure was set at 5 atm in agreement with the high activity increase from 1 to 5 atm, and in this way, avoiding high operation pressures and keeping the process as simple as possible. The proposed reactor can operate as high GHSV values as 14,400 h⁻¹ and still produce a synthetic natural gas with a 95% CH₄, in line with some national legislations related to gas grid injection. The parameters of the design proposal are summarized in Table 3.

Finally, it was evaluated the methanation of a typical industrial biogas produced is by two anaerobic digesters of a wastewater treatment plant (100 Nm³ h⁻¹, 65% of CH₄). In this case, the feed is composed by 240 m³ h⁻¹ (14.6% CO₂ and 58.3% H₂). The maximum temperature registered in the reactive zone was of 673 K and the CO₂ conversion achieved was of 99%. Therefore, with this strategy hot spots were successfully minimized ($\Delta 100\text{ K}$). The profiles of the methane content and temperature are illustrated in Fig. 14 and Fig. 15, respectively. The simulation shows that the proposal has had a good temperature control during the process. Accordingly, it was concluded that about 1000 tubes are required to produce 35 m³ h⁻¹ of SNG at the conditions of the proposed reactor design.

5. Conclusions

The implementation of a nickel–ceria–alumina catalyst on a multitubular heat-exchange reactor for CO₂ methanation was evaluated through Ansys[®] Fluent CFD software. The simulations showed that, in general terms, the reactor behaviour is divided into two zones. At the beginning of the reaction tube, most reaction takes place and the temperature is highly increased due to the exothermicity of the reaction. A proper control of the temperature on this reactor volume is mandatory to minimize the catalyst degradation by sintering or by coke formation. After this initial hot-spots, the temperature drops to equilibrium with the temperature of the wall. Within this second reactor zone, the kinetics are restricted by the relatively low temperature and thermodynamics of the reaction gains relevance. In the thermodynamics regime, it is very important to have an active catalyst at low temperatures to complete the CO₂ conversion.

The temperature of the wall, directly related to the temperature of the cooling fluid, is a key parameter to enhance the methane content at the reactor outlet. Low wall temperatures shifts the reaction toward products and higher conversions can be achieved. In contrast, the effect of the wall temperature on the kinetic zone is negligible. CO₂ conversion can also be enhanced by the pressure of operation. The increase of pressure have a positive effect on the conversion, especially pronounced up to 5 atm. A further increase of pressure can be negative as higher capital and operational costs of the reactor could not be balanced by the decrease of reactor volume. On the other hand, the operation at high gas hour space velocities is interesting to avoid excessive reactor volumes and amount of catalyst. However, it was observed that the increase of flow velocities leads to more pronounced hot-spots. Interestingly, the higher amount of heat as a consequence of high flow velocities can be released by the reduction of the tube diameter as well as by the addition of products at the inlet. Therefore, the methanation of biogas instead of pure CO₂ is positive to avoid reactor hot-spots.

The sensitive analysis of the design parameters was used to propose a reactor with high CO₂ conversion, low hot-spots and low reactor volume. A proper balance was found using a reactor tube of 9.25 mm internal diameter and 250 mm length,

which operates with an inlet temperature of 473 K, a lower wall temperature of 373 K, inlet pressure of 5 atm and gas hour velocity of $14,400 \text{ h}^{-1}$. At this conditions, the maximum increase of the temperature was restricted to 100 K, adequate to avoid catalyst sintering and coke formation. The conversion at the outlet was really high (99%) and should be suitable to obtain a synthetic natural gas quality with the composition required for some European legislations (>95% CH_4). As an illustrative example, the number of tubes required for the methanation of $100 \text{ Nm}^3 \text{ h}^{-1}$ biogas is about 1000. In the future, the proposed reactor tube should be validated experimentally.

Acknowledgement

Authors thank Generalitat de Catalunya for financial support through the CERCA Programme, M2E (2017SGR1246) and XaRMAE network. IREC also gratefully acknowledge the funding of this work by CoSin projec (COMRD15-1-0037), funded by ACCIÓ and the European Regional Development Fund (FEDER) under the RIS3CAT Energy Community. Andreina is grateful to Escuela Superior Politécnica del Litoral (ESPOL) for the support during her postgraduate studies ("Walter Valdano Raffo" program, First edition).

Appendix A. Supplementary data

Supplementary data associated with this article can be found, in the online version, at <https://doi.org/10.1016/j.chedr.2018.10.017>.

References

- Abate, S., Mebrahtu, C., Giglio, E., Deorsola, F., Bensaïd, S., Perathoner, S., Pirone, R., Centi, G., 2016. Catalytic performance of $\gamma\text{-Al}_2\text{O}_3\text{-ZrO}_2\text{-TiO}_2\text{-CeO}_2$ composite oxide supported Ni-based catalysts for CO_2 methanation. *Ind. Eng. Chem. Res.* 55, 4451–4460. <http://dx.doi.org/10.1021/acs.iecr.6b00134>.
- Atzori, L., Cutrufello, M.G., Meloni, D., Cannas, C., Gazzoli, D., Monaci, R., Sini, M.F., Rombi, E., 2018. Highly active NiO–CeO₂ catalysts for synthetic natural gas production by CO_2 methanation. *Catal. Today* 299, 183–192. <http://dx.doi.org/10.1016/j.cattod.2017.05.065>.
- Barbarossa, V., Vanga, G., Viscardi, R., Gattia, D.M., 2014. CO_2 as carbon source for fuel synthesis. *Energy Procedia*, 1325–1329. <http://dx.doi.org/10.1016/j.egypro.2014.01.138>, Elsevier B.V.
- Belimov, M., Metzger, D., Pfeifer, P., 2017. On the temperature control in a microstructured packed bed reactor for methanation of CO/CO_2 mixtures. *AIChE J.* 63, 120–129. <http://dx.doi.org/10.1002/aic.15461>.
- Cai, M., Wen, J., Chu, W., Cheng, X., Li, Z., 2011. Methanation of carbon dioxide on Ni/ZrO₂-Al₂O₃ catalysts: effects of ZrO₂ promoter and preparation method of novel ZrO₂-Al₂O₃ carrier. *J. Nat. Gas Chem.* 20, 318–324. [http://dx.doi.org/10.1016/S1003-9953\(10\)60187-9](http://dx.doi.org/10.1016/S1003-9953(10)60187-9).
- Camacho, A.C.C., 2017. Catalizadores mesoporosos para la valorización del dióxido de carbono a gas natural sintético. UB.
- Chein, R.Y., Chen, W.Y., Yu, C.T., 2016. Numerical simulation of carbon dioxide methanation reaction for synthetic natural gas production in fixed-bed reactors. *J. Nat. Gas Sci. Eng.* 29, 243–251. <http://dx.doi.org/10.1016/j.jngse.2016.01.019>.
- Ducamp, J., 2015. Conception et optimisation d'un réacteur-échangeur structuré pour l'hydrogénation du dioxyde de carbone en méthane de synthèse dédié à la filière de stockage d'énergie électrique renouvelable. *Inst. Chim. procédés pour l'énergie, l'environnement la santé*.
- Ducamp, J., Bengaouer, A., Baurens, P., 2017. Modelling and experimental validation of a CO_2 methanation annular cooled fixed-bed reactor exchanger. *Can. J. Chem. Eng.* 95, 241–252. <http://dx.doi.org/10.1002/cjce.22706>.
- Eigenberger, G., 1992. *Fixed-Bed Reactors*, Vol. 4B. Institut für Chemische Verfahrenstechnik, Universität Stuttgart, Stuttgart, Federal Republic of Germany. https://doi.org/10.1002/14356007.b04_199.
- Feng, Y., Yang, W., Chen, S., Chu, W., 2014. Cerium promoted nano nickel catalysts Ni-Ce/CNTs and Ni-Ce/Al₂O₃ for CO_2 methanation. *Integrated Ferroelectrics*, 116–125. <http://dx.doi.org/10.1080/10584587.2014.901141>.
- Gahleitner, G., 2013. Hydrogen from renewable electricity: an international review of power-to-gas pilot plants for stationary applications. *Int. J. Hydrogen Energy* 38, 2039–2061. <http://dx.doi.org/10.1016/j.ijhydene.2012.12.010>.
- Gao, J., Wang, Y., Ping, Y., Hu, D., Xu, G., Gu, F., Su, F., 2012. A thermodynamic analysis of methanation reactions of carbon oxides for the production of synthetic natural gas. *RSC Adv.* 2, 2358. <http://dx.doi.org/10.1039/c2ra00632d>.
- Garmsiri, S., Rosen, M.A., Smith, G.R., 2014. Integration of wind energy, hydrogen and natural gas pipeline systems to meet community and transportation energy needs: a parametric study. *Sustainability* 6, 2506–2526. <https://doi.org/10.3390/su6052506>.
- Gassner, M., Maréchal, F., 2008. Thermo-economic optimisation of the integration of electrolysis in synthetic natural gas production from wood. *Energy* 33, 189–198. <http://dx.doi.org/10.1016/j.energy.2007.09.010>.
- Golosman, E.Z., Efreinov, V.N., 2012. Industrial catalysts for the hydrogenation of carbon oxides. *Catal. Ind.* 4, 267–283. <http://dx.doi.org/10.1134/S2070050412040071>.
- Götz, M., Koch, A.M., Graf, F., 2014. State of the art and perspectives of CO_2 methanation process concepts for power to gas applications. *International Gas Union Research Conference* 13.
- Götz, M., Lefebvre, J., Mörs, F., McDaniel Koch, A., Graf, F., Bajohr, S., Reimert, R., Kolb, T., 2016. Renewable Power-to-Gas: A technological and economic review. *Renewable Energy* 85, 1371–1390. <http://dx.doi.org/10.1016/j.renene.2015.07.066>.
- Granovskii, M., Dincer, I., Rosen, M.A., 2007. Greenhouse gas emissions reduction by use of wind and solar energies for hydrogen and electricity production: economic factors. *Int. J. Hydrogen Energy* 32, 927–931. <http://dx.doi.org/10.1016/j.ijhydene.2006.09.029>.
- Guilera, J., Ramon Morante, J., Andreu, T., 2018. Economic viability of SNG production from power and CO_2 . *Energy Convers. Manage.* 162, 218–224. <http://dx.doi.org/10.1016/j.enconman.2018.02.037>.
- Jentsch, M., Trost, T., Sterner, M., 2014. Optimal use of Power-to-Gas energy storage systems in an 85% renewable energy scenario. *Energy Procedia*, 254–261. <http://dx.doi.org/10.1016/j.egypro.2014.01.180>, The Authors.
- Jones, W.P., Launder, B.E., 1973. The calculation of low-Reynolds-number phenomena with a two-equation model of turbulence. *Int. J. Heat Mass Transfer* 16, 1119–1130. [http://dx.doi.org/10.1016/0017-9310\(73\)90125-7](http://dx.doi.org/10.1016/0017-9310(73)90125-7).
- Kroposki, B., Levene, J., Harrison, K., Sem, P. K., Novacek, F., 2006. Electrolysis: information and opportunities for electric power utilities, NREL/TP-581-40605, <https://doi.org/10.2172/892998>.
- Levenspiel, O., 1999. *Chemical reaction engineering*. *Ind. Eng. Chem. Res.* <http://dx.doi.org/10.1021/ie990488g>.
- Martinez Molina, M., Kern, C., Jess, A., 2016. Catalytic hydrogenation of carbon dioxide to methane in wall-cooled fixed-bed reactors. *J. Chem. Eng. Technol.* 39, 2404–2415. <http://dx.doi.org/10.1002/ceat.201500614>.
- NIST, 2018. NIST database [WWW Document]. *Natl. Inst. Stand. Technol.* URL <http://webbook.nist.gov/chemistry/>.
- Rönsch, S., Schneider, J., Matthischke, S., Schlüter, M., Götz, M., Lefebvre, J., Prabhakaran, P., Bajohr, S., 2016. Review on methanation — from fundamentals to current projects. *Fuel*, <http://dx.doi.org/10.1016/j.fuel.2015.10.111>.

- Schaaf, T., Grünig, J., Schuster, M.R., Rothenfluh, T., Orth, A., 2014. Methanation of CO₂ – storage of renewable energy in a gas distribution system. *Energy. Sustainability Soc.* 4, 1–14, <http://dx.doi.org/10.1186/s13705-014-0029-1>.
- Stangeland, K., Kalai, D., Li, H., Yu, Z., 2017. CO₂ methanation: the effect of catalysts and reaction conditions. *Energy Procedia*, 2022–2027, <http://dx.doi.org/10.1016/j.egypro.2017.03.577>.
- Sun, D., Simakov, D.S.A., 2017. Thermal management of a Sabatier reactor for CO₂ conversion into CH₄: simulation-based analysis. *J. CO₂ Util.* 21, 368–382, <http://dx.doi.org/10.1016/j.jcou.2017.07.015>.
- Tada, S., Shimizu, T., Kameyama, H., Haneda, T., Kikuchi, R., 2012. Ni/CeO₂ catalysts with high CO₂ methanation activity and high CH₄ selectivity at low temperatures. *Int. J. Hydrogen Energy* 37, 5527–5531, <http://dx.doi.org/10.1016/j.ijhydene.2011.12.122>.
- Varone, A., Ferrari, M., 2015. Power to liquid and power to gas: an option for the German Energiewende. *Renewable Sustainable Energy Rev.* 45, 207–218, <http://dx.doi.org/10.1016/j.rser.2015.01.049>.
- Wang, W., Gong, J., 2011. Methanation of carbon dioxide: an overview. *Front. Chem. Eng. China* 5, 2–10, <http://dx.doi.org/10.1007/s11705-010-0528-3>.
- Zhao, A., Ying, W., Zhang, H., Hongfang, M., Fang, D., 2012. Ni/Al₂O₃ catalysts for syngas methanation: effect of Mn promoter. *J. Nat. Gas Chem.* 21, 170–177, [http://dx.doi.org/10.1016/S1003-9953\(11\)60350-2](http://dx.doi.org/10.1016/S1003-9953(11)60350-2).

ARTICLE IN PRESS

Fuel Processing Technology xxx (xxxx) xxx



Contents lists available at ScienceDirect

Fuel Processing Technology

journal homepage: www.elsevier.com/locate/fuproc

Research article

An insight into the heat-management for the CO₂ methanation based on free convectionAndreina Alarcón^{a,b}, Jordi Guilera^{a,*}, Teresa Andreu^a^a Catalonia Institute for Energy Research (IREC), Jardins de les Dones de Negre 1, 08930 Sant Adrià de Besòs, Spain^b Escuela Superior Politécnica del Litoral, ESPOL, Facultad de Ingeniería en Ciencias de la Tierra, Campus Gustavo Galindo Km.30.5 Vía Perimetral, P.O. Box 09-01-5863, Guayaquil, Ecuador

ARTICLE INFO

Keywords:

CO₂ methanation
 Synthetic natural gas
 Reactor design
 Heat-management
 Computational fluid dynamics

ABSTRACT

This article presents a novel heat-management approach for CO₂ valorization to synthetic natural gas based on free convection to the environment, without requirements of heat-exchange services. With this aim, a reactor channel was built ($d = 4.6$ mm, $L = 250$ mm) and tested at different conditions of inlet temperatures, gas hourly space velocities and pressures using an active nickel/ceria-based catalyst. After experimentation, a CFD model was developed, validated and employed for an efficient sensitive analysis of the most suitable reaction conditions. The simulation criteria were obtaining high CO₂ conversion level and restricting overheating to avoid catalyst and reactor degradation. Then, the optimal conditions found by CFD modelling were successfully validated at lab-scale. The CO₂ conversion level experimentally obtained was 93%, by using a decreasing temperature profile in the range of 830–495 K, operating at a pressure of 5 atm and a gas hourly space velocity of $11,520$ h⁻¹. The proposed reactor configuration guarantees an efficient heat management along the reactor channel by using feasible conditions of pressure, temperature and flowrate for its implementation in small-scale applications, where the use of the exothermic heat is less profitable.

1. Introduction

The production of synthetic methane through carbon dioxide (CO₂) methanation reaction has high interest in the context of Power-to-Gas (PtG) [1–6]. The methanation reaction allows to store the intermittent electricity production derived from renewable energy sources [7,8]; and besides it allows the valorization of carbon dioxide to renewable natural gas [9–12]. The starting point of the overall PtG process is the utilization of renewable electricity to produce green hydrogen (H₂) through water electrolysis. Then, in an additional processing step, the formed H₂ is combined with CO₂ and converted to methane (CH₄). In this way, the energy carrier is in the form of CH₄, which is the main compound of natural gas. Hence, this product is known as synthetic natural gas (SNG). The main advantage of SNG, in comparison with other synthetic fuels, is that it can be fed into the existing gas infrastructure without any limitations or any further processing. This is a clear advantage as transportation using pipelines is more energy-efficient and environmentally friendly than road transport.

The thermochemical CO₂ methanation process is carried out through Sabatier reaction (1). This reaction is reversible, exothermic and

thermodynamically favoured at low temperatures and high pressures. As kinetics of the reaction are limited at the mentioned conditions, an active catalytic system is required to obtain SNG at reasonable reaction times. Most works on catalyst design for this reaction are based on noble- and transition-metal materials (Ru, Rh, Pd and Ni) supported on metal oxides (Al₂O₃, CeO₂, ZrO₂, TiO₂, SiO₂, La₂O₃ or combination between them) [13,14]. In recent times, it has been reported that the modification of the support through the incorporation of promoters (CeO₂, La₂O₃, Pr₂O₃, Gd₂O₃, ZrO₂, MnO₂ and MgO) improves the catalyst stability and even tolerance to industrial impurities [15–19].



Beyond catalyst advances, the design of a reactor with efficient heat removal is another challenge to face in CO₂ methanation technology, especially for decentralized application. Catalytic reactors, such as multi-tubular fixed-bed [20–26], microchannel [27], fluidized bed [28], stirred-tank slurry [29], microstructured [30–37], honeycomb [38] and compact wall [39] are interesting approaches able to conduct the Sabatier reaction. Among them, the fixed-bed reactor tube coupled with an oil cooling system was already implemented at industrial level

* Corresponding author.

E-mail address: jguilera@irec.cat (J. Guilera).<https://doi.org/10.1016/j.fuproc.2020.106666>

Received 16 July 2020; Received in revised form 16 October 2020; Accepted 3 November 2020

0378-3820/© 2020 Elsevier B.V. All rights reserved.

already in 2013 [40]. Recent advances are related to the utilization of micro- or milli- size reactor for process intensification and temperature control. Miniaturized packed-bed reactors exhibit unique heat and mass transfer characteristics because of high surface-to-volume ratios [41]. Higher heat transfer capacity is achieved by decreasing the inner channel dimensions. Consequently, it was inferred that micro-reactors work at much higher gas flowrates than conventional units [42]. However, the heat generated from the Sabatier reaction is typically released to another fluid by means of the incorporation of complex heat-management systems and several auxiliary devices.

A reactor configuration with a heat-management approach based on free convection is a promising alternative because then the reactor engineering is significantly simplified [43]. As Sabatier reaction is an exothermic process, the released heat can be controlled by some reaction parameters and heat can be released to the environment without the implementation of intensive cooling systems [44]. A free convection heat transfer to the surroundings for the reactor cooling can be a technological alternative for lowering the investment costs in small-size plants. Note that the definition of this novel reactor approach differs from an autothermal approach, as in this second case, the cooling is performed in-situ by an endothermic reaction; e.g. autothermal steam reformers [45]. This “simple as possible” strategy is an interesting approach to expand the application of CO₂ methanation in decentralized locations with low production capacity, where it has been demonstrated that high investments are not profitable.

The operation of reactor using polytropic temperature profiles is required to achieve high SNG productions in smaller volumes [21,23]. Recently, Mooli et al. [46] proposed a model-based determination of the optimal reactor concept for Sabatier reaction by controlling the heat transfer. They found that the reactor can be divided into three zones: an initial zone for reaction activation, a central zone to remove excess heat and a final zone to reach the thermodynamic equilibrium curve. For an unsteady state and more flexible process operation, also known as dynamic operation, Bremer et al. [47] applied stabilizing control to moderate the reactive zone (hot spot) via adaptive coolant temperature variations. They suggested that through this strategy it is possible to obtain unconventional operating points in regions of steady-state multiplicity that offer reduced catalyst temperature, while maintaining elevated reactor performance. In another study, Zhang et al. [48] developed a steady-state solver based on the open-source toolbox. The numerical study proposed heat transfer between the reacting gas in a porous catalyst layer, reactor tube, and coolant in a shell-and-tube reactor. They concluded that through the computational fluid dynamic simulations it was possible to predict the trends of temperature profiles both in axial and radial directions. Therefore, computational fluid dynamic (CFD) modelling seems a powerful tool for reactor design and especially to avoid experimental trial-and-error methodologies.

The aim of this work is to propose a simple heat-management reactor configuration based on free convection to the environment for lowering the overall investment costs in decentralized small-scale CO₂ methanation units. With this aim, a combination of experimentation on a reactor channel (diameter of 4.6 mm and length of 250 mm) and CFD simulation was carried out. The reaction conditions (T_{inlet} , GHSV, P , T_{air}), in which the proposed configuration is able to operate without the use of external cooling/heating systems and to achieve a high CO₂ conversion level ($\geq 90\%$) are hereby presented. The scale-up of the reactor approach considering a representative industrial small-scale CO₂ methanation case ($1 \text{ Nm}^3 \text{ h}^{-1}$ of SNG production) together with the main advantages and disadvantages of this heat-management configuration are further discussed.

2. Experimental

2.1. Catalyst preparation

The catalyst used in this study was a ternary catalytic system based

on Ni as active phase (25 wt%), CeO₂ as promoter (20 wt%) and γ -Al₂O₃ micro-spheres as support (55 wt%). Catalyst design, synthesis and formulation was optimized in previous works [49,50] and validated in a relevant environment [42]. Specifications of the catalyst can be found in those publications. To summarize, 50 g batch was prepared by dissolving salt precursors of nickel (II) nitrate hexahydrate ([Ni(NO₃)₂·6H₂O] with 98% purity, Alfa Aesar) and cerium (III) nitrate hexahydrate ([Ce(NO₃)₃·6H₂O] with 99% purity, Fluka) in distilled water. Then, the aqueous solution was mixed with γ -Al₂O₃ commercial support in shape of microspheres with particle diameters $d_p = 450\text{--}500 \mu\text{m}$ (NorPro Saint-Gobain), on a rotary vacuum evaporator with constant stirring (25 rpm) at room temperature for 1 h. Subsequently, the solvent was in-situ evaporated at 358 K and $P = 0.8 \text{ bar-g}$ for 6 h. Finally, the impregnated micro-spheres were first dried overnight at 378 K and then calcined at 723 K for 30 min with a heating ramp of 1 K-min^{-1} .

2.2. Experimental setup

CO₂ methanation reaction was conducted in the homemade reactor setup, illustrated in Fig. 1. The gases H₂/CO₂ mixture (99.999%, Linde) and H₂ (99.999%, Linde) were supplied through a set of mass flow controllers (MFC, Bronkhorst). A heating tape (Omegalux) monitored by a thermoregulation system (Horst GmbH) was used to pre-heat the gas mixture to the desired temperature. Reactor channel dimensions (inner diameter of 4.6 mm and length of 250 mm) were selected to facilitate the heat transfer to the environment, as it is highly promoted when the inner diameter is reduced from 10 mm [51]. The tube was filled with approximately 3.52 g of catalyst. Temperature was measured by six type K thermocouples (1/16 in, Omega Engineering Inc.); two of them were placed outside of the reactive zone (inlet and outlet of the reactor) and four along the reactive zone (axial position of 28, 53, 99 and 188 mm). Fiberglass tape, 40 mm mineral wool and aluminum foil was used to insulate the reactor. Pressure was regulated by a manual valve placed at the outlet. Then, the unconverted gases and the reaction products leaving the reactor were cooled down to 278 K by using a circulation chiller (VWR, 1160S model) and cold liquid-gas separator to condense and trap water produced, respectively. Prior to the analysis of the composition of the gases, a coalescence filter (Classic filter, SS127.221-C-5CS) was additionally used to ensure the total water removal. At this point, the dry gas flow was measured by a flow meter (FM, Bronkhorst) and its composition was successively analysed by an on-line gas micro-chromatograph (490 microGC, Agilent Technologies). This was equipped with three columns, two molecular sieve (M5SA) for H₂, Ar, N₂, CO and CH₄ analysis, one porous polymer (PPU) for CO₂ and light hydrocarbons. Each column is followed by a thermal conductivity detector (TCD).

2.3. Procedure

Prior to reactor start-up, catalyst was reduced in a tubular furnace using 5 vol% H₂/Ar at a flowrate of 100 mL-min^{-1} . The temperature was increased up to 773 K for 3 h with a heating ramp of 1 K-min^{-1} , followed by a cooled-down to room temperature. Then, the catalytic bed was filled with the reduced catalyst. Experiments were conducted in the range of $P = 1\text{--}5 \text{ atm}$, $T_{inlet} = 503\text{--}573 \text{ K}$, a stoichiometric H₂/CO₂ ratio of 4 and using gas hourly space velocities (GHSVs) in the range from 3,039 to $18,235 \text{ h}^{-1}$. GHSV was calculated by Eq. (2):

$$\text{GHSV} = \frac{F}{\frac{m_{\text{Cat}}}{\rho_{\text{Cat}}}} \quad (2)$$

where F is inlet gas mixture, in the range from 200 to $1200 \text{ NmL-min}^{-1}$, m_{Cat} is the catalyst mass (3.52 g) and $\rho_{\text{Cat}} = 0.891 \text{ g}_{\text{cat}} \cdot \text{mL}^{-1}$ is the measured catalyst density. The performance of the process was evaluated through CO₂ conversion (Eq. (3)), CH₄ selectivity (Eq. (4)) and CH₄ productivity rate (Eq. (5)).

ARTICLE IN PRESS

A. Alarcón et al.

Fuel Processing Technology xxx (xxxx) xxx

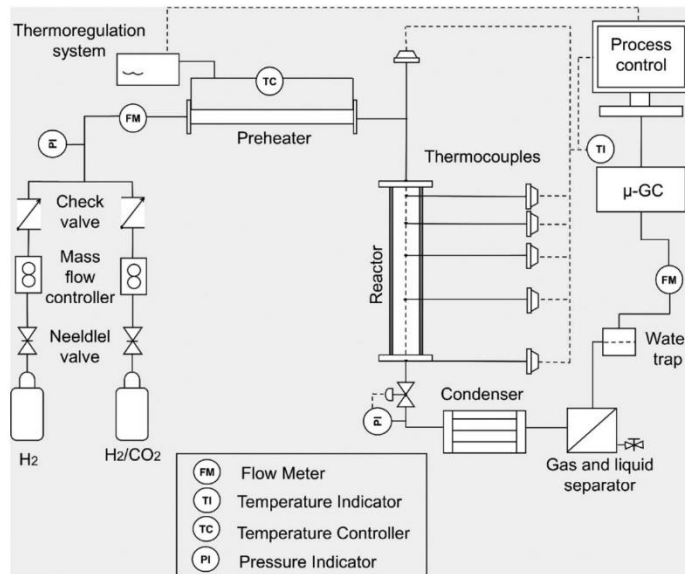


Fig. 1. Schematic illustration of the reactor testing setup.

$$X_{CO_2} [\%] = \frac{n_{CO_2, in} - n_{CO_2, out}}{n_{CO_2, out}} \cdot 100$$

$$S_{CH_4} = \frac{n_{CH_4, out}}{n_{CH_4, out} + n_{CO_2, out}} \cdot 100$$

$$r_{CH_4} [\text{mol} \cdot \text{h}^{-1} \cdot \text{kg}^{-1}] = \frac{n_{CH_4, out}}{m_{Cat}}$$

- (3) where n_j represents the molar flow rate of species j ($j = CO_2$ and CH_4) in the inlet and outlet gas. Sub-products, such as CO and C_{2+} hydrocarbons were not detected. Therefore, methane selectivity was close to 100%. As a representative example, Figure S11–3 show raw chromatograms of the analytics, confirming complete selectivity to CH_4 formation.
- (4)
- (5)

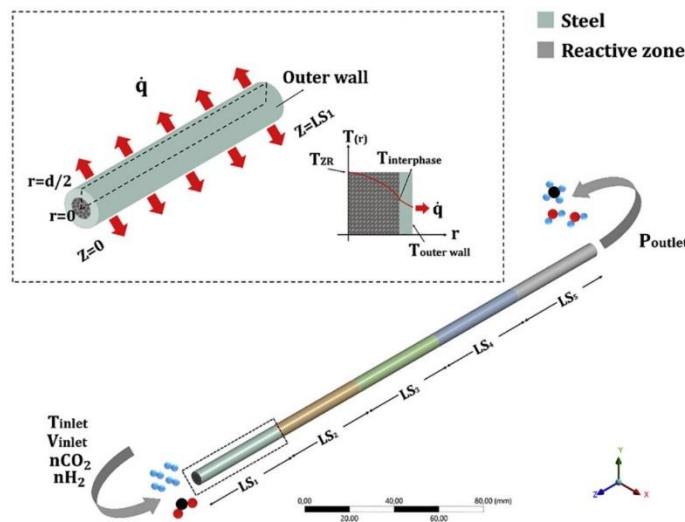


Fig. 2. Geometry design of the fixed-bed reactor tube used on CFD model.

ARTICLE IN PRESS

A. Alarcón et al.

Fuel Processing Technology xxx (xxxx) xxx

3. CFD model

The CFD model proposed in this work was developed using the Ansys®Fluent software, 2019 R2 version. The geometry used for simulation presented the same dimensions than the lab-scale reactor. A schematic representation of the methanation reactor is shown in Fig. 2. In the modelling, the length of the reactor was divided into five symmetric sections of 50 mm (LS_{i=1-5}) to adjust individual heat transfer rates along the reactor tube.

A dynamic meshing design of the 3D geometry model was created with a total of six cell zones using 43,078 nodes. One cell zone was identified as the reactive zone with homogeneous porous medium composed by catalyst and gas mixture and the others five as solid zones. Eight principal zones were also defined as boundary conditions: the gas inlet mixture, the gas outlet mixture, the tube length sections (LS_{i=1-5}), and the interface. The set of partial differential equations involved in the mathematical model were derived from the integration of three sub-models: i) energy, ii) species transport, and iii) viscous. The governing equations of the Ansys®Fluent software can be found in the Appendix of the Supporting Information.

The apparent kinetic parameters were obtained in a previous work [51]. Two empirical power law rate expressions were used for the forward and the backward reaction, presuming arbitrary orders only for CO₂ and H₂ (Eqs. (6) and (7)), while reverse water gas shift reaction was neglected in the model. A more detailed experimental kinetic study on this catalyst could improve adjust of the kinetic model to experimental conditions. For instance, by adjusting the influence of CH₄ and H₂O products to the kinetics and to evaluate the influence of CO formation in the model.

Kinetic expression for forward reaction

$$r_f (\text{mol} \cdot \text{m}^{-3} \cdot \text{s}^{-1}) = 8.38 \cdot 10^7 e^{-6.20 \cdot 10^7 / RT} \cdot (C_{\text{CO}_2})^{0.171} \cdot (C_{\text{H}_2})^{0.683} \quad (6)$$

Kinetic expression for backward reaction

$$r_b (\text{mol} \cdot \text{m}^{-3} \cdot \text{s}^{-1}) = 8.78 \cdot 10^{17} e^{-2.33 \cdot 10^8 / RT} \cdot (C_{\text{CO}_2})^{-0.829} \cdot (C_{\text{H}_2})^{-3.316} \quad (7)$$

The physical properties for the reactive zone (rz), such as specific heat ($C_{p,rz} = 6,433 \text{ J} \cdot \text{kg}^{-1} \cdot \text{K}^{-1}$), thermal conductivity ($\lambda_{r,z} = 0.34 \text{ W} \cdot \text{m}^{-1} \cdot \text{K}^{-1}$) and viscosity ($\mu_{r,z} = 1.23 \cdot 10^{-06} \text{ kg} \cdot \text{m}^{-1} \cdot \text{K}^{-1}$) were obtained through the NIST data base [52] and defined as constant values. The species (H₂, CO₂, CH₄ and H₂O) were modelled as ideal gas and their mass diffusivity were calculated by the kinetic theory. Steel was selected as material of the reactor tube and its thermal conductivity (λ_s) was $16.27 \text{ W} \cdot \text{m}^{-1} \cdot \text{K}^{-1}$. Newton's law of cooling (Eq. (8)) was used to model the convective heat loss to the surroundings from the outer wall.

$$\dot{q} = h\Delta T = h(T_{\text{outerwall}} - T_{\infty}) \quad (8)$$

where \dot{q} is the heat flux density [$\text{W} \cdot \text{m}^{-2}$], h is the free convective heat coefficient of the fluid [$\text{W} \cdot \text{m}^{-2} \cdot \text{K}^{-1}$] and ΔT is the temperature difference [K] between outer wall temperature ($T_{\text{outerwall}}$) and the bulk temperature (T_{∞}). The heat flux, \dot{q} , for each reactor section was estimated assuming a bulk temperature of 298 K and considering the temperature connexion between reactive zone, tube innerwall as well as tube outerwall. Temperature behaviour between them was simulated by using a coupling tool under the assumption that the reduction of temperature was from reactive zone to tube outerwall.

The reactor modelling was carried out under the following assumptions: the gas mixture was preheated to the inlet temperature, the gas velocity was uniform, the operating pressure was defined at outlet reactor tube, the pressure drop along the axial reactor coordinate was neglected and the heat of the reaction was transferred from the pipe wall to the surroundings. A summary of reactor dimensions, properties and operating parameters used in the simulations are presented in Table 1. The set of partial equations were solved by the pressure-based Navier-Stokes algorithm with a steady-state time dependence. The pressure-

Table 1

Summary of reactor dimensions, properties and operating parameters used on the CFD model.

Reactor dimension	Symbol	Value	Unit
Inner diameter	D _i	4.6	mm
Outer diameter	D _o	6.4	mm
Length	L	250	mm
Length sections	LS _{i=1-5}	50	mm
Property	Symbol	Value	Unit
Thermal conductivity of the steel reactor tube	λ_s	16.27	$\text{W} \cdot \text{m}^{-1} \cdot \text{K}^{-1}$
Specific heat of the reactive zone ^a	C _{p,rz}	6433	$\text{J} \cdot \text{kg}^{-1} \cdot \text{K}^{-1}$
Thermal conductivity of the reactive zone ^a	$\lambda_{r,z}$	0.34	$\text{W} \cdot \text{m}^{-1} \cdot \text{K}^{-1}$
Viscosity of the reactive zone ^a	$\mu_{r,z}$	$1.23 \cdot 10^{-06}$	$\text{kg} \cdot \text{m}^{-1} \cdot \text{K}^{-1}$
Temperature of the exterior	T _∞	298	K
Heat transfer coefficient of air ^b	h _{air}	19.45	$\text{W} \cdot \text{m}^{-2} \cdot \text{K}^{-1}$
Operating parameter	Symbol	Value	Unit
Molar ratio of H ₂ /CO ₂	–	4	–
Mole fraction of H ₂	m _{H2}	80	%
Mole fraction of CO ₂	m _{CO2}	20	%
Temperature of the inlet	T _{inlet}	473–673	K
Pressure	P	1–20	atm
Gas hourly space velocity	GHSV	6834–13,676	h^{-1}

^a Calculated using NIST data base.

^b Calculated at V_{air} = 1 m·s⁻¹ to guarantee a free convection.

velocity coupling with a Simplec scheme was selected as solution methods. The number of iterations used in each simulation was 2000.

4. Result and discussion

4.1. CO₂ methanation tests

The first CO₂ methanation tests were conducted in the reactor setup by varying the gas flowrate in the range of GHSV = 3,039–18,235 h⁻¹ at atmospheric pressure. The reaction start-up was carried out by pre-heating of inlet gas at T_{inlet} of 573 K. As soon as the reaction started, temperatures along the reactor increased gradually due to the exothermicity of the methanation reaction. Steady-state conditions were obtained after 35–85 min, depending on the used gas flowrate. The maximum temperature of the reactor was self-restricted at T_{max} < 823 K to avoid catalyst degradation by limiting the inlet gas flowrates.

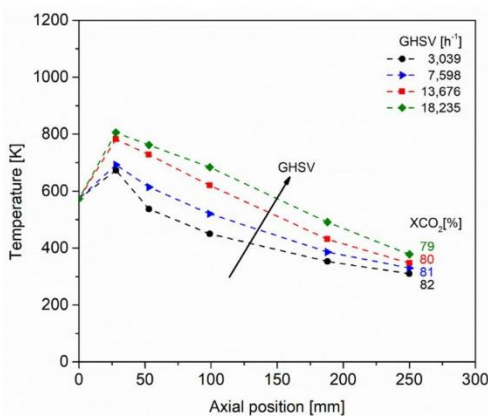


Fig. 3. Experimental temperature profiles by varying GHSV at P = 1 atm and T_{inlet} = 573 K.

As it can be observed in Fig. 3, non-isothermal temperature profiles were always obtained. The operation using decreasing temperature profiles is preferred to isothermal operation to reduce the reactor volume by a compromise of kinetics and equilibrium conditions [53]. Otherwise, in isothermal operation, a higher temperature can lead to equilibrium restrictions and lower temperature to kinetics ones. The highest temperatures ($T_{\max} = 673\text{--}806\text{ K}$) were detected close to the reactor inlet (axial position 28 mm) and the lowest ones ($T_{\min} = 310\text{--}378\text{ K}$) were recorded at the reactor outlet (axial position 250 mm). This first series of experiments revealed that higher temperatures along the reactor were obtained at higher GHSV values. Accordingly, it was confirmed that a simple way to control the temperature profile in the proposed reactor heat-management configuration is by adjusting the inlet gas flowrate. In such a way that the reactor can be heated up by increasing the gas flowrate and cooled-down by lowering it.

At the tested conditions, CO_2 conversions slightly decreased from 82 to 79% by increasing the GHSV from $3,039$ to $18,235\text{ h}^{-1}$. In this aspect, the decrease of the conversion ($\sim 3\%$) was really low compared to the reduction of the gas residence time in the reactor ($\sim 88\%$). The CO_2 conversion pattern was a consequence of two opposite effects; high GHSV led to higher reaction temperatures but lower residence times for reaction. As observed, the operation at higher temperatures was more decisive than lowering the gas residence time. This behaviour is probably a consequence that kinetic values depend exponentially on the temperature, while residence time does not have this strong dependence on the reaction rates. In any case, the maximum experimental CO_2 conversion achieved during this first set of experiments was 82%.

The achieved level of conversion is still too low for industrial applications [53], and below the scope of the present work ($\geq 90\%$). An experimental alternative to achieve conversion close (91–84%) to the equilibrium at these conditions was adjusting the temperatures by addition of external heat to the last zone of the reactor. In this second set of experiments (see Figure S15), the most favourable conditions were obtained when the lowest temperature was higher than 573 K. Therefore, optimal conditions cannot be obtained by simply adjusting the inlet flowrate. A suitable and effective technique to obtain the optimum reaction conditions able to achieve a high conversion level is by CFD modelling.

4.2. CFD model validation

At first, the CFD model was validated using the experimental case carried out at $P = 1\text{ atm}$, $T_{\text{inlet}} = 573\text{ K}$ and $\text{GHSV} = 13,676\text{ h}^{-1}$. The parameters used in this simulation are described in Table 1. The length of the reactor was divided into five symmetric sections of 50 mm ($LS_{i=1-5}$) and the heat transfer values from the system to the surrounding were adjusted in each reaction zone. At the selected experimental condition, the amount of heat released to the surroundings was in the range of $[-9,415\text{--}2,053]\text{ W}\cdot\text{m}^{-2}$. The amount of heat transferred was higher at the initial reaction zone and decreased along the reactor tube. This is a consequence of higher driving force, i.e. higher temperature difference between the system and the surroundings.

Fig. 4 compares the experimental and the CFD simulation results. As can be seen, the temperature profile and the conversion level obtained from simulation were very close to the experimental results. The highest temperature ($T_{\max} = 775\text{ K}$) was detected close to the reactor inlet and the lowest temperature ($T_{\min} = 358\text{ K}$) at reactor outlet. Only small divergences were obtained in the conversion level ($\pm 2\%$). In fact, the lower experimental conversion ($X_{\text{CO}_2} = 80\%$) can be a consequence of the lower temperature at the reactor outlet. Therefore, these results confirmed the suitability of the proposed CFD model to optimize the reactor parameters, as well as, to determine the heat fluxes of the proposed reactor design.

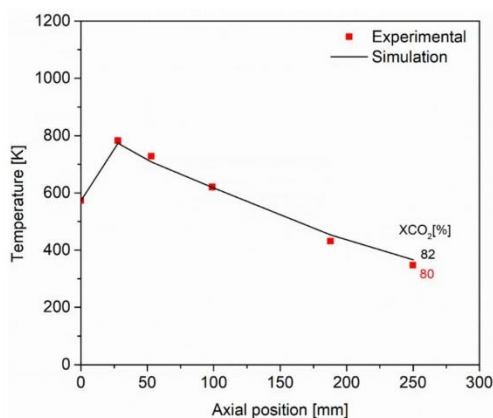


Fig. 4. CFD model validation: comparison between experimental and simulated temperature profiles. Reaction conditions: $\text{GHSV} = 13,676\text{ h}^{-1}$, $T_{\text{inlet}} = 573\text{ K}$ and $P = 1\text{ atm}$.

4.3. Sensitive analysis of the reaction conditions

As the experimental results were successfully described by the developed CFD model, the influence of the operational parameters was further evaluated using this tool. The influence of P , T_{inlet} and GHSV on temperature profile was studied in the range of $473\text{--}673\text{ K}$, $1\text{--}20\text{ atm}$ and $6837\text{--}13,676\text{ h}^{-1}$, respectively. The sensitive analysis of the reaction parameters was performed using the following 2 criteria i) CO_2 conversion higher than 90%, ii) maximum temperature lower than 830 K. A total of 29 reactor configurations were studied. All simulation results are summarized in the Table S1.

As representative example, the influence of the pressure on temperature profiles at $T_{\text{inlet}} = 573\text{ K}$ and $\text{GHSV} = 13,676\text{ h}^{-1}$ is displayed in Fig. 5. Note that solid lines are used in the graphs for the conditions that met these criteria, while dashed for those that do not. As a general rule, it was observed that temperatures along the reactor was increased when the pressure was higher. Furthermore, the increase of pressure impacted

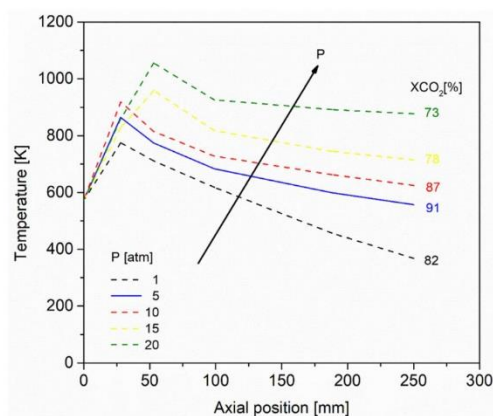


Fig. 5. Influence of P on the temperature profile and the conversion level at $\text{GHSV} = 13,676\text{ h}^{-1}$ and $T_{\text{inlet}} = 573\text{ K}$ obtained by CFD simulation.

ARTICLE IN PRESS

A. Alarcón et al.

Fuel Processing Technology xxx (xxxx) xxx

highly positive to the conversion, attaining 91% at 5 atm. In contrast, a significant reduction on the CO₂ conversion values ($\leq 87\%$) was unexpectedly observed at high pressures ($P \geq 10$ atm). This pattern was related to the reaction equilibrium limits the conversion level at high temperatures ($T_{\max} > 823$ K), which are not favourable to produce CH₄ [54]. Therefore, this highlight allowed the identification of the optimal pressure condition in which the proposed catalytic system can achieve an efficient CO₂ conversion.

The effect of the inlet temperature was evaluated at 5 atm and GHSV = 13,676 h⁻¹ in order to avoid catalyst and reactor degradation due to overheating. The influence of the inlet temperature at those conditions is displayed in Fig. 6, which suggests that the inlet temperature is a strategic parameter to control the formation of the hot spots (T_{\max}) inside of the reactor. A reduction of the inlet temperature below 573 K was positive as increased the conversion level and decreased the overheating, even though more molecules of methane were formed and thus more heat was released. At these conditions, the T_{\max} was lower than 823 K and CO₂ conversions were higher than 92%. These positive results can be related to thermodynamic reaction equilibrium. It well known that high pressures and low temperatures leads to high methane production.

The last parameter evaluated in the sensitive analysis was the GHSV. Fig. 7 shows the temperatures along the reactor tube as a function of the GHSV values at $T_{\text{inlet}} = 523$ K and $P = 5$ atm. As it can be seen, the influence of the inlet GHSV was relevant in both the conversion and the temperature profiles. The highest level of conversion was achieved (97%) at the lowest GHSV (6838 h⁻¹), despite the low reaction temperatures. From these results, it is inferred that the reactor can work, in principle, at GHSV values in the range of $12,307 \text{ h}^{-1} \geq \text{GHSV} \geq 8,205 \text{ h}^{-1}$ at 5 atm without the installation of neither a cooling nor a heating system. At these conditions, temperature of the reaction along the reactor tube can be controlled by the inlet flowrate. On one hand, operation at higher values ($\text{GHSV} \geq 13,676 \text{ h}^{-1}$) demands of an external cooling system to restrict $T_{\max} \leq 823$ K to avoid catalyst degradation. On the other hand, operation at low values ($\text{GHSV} \leq 6838 \text{ h}^{-1}$) demands of an external heating system at the last zone of the reactor to achieve high conversion values. The obtained heat fluxes from the simulations are presented in Table S2.

As mentioned, the target of the present reactor approach is to avoid external cooling and heating of the reactor channel. In short, CFD simulations showed that the conditions for CO₂ methanation can be reached by adjusting the gas flowrate and the pressure. The operation at the

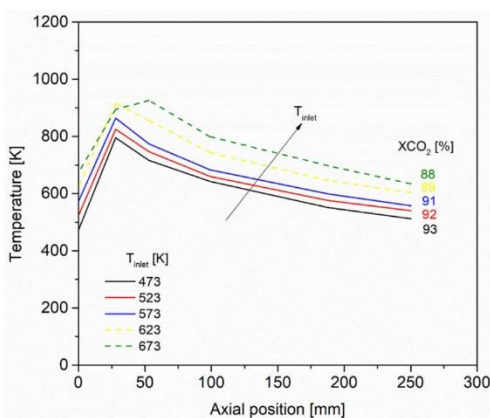


Fig. 6. Influence of T_{inlet} on the temperature profile and the conversion level at $\text{GHSV} = 13,676 \text{ h}^{-1}$ and $P = 5$ atm obtained by CFD simulation.

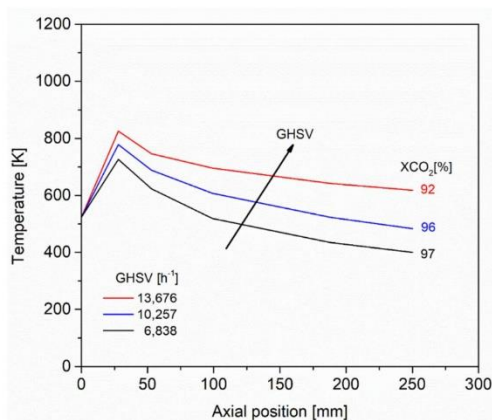


Fig. 7. Influence of GHSV on the temperature profile and the conversion level at $T_{\text{inlet}} = 523$ K and $P = 5$ atm obtained by CFD simulation.

potential zone ($6838 \geq \text{GHSV} \geq 13,676 \text{ h}^{-1}$) can be finally adjusted by the inlet temperature of the gases. As the reactor temperature rose with increasing the inlet temperature (see Fig. 6), a slight decrease of the inlet temperature allows to work at higher GHSV values without exceeding the self-imposed limit temperature.

4.4. Reaction conditions proposal

CFD simulations revealed that a compromise between kinetic, thermodynamic limitations and suitable heat-management is required to achieve high CO₂ conversions. In this aspect, the inlet temperature of the proposed reactor was set at 503 K and the pressure at 5 atm, the minimum values in which $\geq 90\%$ of conversion was achieved. Both conditions are technically feasible in a relevant environment. On the other hand, a $\text{GHSV} = 11,520 \text{ h}^{-1}$ was selected considering the maximum GHSV, in which is possible the operation of the reactor without the implementation of an external cooling and heating system. The increase of the GHSV parameter benefits from a reduction of the necessary reactor volume. A summary of the operational conditions of the reactor design proposal are presented in Table 2.

The temperature profile of the proposed configuration is displayed in Fig. 8, which indicates the feasibility of this reactor approach. At the selected conditions, the simulated CO₂ conversion was 96% and the decreasing temperatures along the reactor tube was in the range of 817–505 K. The main effect of each parameter is described as follows. The temperature of gas pre-heating enables the restriction of the

Table 2
Design proposal for reactor.

Operating parameter	Symbol	Value	Unit
Molar ratio of H ₂ /CO ₂	H ₂ /CO ₂	4	-
Mole fraction of H ₂	m_{H_2}	80	%
Mole fraction of CO ₂	m_{CO_2}	20	%
Temperature of gas mixture	T_{inlet}	503	K
Pressure	P	5	atm
Gas hourly space velocity	GHSV	11,520	h ⁻¹
Heat flux	$\dot{q}_{l,s1}$	17,135	W·m ⁻²
	$\dot{q}_{l,s2}$	15,229	
	$\dot{q}_{l,s3}$	12,979	
	$\dot{q}_{l,s4}$	11,055	
	$\dot{q}_{l,s5}$	9900	

ARTICLE IN PRESS

A. Alarcón et al.

Fuel Processing Technology xxx (xxxx) xxx

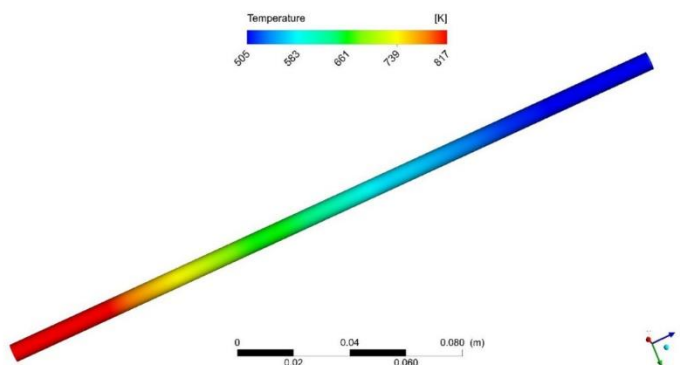


Fig. 8. Temperature profile of the reactor obtained by CFD simulation. Reaction conditions: $GHSV = 11,520 \text{ h}^{-1}$, $T_{\text{inlet}} = 503 \text{ K}$, $P = 5 \text{ atm}$ and H_2/CO_2 molar ratio = 4.

maximum temperature at the initial reaction zone and thus to avoid excessive hot-spots, GHSV allows the management of the reaction temperature along the reactor tube and to avoid external heating or cooling units, and finally, a compromise between the pressure leads to higher conversions.

The validation of the proposed reactor configuration was carried out under the simulated conditions. In this experiment, the operation of the reactor started by fixing the pressure at 5 atm, followed by setting the flow rate at the proposed GHSV of $11,520 \text{ h}^{-1}$ ($F = 930 \text{ NmL}\cdot\text{min}^{-1}$) and switching on the preheater to rise the inlet gas mixture temperature to the desired temperature of 503 K. At these conditions, the experimental temperature profile was quite similar as the simulated one, as shown in Fig. 9. Accordingly, the technical feasibility of the reactor was experimentally validated at lab-scale, as no external heating or cooling was necessary. The experimental temperature was in the range of 830–495 K with a CO_2 conversion equal to 93%, very close to the simulated results. At the low temperature of the outlet, the chemical equilibrium is totally shifted to products. Thus, in principle 100% of conversion could be achieved at very high residence time (see equilibrium data in Fig. S4).

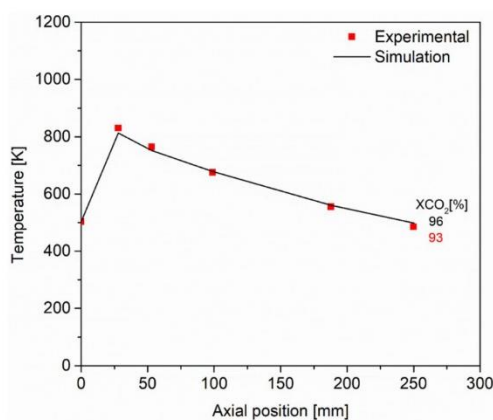


Fig. 9. Experimental and simulation comparison of the proposed reactor conditions. $GHSV = 11,520 \text{ h}^{-1}$, $T_{\text{inlet}} = 503 \text{ K}$, $P = 5 \text{ atm}$ and H_2/CO_2 molar ratio = 4.

With regard to the total heat released to the ambient and CH_4 productivity rate obtained during the process, it was estimated for this proposed reactor design a total heat of 0.07 [kW] and a CH_4 productivity rate of $95.68 \text{ mol}\cdot\text{h}^{-1}\cdot\text{kg}_{\text{cat}}^{-1}$.

Considering that the proposed reactor design can be exposed to the unpredictable variations of the ambient air temperature (T_{air}), additional simulations were then performed to evaluate its effect on temperature profiles and CO_2 conversions. This set of simulations was carried out in a T_{air} range of 273 to 323 K. As is shown in Fig. 10, the thermal operation performance of the proposed reactor design is slightly influenced by the T_{air} . An increase in the temperature along the reactor was detected as soon as the air temperature increases. Nevertheless, all temperatures ($T_{\text{max}} \leq 827$) and CO_2 conversions ($X_{\text{CO}_2} \geq 92\%$) were above the target criteria ($T_{\text{max}} \leq 830 \text{ K}$ and $X_{\text{CO}_2} \geq 90\%$). The most unfavourable result was observed when the T_{air} was the too high, 323 K. At these environment conditions, CO_2 conversion was reduced by 4% and the temperature profile was in the range of 827 to 523 K. Consequently, it is inferred that T_{air} can modify the behaviour of the proposed heat-management approach to a certain degree, which is obviously a drawback of the proposed configuration.

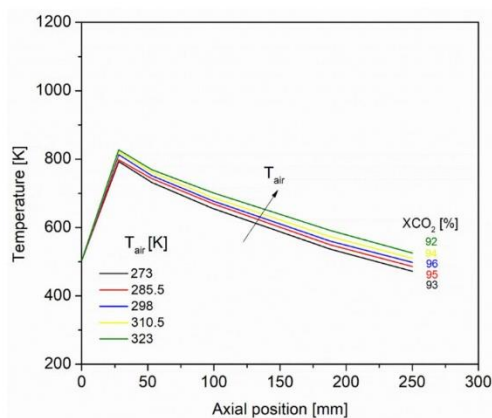


Fig. 10. Influence of T_{air} on the temperature profile and the conversion level at $GHSV = 11,520 \text{ h}^{-1}$, $T_{\text{inlet}} = 503 \text{ K}$, $P = 5 \text{ atm}$ and H_2/CO_2 molar ratio = 4.

4.5. Comparison with other heat-management approaches

The production of $1 \text{ Nm}^3 \cdot \text{h}^{-1}$ of SNG based on a pure CO_2/H_2 mixture was selected as the representative industrial small-scale CO_2 methanation case. According to the reactor dimensions ($d = 4.6 \text{ mm}$, $L = 250 \text{ mm}$), 23 channels will be required to achieve the targeted SNG production rate. It is important to point out that the reactor proposal even works at slightly higher GHSV values ($11,520 \text{ h}^{-1}$) with respect to the commercial technology (9000 h^{-1}) at industrial scale [55]. On the contrary, at much lower GHSV values than the advanced micro-structured reactors ($54,000 \text{ h}^{-1}$) [42] that are in a pre-commercialization state. This as simple as possible thermal approach requires of similar, or slightly lower, volume and catalyst amount than conventional multi-tubular reactors. Nevertheless, in a large-scale power-to-gas application the amount of tubes would be 30-fold larger, considering 25 mm diameter as standard tube diameter for conventional bundle reactors. In this sense, the amount of necessary auxiliaries would be lower, while the amount of tubes would be much larger due to the compromise between reduced dimensions of the tube diameter and operational GHSV values.

On the other hand, the steady-state temperature profile obtained during its experimental validation was reached after approximately 56 min, as it is shown in Fig. 11. It is anticipated that the start-up of the proposed reactor is slower than reactors that include an internal heat exchange system. As an example, the start-up of a micro-structured reactor is carried out in approximately 8–30 min, using both heating and cooling auxiliaries [42]. Another aspect to consider in this heat-management approach is the reaction safety. Reactor runaway can occur in exothermic reactions because of irregular composition of the reactants or some fluctuation of inlet temperature. In those cases, an increase of the reaction temperature can change conditions in a way that it causes a further increase in temperature, leading to a destructive result. This fact can be problematic as no cooling system is proposed to actively control the reactor temperature. Fortunately, this undesired situation can be easily avoided by stopping the CO_2 dosage into the reactor and/or by injecting an auxiliary gas as nitrogen. As soon as no CO_2 is introduced to the reactor, the reactor temperature immediately drops.

In the present work, the main pros and cons of a heat-management for CO_2 methanation based on free convection were disclosed. The main advantage of the present approach is the simple design and low auxiliary requirements of this reactor, especially in decentralized locations where the integration of the exothermic heat to another industrial unit is not technically feasible or, more probably, not economically profitable. In this sense, the proposed reactor can be an alternative to consider for producing synthetic natural gas at reasonable GHSV in decentralized small-scale Power-to-Gas installations, as in most biogenic CO_2 sources.

5. Conclusions

A reactor design using a simple heat-management based on free convection was proposed in this work. The application of this approach is intended for the small-size production of synthetic natural gas from CO_2 catalytic methanation. The technical feasibility of the proposed heat-management was studied through experimentation on a lab-scale single reactor channel (diameter of 4.6 mm and length of 250 mm) and conducting a sensitive analysis by means of a CFD model to disclose the most favourable reaction conditions.

The experimental results revealed that the reaction conditions should be carefully selected as no external heating or cooling units can be used to adjust the temperature profiles and thus to obtain high conversion levels. The experimental data was successfully described by means of the CFD model. Accordingly, CFD modelling appears as a powerful tool that can be used for the optimization of the reaction parameters, rather than excessive experimentation. The sensitive analysis

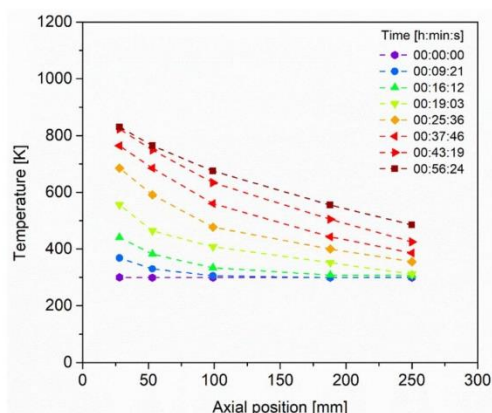


Fig. 11. Experimental evolution of the temperature profile during the reaction start-up. Reaction conditions: GHSV = $11,520 \text{ h}^{-1}$, $T_{\text{inlet}} = 503 \text{ K}$, $P = 5 \text{ atm}$ and H_2/CO_2 molar ratio = 4.

conducted by CFD simulations showed that the operation of the reactor is feasible through a compromise between 3 operation parameters: gas hourly space velocity, inlet temperature and pressure. In parallel, it was observed that the environmental temperature can have an influence on the reactor yield.

The optimal conditions, which met CO_2 conversion higher than 90% and temperature lower than 830 K criteria, were obtained by CFD simulation, and then, experimentally validated. Those conditions were GHSV at $11,520 \text{ h}^{-1}$, inlet temperature of 503 K, pressure of 5 atm, and air temperature of 298 K. Under those conditions, an interesting level of CO_2 conversion (93%) was successfully achieved. The decreasing temperature profile along the reactor was in the range of 830 to 495 K, without the need of external heating or cooling units. Therefore, the proof-of-concept of the operation for CO_2 methanation based on free convection is hereby validated in a single channel reactor at lab-scale. According to the proposed reactor dimensions, 23 channels will be required to achieve the industrial small-scale production of $1 \text{ Nm}^3 \cdot \text{h}^{-1}$ of synthetic natural gas.

Declaration of Competing Interest

None.

Acknowledgements

Authors thank Generalitat de Catalunya for financial support through the CERCA Programme, M2E (2017SGR1246) and XaRMAE network. IREC also gratefully acknowledge the funding of this work by the CoSin project (COMRD15-1-0037), funded by ACCIÓ and the European Regional Development Fund (ERDF) under the framework of RIS3CAT Energy Community. Andreina Alarcón is grateful to Escuela Superior Politécnica del Litoral (ESPOL) for the support during her postgraduate studies (“Walter Valdano Raffo” Program, First edition).

Appendix A. Supplementary data

Supplementary data to this article can be found online at <https://doi.org/10.1016/j.fuproc.2020.106666>.

References

- [1] M. Lehner, R. Tichler, H. Steinmüller, M. Koppe, *Power-to-Gas: Technology and Business Models*, Springer International Publishing, Cham, 2014, <https://doi.org/10.1007/978-3-319-03995-4>.
- [2] M. Götz, J. Lefebvre, F. Mörz, A. McDaniel Koch, F. Graf, S. Bajohr, R. Reimert, T. Kolb, Renewable power-to-gas: a technological and economic review, *Renew. Energy* 85 (2016) 1371–1390, <https://doi.org/10.1016/j.renene.2015.07.066>.
- [3] J. Guileira, J. Ramon Morante, T. Andreu, Economic viability of SNG production from power and CO₂, *Energy Convers. Manag.* 162 (2018) 218–224, <https://doi.org/10.1016/j.enconman.2018.02.037>.
- [4] R.R. Boggula, D. Fischer, R. Casaretto, J. Born, Methanation potential: Suitable catalyst and optimized process conditions for upgrading biogas to reach gas grid requirements, *Biomass Bioenergy* 133 (2020) 105447, <https://doi.org/10.1016/j.biombioe.2019.105447>.
- [5] S. Belleochi, M. De Falco, M. Gambini, M. Manno, T. Stilo, M. Vellini, Opportunities for power-to-gas and power-to-liquid in CO₂-reduced energy scenarios: the Italian case, *Energy*, 175 (2019) 847–861, <https://doi.org/10.1016/j.energy.2019.03.116>.
- [6] J. Lindorfer, M. Lehner, D.C. Rosenfeld, B. Hans, Scenario analysis of implementing a power-to-gas and biomass gasification system in an integrated steel plant: a techno-economic and environmental study, *Renew. Energy* 147 (2020) 1511–1524, <https://doi.org/10.1016/j.renene.2019.09.053>.
- [7] X. Wang, Z. Bie, F. Liu, Y. Kou, L. Jiang, Bi-level planning for integrated electricity and natural gas systems with wind power and natural gas storage, *Int. J. Electr. Power Energy Syst.* 118 (2020) 105738, <https://doi.org/10.1016/j.ijepes.2019.105738>.
- [8] A. Basnet, J. Zhong, Electrical power and energy systems integrating gas energy storage system in a peer-to-peer community energy market for enhanced operation, *Electr. Power Energy Syst.* 118 (2020) 105789, <https://doi.org/10.1016/j.ijepes.2019.105789>.
- [9] R. Chauvy, L. Dubois, P. Lybaert, D. Thomas, G. De Weireld, Production of synthetic natural gas from industrial carbon dioxide, *Appl. Energy* 260 (2020) 114249, <https://doi.org/10.1016/j.apenergy.2019.114249>.
- [10] A. Crivellari, V. Cozzani, Offshore renewable energy exploitation strategies in remote areas by power-to-gas and power-to-liquid conversion, *Int. J. Hydrog. Energy* 45 (2020) 2936–2953, <https://doi.org/10.1016/j.ijhydene.2019.11.215>.
- [11] A.K. Karmaker, M.M. Rahman, M.A. Hossain, M.R. Ahmed, Exploration and corrective measures of greenhouse gas emission from fossil fuel power stations for Bangladesh, *J. Clean. Prod.* 244 (2020) 118645, <https://doi.org/10.1016/j.jclepro.2019.118645>.
- [12] A. Malara, P. Frontera, P. Antonucci, A. Macario, Smart recycling of carbon oxides: current status of methanation reaction, *Curr. Opin. Green Sustain. Chem.* 100376 (2020), <https://doi.org/10.1016/j.cogsc.2020.100376>.
- [13] P. Frontera, A. Macario, M. Ferraro, P. Antonucci, Supported catalysts for CO₂ methanation: a Review, *Catalysts* 7 (2017) 59, <https://doi.org/10.3390/catal7020059>.
- [14] W. Wei, G. Jinlong, Methanation of carbon dioxide: an overview, *Front. Chem. Sci. Eng.* 5 (2011) 2–10, <https://doi.org/10.1007/s11705-010-0528-3>.
- [15] W. Ahmad, M.N. Younis, R. Shawabkeh, S. Ahmed, Synthesis of lanthanide series (La, Ce, Pr, Eu & Gd) promoted Ni/Ti-Al₂O₃ catalysts for methanation of CO₂ at low temperature under atmospheric pressure, *Catal. Commun.* 100 (2017) 121–126, <https://doi.org/10.1016/j.catcom.2017.06.044>.
- [16] J. Liu, W. Shen, D. Cui, J. Yu, F. Su, G. Xu, Syngas methanation for substitute natural gas over Ni-Mg/Al₂O₃ catalyst in fixed and fluidized bed reactors, *Catal. Commun.* 38 (2013) 35–39, <https://doi.org/10.1016/j.catcom.2013.04.014>.
- [17] A. Zhao, W. Ying, H. Zhang, H. Ma, D. Fang, La and Mn promotion of Ni/Al₂O₃ catalysts for syngas methanation, *Energy Sour. Part A: Recover. Util. Environ. Effect* 36 (2014) 1049–1056, <https://doi.org/10.1080/15567036.2012.666621>.
- [18] J. Guileira, J. del Valle, A. Alarcón, J.A. Díaz, T. Andreu, Metal-oxide promoted Ni/Al₂O₃ as CO₂ methanation micro-size catalysts, *J. CO₂ Util.* 30 (2019) 11–17, <https://doi.org/10.1016/j.jcou.2019.01.003>.
- [19] G. Garbarino, C. Wang, T. Cavattoni, E. Finocchio, P. Riani, M. Flytzani-Stephanopoulos, G. Busca, A study of Ni/La-Al₂O₃ catalysts: a competitive system for CO₂ methanation, *Appl. Catal. B Environ.* 248 (2019) 286–297, <https://doi.org/10.1016/j.apcatb.2018.12.063>.
- [20] L. Kiewidt, J. Thöming, Predicting optimal temperature profiles in single-stage fixed-bed reactors for CO₂-methanation, *Chem. Eng. Sci.* 132 (2015) 59–71, <https://doi.org/10.1016/j.ces.2015.03.068>.
- [21] M. Martinez Molina, C. Kern, A. Jess, Catalytic hydrogenation of carbon dioxide to methane in wall-cooled fixed-bed reactors, *Chem. Eng. Technol.* 39 (2016) 2404–2415, <https://doi.org/10.1002/ceat.201500614>.
- [22] J. Bremer, H.G.R. Karsten, K. Sundmacher, CO₂ Methanation: optimal start-up control of a fixed-bed reactor for power-to-gas applications, *Am. Inst. Chem. Eng.* 63 (2017) 23–31, <https://doi.org/10.1002/aic>.
- [23] J. Ducamp, A. Bengouer, P. Baurens, Modelling and experimental validation of a CO₂ methanation annular cooled fixed-bed reactor exchanger, *Can. J. Chem. Eng.* 95 (2017) 241–252, <https://doi.org/10.1002/cjce.22706>.
- [24] C. Schüler, M. Wolf, O. Hinrichsen, Contactless temperature measurements under static and dynamic reaction conditions in a single-pass fixed bed reactor for CO₂ methanation, *J. CO₂ Util.* 25 (2018) 158–169, <https://doi.org/10.1016/j.jcou.2018.03.016>.
- [25] R. Currie, S. Mottaghi-tabar, Y. Zhuang, D.S.A. Simakov, Design of an air-cooled Sabatier reactor for thermochemical hydrogenation of CO₂: experimental proof-of-concept and model-based feasibility analysis, *Ind. Eng. Chem. Res.* 58 (2019) 12964–12980, <https://doi.org/10.1021/acs.iecr.9b01426>.
- [26] E. Giglio, F.A. Deorsola, M. Gruber, S.R. Harth, E.A. Morosanu, D. Trimis, S. Bensaïd, R. Pirone, Power-to-gas through high temperature electrolysis and carbon dioxide methanation: reactor design and process modeling, *Ind. Eng. Chem. Res.* 57 (2018) 4007–4018, <https://doi.org/10.1021/acs.iecr.8b00477>.
- [27] N. Engelbrecht, S. Chiuta, R.C. Everson, H.W.J.P. Neomagus, D.G. Bessarabov, Experimentation and CFD modelling of a microchannel reactor for carbon dioxide methanation, *Chem. Eng. J.* 313 (2017) 847–857, <https://doi.org/10.1016/j.cej.2016.10.131>.
- [28] C. Jia, Y. Dai, Y. Yang, J.W. Chew, A fluidized-bed model for NiMgW-catalyzed CO₂ methanation, *Particuology* 49 (2020) 55–64, <https://doi.org/10.1016/j.partic.2019.05.004>.
- [29] J. Lefebvre, N. Trudel, S. Bajohr, T. Kolb, A study on three-phase CO₂ methanation reaction kinetics in a continuous stirred-tank slurry reactor, *Fuel* 217 (2018) 151–159, <https://doi.org/10.1016/j.fuel.2017.12.082>.
- [30] Y. Rodríguez-Guerra, L.A. Gerling, E.A. López-Guajardo, F.J. Lozano-García, K.D. P. Nigam, A. Montesinos-Castellanos, Design of micro- and milli-channel heat exchanger reactors for homogeneous exothermic reactions in the laminar regime, *Ind. Eng. Chem. Res.* 55 (2016) 6435–6442, <https://doi.org/10.1021/acs.iecr.6b00323>.
- [31] R. Dittmeyer, T. Boeltken, P. Piermartini, M. Selinsek, M. Loewert, F. Dallmann, H. Kreuder, M. Cholewa, A. Wunsch, M. Belimov, S. Farsi, P. Pfeifer, Micro and micro membrane reactors for advanced applications in chemical energy conversion, *Curr. Opin. Chem. Eng.* 17 (2017) 108–125, <https://doi.org/10.1016/j.coche.2017.08.001>.
- [32] D. Türks, H. Mena, U. Armbruster, A. Martin, Methanation of CO₂ on Ni/Al₂O₃ in a structured fixed-bed reactor—a scale-up study, *Catalysts* 7 (2017) 152, <https://doi.org/10.3390/catal7050152>.
- [33] B. Kreitz, G.D. Wehinger, T. Turek, Dynamic simulation of the CO₂ methanation in a micro-structured fixed-bed reactor, *Chem. Eng. Sci.* 195 (2019) 541–552, <https://doi.org/10.1016/j.ces.2018.09.053>.
- [34] M. Neubert, A. Hauser, B. Pourhossein, M. Dillig, J. Karl, Experimental evaluation of a heat pipe cooled structured reactor as part of a two-stage catalytic methanation process in power-to-gas applications, *Appl. Energy* 229 (2018) 289–298, <https://doi.org/10.1016/j.apenergy.2018.08.002>.
- [35] S. Pérez, J.J. Aragón, I. Pecina, E.J. Garcia-Suarez, Enhanced CO₂ methanation by new microstructured reactor concept and design, *Top. Catal.* (2019), <https://doi.org/10.1007/s11244-019-01139-4>.
- [36] S. Neuberger, H. Pennemann, V. Shanmugam, R. Thiermann, R. Zapf, W. Gac, M. Greluk, W. Zawadzki, G. Kolb, CO₂ methanation in microstructured reactors – catalyst development and process design, *Chem. Eng. Technol.* 42 (2019) 2076–2084, <https://doi.org/10.1002/ceat.201900132>.
- [37] M. Belimov, D. Metsger, P. Pfeifer, On the temperature control in a micro structured packed bed reactor for methanation of CO/CO₂ mixtures, *Am. Inst. Chem. Eng. J.* 61 (2014) 1–15, <https://doi.org/10.1002/aic>.
- [38] D. Schollenberger, S. Bajohr, M. Gruber, R. Reimert, T. Kolb, Scale-up of innovative honeycomb reactors for power-to-gas applications – the project Store&Go, *Chemie-Ingenieur-Technik* 90 (2018) 696–702, <https://doi.org/10.1002/cite.201700139>.
- [39] M. Gruber, C. Wisland, P. Habisreuther, D. Trimis, D. Schollenberger, S. Bajohr, O. VonMorstein, S. Schirmmeister, Modeling and design of a catalytic wall reactor for the methanation of carbon dioxide, *Chem. Ingenieur Tech.* 90 (2018) 615–624, <https://doi.org/10.1002/cite.201700160>.
- [40] S. Rönisch, J. Schneider, S. Marthuschke, M. Schlüter, M. Götz, J. Lefebvre, P. Prabhakaran, S. Bajohr, Review on methanation – from fundamentals to current projects, *Fuel* 166 (2016) 276–296, <https://doi.org/10.1016/j.fuel.2015.10.111>.
- [41] Z. Anstiommez, M. Cabassud, C. Goudon, P. Tochon, Heat exchanger/reactors (HEX reactors): concepts, technologies, *Chem. Eng. Process. Process Intensif.* 42 (2008) 2029–2050.
- [42] J. Guileira, T. Boeltken, F. Timm, I. Mallol, A. Alarcón, T. Andreu, Pushing the limits of SNG process intensification: high GHSV operation at pilot scale, *ACS Sustain. Chem. Eng.* 8 (2020) 8409–8418.
- [43] N. Engelbrecht, R.C. Everson, D. Bessarabov, Thermal Management and Methanation Performance of a Microchannel-Based Sabatier Reactor/Heat Exchanger Utilising Renewable Hydrogen 208, 2020, <https://doi.org/10.1021/acscuschemeng.0c02642>.
- [44] Z. Shao, S.M. Haile, J. Ahn, P.D. Ronney, Z. Zhan, S.A. Barnett, A thermally self-sustained micro solid-oxide fuel-cell stack with high power density, *Nature* 435 (2005) 795–798, <https://doi.org/10.1038/nature03673>.
- [45] B.F. Hagh, Optimization of autothermal reactor for maximum hydrogen production, *Int. J. Hydrog. Energy* 28 (2003) 1369–1377, [https://doi.org/10.1016/S0360-3199\(02\)00292-6](https://doi.org/10.1016/S0360-3199(02)00292-6).
- [46] E. Moio, N. Gallandat, A. Züttel, Model based determination of the optimal reactor concept for Sabatier reaction in small-scale applications over Ru/Al₂O₃, *Chem. Eng. J.* 371 (2019) 121954, <https://doi.org/10.1016/j.cej.2019.121954>.
- [47] J. Bremer, K. Sundmacher, Operation range extension via hot-spot control for catalytic CO₂ methanation reactors, *React. Chem. Eng.* 4 (2019) 1019–1037, <https://doi.org/10.1039/C9RE00147F>.
- [48] W. Zhang, H. Machida, H. Takano, K. Izumiya, K. Norinaga, Computational fluid dynamics simulation of CO₂ methanation in a shell-and-tube reactor with multi-region conjugate heat transfer, *Chem. Eng. Sci.* 211 (2020) 115276, <https://doi.org/10.1016/j.ces.2019.115276>.
- [49] A. Alarcón, J. Guileira, J.A. Díaz, T. Andreu, Optimization of nickel and ceria catalyst content for synthetic natural gas production through CO₂ methanation, *Fuel Process. Technol.* 193 (2019) 114–122, <https://doi.org/10.1016/j.fuproc.2019.05.008>.

ARTICLE IN PRESS

A. Alarcón et al.

Fuel Processing Technology xxx (xxxx) xxx

- [50] A. Alarcón, J. Guilera, R. Soto, T. Andreu, Higher tolerance to sulfur poisoning in CO₂ methanation by the presence of CeO₂, *Appl. Catal. B Environ.* 263 (2020) 118346, <https://doi.org/10.1016/j.apcatb.2019.118346>.
- [51] A. Alarcón, J. Guilera, T. Andreu, CO₂ conversion to synthetic natural gas: Reactor design over Ni-Ce/Al₂O₃ catalyst, *Chem. Eng. Res. Des.* (2018), <https://doi.org/10.1016/j.cherd.2018.10.017>.
- [52] J.J. Freeman, NIST Chemistry WebBook, SRD 69, National Institute of Standards and Technology. <http://webbook.nist.gov/chemistry/>, 2017 (accessed 11 July 1968).
- [53] J. Guilera, T. Andreu, N. Basset, T. Boeltken, F. Timm, I. Mallol, J.R. Morante, Synthetic natural gas production from biogas in a waste water treatment plant, *Renew. Energy* 146 (2020) 1301–1308, <https://doi.org/10.1016/j.renene.2019.07.044>.
- [54] J. Gao, Y. Wang, Y. Ping, D. Hu, G. Xu, F. Gu, F. Su, A thermodynamic analysis of methanation reactions of carbon oxides for the production of synthetic natural gas, *RSC Adv.* 2 (2012) 2358, <https://doi.org/10.1039/c2ra00632d>.
- [55] Man Energy Solutions, Methanation Reactors. [https://dwe.man-es.com/chemical-reactors/tubular-reactors-with-atr-oil-boiling-and-pressure-water-cooling/methanation-reactors-\(sng\)](https://dwe.man-es.com/chemical-reactors/tubular-reactors-with-atr-oil-boiling-and-pressure-water-cooling/methanation-reactors-(sng)), 2018.

Chapter

*Conclusions, outlook, and
recommendations*

Conclusions

In this thesis, it was designed a high-performance ternary catalyst composed by Ni as active phase, CeO₂ as promoter and γ -Al₂O₃ microspheres as support. A straightforward and scalable wet impregnation method was implemented to manufacture the proposed Ni-CeO₂/ γ -Al₂O₃ catalyst. Special focus was done on evaluating its catalytic performance, stability, sulfur tolerance, and implementation in a relevant industrial environment (CoSin project) in order to prove its technical feasibility. Moreover, CFD models based on experimental kinetic data were developed to understand the role of the operation conditions, to optimize conventional fixed-bed reactor prototype, and to propose a novel fixed-bed reactor configuration.

The main conclusions of this thesis are:

- Metal-oxides (CeO₂, La₂O₃, Y₂O₃, Sm₂O₃ and ZrO₂) were implemented as the promoter phase (X) on micro-sized Ni-X/ γ -Al₂O₃ catalysts. The strategy of adding promoters was found to be positive in terms of both initial activity and stability. La₂O₃ and CeO₂ were the most promising promoters and they provided similar physicochemical properties, as it was identified by characterization analysis. The beneficial effects of the promoters on CO₂ conversion were mainly explained by the enhanced interaction between CO₂ and catalyst. In particular, it was found that La₂O₃ and CeO₂ promote the formation of moderate basic sites, thereby enhancing the ability of CO₂ adsorption and catalytic stability. Between both, CeO₂ was selected as more cost-effective promoter.
- The selected ternary catalyst based on Ni as active, CeO₂ as promoter and γ -Al₂O₃ micro-spheres as support was further optimized through an innovative systematic experimental design to find an optimum Ni-CeO₂/ γ -Al₂O₃ formulation. A proper balance between the positive effects of each component of this ternary catalytic system was found when 25 wt.% Ni and 20 wt.% CeO₂ were impregnated on 55 wt.% γ -Al₂O₃. The optimized Ni-CeO₂/ γ -Al₂O₃ catalyst displayed a high activity ($X_{\text{CO}_2} \approx 91\%$) and a high reaction rate ($6.46 \text{ mol} \cdot \text{h}^{-1} \cdot \text{g}_{\text{Ni}}^{-1}$), when compared with other similar catalysts in literature. Furthermore, the catalyst presented successful stability over 120 h run at 300 °C and 5 bar-g.
- The effect of the active phase (Ni), promoter (CeO₂) and support (γ -Al₂O₃ microspheres) were identified by means of advanced characterization analysis. The main contribution of each component in the optimized Ni-CeO₂/ γ -Al₂O₃ formulation was described as follows: Ni mainly provides a proper metallic surface area for reaction; CeO₂ is a key component to enhances both the reducibility of the Ni and the activation of acidic CO₂ on the catalyst support's surface; and, γ -

Al_2O_3 contributes with enough porosity for nickel dispersion and gas transfer. The synergy effects between all optimized components allowed that the Ni-CeO₂/ γ -Al₂O₃ catalyst achieved +25% of productivity than a commercial reference.

- The catalytic stability and sulfur tolerance over the optimized Ni-CeO₂/ γ -Al₂O₃ catalyst was evaluated under high temperature (T=500 °C), with and without the presence of H₂S impurities (1-5 ppm). The high stability (X_{CO_2} =88%) detected at T=500 °C was explained by the formation of nanocomposite between Ni and CeO₂ particles that promotes the metal-promoter interaction. On the other hand, the high tolerance (X_{CO_2} =25%) achieved in presence of H₂S impurities was derived by the presence of Ce₂O₂S. The formation of this phase was thermodynamically favourable and it restricts the formation of nickel sulfide, as it was confirmed by HRTEM analysis. Therefore, the promoted CeO₂ particles on the Ni/ γ -Al₂O₃ catalyst act as sacrificial functional groups that make the catalyst lifespan longer lasting.
- The implementation of the micro-sized Ni-CeO₂/ γ -Al₂O₃ catalyst was evaluated at relevant industrial environment (CoSin project). The catalyst was implemented on a two-stage microstructured reactor system to evaluate its technical feasibility using biogas or upgraded CO₂ as carbon source from a wastewater treatment plant. The scale-up of the catalyst manufacture was performed using a straightforward wet impregnation method. Using this technique, it was delivered a catalyst production of 105 g to the plant. The desired gas composition for grid injection ($\geq 92.5\%$ CH₄, $\leq 5\%$ H₂, and $\leq 2.5\%$ CO₂) over the micro-size catalyst was achieved after the second methanation step using a non-isothermal temperature profile (T= 275-475 °C) and pressure of 5 bar.g. Catalyst deactivation during the 2000 h of experimentation was not evidenced. Therefore, the successful performance and stability achieved on the industrial-scale two-stage microstructured reactor system demonstrated the technical feasibility of this micro-sized Ni-CeO₂/ γ -Al₂O₃ for CO₂ methanation.
- The implementation of a nickel-cerium-alumina catalyst on a designed multitubular fixed-bed exchanger reactor for CO₂ methanation was studied. A 3D CFD mathematical model based on kinetic data was developed to optimize its temperature profile and propose this reactor approach for a mid-size SNG capacity plant. An balance to obtain an optimum temperature profile aiming a high conversion (X_{CO_2} =99%) was found using a reactor tube with an inner diameter of 9.25 mm and a length of 250 mm, which operates at $T_{\text{inlet}}=473$ K, $T_{\text{wall}}=373$ K, GHSV=14,400 h⁻¹, P=5 atm. Simulations proved that design reactor parameters, specially the reactor inner diameter is a key parameter to reduce the formation of hot spot ($\Delta T=100$ K) on the reactor tube. According to the proposed reactor tube

dimensions, almost of 1000 tubes will be required for CO₂ methanation of 100 Nm³·h⁻¹ biogas.

- For small-scale SNG production, a different fixed-bed reactor design was studied. In this case, a novel heat-management approach based on free convection was proposed for reducing the investment costs. To explore this novel reactor design approach, a reactor tube ($d_i= 4.6$ mm and $L=250$ mm) was built at lab-scale, experimentally evaluated, and then simulated through a 3D CFD mathematical model to optimize the reaction parameters. According to simulation, the optimal conditions to guarantee high CO₂ conversion without the need of external heating or cooling units were found at GHSV=11,520 h⁻¹, $T_{inlet}=503$ K, $P= 5$ atm and $T_{air}=298$ K. The feasibility of the simulated reactor approach was further experimental validated over the micro-sized nickel-cerium-alumina catalyst. A non-isothermal temperature profile ($T=830$ to 495 K) with high level of CO₂ conversion ($X_{CO_2}=93\%$) was successfully achieved. For the small-scale production of 1 Nm³·h⁻¹ of SNG, 23 channels will be required to achieve the targeted production rate. The main advantage of the proposed approach is the simple design and low auxiliary requirements of this reactor, especially in decentralized locations where the integration of the exothermic heat to another industrial unit is not technically feasible or, more probably, not economically profitable.

To summarize, Ni-CeO₂/γ-Al₂O₃ micro-size catalyst for SNG production was synthesized and optimized in laboratory conditions. Further, it was validated successfully in an industrial reactor under real operation conditions. The catalyst has proven to be active, stable, and scalable. Moreover, the optimized catalyst was used as a benchmark to design a novel reactor approach for CO₂ methanation based on free convection. The developed reactor design combined with the micro-sized catalyst can provide a promising alternative for CO₂ methanation process intensification and, therefore, make this technology more commercially attractive.

Outlook and recommendations

As an outlook, and based on the present results, it is projected the scale-up, construction and experimentation of the small-scale methanation reactor in a pilot plant. These steps are important to value its technical feasibility at industrial conditions. Currently, the catalyst commercialization is being valued through the framework of the LLAVOR (LLAV-2018-00066) and PRODUCTE (PROD-2019-00091) projects. In the short-term future, the author's motivation is that the technology proposal (catalyst + reactor) could penetrate to the market competing at the sacrifice of other costly CO₂ methanation technologies that show lower efficiencies. We believe that the implementation of a cost-efficient CO₂ methanation technology can contribute to the future of environmentally friendly energy systems.

In this line, the author recommends the evaluation of the following aspects by future research:

- For the implementation of the fixed-bed reactor design approach in industry, further research should be focused on the scale-up of the reactor approach. As it was reported, 23 tubes will be required for small-size SNG production. A simulation-based study should be performed to find an optimum arrangement of the tubes. Different arrangements, such as square, circular, triangular or rhombus could be evaluated. At this point, the influence of the spacing between each reactor tube should be taken into account in order to select the optimum solution of the arrangement and to propose the simplest tube bundle reactor configuration. Once the best tube bundle reactor has been selected, this must be built and tested its feasibility at different scales (from lab to pilot plant).
- It is recommended to use a more complex rate law to represent the reaction kinetics. Under the non-isothermal conditions, it is plausible that reaction is governed by the equilibrium restriction. On the bases of reaction mechanism proposed for the Ni-CeO₂/γ-Al₂O₃ catalyst, a LHHW kinetic model could be developed including the product adsorption on the catalyst. In addition to Sabatier reaction, kinetic experiments should be designed in order to evaluate the formation of the RWG reaction and the influence of the products (CH₄ and H₂O). Preliminary experiments proved that the addition of water in the stream limits the rate of the reaction. Therefore, the implementation of this more complex kinetic model on the developed CFD model approaches might assist future studies on the design and operation of catalytic fixed-bed reactors, getting closer to reality.
- Taking into consideration that the Ni-CeO₂/Al₂O₃ catalyst work under a decreasing temperature profile along the catalytic bed reactor, a catalyst characterization study using advanced post-mortem technics should be performed in order to propose improvements. A comparative examination of the surface characteristics of the fresh and spent catalyst can be quite revealing and instructive to identify the physical properties limiting catalyst performance and to make predictions of the catalyst lifetime.
- Further research on the catalyst in-situ regeneration of S-poisoned Ni-CeO₂/γ-Al₂O₃ catalyst should be considered. As it was demonstrated in this thesis, a non-expected compound was formed between by the interaction of the poison and the catalyst. The Ni-CeO₂/γ-Al₂O₃ catalyst achieved a higher sulfur tolerance thanks to the favourable formation of Ce₂O₂S species that restricts the formation of NiS. Form this fact, several scientific questions may arise. This finding is key since steps can be taken to remove the poison or replenish

the active catalyst components (CeO_2 and Ni) that reacted with the poison ($\text{Ce}_2\text{O}_2\text{S}$ and NiS). To understand the adsorption type (reversible or irreversible) of the poison precursor on or with the surface can be crucial for extending the catalyst lifetime. With these insights, catalyst regeneration procedures will be also developed for those industrial cases where the sulfur cleaning devices present cannot remove completely the sulfur.

Appendix

*Tables of the state-of-art of the
proposed kinetic models
and catalysts*

Appendix 1 includes five tables, in which the state-of-art of the proposed kinetic models, and catalysts for CO₂ methanation are presented. In Table A1.1, an overview of the kinetic models developed over Ni-based catalysts is displayed. For each case, the kinetic rate expressions and the estimated activation energy values are shown. In addition, catalysts reported in literature are listed in Tables A1.2-A1.4. According to the catalyst strategy design, they are classified as bimetallic catalysts (Table A1.2), supported metal-based catalysts (Table A1.3) and metal-oxide promoted Ni-based catalysts (Table A1.4). In these tables, the reaction conditions at which the catalysts showed their most promising catalytic performance are detailed. Finally, the main preparation methods implemented for Ni-based catalyst synthesis are specified in Table A1.5. In particular, the table shows the main findings found over the physicochemical properties of the catalysts.

Table A1.1. An overview of the Kinetic rate expressions of CO₂ methanation on Ni-based catalysts

Catalyst	Reaction Conditions T[K] P[atm] H ₂ /CO ₂ [-]	Reaction & Model	Rate Equation		E _a [kJ·mol ⁻¹]	
			(rate constant) *(driving-force)	(adsorption term)		
Ni/kieselguhr [53]	533-673 [K] 1 [atm] 0.4-4 [-]	$r(CO_2 \rightarrow CH_4)$ LHHW	$k \cdot p_{CO_2} \cdot p_{H_2}^2$	$\frac{1}{\left(1 + K_{H_2} \cdot p_{H_2}^{1/2} + K_{CO_2} \cdot p_{CO_2}\right)^5}$	$\left(1 - \frac{p_{H_2O}^2 \cdot p_{CH_4}}{p_{CO_2} \cdot p_{H_2}^4 \cdot K_{eq}}\right)$	-
Ni/kieselguhr [54]	555-673 [K] 2-30 [atm] 0.1-19 [-]	$r(CO_2 \rightarrow CH_4)$ LHHW	$k \cdot p_{CO_2} \cdot p_{H_2}^4$	$\frac{1}{\left(1 + K_{H_2} \cdot p_{H_2} + K_{CO_2} \cdot p_{CO_2}\right)^5}$	-	55-58
33.6 wt.% NiO/γ-Al ₂ O ₃ [55]	473-503 [K] 1 [atm] 40-450 [-]	$r(CO_2 \rightarrow CH_4)$ LHHW	$k \cdot p_{CO_2}$	$\frac{1}{1 + K_{CO_2} \cdot p_{CO_2}}$	-	106
3 wt.% Ni/SiO ₂ [27]	500-600 [K] 4-15 [atm] 2-20 [-]	$r(CO_2 \rightarrow CH_4)$ LHHW	$k \cdot p_{CO_2}^{1/2} \cdot p_{H_2}^{1/2}$	$\frac{1}{\left(1 + K_1 \cdot p_{CO_2}^{1/2} \cdot p_{H_2}^{-1/2} + K_2 \cdot p_{CO_2}^{1/2} \cdot p_{H_2}^{1/2} + K_{CO} \cdot p_{CO}\right)^2}$	-	94
58 wt.% Ni/kieselguhr [56]	550-592 [K] 11-18 [atm] 2-5 [-]	$r(CO_2 \rightarrow CH_4)$ LHHW	$k \cdot p_{H_2}^{0.21} \cdot p_{CO_2}^{0.66}$ $k \cdot p_{H_2} \cdot p_{CO_2}$	$\frac{1}{1 + K_{H_2} \cdot p_{H_2} + K_{CO_2} \cdot p_{CO_2}}$	-	61 19
Ni [57]	523-623 [K] 1 [atm] 5-20 [-]	$r(CO_2 \rightarrow CH_4)$ LHHW	$k \cdot p_{H_2} \cdot p_{CO_2}^{1/3}$	$\frac{1}{1 + K_{H_2} \cdot p_{H_2} + K_{CO_2} \cdot p_{CO_2} + K_{H_2O} \cdot p_{H_2O}}$	-	-

Table A1.1. An overview of the Kinetic rate expressions of CO₂ methanation on Ni-based catalysts

Catalyst	Reaction Conditions T[K] P[atm] H ₂ /CO ₂ [·]	Reaction & Model	Rate Equation		Ea [kJ·mol ⁻¹]
			(rate constant) *(driving-force)	(adsorption term)	
20 wt.% Ni-La ₂ O ₃ [58]	513-593 [K] 1 [atm] 0.6-30 [-]	$\tau(CO_2 \rightarrow CH_4)$ LHHW	$k \cdot p_{H_2}^{1/2} \cdot p_{CO_2}^{1/3}$	$\frac{1}{(1 + K_{H_2} \cdot p_{H_2}^{1/2} + K_{CO_2} \cdot p_{CO_2} + K_{H_2O} \cdot p_{H_2O})^2}$	73
15 wt.% Ni/MgAl ₂ O ₃ [59]	573-673 [K] 10 [atm]	$\tau(CO_2 \rightarrow CH_4)$ LHHW	$\frac{k_3 \cdot p_{H_2O}^2 \cdot p_{H_2}}{p_{H_2}^{3.5}}$	$\left(1 - \frac{p_{H_2} \cdot p_{CO_2}}{p_{H_2O} \cdot p_{H_2} \cdot K_2}\right)$	240
		$\tau(CO_2 \rightarrow CO)$ LHHW	$\frac{k_2 \cdot p_{H_2O} \cdot p_{H_2}}{p_{H_2}}$	$\left(1 - \frac{p_{H_2} \cdot p_{CO_2}}{p_{H_2O} \cdot p_{H_2} \cdot K_2}\right)$	67
		$\tau(CO \rightarrow CH_4)$ LHHW	$\frac{k_1 \cdot p_{H_2O} \cdot p_{CH_4}}{p_{H_2}^{2.5}}$	$\left(1 - \frac{p_{H_2}^3 \cdot p_{CO}}{p_{H_2O} \cdot p_{CH_4} \cdot K_1}\right)$	244
NiAl(O) _x [60]	523-613 [K] 1-15 [atm] 4 [-]	$\tau(CO_2 \rightarrow CH_4)$ PL	$k \cdot p_{H_2}^{n_{H_2}} \cdot p_{CO_2}^{n_{CO_2}}$	-	83
		$\tau(CO_2 \rightarrow CH_4)$ PL-H ₂ O	$k \cdot \frac{p_{H_2}^{n_{H_2}} \cdot p_{CO_2}^{n_{CO_2}}}{p_{H_2O}^{n_{H_2O}}}$	-	94
		$\tau(CO_2 \rightarrow CH_4)$ PL-WI	$k \cdot p_{H_2}^{n_{H_2}} \cdot p_{CO_2}^{n_{CO_2}}$	$\frac{1}{1 + K_{H_2O} \cdot p_{H_2O}^{n_{H_2O}}}$	-

Table A1.1. An overview of the kinetic rate expressions of CO₂ methanation on Ni-based catalysts

Catalyst	Reaction Conditions T[K] P[atm] H ₂ /CO ₂ [-]	Reaction & Model	Rate Equation		E _a [kJ·mol ⁻¹]
			(rate constant) *(driving-force)	(adsorption term)	
NiAl(O) _x [60]	523-613 [K] 1-15 [atm] 4 [-]	$r(CO_2 \rightarrow CH_4)$ PL-HI	$k \cdot p_{H_2}^{n_{H_2}} \cdot p_{CO_2}^{n_{CO_2}}$	$\frac{1}{1 + K_{OH} \cdot \frac{p_{H_2O}}{p_{H_2}}^{1/2}}$	-
		$r(CO_2 \rightarrow CH_4)$ LHHW	$k \cdot p_{H_2}^{n_{H_2}} \cdot p_{CO_2}^{n_{CO_2}}$	$\frac{1}{\left(1 + K_{OH} \cdot \frac{p_{H_2O}}{p_{H_2}}^{0.5} + K_{H_2} \cdot p_{H_2}^{0.5} + K_{mix} \cdot p_{CO_2}^{0.5}\right)^2}$	78
12 wt.% Ni/ γ -Al ₂ O ₃ [61]	445-497 [K] 1-20 [atm] 4 [-]	$r(CO_2 \rightarrow CH_4)$ LHHW	$a_{II} \cdot p_{CO_2}^{0.5} \cdot p_{H_2}^{0.5}$	$\frac{1}{\left(1 + b_{II} \cdot \left(\frac{p_{CO_2}}{p_{H_2}}\right)^{0.5} + c_{II} \cdot p_{CO_2}^{0.5} \cdot p_{H_2} + d_{III} \cdot p_{H_2O}\right)^2}$	85
54 wt.% Ni [62]	423-523 [K] 1 [atm] 5 [-]	$r(CO_2 \rightarrow CH_4)$ PL	$k \cdot p_{H_2}^{0.2} \cdot p_{CO_2}^{0.3}$	-	84
14-17 wt.% Ni/Al ₂ O ₃ [63]	573-673 [K] 1-10 [atm] 4 [-]	$r(CO_2 \rightarrow CH_4)$ LHHW	$\frac{k_3 \cdot p_{H_2O}^2 \cdot p_{H_2}}{p_{H_2}^{3.5}}$	$\frac{1}{\left(1 + K_{CO} \cdot p_{CO} + K_{H_2} \cdot p_{H_2} + K_{CH_4} \cdot p_{CH_4} + K_{H_2O} \cdot p_{H_2O} / p_{H_2}\right)^2}$	210
		$r(CO_2 \rightarrow CO)$ LHHW	$\frac{k_2 \cdot p_{H_2O} \cdot p_{H_2}}{p_{H_2}}$	$\frac{1}{\left(1 + \frac{p_{H_2} \cdot p_{CO_2}}{p_{H_2O} \cdot p_{H_2}} \cdot K_2\right)}$	219

Table A1.1. An overview of the Kinetic rate expressions of CO₂ methanation on Ni-based catalysts

Catalyst	Reaction Conditions T[K] P[atm] H ₂ /CO ₂ [·]	Reaction & Model	Rate Equation		Ea [kJ·mol ⁻¹]
			(rate constant) *(driving-force)	(adsorption term) (Equilibrium term)	
14-17 wt.% Ni/Al ₂ O ₃ [63]	573-673 [K] 1-10 [atm] 4 [-]	r(CO → CH ₄) LHHW	$\frac{k_1 \cdot p_{H_2O} \cdot p_{CH_4}}{p_{H_2}^{2.5}}$	$\frac{1}{(1 + K_{CO} \cdot p_{CO} + K_{H_2} \cdot p_{H_2} + K_{CH_4} \cdot p_{CH_4} + K_{H_2O} \cdot p_{H_2O}/p_{H_2})^2}$	59
20-25 wt.% Ni/γ-Al ₂ O ₃ (METH 134) [64]	523- 623 [K] 1 [atm] 4 [-]	r(CO ₂ → CH ₄) LHHW	$k \cdot p_{CO_2}^{0.5} \cdot p_{H_2}^{0.5}$	$\frac{1}{(1 + K_{OH} \cdot \frac{p_{H_2O}}{p_{H_2}})^2}$	119
75 wt.% NiO Ni/Al Hydrotalcite [65]	543-663 [K] 1 [atm] 4 [-]	r(CO ₂ → CO) LHHW r(CO → CH ₄) PL	$k_1 \cdot K_{CO_2}^{0.5} \cdot p_{H_2}^{0.5}$ $k_2 \cdot K_{H_2}^{0.2} \cdot p_{CO_2}^{0.03}$	$\frac{1}{(1 + \sqrt{K_{H_2} \cdot p_{H_2}} + K_{mix} \cdot p_{CO_2}^{0.5} + K_{OH} \cdot \sqrt{\frac{p_{H_2O}}{p_{H_2}}})^2}$ $(1 - \frac{p_{CH_4} \cdot p_{H_2O}^2}{p_{CO_2} \cdot p_{H_2}^4 \cdot K_{eq} \cdot CO_2Meth})$ $(1 - \frac{p_{H_2O} \cdot p_{CO}}{p_{CO_2} \cdot p_{H_2} \cdot K_{eq}WGS})$	69 85
14-17 wt.% Ni/Al ₂ O ₃ [66]	623-723 [K] 1 [atm] 4.35 [-]	r(CO ₂ → CO) LHHW r(CO → CH ₄) LHHW	$k_{RWGS} \cdot K_{CO_2} \cdot K_{CO_2}$ $k_{COmeth} \cdot K_{H_2} \cdot K_{CO} \cdot p_{H_2} \cdot p_{CO}$	$\frac{1}{(1 + K_{CO_2} \cdot p_{CO_2} + K_{H_2} \cdot p_{H_2} + K_{H_2O} \cdot p_{H_2O} + K_{CO} \cdot p_{CO})^2}$ $(1 - \frac{p_{CO} \cdot p_{H_2O}}{p_{H_2} \cdot p_{CO_2} \cdot K_{eq}RWGS})$ $(1 - \frac{p_{CH_4} \cdot p_{H_2O}}{p_{H_2}^3 \cdot p_{CO} \cdot K_{eq}COmeth})$	97

Table A1.1. An overview of the Kinetic rate expressions of CO₂ methanation on Ni-based catalysts

Catalyst	Reaction Conditions T[K] P[atm] H ₂ /CO ₂ [-]	Reaction & Model	Rate Equation		Ea [kJ·mol ⁻¹]
			(rate constant) *(driving-force)	(adsorption term)	
14-17 wt.% Ni/Al ₂ O ₃ [66]	623-723 [K] 1 [atm] 4.35 [-]	$r(CO_2 \rightarrow CH_4)$ LHHW	$k_{CO_2, meth} \cdot K_{H_2} \cdot K_{CO_2} \cdot p_{H_2} \cdot p_{CO_2}$	$\frac{1}{(1 + K_{CO_2} \cdot p_{CO_2} + K_{H_2} \cdot p_{H_2} + K_{H_2O} \cdot p_{H_2O} + K_{CO} \cdot p_{CO})^2}$	110
		$r(CO_2 \rightarrow CO)$ LHHW	$k_1 \cdot p_{CO_2}^{0.5} \cdot p_{H_2}^{0.5}$	$\left(1 - \frac{p_{CO} \cdot p_{H_2O}}{p_{H_2} \cdot p_{CO_2} \cdot K_{RWGS}}\right)$	
17 wt.% Ni3Fe [67]	573-723 [K] 2-18 [atm] 4 [-]	$r(CO \rightarrow CH_4)$ LHHW	$k_1 \cdot p_{CO}^{0.5} \cdot p_{H_2}^{0.5}$	$\frac{1}{(1 + K_{H_2O} \cdot p_{H_2O})^2}$	167
		$r(CO_2 \rightarrow CO)$ LHHW	$k_2 \cdot p_{CO_2}^{0.5} \cdot K_{H_2} \cdot p_{H_2}$	$\left(1 - k_{\beta} \cdot \frac{p_{CO} \cdot p_{H_2O}}{p_{H_2} \cdot p_{CO_2} \cdot K_{eqRWGS}}\right)$	195
30 wt.% Ni/ γ -Al ₂ O ₃ [68]	593-693 [K] 1-7 [atm] 4 [-]	$r(CO \rightarrow CH_4)$ LHHW	$k_1 \cdot K_{COH} \cdot p_{CO_2}^{0.5} \cdot K_{H_2} \cdot p_{H_2}$	$\frac{1}{\left(1 + K_{COH} \cdot p_{CO_2}^{0.5} \cdot K_{H_2}^{0.5} \cdot p_{H_2}^{0.5} + \sqrt{K_{H_2} \cdot p_{H_2} + K_{OH} \cdot \frac{p_{H_2O}}{p_{H_2}}}\right)^2}$	80

Table A1.1. An overview of the Kinetic rate expressions of CO₂ methanation on Ni-based catalysts

Catalyst	Reaction Conditions T[K] P[atm] H ₂ /CO ₂ [-]	Reaction & Model	Rate Equation		E _a [kJ·mol ⁻¹]
			(rate constant) r [*] (driving-force)	(adsorption term)	
30 wt.% Ni/γ-Al ₂ O ₃ [68]	593–693 [K] 1-7 [atm] 4 [-]	r(CO ₂ → CO) LHHW	$k_2 \cdot K_{HCOO} \cdot p_{CO_2}$ $\cdot K_{H_2}^{0.5} \cdot p_{H_2}^{0.5}$	$\left(1 - k_{\beta} \cdot \frac{p_{CO} \cdot p_{H_2O}}{p_{H_2} \cdot p_{CO_2} \cdot K_{eqRWGS}}\right)$	179
		r(CO → CH ₄) LHHW	$k_1 \cdot K_{HCOO} \cdot p_{CO_2}$ $\cdot K_{H_2}^{0.5} \cdot p_{H_2}^{0.5}$	$\left(1 - \frac{p_{H_2O}^2 \cdot p_{CH_4}}{p_{H_2}^4 \cdot p_{CO_2} \cdot K_{eqM}}\right)$	23
14-17 wt.% Ni/γ-Al ₂ O ₃ [69]	523-673 [K] 5-10 [atm] 4 [-]	r(CO ₂ → CO) LHHW	$k_{RWGS} \cdot p_{CO_2}$	$\left(1 - \frac{p_{CO} \cdot p_{H_2O}}{p_{H_2} \cdot p_{CO_2} \cdot K_{eqRWGS}}\right)$	72
		r(CO → CH ₄) LHHW	$k_{CO_2, meth} \cdot p_{CO_2}^{0.5}$ $\cdot p_{H_2}^{0.5}$	$\left(1 - \frac{p_{CO} \cdot p_{CH_4}}{p_{H_2}^4 \cdot p_{CO_2} \cdot K_{eqCO_2, meth}}\right)$	99
		-	-	$-\frac{d_a}{d_t} = k_{a, T, ref} \cdot \exp\left(\frac{E_{a,a}}{R} \left(\frac{1}{T_{ref}} - \frac{1}{T}\right)\right) \cdot a^{im}$	61

Table A1.2. A summary of the bimetallic catalysts

Metal	Bi-metallic catalyst	Content [wt.%]	Preparation method	Operational parameter				Catalytic performance		Stability test		Ref.
				T [K]	P [atm]	H ₂ :CO ₂ [-]	GHSV ^a [h ⁻¹]	XCO ₂ [%]	SCH ₄ [%]	Time [h]	XCO ₂ [%]	
Fe	Ni-Fe/Al ₂ O ₃	Ni: 7.5 Fe: 2.5	IWI	523	1	4	32,000	22	97	4	67	[127]
Pt	Ni-Pt/Al ₂ O ₃	Ni: 10 Pt: 0.5	CI	523	1	4	5,700	67	97	4	67	[128]
Pd	Ni-Pd/Al ₂ O ₃	Ni: 10 Pd: 0.5	CI	523	1	4	5,700	75	97	4	75	[128]
Co	Ni-Co/Al ₂ O ₃	Ni: 8 Co: 2	EISA	523	1	4	15,000	~18	90	50	80 673 K	[129]
Ru	Ni-Ru	Ni: 10 Ru: 1		623	1	5	5,835	82	-	7	78	[130]

IWI: incipient wetness impregnation; CI: co-impregnation; EISA: evaporation-induced self-assembly process
^a GHSV assuming a $\rho_{\text{cat}}=1 \text{ g}\cdot\text{mL}^{-1}$

Table A 1.3. A summary of the metal-supported catalysts

Catalyst	Active metal content [wt. %]	Preparation method	Operational parameter				Catalytic performance		Stability test		Deactivation	Ref.
			T [K]	P [atm]	H ₂ :CO ₂ [-]	GHSV ^a [h ⁻¹]	XCO ₂ [%]	SCH ₄ [%]	Time [h]	XCO ₂ [%]		
Ru _{0.04} Ce _{0.95} O ₂	5	SC	722	1	4	10,286	55	99	-	-	[105]	
Ru/γ -Al ₂ O ₃	3	IWI	673	1	4	60,000	80	90	-	-	[106]	
Ru/γ -Al ₂ O ₃	3	-	573	1	4	15,000	96	100	-	-	[107]	
Ru/γ -Al ₂ O ₃	5	P	598	4	4	60,000	-93	-	-	-	[119]	
Ru/CeO ₂ /Al ₂ O ₃	2	WI	573	1	4	10,000	-63	100	-	-	[118]	
Ru/CeO ₂	-	WI	622	1	4	72,000	-77	100	24	-77	[117]	
Rh/γ -Al ₂ O ₃	2	WI	473	1	4	18,000	6.2 ^b	-	-	-	[108]	
Rh/CeO ₂	3	IWI	623	1	4	60,000	44	-	-	-	[110]	
Pt/Ga ₂ O ₃	-	WI	723	5	4	60,000	250 ^c	85	-	-	[109]	
Fe/13X	1	WI	623	10	4	4,186	-85	76	-	-	[112]	

SC: solution combustion; IWI: incipient wetness impregnation; WI: wet impregnation; P: polyol
^a GHSV assuming a p_{cat}=1 g·mL⁻¹; ^b Differential condition (<10%); ^c CO₂ conversion rate [10⁻⁵mol·g⁻¹·s⁻¹]

Table A1.3. A summary of the metal-supported catalysts

Catalyst	Active metal content [wt.%]	Preparation method	Operational parameter				Catalytic performance		Stability test		Deactivation	Ref.
			T [K]	P [atm]	H ₂ :CO ₂ [-]	GHSV ^a [h ⁻¹]	XCO ₂ [%]	SCH ₄ [%]	Time [h]	XCO ₂ [%]		
Co/KIT-6	25	IWI	633	1	4	60,000	52.6	95	-	-	[115]	
Unsupported Co	-	R	773	1	4	55,000	49	80	-	Carbon formation	[113]	
Co/SiO ₂	10	GI	633	1	4	60,000	44.3	87	-	-	[137]	
Ni/ γ -Al ₂ O ₃	16	-	673	1	4	52,000	50	100	-	-	[111]	
Ni/ γ -Al ₂ O ₃	20	IWI	623	1	3.5	9,000	~75	100	10	-	[132]	
Ni/CeO ₂	10	WI	573	1	4	10,000	~90	100	-	-	[133]	
Ni/CeO ₂	5	WI	523	1	4	66,000	~30	100	50	Reconstruction of Ni surface	[175]	
Ni/SiO ₂	10	IWI	623	1	4	-	~5 ^b	~48	-	-	[136]	

IWI: incipient wetness impregnation; WI: wet impregnation; R: reduction; GI: grid-impregnation
^a GHSV assuming a p_{cat}=1 g·mL⁻¹; ^b Differential condition (<10%)

Table A1.3. A summary of the metal-supported catalysts

Catalyst	Active metal content [wt. %]	Preparation method	Operational parameter				Catalytic performance		Stability test		Deactivation	Ref.
			T [K]	P [atm]	H ₂ :CO ₂ [-]	GHSV ^a [h ⁻¹]	XCO ₂ [%]	SCH ₄ [%]	Time [h]	XCO ₂ [%]		
Ni/TiO ₂	6.17	DBD	623	1	4	60,000	73	--	-	-	-	[138]
Ni/ZrO ₂	15	SC	573	1	4	48,000	60	100	150	83 673 K	-	[143]
Ni/CaZrO ₂	4	WI	623	1	4	24,000	-69	99	-	-	-	[141]
Ni-(Zr+Ca)	50	WI	673	1	4	400,000	-84	100	-	-	-	[140]
Ni-Fe/ZrO ₂	30	CI	603	1	4	10,000	100	94	-	-	-	[142]
Ni ₆ W ₆ MgO _x	a/b=1	IWI	573	1	4	40,000	86	100	100	79 673 K	-	[47]
Ni/Y ₂ O ₃	10	IWI	573	1	4	20,000	77	98	50	74	-	[30]
Ni/Y ₂ O ₃	10	H&IWI	623	1	4	40,000	88	100	80	54 548 K	-	[145]

DBD: dielectric barrier discharge (DBD) plasma; SC: Combustion; WI: incipient wetness impregnation; IWI: wet impregnation; H: hydrothermal; CI: co-impregnation
^a GHSV assuming a P_{cat}=1 g·mL⁻¹

Table A1.3. A summary of the metal-supported catalysts

Catalyst	Active metal content [wt.%]	Preparation method	Operational parameter				Catalytic performance		Stability test		Deactivation	Ref.
			T [K]	P [atm]	H ₂ :CO ₂ [-]	GHSV ^a [h ⁻¹]	XCO ₂ [%]	SCH ₄ [%]	Time [h]	XCO ₂ [%]		
Ni/Y ₂ O ₃	25	SC	623	1	3	10,000	81	90	200	80	-	[146]
Ni/La ₂ O ₃	10	IWI	623	15	4	30,000	80	100	-	-	-	[147]
Ni-CZ	5	SG&WI	623	1	4	43,000	80	99	90	68	-	[39]
Ni-Ce _x Zr _{1-x} O _x	5	SG	623	1	4	43,000	80	99	150	66	Ni particles sintering	[151]
Ni/Ce _{0.5} Zr _{0.5} O ₂	7	IWI	613	30	4.5	20,000	70	-	-	-	-	[40]
Ni-Ce-Zr-O ₆	71	H	573	1	4	10,000	91	100	48	91	-	[149]
Ni-Co/CeO ₂ -ZrO ₂	15	WI	573	1	4	12,000	61	97	40	61	-	[150]
Ni/Al ₂ O ₃ -ZrO ₂	15	CI	573	1	4	40,000	54	-	-	-	-	[153]

SC: solution combustion; IWI: incipient wetness impregnation; WI: wet impregnation; H: hydrothermal; SG: sol-gel; CI: co-impregnation
^a GHSV assuming a P_{cat}=1 g·mL⁻¹

Table A1.3. A summary of the metal-supported catalysts

Catalyst	Active metal content [wt.%]	Preparation method	Operational parameter				Catalytic performance		Stability test		Deactivation	Ref.
			T [K]	P [atm]	H ₂ :CO ₂ [-]	GHSV ^a [h ⁻¹]	XCO ₂ [%]	SCH ₄ [%]	Time [h]	XCO ₂ [%]		
Ni/Y ₂ O ₃ -ZrO ₂	12	WI	623	1	4	60,000	45	83	-	-	-	[152]
Ni/Al ₂ O ₃ -ZrO ₂ -TiO ₂ -CeO ₂	20	WI	598	1	4	20,000	83	93	~7	78 ^b	-	[154]
NiRu/CaO-Al ₂ O ₃	10	EISA	653	1	4	30,000	84	100	109	65 823 K	-	[157]
Ni/GDC	50	WI	673	1	5	30,000	92	100	-	-	-	[156]
Ni/MIL-101-Al ₂ O ₃	10	DS	623	1	5	4,650	85	93	5	55 553 K	-	[155]
Ni-Ce/MCM-41	15	IWI	623	1	4	48,000	-60	~95	-	-	-	[158]
Ni/MSN	5	SG&WI	573	1	4	50,000	64	100	200	64	-	[159]

IWI: incipient wetness impregnation; WI: wet impregnation; DS: double solvent; SG: sol gel; EISA: evaporation-induced self-assembly
^a GHSV assuming a $\rho_{cat}=1 \text{ g}\cdot\text{mL}^{-1}$; ^b Stability at T=673 K, P=5 atm & GHSV=4,000 h⁻¹

Table A1.3. A summary of the metal-supported catalysts

Catalyst	Active metal content [wt. %]	Preparation method	Operational parameter				Catalytic performance		Stability test		Deactivation	Ref.
			T [K]	P [atm]	H ₂ :CO ₂ [-]	GHSV ^a [h ⁻¹]	XCO ₂ [%]	SCH ₄ [%]	Time [h]	XCO ₂ [%]		
Ni/Mg@MCM-41	8.7	H	593	10	4	6,420	90	84	120	84	-	[179]
Ni@MOF-5	10	-	553	1	4	20,000	47	100	100	47	-	[180]
Ni-V/KIT-6	20	-	623	1	4	96,000	87	100	60	70 773 K	-	[181]
NiHNaUSY	14	I	673	1	4	43,000	66	94	10	60	-	[166]
NiCeHNaUSY	14	I	673	1	4	43,000	68	95	-	-	-	[166]
Ni/USY	15	I	723	1	4	43,000	67	93	-	-	-	[171]
Ni/13X	5	WI	593	1	4	13,333	79	100	200	79	-	[169]
Ni/X	15	IWI	723	1	4	12,000	53	-	-	-	-	[170]

IWI: incipient wetness impregnation; WI: wet impregnation; H: hydrothermal
^a GHSV assuming a P_{cat}=1 g·mL⁻¹

Table A1.3. A summary of the metal-supported catalysts

Catalyst	Active metal content [wt. %]	Preparation method	Operational parameter					Catalytic performance		Stability test		Deactivation	Ref.
			T [K]	P [atm]	H ₂ :CO ₂ [-]	GHSV ^a [h ⁻¹]	XCO ₂ [%]	SCH ₄ [%]	Time [h]	XCO ₂ [%]			
Ni@HZSM-5	10	WI	623	1	3	3,600	66	100	40	63	-	[178]	
Ni-Ce/CNTs	12	IWI	623	1	4	-	83	-	7	83	-	[160]	
NiCa/AC	15	IWI	633	1	4	-	76	-	7	71	-	[161]	
Ni-ZrO ₂ /CNT	5	SI	623	1	5	75,000	45	100	50	40	-	[162]	
Ni-Mn-CNTs	15	CI	633	1	4	30,000	81	100	140	81	-	[163]	
Ni/N-CNT	10	IWI	633	1	4-6	120,000	73-92	94-98	60	80 60,000 h ⁻¹	-	[164]	
Ni-Ga/CNx-2	14	-	553	20	3	6,000	5	11	-	-	-	[165]	
Ni/Olivine	6	IWI	673	1	6	11,000	98	99	-	-	-	[182]	
Ni/Al@Al ₂ O ₃	10	DP	582	1	4	60,000	93	100	50	90	Ni particles sintering	[183]	

IWI: incipient wetness impregnation; WI: wet impregnation; SI: sequential impregnation; CI: co-impregnation; DP: deposition-precipitation
^a GHSV assuming a $\rho_{cat}=1 \text{ g}\cdot\text{mL}^{-1}$

Table A1.3. A summary of the metal-supported catalysts

Catalyst	Active metal content [wt.-%]	Preparation method	Operational parameter					Catalytic performance		Stability test		Deactivation	Ref.
			T [K]	P [atm]	H ₂ :CO ₂ [-]	GHSV ^a [h ⁻¹]	XCO ₂ [%]	SCH ₄ [%]	Time [h]	XCO ₂ [%]			
Ni/attapulgit	15	WI	673	1	4	16,000	~78	-	-	-	Carbon deposition	[184]	
Ni/KCC-1	20	IWI	673	1	4	12,000	80	90	50	73	-	[185]	

IWI: incipient wetness impregnation; WI: wet impregnation

^a GHSV assuming a $\rho_{\text{cat}}=1 \text{ g}\cdot\text{mL}^{-1}$

Table A1.4. A summary of the metal-oxide promoted Ni/Al₂O₃ catalysts

Promoter	Catalyst	Content [wt.%]	Preparation method	Operational parameter				Catalytic performance		Stability test		Ref.
				T [K]	P [atm]	H ₂ :CO ₂ [-]	GHSV ^a [h ⁻¹]	XCO ₂ [%]	SCH ₄ [%]	Time [h]	XCO ₂ [%]	
CeO ₂	Ni-CeO ₂ /Al ₂ O ₃	Ni: 15 CeO ₂ : 2	WI	623	1	4	15,000	85	100	120	83	[186]
		Ni: 20 CeO ₂ : 2	SI	623	1	3.5	9,000	80	100	10	78	[188]
La ₂ O ₃	Ni-La ₂ O ₃ /Al ₂ O ₃	Ni: 10 CeO ₂ : 2.5	UII	673	1	4	7,200	74	100	-	-	[187]
		Ni- La: 20	SC	573	1	4	72,000	75	98	4	65 548 K	[189]
Pr	Ni-Pr/Al ₂ O ₃	Ni: 13.6 La ₂ O ₃ : 14	IWI	625	1	5	55,000	90	100	-	-	[190]
		Ni: 12 Pr: 5	WI	573	1	5	6,000	98	100	48	98	[191]
Mn	Ni-Mn/Al ₂ O ₃	Ni: 15 Mn: 1.71	IWI	723	1	4	84,000	72	100	-	-	[192]

WI: wetness impregnation; SI: sequential impregnation; UII: ultrasonic incipient impregnation; SC: solution combustion
^a GHSV assuming a $p_{\text{cat}}=1 \text{ g}\cdot\text{mL}^{-1}$

Table A1.4. A summary of the metal-oxide promoted Ni/Al₂O₃ catalysts

Promoter	Catalyst	Content [wt.%]	Preparation method	Operational parameter				Catalytic performance		Stability test		Ref.
				T [K]	P [atm]	H ₂ :CO ₂ [-]	GHSV ^a [h ⁻¹]	XCO ₂ [%]	SCH ₄ [%]	Time [h]	XCO ₂ [%]	
Ca	Ni- Ca/Al ₂ O ₃	Ni: 10 Ca: 8	EISA	673	1	4	15,000	80	98	50	80	[194]
Zeolita	Ni- Zeolita/Al ₂ O ₃	Ni: 10 Zeolita: 2	WI	623	1	4	72,000	99	56	10	99	[195]

EISA: evaporation-induced self-assembly process; WI: wetness impregnation; LWI: incipient wetness impregnation
^a GHSV assuming a $p_{cat}=1 \text{ g}\cdot\text{mL}^{-1}$

Table A1.5. Preparation methods for the synthesis of Ni-based catalysts

Catalyst	Method	Major findings	Remarks	Ref.
Ni/Al ₂ O ₃	Wet Impregnation (WI)	<ul style="list-style-type: none"> • High Catalytic performance • High Stability 	<ul style="list-style-type: none"> • BET [m²·g⁻¹]: 47 	[133]
10wt.% Ni/1wt.%MgO/SiO ₂	Co-Impregnation (CI)	<ul style="list-style-type: none"> • High Catalytic performance • Small Ni particle size • High nickel dispersion 	<ul style="list-style-type: none"> • Ni particle size [nm]: 31.7 	[198]
Ni/ZrO/CNT	Sequential Impregnation (SI)	<ul style="list-style-type: none"> • High Catalytic performance • High stability • High Ni-ZrO₂ interface • High basicity 	<ul style="list-style-type: none"> • Ni particle size [nm]: 5-10 	[162]
15 wt.%Ni/TiO ₂	Deposition-Precipitation (DP)	<ul style="list-style-type: none"> • High catalytic performance • High nickel dispersion 	<ul style="list-style-type: none"> • BET [m²·g⁻¹]: 54.9 • Ni particle size [nm]: 2 • Ni dispersion [%]: 39.5 	[199]
15 wt.%Ni/Zr ₂ O ₃	Solution combustion (SC)	<ul style="list-style-type: none"> • High Catalytic performance • Small Ni particle size • High carbon deposition resistance 	<ul style="list-style-type: none"> • Ni particle size [nm]: 6.11 • Ni dispersion [%]: 16.54 • Ni metal surface area [m²·g⁻¹]: 110.27 	[143]
Ni(4.4)@CZ	Combination between Colloidal (C) and sol-gel (SG)	<ul style="list-style-type: none"> • High Catalytic performance • Accurate particle size control • Small particle size 	<ul style="list-style-type: none"> • Ni particle size [nm]: 4.4 	[201]

Table A1.5. Preparation methods for the synthesis of Ni-based catalysts

Catalyst	Method	Major findings	Remarks	Ref.
NiO/TiO ₂	Dielectric barrier discharge (DBD) plasma	<ul style="list-style-type: none"> High catalytic performance Ni (111) as the principal exposing facet Small particle size High dispersion 	<ul style="list-style-type: none"> Ni particle size [nm]: 14.4 	[138]
15 wt.% NiCe(x)_HT	Hard template (HT)	<ul style="list-style-type: none"> High Catalytic performance High oxide-support interactions 	<ul style="list-style-type: none"> Ni particle size [nm]: 9 Ni specific metal surface area [m².g⁻¹]: 176 	[203]
15 wt.% Ni-OMA-773K	Evaporation-induced self-assembly process (EISA)	<ul style="list-style-type: none"> High activity Complete mesoporous structure Small and highly dispersed nickel clusters 	<ul style="list-style-type: none"> Ni particle size [nm]: 4 	[200]
10 wt.% Ni/YSZ	Wet Impregnation with EDTA complex	<ul style="list-style-type: none"> High stability High nickel dispersion 	<ul style="list-style-type: none"> Ni dispersion [%]: 5.3 Ni particle size [nm]:19 	[197]
Ni/SiO ₂	Ammonia Evaporation (AE)	<ul style="list-style-type: none"> High activity High metal-support interaction High surface area Small Ni: metal particles 	<ul style="list-style-type: none"> BET [m².g⁻¹]: 446.3 Ni particle size [nm]: 4.2 	[205]
10 wt.% Ni@HZSM-5	Hydrothermal (H)	<ul style="list-style-type: none"> High stability High catalytic performance Well-defined structures 	<ul style="list-style-type: none"> Ni dispersion [%]: 15.1 Ni particle size [nm]: 7.6 	[178]

Table A1.5. Preparation methods for the synthesis of Ni-based catalysts

Catalyst	Method	Major findings	Remarks	Ref.
Ni/Al ₂ O ₃	Electrolysis (E)	<ul style="list-style-type: none"> • High activity • Small Ni metal particles • High mesopores volume 	<ul style="list-style-type: none"> • BET [m²·g⁻¹]: 190 	[204]
NaY-Nix-C	Self-Sacrificial Template (SST)	<ul style="list-style-type: none"> • High stability • Improve the anti-sintering • High carbon deposition resistance 	<ul style="list-style-type: none"> • H₂ uptake [mmol·g⁻¹]: 531 • Ni dispersion [%]: 10.9 	[202]

Appendix

Supporting information

Supporting information

Metal-oxide promoted Ni/Al₂O₃ as CO₂ methanation micro-size catalysts

Jordi Guílera, Jaime Valle, Andreina Alarcón, José Antonio Díaz, Teresa Andreu

Table S1. Chemical composition determined by EDX analysis.

sample		metal content [wt.%]	
		Ni	promoter ^a
Ni	fresh	25 ± 2	-
	used	27 ± 1	-
Ni-CeO ₂	fresh	23 ± 1	16 ± 1
	used	23 ± 2	16 ± 1
Ni-La ₂ O ₃	fresh	28 ± 2	14 ± 1
	used	27 ± 2	15 ± 1

^apromoter amount is expressed as metal (Ce, La)

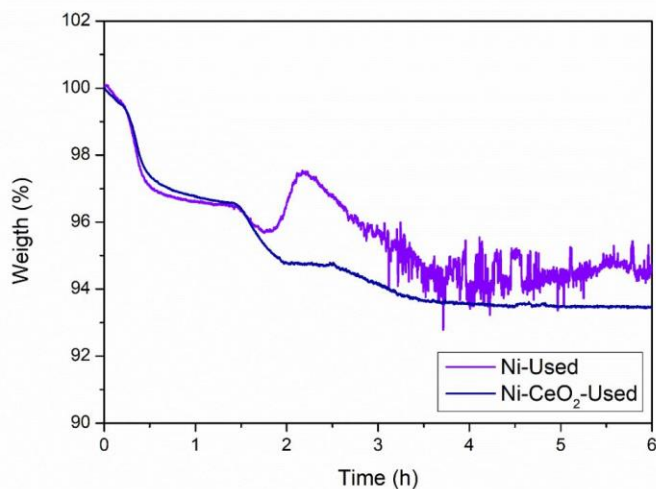


Figure S1. Mass profiles for used Ni and Ni-CeO₂ catalysts during TPO experiments.

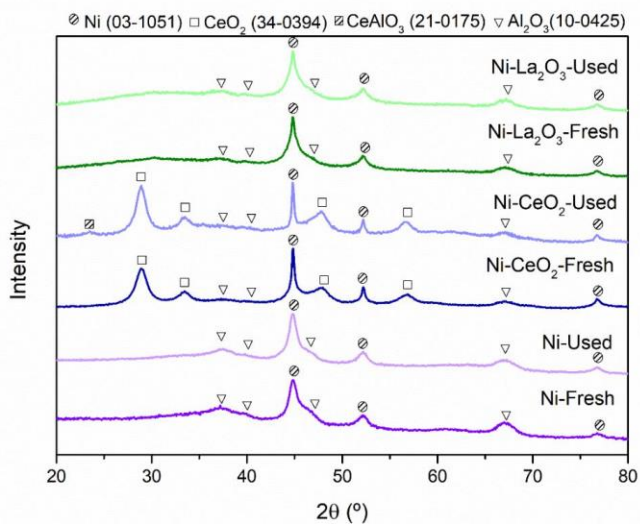


Figure S2. XRD patterns of fresh (pre-reduced) and used catalysts.

Table S2. XRD crystal size of fresh (pre-reduced) and spent catalysts.

sample		d _{Ni} nm
Ni	fresh	7.8 ± 0.3
	used	8.6 ± 0.3
Ni-CeO ₂	fresh	17.9 ± 1.4
	used	15.1 ± 1.0
Ni-La ₂ O ₃	fresh	10.7 ± 0.5
	used	9.9 ± 0.4

Supporting information

Optimization of nickel and ceria catalyst content for synthetic natural gas production through CO₂ methanation

Andreina Alarcón,^{a,b} Jordi Guilera^{a,*}, José Antonio Díaz^c and Teresa Andreu^a

^aCatalonia Institute for Energy Research (IREC), Jardins de les Dones de Negre 1, 08930 Sant Adrià de Besòs, Spain

^bEscuela Superior Politécnica del Litoral, ESPOL, Facultad de Ingeniería en Ciencias de la Tierra, Campus Gustavo Galindo Km.30.5 Vía Perimetral, P.O. Box 09-01-5863, Guayaquil, Ecuador.

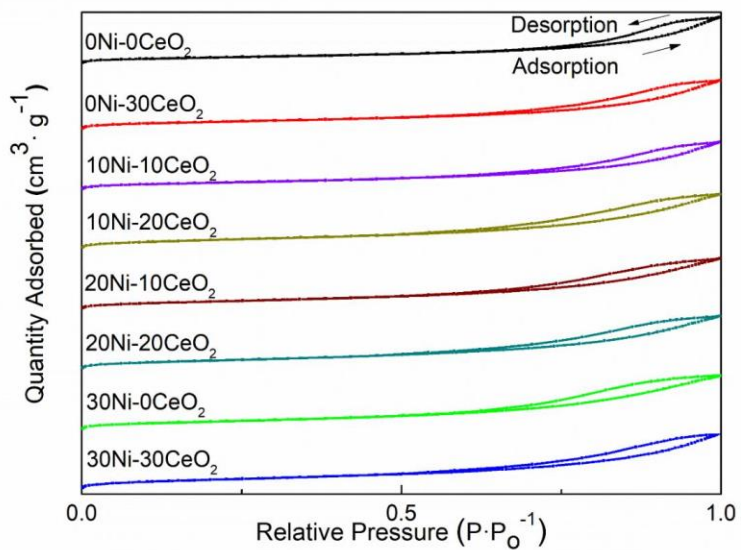
^cDepartment of Mechanical, Chemical and Industrial Design Engineering, ETSIDI, Universidad Politécnica de Madrid (UPM), 28012 Madrid, Spain

Contents

Fig. S1. Isotherms from N ₂ -Physisorption.	2
Fig. S2. V _{pore} (cm ³ ·g ⁻¹) from BJH desorption.	3
Fig. S3. XRD patterns of calcined catalysts.	4
Fig. S4. d _{Ni} (nm) from XRD measurements.	5
Fig. S5. H ₂ -TPR profiles of 10Ni-10CeO ₂ , 10Ni-20CeO ₂ , 20Ni-10CeO ₂ and 20Ni-20CeO ₂ catalysts.	6
Fig. S6. H ₂ uptake (mmol·g _{cat} ⁻¹) estimated from H ₂ -TPR profiles.	7
Fig. S7. CO ₂ conversion of 10Ni-10CeO ₂ , 10Ni-20CeO ₂ , 20Ni-10CeO ₂ and 20Ni-20CeO ₂ catalysts as function of reaction temperature. Reaction conditions: P = 0 bar·g, F = 200 NmL·min ⁻¹ and H ₂ :CO ₂ molar ratio = 4.	8
Fig. S8. Ni dispersion (%) from CO-chemisorption.	9
Fig. S9. Heat of adsorption (-kJ·mol _{CO₂} ⁻¹) from TGA-DSC.	10
Fig. S10. CO ₂ conversion of 20Ni-20CeO ₂ , 25Ni-20CeO ₂ and 30Ni-30CeO ₂ . Reaction conditions: P = 0 bar·g, F = 200 NmL·min ⁻¹ and H ₂ :CO ₂ molar ratio = 4.	11
Fig. S11. XRD patterns of used catalyst.	12

Table S1 Apparent bulk density of calcined catalysts

Catalyst	ρ [g·mL ⁻¹]
0Ni-0CeO ₂	0.58
10Ni-10CeO ₂	0.78
10Ni-20CeO ₂	0.85
20Ni-10CeO ₂	0.88
20Ni-20CeO ₂	0.89
30Ni-0CeO ₂	0.87
0Ni-30CeO ₂	0.82
30Ni-30CeO ₂	0.95
25Ni-20CeO ₂	0.90
METH® 134	0.77

Fig. S1. Isotherms from N₂-Physorption.

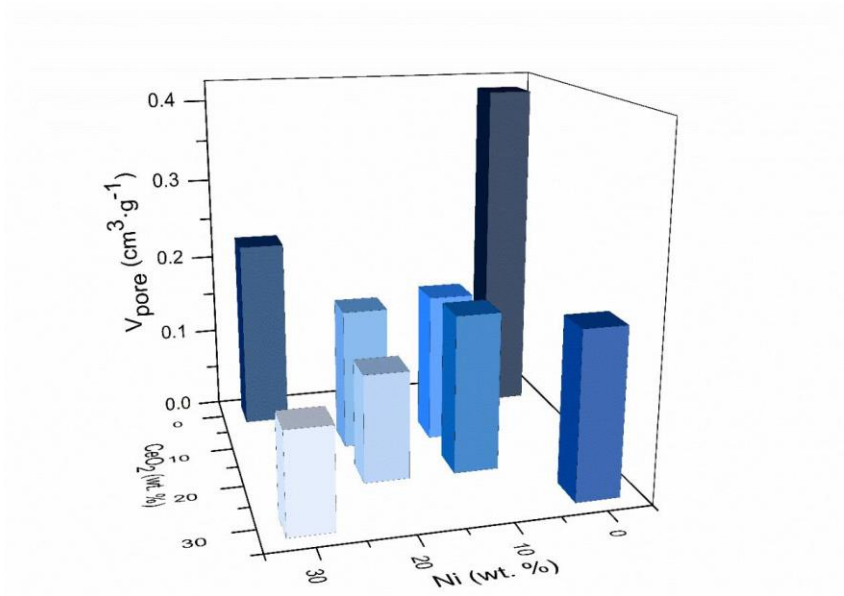


Fig. S2. V_{pore} ($\text{cm}^3 \cdot \text{g}^{-1}$) from BJH desorption.

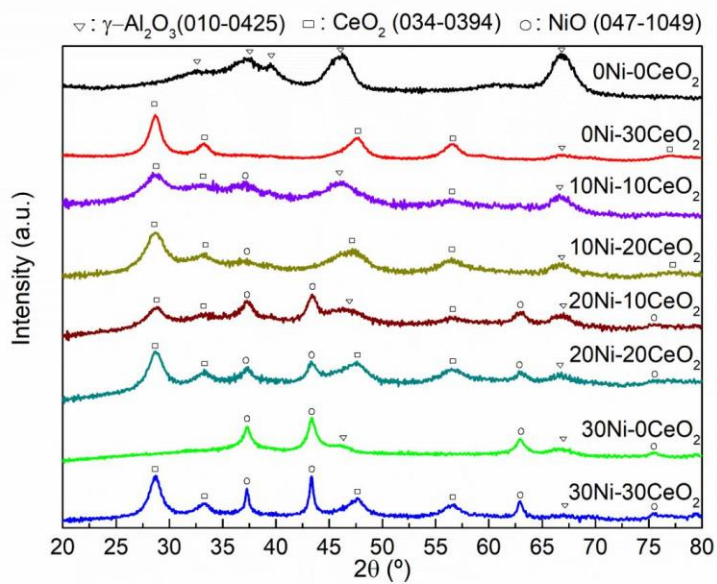


Fig. S3. XRD patterns of calcined catalysts.

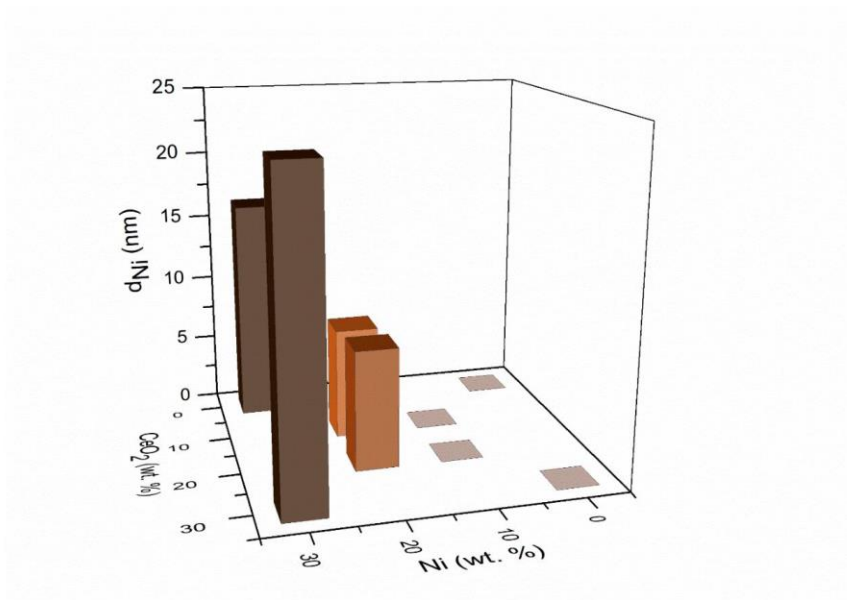


Fig. S4. d_{Ni} (nm) from XRD measurements.

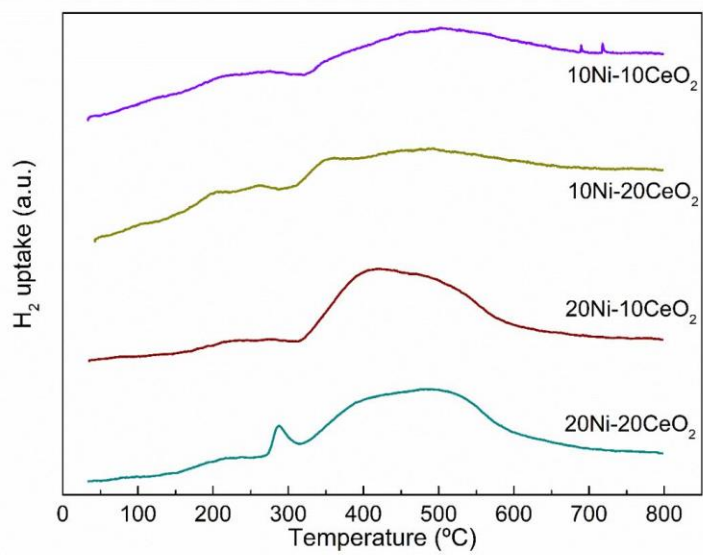


Fig. S5. H₂-TPR profiles of 10Ni-10CeO₂, 10Ni-20CeO₂, 20Ni-10CeO₂ and 20Ni-20CeO₂ catalysts.

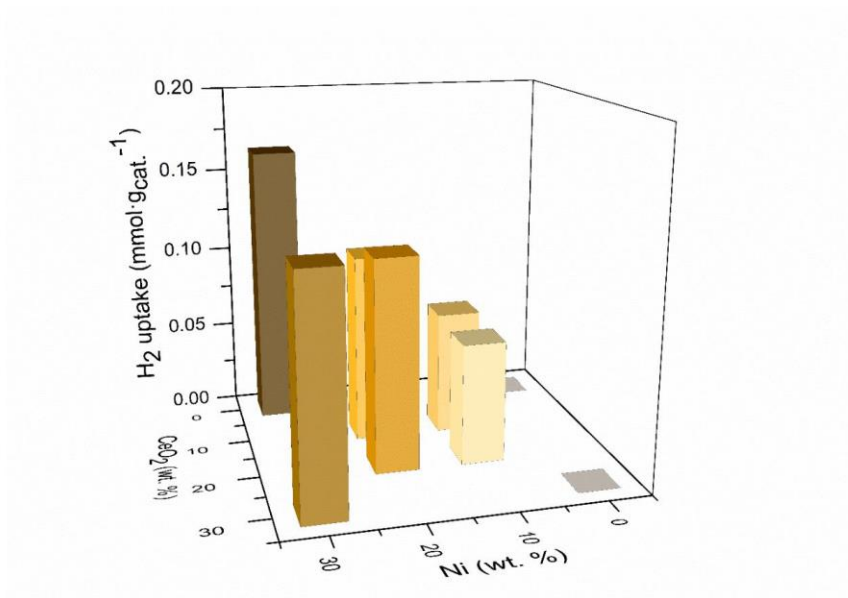


Fig. S6. H₂ uptake (mmol·g_{cat.}⁻¹) estimated from H₂-TPR profiles.

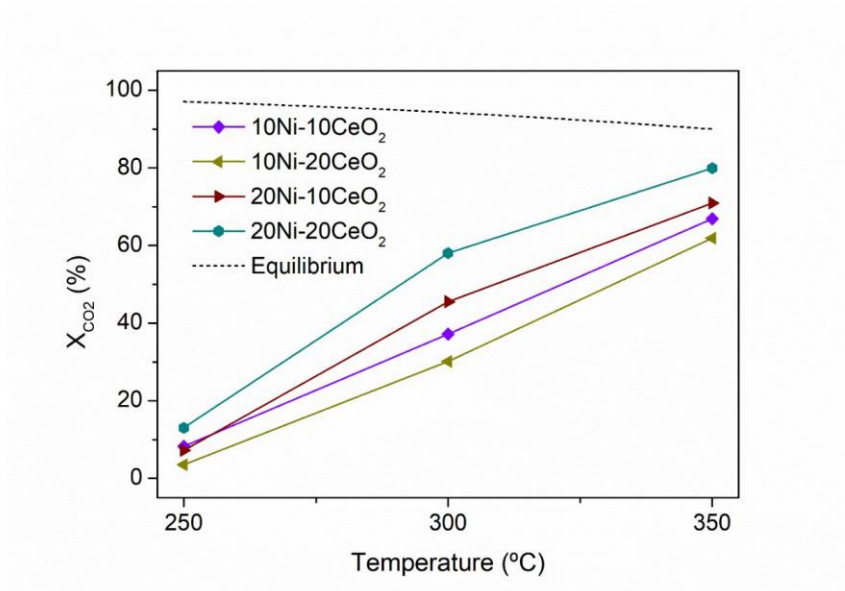


Fig. S7. CO₂ conversion of 10Ni-10CeO₂, 10Ni-20CeO₂, 20Ni-10CeO₂ and 20Ni-20CeO₂ catalysts as function of reaction temperature. Reaction conditions: P = 0 bar-g, F = 200 NmL·min⁻¹ and H₂:CO₂ molar ratio = 4.

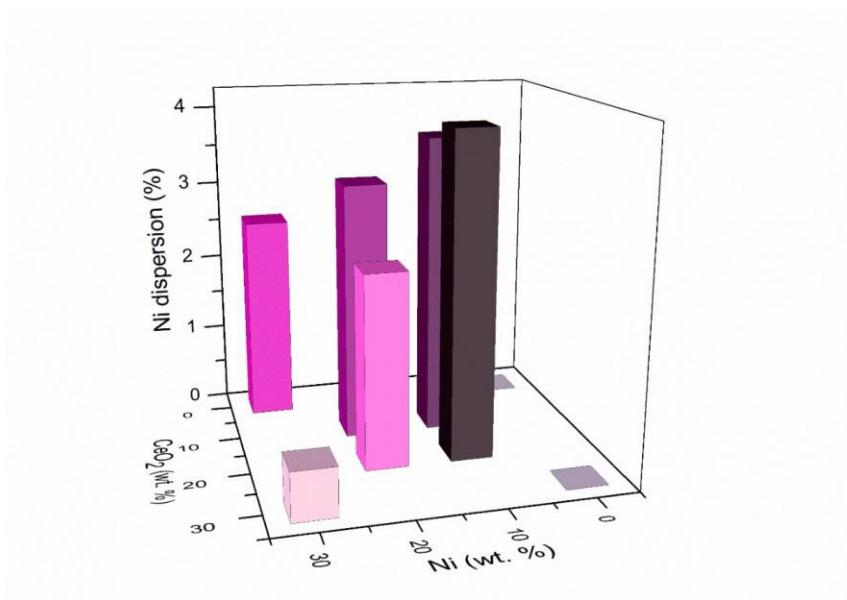


Fig. S8. Ni dispersion (%) from CO-chemisorption.

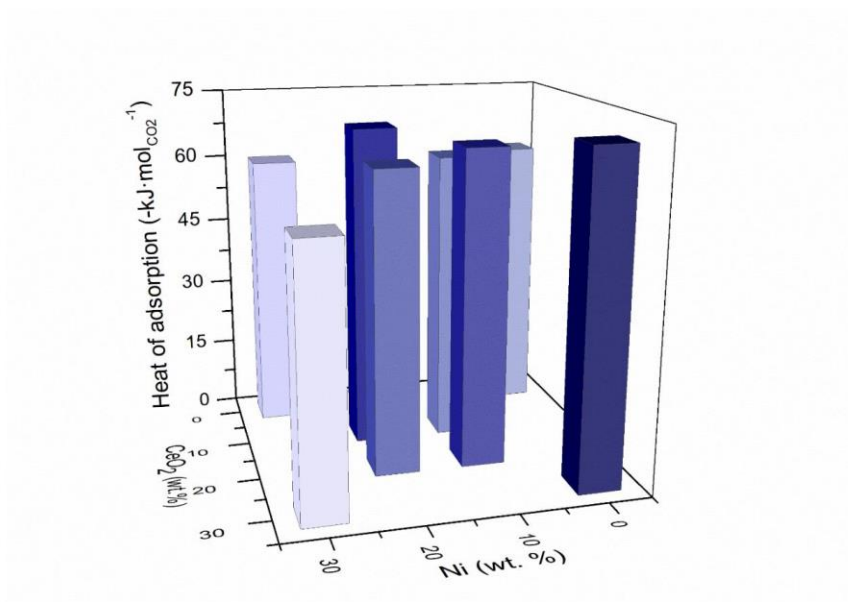


Fig. S9. Heat of adsorption ($\text{kJ}\cdot\text{mol}_{\text{CO}_2}^{-1}$) from TGA-DSC.

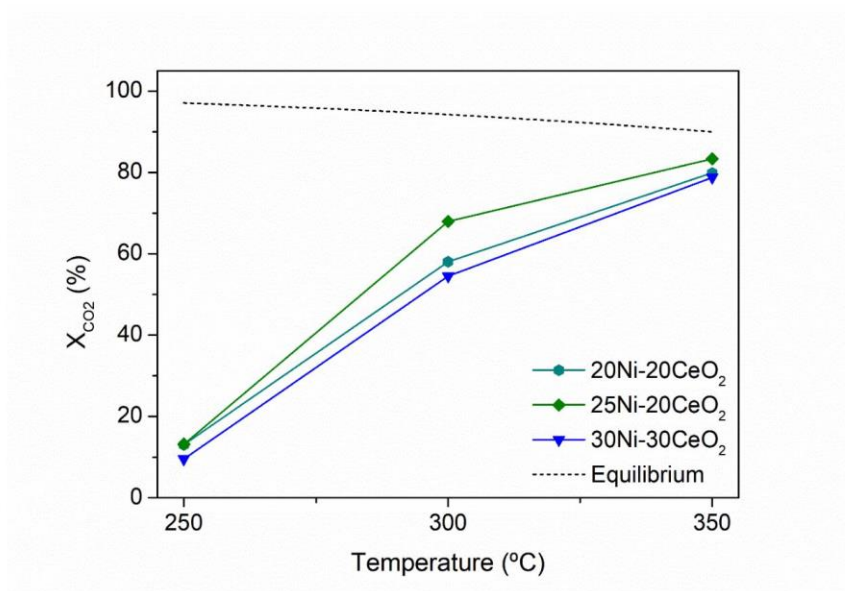


Fig. S10. CO₂ conversion of 20Ni-20CeO₂, 25Ni-20CeO₂ and 30Ni-30CeO₂. Reaction conditions: P = 0 bar-g, F = 200 NmL·min⁻¹ and H₂:CO₂ molar ratio = 4.

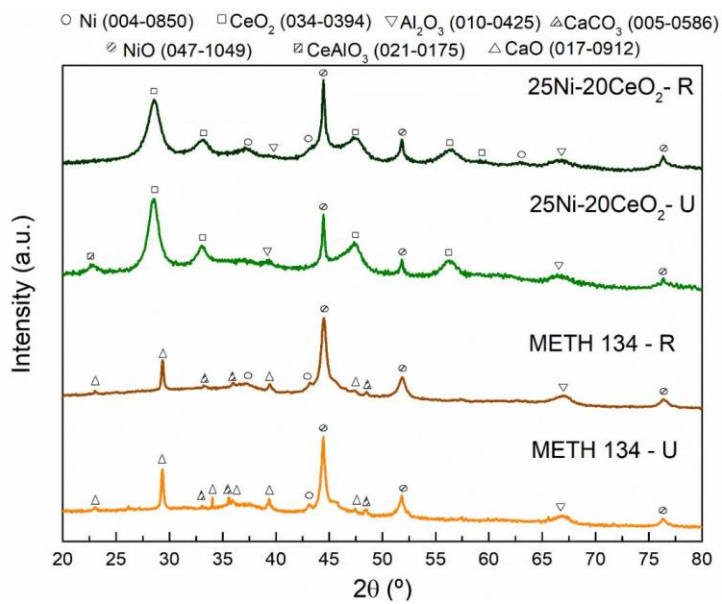


Fig. S11. XRD patters of used catalyst.

Supporting Information

Higher tolerance to sulfur poisoning in CO₂ methanation by the presence of CeO₂

Andreina Alarcón^{a,b}, Jordi Guilera^{a*}, Rodrigo Soto^c and Teresa Andreu^a

^aCatalonia Institute for Energy Research (IREC), Jardins de les Dones de Negre 1, 08930 Sant Adrià de Besòs, Spain.

^bEscuela Superior Politécnica del Litoral (ESPOL), Facultad de Ingeniería en Ciencias de la Tierra, Campus Gustavo Galindo Km.30.5 Vía Perimetral, P.O. Box 09-01-5863, Guayaquil, Ecuador.

^cSynthesis and Solid State Pharmaceutical Centre (SSPC), Bernal Institute, Department of Chemical and Environmental Science, University of Limerick. Limerick V94 T9PX, Ireland.

*corresponding author: jguilera@irec.cat

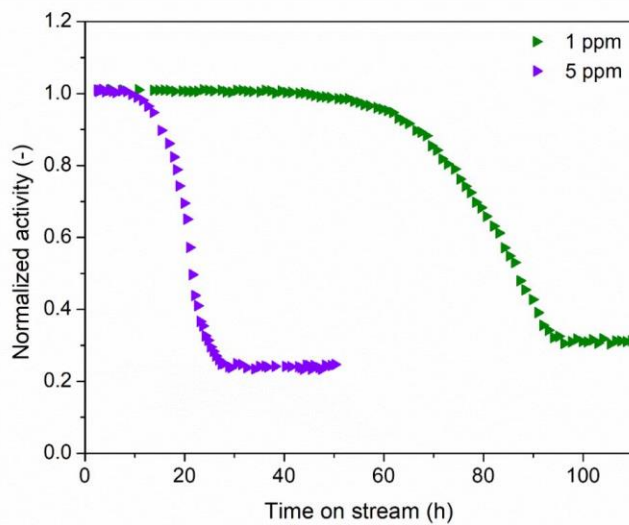


Figure S1. Effects of H₂S impurities over catalytic activity in the Ni-CeO₂ catalyst. Reaction condition: T = 500 °C, P = 5 bar·g, F = 200 mL·min⁻¹, H₂/CO₂ molar ratio = 4 and 1-5 ppm of H₂S.

Table S1. Elemental composition from EDX analysis of the Ni and Ni-CeO₂ catalysts.

Sample	State	Elemental Composition [wt. %]			
		Ni	CeO ₂	Al	S
Ni	fresh	26 ± 1	-	33 ± 1	-
	used	26 ± 1	-	33 ± 1	-
	used-H ₂ S	25 ± 1	-	33 ± 1	0.51 ± 0.05
Ni-CeO ₂	fresh	26 ± 1	21 ± 1	24 ± 1	-
	used	27 ± 1	21 ± 1	24 ± 1	-
	used-H ₂ S	26 ± 1	21 ± 1	24 ± 1	0.54 ± 0.05

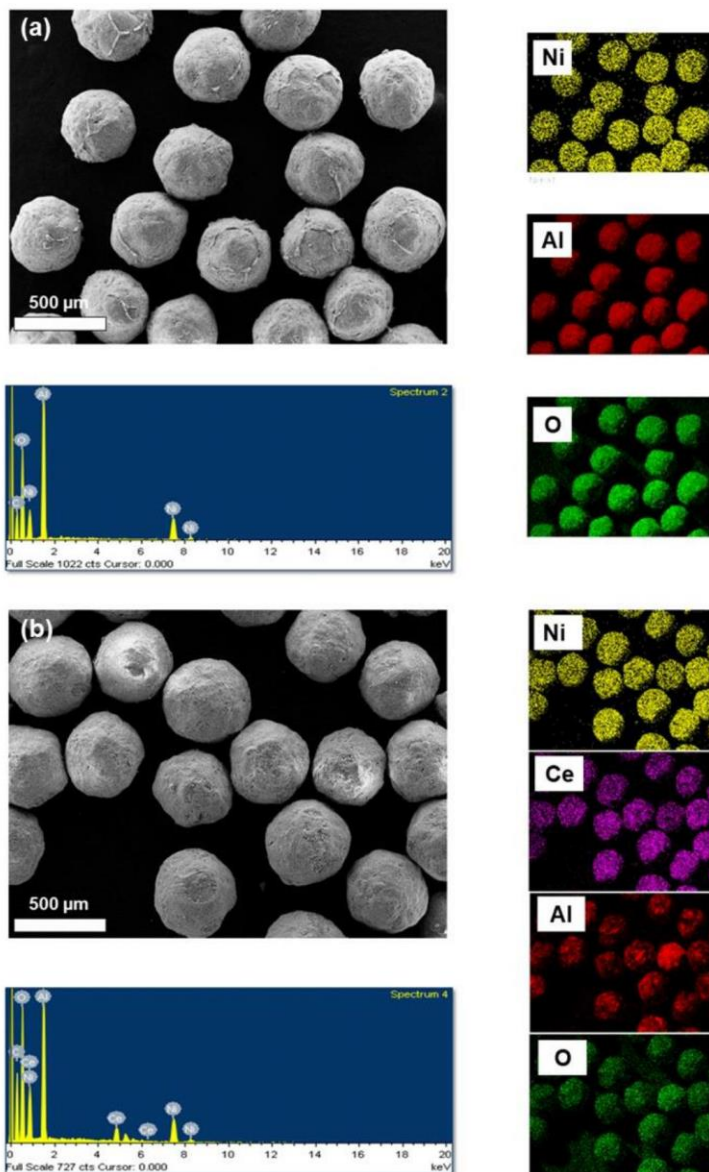
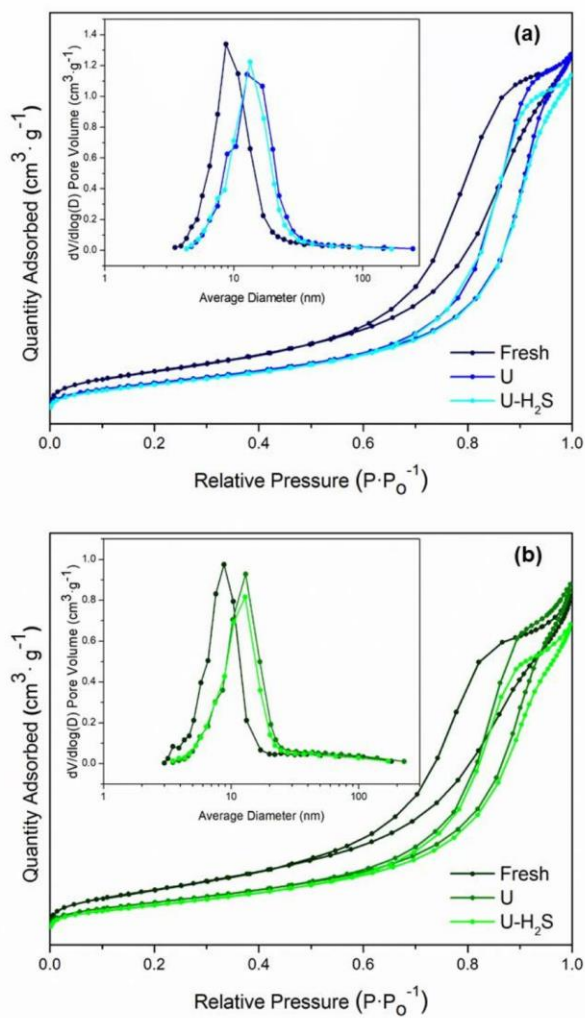


Figure S2. EDX elemental mapping images of the fresh micro-spheres catalysts: a) Ni and b) Ni-CeO₂

Figure S3. Adsorption/desorption isotherms of the a) Ni and b) Ni-CeO₂ Catalysts

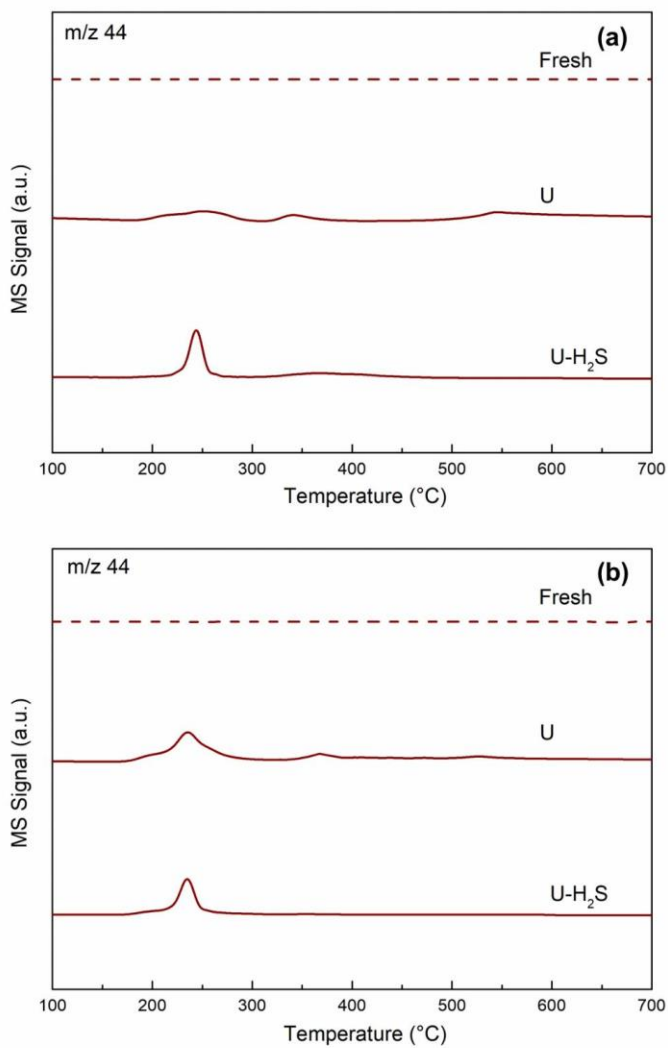


Figure S4. MS analysis during the temperature programmed oxidation shown in Figure 3. Tracked mass $m/z=44$ corresponds to CO_2 .

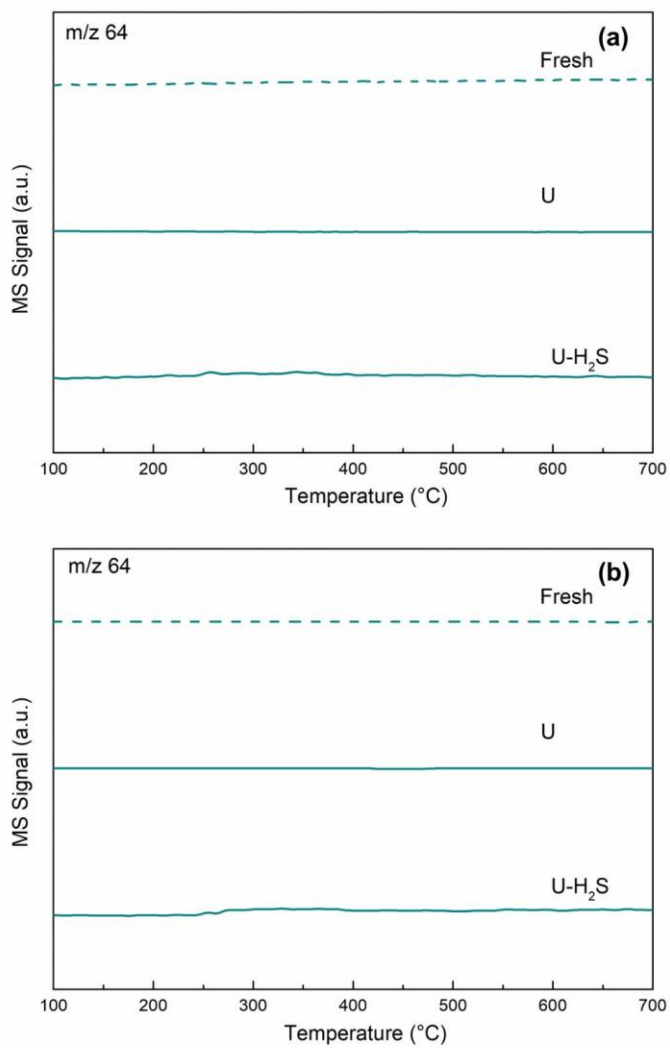


Figure S5. MS analysis during the temperature programmed oxidation shown in Figure 3. Tracked mass $m/z=64$ corresponds to SO_2 .

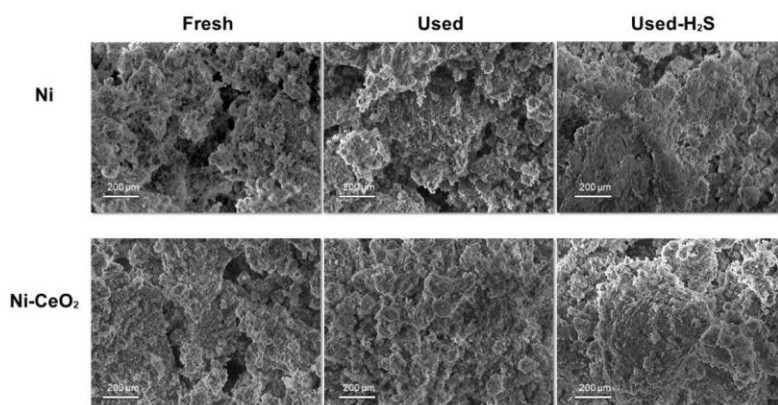
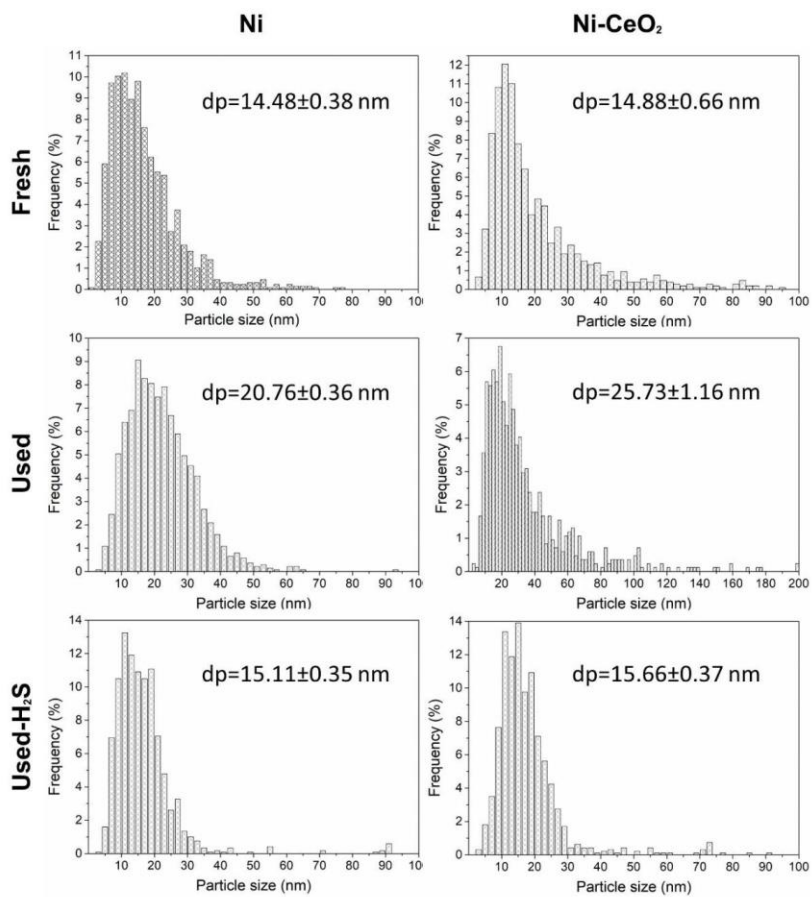


Figure S6. SEM images of crushed Ni and Ni-CeO₂ catalysts

Figure S7. Particle size distributions of the Ni and Ni-CeO₂ catalysts.

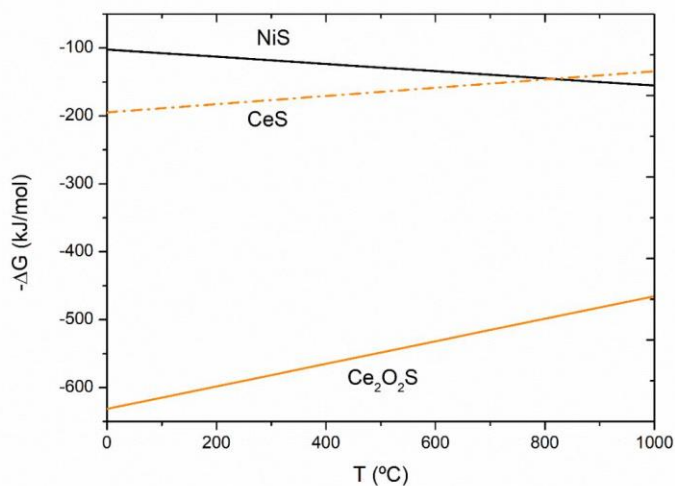


Figure S8. Gibbs free energy of formation for nickel and cerium sulfides as a function of temperature.

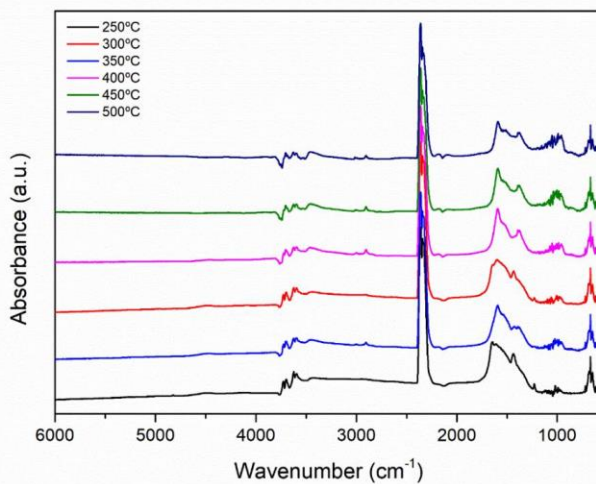


Figure S9. In-situ DRIFTS spectra during CO_2 methanation reaction over CeO_2/Al_2O_3 catalyst at the temperature range 250-500 °C.

Appendix A

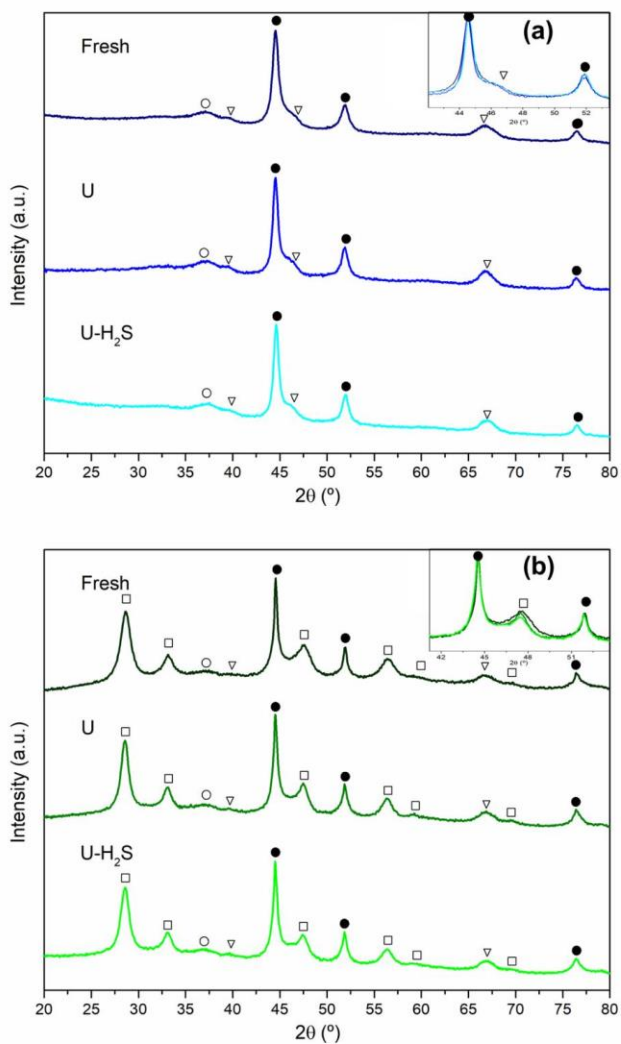


Figure 1. XRD profiles of the a) Ni and b) Ni-CeO₂ catalysts. [●] Ni: (111), (200) and (220); [○] NiO (111); [□] CeO₂: (111), (200), (220), (311), (222) and (400); [▽] γ -Al₂O₃: (222) and (440).

Figure A1 illustrates the XRD diffractograms of Ni and Ni-CeO₂ catalysts in their three experimental states. For fresh Ni catalyst (Figure A1a), the diffraction peaks at $2\theta = 44.50$, 51.84 and 76.35° represent the Ni (111), (200) and (220) lattice planes, respectively. The diffraction peak around of $2\theta = 37.25^\circ$ was associated with NiO (101) lattice plane and the two diffraction peaks at $2\theta = 39.49$ and 66.79° were assigned to the planes Al₂O₃ (222) and (440). Apart from Ni, NiO and Al₂O₃ phases, CeO₂ was detected in the fresh Ni-CeO₂ catalyst (Figure A1b). The diffraction peaks were identified at $2\theta = 28.54$, 33.05 , 47.36 , 56.31 , 59.17 and 69.45° , and related to the CeO₂ (111), (200), (220), (311), (222) and (400) lattice planes. For the U and U-H₂S catalysts, only intensity alterations of the diffraction peaks were distinguished for both samples, implying the growth of metallic Ni and CeO₂ particles.

Appendix B

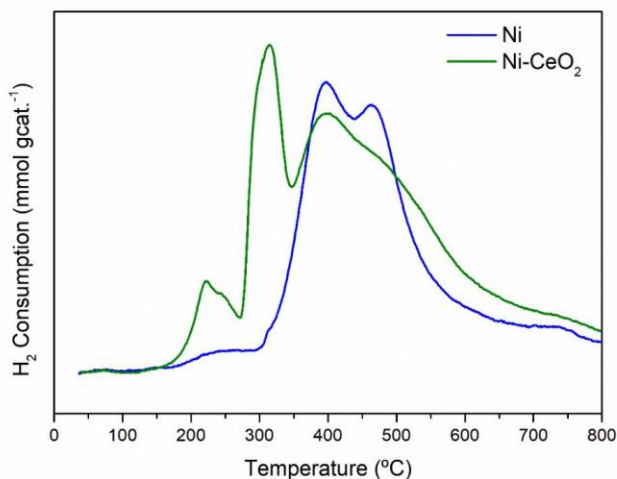


Figure B1. H₂-TPR profiles of the fresh Ni and Ni-CeO₂ catalysts.

Figure B1 shows the H₂-TPR profiles of fresh Ni and Ni-CeO₂ catalysts. Reduction peaks around 221, 316, 399, and 475 °C were observed for Ni-CeO₂ catalyst, while only two peaks were detected at 397 and 465 °C for Ni catalyst. For Ni-CeO₂ catalyst, the two peaks formed at relatively low temperature (<350 °C) were linked to the interaction between CeO₂ and Ni, as well as to the reduction of α -type NiO species with weak or even no interaction with γ -Al₂O₃ support. The peaks at around 399 °C with a shoulder at 475 °C were attributed to the reduction of NiO particles interacting weakly (β_1 -type) and strongly (β_2 -type) with the support. It is worth noting that the high temperature of NiO reduction for Ni-CeO₂ catalyst shifted to lower temperature compared to that of Ni catalyst ($T > 395$ °C), which reflects a better dispersion of metal components. This is probably due to the fact that CeO₂ phase weakens the strong NiO-support interactions. The H₂ consumption of the Ni-CeO₂ catalyst was of 2.59 mmol·g_{cat}⁻¹, being higher than that for Ni (2.44 mmol·g_{cat}⁻¹) within the temperature range 25-800 °C. Besides, the Ni-CeO₂ (83.22%) showed a higher Ni reducibility than the Ni sample (82.46%) at the selected reduction temperature of 500 °C. Based on H₂-TPR information, the catalyst of Ni-CeO₂ presents the best reducibility of Ni and the active sites Ni⁰ on the catalyst surface.

Supporting Information

Pushing the limits of SNG process intensification: high GHSV operation at pilot scale

Jordi Guilera^a, Tim Boeltken^b, Friedemann Timm^b, Ignasi Mallo^c, Andreina Alarcón^{a,d}
Teresa Andreu^a

^aCatalonia Institute for Energy Research (IREC), Jardins de les Dones de Negre 1, 08930 Sant Adrià de Besòs, Spain

^bINERATEC GmbH, Siemensallee 84, 76187 Karlsruhe, Germany

^cNaturgy, Plaça del Gas 1-4, 08003 Barcelona, Spain

^dEscuela Superior Politécnica del Litoral, ESPOL, Facultad de Ingeniería en Ciencias de la Tierra, Campus Gustavo Galindo Km.30.5 Vía Perimetral, P.O. Box 09-01-5863, Guayaquil, Ecuador.

*corresponding author: jguilera@irec.cat

Contents (8)

1. Preliminary experiments	S2
2. Detailed experimental data	S4
3. Post-mortem analysis of catalyst composition.....	S7
4. Compression costs	S8

Figures (1)

Figure S1. Temperature profile of the lab-scale reactor preliminary experiments	S2
---	----

Tables (13)

Table S1. Dry gas composition at the outlet of the lab-scale reactor	S3
Table S2. Dry gas composition during CO ₂ methanation at 2.5 bar.g.....	S4
Table S3. Dry gas composition during CO ₂ methanation at 5.0 bar.g.....	S4
Table S4. Dry gas composition during CO ₂ methanation at 7.5 bar.g.....	S4
Table S5. Dry gas composition during CO ₂ methanation at 37,500 h ⁻¹	S4
Table S6. Dry gas composition during biogas methanation at 2.5 bar.g.....	S5
Table S7. Dry gas composition during biogas methanation at 5.0 bar.g.....	S5
Table S8. Dry gas composition during biogas methanation at 7.5 bar.g.....	S5
Table S9. Dry gas composition during biogas methanation at 37,500 h ⁻¹	S6
Table S10. Elemental composition (±1) of fresh and used catalysts.....	S7
Table S11. Considerations for the compression.....	S8
Table S12. CO ₂ compression at different operating pressures	S8
Table S13. Biogas compression at different operating pressures	S8

1. Preliminary experiments

Preliminary CO₂ methanation experiments were carried out at Karlsruhe Institute of Technology (KIT) laboratory premises to adjust the amount of catalyst mass to be loaded at the pilot plant. The catalyst tested was identical to the used one in pilot plant (Ni-CeO₂/Al₂O₃, d_p=400-500 μm). The laboratory reactor consisted of two parallel reaction channels in form of rectangular ducts with 2 mm in height, 50 mm in width and 100 mm in length. Further details of the setup and analytics can be found elsewhere.³³

The reactor was filled with 7.5 g of catalyst and diluted with 11 g of silicon carbide with d_p=400 μm. Prior to experimentation, the catalyst was reduced in-situ following the same procedure than the pilot plant. Once the catalyst was reduced, reactants were pre-heated at 300°C and introduced to the reactor. The pressure on reactor was maintained at 5 bar·g. All experiments were carried out by feeding the stoichiometric H₂:CO₂ molar ratio = 4. Temperature profiles were adjusted by using both vaporizing water (P=10 bar·g) and heating cartridges to obtain the highest methane content at the outlet.

The experimental design of the preliminary experiments consisted on reproduce 3 different cases of the pilot plant.

1. CO₂ methanation
 - Reactor 1 (F_{CO₂}=0.250 Nm³/h, F_{H₂}=1.000 Nm³/h, F_{CH₄}=0.000 Nm³/h)
 - Reactor 2 (F_{CO₂}=0.025 Nm³/h, F_{H₂}=0.100 Nm³/h, F_{CH₄}=0.225 Nm³/h)
2. Biogas methanation
 - Reactor 1 (F_{CO₂}=0.250 Nm³/h, F_{H₂}=1.000 Nm³/h, F_{CH₄}=0.464 Nm³/h)

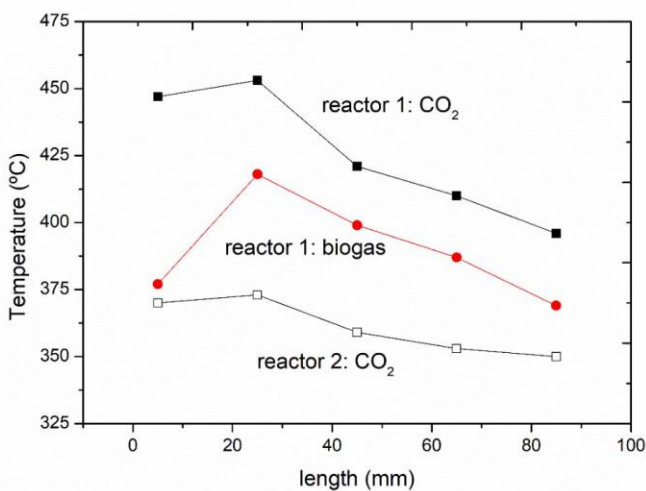


Figure S1. Temperature profile of the lab-scale reactor preliminary experiments.

Figure S1 shows that higher temperatures were always reached in the first reactor compared to the second one. As regards to reactor 1, higher temperatures were obtained (T=396-453 °C) when pure CO₂ was used as reactant. Once CH₄ was introduced with CO₂, the temperature profile decreased significantly (T=369-418°C). As regards to reactor 2, temperatures were kept in the

range of $T=350-370^{\circ}\text{C}$. Therefore, higher temperatures were reached at higher carbon dioxide concentration and higher gas flowrates.

Table S2 presents the dry gas composition obtained in those experiments. It was observed that the amount of CH_4 after the first reactor was in the range of 64% (CO_2 experiment) - 82% (biogas experiment). After the second reactor, CH_4 content was upgraded to 92%, quite close to the desired composition for gas grid purposes.

Table S1. Dry gas composition at the outlet of the lab-scale reactor.

	CO_2 (%)	H_2 (%)	CH_4 (%)
reactor 1: CO_2	7.27	29.08	63.65
reactor 2: CO_2	1.27	5.89	92.38
reactor 1: biogas	3.86	14.62	81.61

2. Detailed experimental data

Upgraded CO₂ methanation

Table S2. Dry gas composition during CO₂ methanation at 2.5 bar-g.

GHSV (h ⁻¹)	reactor 1			reactor 2		
	CO ₂ (%)	H ₂ (%)	CH ₄ (%)	CO ₂ (%)	H ₂ (%)	CH ₄ (%)
19,500	8.46	24.00	67.53	1.91	4.95	93.14
25,500	9.24	26.39	64.37	2.24	6.12	91.64
31,500	11.25	27.87	60.88	3.91	6.79	89.3
35,625	10.81	32.81	56.38	2.45	9.48	88.07
37,500	12.14	33.99	53.87	3.63	9.63	86.74

Table S3. Dry gas composition during CO₂ methanation at 5.0 bar-g.

GHSV (h ⁻¹)	reactor 1			reactor 2		
	CO ₂ (%)	H ₂ (%)	CH ₄ (%)	CO ₂ (%)	H ₂ (%)	CH ₄ (%)
19,500	5.11	17.54	77.35	1.38	3.26	95.36
25,500	6.36	20.07	73.57	1.17	3.84	94.99
31,500	7.61	22.61	69.79	1.71	4.44	93.85
35,625	7.16	25.12	67.72	0.79	6.39	92.82
37,500	7.82	25.97	66.21	1.95	5.44	92.61

Table S4. Dry gas composition during CO₂ methanation at 7.5 bar-g.

GHSV (h ⁻¹)	reactor 1			reactor 2		
	CO ₂ (%)	H ₂ (%)	CH ₄ (%)	CO ₂ (%)	H ₂ (%)	CH ₄ (%)
19,500	5.14	15.29	79.57	1.37	3.15	95.48
25,500	5.98	16.86	77.16	1.21	3.4	95.39
31,500	7.10	20.48	72.42	1.44	3.83	94.73
35,625	6.52	22.89	70.37	0.88	4.81	94.31
37,500	7.80	22.73	69.47	1.83	4.32	93.85

Table S5. Dry gas composition during CO₂ methanation at 37,500 h⁻¹.

P (bar-g)	reactor 1			reactor 2		
	CO ₂ (%)	H ₂ (%)	CH ₄ (%)	CO ₂ (%)	H ₂ (%)	CH ₄ (%)
0	-	-	-	-	-	-
0.5	-	-	-	-	-	-
1.0	12.83	40.67	46.5	3.83	17.25	78.92
1.5	13.56	48.22	38.22	3.52	15.74	80.74
2.23	11.56	35.62	52.82	2.95	11.79	85.26
2.5	22.12	22.62	55.26	2.66	9.70	87.64
3.0	10.68	32.15	57.17	2.42	8.42	89.16
3.5	10.15	30.46	59.39	2.19	7.4	90.41

4.0	9.47	28.45	62.08	2.04	6.53	91.43
4.5	9.00	27.01	63.99	1.83	6.05	92.12
5.0	8.12	25.93	65.95	1.88	5.42	92.7
5.5	8.23	25.45	66.32	1.73	5.19	93.08
6.0	8.31	23.47	68.22	1.69	5.04	93.27
6.5	7.54	23.03	69.43	1.60	4.69	93.71
7.0	6.88	23.02	70.1	0.89	4.95	94.16
7.5	6.76	22.86	70.38	0.83	4.86	94.31
8.0	5.78	23.52	70.7	0.29	5.27	94.44
8.5	5.64	23.23	71.13	0.40	5.03	94.57
9.0	5.85	22.93	71.22	0.52	4.47	95.01

Biogas methanation

Table S6. Dry gas composition during biogas methanation at 2.5 bar-g.

GHSV (h ⁻¹)	reactor 1			reactor 2		
	CO ₂ (%)	H ₂ (%)	CH ₄ (%)	CO ₂ (%)	H ₂ (%)	CH ₄ (%)
19,500	5.04	78.84	16.12	2.23	5.14	92.63
25,500	4.34	77.84	17.82	2.12	4.56	93.32
31,500	4.69	73.19	22.12	2.01	6.43	91.56
35,625	7.16	69.03	23.81	2.49	6.95	90.56
37,500	8.29	65.88	25.83	2.62	7.28	90.1

Table S7. Dry gas composition during biogas methanation at 5.0 bar-g.

GHSV (h ⁻¹)	reactor 1			reactor 2		
	CO ₂ (%)	H ₂ (%)	CH ₄ (%)	CO ₂ (%)	H ₂ (%)	CH ₄ (%)
19,500	5.04	77.59	17.37	1.36	3.48	95.16
25,500	4.88	77.51	17.61	1.82	3.15	95.03
31,500	4.69	77.23	18.08	1.91	3.68	94.41
35,625	6.09	75.67	18.24	1.62	4.77	93.61
37,500	6.4	72.66	20.94	1.67	4.85	93.48

Table S8. Dry gas composition during biogas methanation at 7.5 bar-g.

GHSV (h ⁻¹)	reactor 1			reactor 2		
	CO ₂ (%)	H ₂ (%)	CH ₄ (%)	CO ₂ (%)	H ₂ (%)	CH ₄ (%)
19,500	2.41	12.43	85.17	0.85	2.55	96.6
25,500	5.71	11.81	82.49	1.49	2.17	96.34
31,500	4.69	18.08	80.81	1.02	2.62	96.36
35,625	5.95	13.26	80.37	1.43	2.51	96.06
37,500	5.33	14.16	80.51	1.79	2.87	95.34

Table S9. Dry gas composition during biogas methanation at 37,500 h⁻¹.

P (bar-g)	reactor 1			reactor 2		
	CO ₂ (%)	H ₂ (%)	CH ₄ (%)	CO ₂ (%)	H ₂ (%)	CH ₄ (%)
0	-	-	-	-	-	-
0.5	-	-	-	-	-	-
1.0	-	-	-	-	-	-
1.5	-	-	-	-	-	-
2.23	8.52	26.26	65.22	2.76	10.21	87.03
2.5	8.37	25.60	66.03	1.71	9.08	89.21
3.0	7.99	24.88	67.13	2.23	8.00	89.77
3.5	7.43	24.34	68.23	2.00	7.77	90.23
4.0	6.82	23.19	69.99	2.01	6.32	91.67
4.5	7.71	20.90	71.39	2.11	5.14	92.75
5.0	6.33	20.46	73.21	2.09	4.92	92.99
5.5	6.11	19.02	74.87	1.86	4.90	93.24
6.0	5.99	16.69	77.32	1.56	3.58	94.86
6.5	5.65	15.12	79.23	1.23	3.78	94.99
7.0	5.47	13.78	80.75	1.24	3.75	95.01
7.5	5.21	13.76	81.03	1.33	3.22	95.45
8.0	5.22	12.57	82.21	1.35	3.14	95.51
8.5	5.14	10.92	83.94	1.30	3.13	95.57
9.0	5.07	10.81	84.12	1.32	2.55	96.13

3. Post-mortem analysis of catalyst composition

Elemental analysis of the catalysts was studied in reduced form by scanning electron microscopy (SEM, Zeiss Auriga 60) equipped with an energy dispersive X-ray spectrometer (EDX, Oxford Inca Energy). No relevant changes in the elemental composition were observed of the spent catalyst with respect to fresh catalysts.

Table S10. Elemental composition (± 1) of fresh and used catalysts.

sample	T (°C)	time (h)	Ni	Ce
fresh catalyst ^{1,2}	-	-	26	21
used (pure reactants) ¹	300	120	26	21
used (pure reactants) ²	500	142	27	21
used (1 ppm H ₂ S) ²	500	141	26	21
used (1 st reactor)	≤500	2,000	25	20
used (2 nd reactor)	≤400	2,000	26	20

- (1) Alarcón, A.; Guilera, J.; Díaz, J. A.; Andreu, T. Optimization of Nickel and Ceria Catalyst Content for Synthetic Natural Gas Production through CO₂ Methanation. *Fuel Process. Technol.* **2019**, *193*, 114–122. <https://doi.org/https://doi.org/10.1016/j.fuproc.2019.05.008>.
- (2) Alarcón, A.; Guilera, J.; Soto, R.; Andreu, T. Higher Tolerance to Sulfur Poisoning in CO₂ Methanation by the Presence of CeO₂. *Appl. Catal. B Environ.* **2020**, *263*, 118346. <https://doi.org/10.1016/j.apcatb.2019.118346>.

4. Compression costs

Table S11. Considerations for the compression

compressor efficiency	85	%
specific power required	0.037	kWh·m ⁻³ ·bar ⁻¹
electricity costs	0.07	€/kWh
LHV_{CH4}	9.97	kWh·Nm ⁻³

Table S12. CO₂ compression at different operating pressures

gas compression (bar)	power required (kWh·m ⁻³)	compression cost (€·m ⁻³)	% energy consumed (kW _{in} /kW _{out} ·100)
0.0	0.000	0.000	0.00
2.5	0.093	0.006	0.09
5.0	0.185	0.013	0.19
7.5	0.278	0.019	0.28
10.0	0.370	0.026	0.37
12.5	0.463	0.032	0.46
15.0	0.556	0.039	0.56
17.5	0.648	0.045	0.65
20.0	0.741	0.052	0.74
22.5	0.833	0.058	0.84
25.0	0.926	0.065	0.93
27.5	1.019	0.071	1.02
30.0	1.111	0.078	1.11

Table S13. Biogas compression at different operating pressures

gas compression (bar)	power required (kWh·m ⁻³)	compression cost (€·m ⁻³)	% energy consumed (kW _{in} /kW _{out} ·100)
0.0	0.000	0.000	0.00
2.5	0.264	0.018	0.26
5.0	0.528	0.037	0.53
7.5	0.792	0.055	0.79
10.0	1.056	0.074	1.06
12.5	1.319	0.092	1.32
15.0	1.583	0.111	1.59
17.5	1.847	0.129	1.85
20.0	2.111	0.148	2.12
22.5	2.375	0.166	2.38
25.0	2.639	0.185	2.65
27.5	2.903	0.203	2.91
30.0	3.167	0.222	3.18

Supporting information

CO₂ conversion to synthetic natural gas: Reactor design over Ni-Ce/Al₂O₃ catalyst

Andreina Alarcón, Jordi Guilera, Teresa Andreu

Catalonia Institute for Energy Research (IREC), Jardins de les Dones de Negre 1,
08930 Sant Adrià de Besòs, Spain

Reaction kinetics of methane formation

Table SI 1 shows the 45 experimental rate data conducted over the 15Ni-10Ce/Al₂O₃ catalyst at temperature range of 473-673K.

Table SI 1. Experimental rate data of the methane formation at the temperature range of 473-673K.

	T	F _{feed}	F _{Ar}	m _{cat}	c _{CO2}	c _{CH2}	Y _{CH4}	n _{CH4} ·10 ⁵	r _{CH4}
exp.	K	mL·min ⁻¹	mL·min ⁻¹	mg	mol·m ⁻³	mol·m ⁻³	%	mol·s ⁻¹	mol·(m ⁻³ ·s ⁻¹)
1	473	200	0	182	5.09	20.34	0.62	1.04	33
2	473	200	0	60	5.09	20.34	0.30	0.51	49
3	498	50	150	182	1.21	4.83	4.93	1.98	63
4	498	100	100	182	2.42	9.66	2.77	2.23	71
5	498	200	0	60	4.83	19.32	0.77	1.24	120
6	498	150	50	182	3.62	14.49	3.43	4.14	132
7	498	200	0	55	4.83	19.32	1.10	1.77	187
8	498	200	0	182	4.83	19.32	3.85	6.20	198
9	523	50	150	60	1.15	4.60	1.73	0.66	64
10	523	50	150	182	1.15	4.60	16.04	6.15	196
11	523	100	100	182	2.30	9.20	12.82	9.83	313
12	523	200	0	60	4.60	18.40	2.29	3.51	339
13	523	150	50	182	3.45	13.80	9.37	10.78	343
14	523	200	0	55	4.60	18.40	2.53	3.88	409
15	523	200	0	182	4.60	18.40	11.77	18.05	575
16	548	50	150	60	1.10	4.39	6.60	2.41	233
17	548	100	100	60	2.19	8.78	6.85	5.01	484
18	548	150	50	60	3.29	13.17	6.62	7.26	702
19	548	200	0	60	4.39	17.56	6.10	8.92	863
20	548	200	0	55	4.39	17.56	6.48	9.48	1000
21	573	50	150	60	1.05	4.20	16.47	5.76	557
22	573	75	125	60	1.57	6.30	15.20	7.97	771
23	573	100	100	60	2.10	8.40	14.37	10.06	972
24	573	125	75	60	2.62	10.50	13.71	12.00	1160
25	573	150	50	60	3.15	12.59	12.67	13.29	1285
26	573	175	25	60	3.67	14.69	11.87	14.54	1405

27	573	200	0	60	4.20	16.79	12.70	17.77	1718
28	598	50	150	29	1.01	4.02	17.01	5.70	1141
29	598	100	100	29	2.01	8.05	13.53	9.07	1814
30	598	150	50	29	3.02	12.07	10.92	10.98	2195
31	598	200	0	29	4.02	16.09	8.59	11.52	2305
32	598	200	0	8	4.02	16.09	2.54	3.40	2466
33	598	175	25	8	3.38	13.51	5.04	5.67	4114
34	598	200	0	8	3.86	15.45	4.42	5.68	4122
35	648	50	150	8	0.93	3.71	10.02	3.10	2247
36	648	100	100	8	1.86	7.42	8.91	5.51	3998
37	648	150	50	8	2.78	11.14	8.30	7.70	5583
38	648	200	0	8	3.71	14.85	7.36	9.11	6606
39	673	50	150	8	0.89	3.57	13.26	3.95	2864
40	673	75	125	8	1.34	5.36	12.68	5.66	4106
41	673	100	100	8	1.79	7.15	12.53	7.46	5412
42	673	125	75	8	2.23	8.94	11.54	8.60	6233
43	673	150	50	8	2.68	10.72	11.65	10.41	7546
44	673	175	25	8	3.13	12.51	11.48	11.97	8679
45	673	200	0	8	3.57	14.30	11.74	13.99	10144

Supporting information

An insight into the heat-management for the CO₂ methanation based on free convection

Andreina Alarcón^{a,b}, Jordi Guilera^{a*} and Teresa Andreu^a

^aCatalonia Institute for Energy Research (IREC), Jardins de les Dones de Negre 1, 08930 Sant Adrià de Besòs, Spain

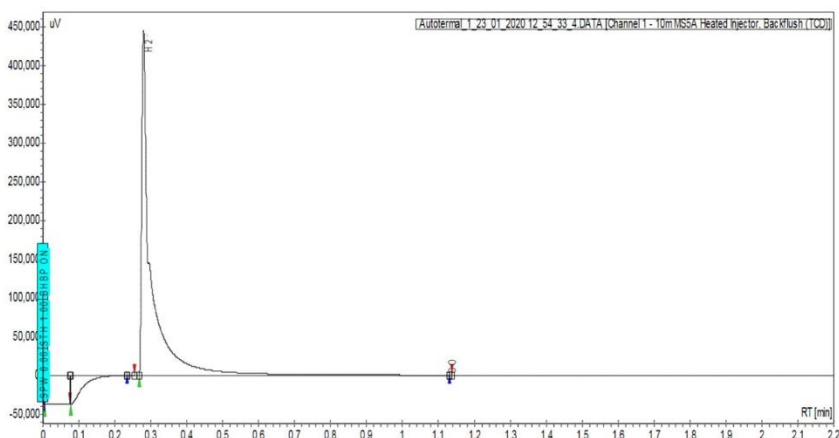
^bEscuela Superior Politécnica del Litoral, ESPOL, Facultad de Ingeniería en Ciencias de la Tierra, Campus Gustavo Galindo Km.30.5 Vía Perimetral, P.O. Box 09-01-5863, Guayaquil, Ecuador.

*corresponding author. jguilera@irec.cat

Chromatogram: Autotermal_1_23_01_2020_12_54_33_4_channel1

System: 490
Method: 2017-SNG-Run
User: aalarcon

Acquired: 23/01/2020 13:05:53
Processed: 23/01/2020 13:09:02
Printed: 24/08/2020 11:34:15



Peak Results:

Autotermal_1_23_01_2020_12_54_33_4.DATA[Channel 1-10m MS5A Heated Injector, Backflush (TCD)]

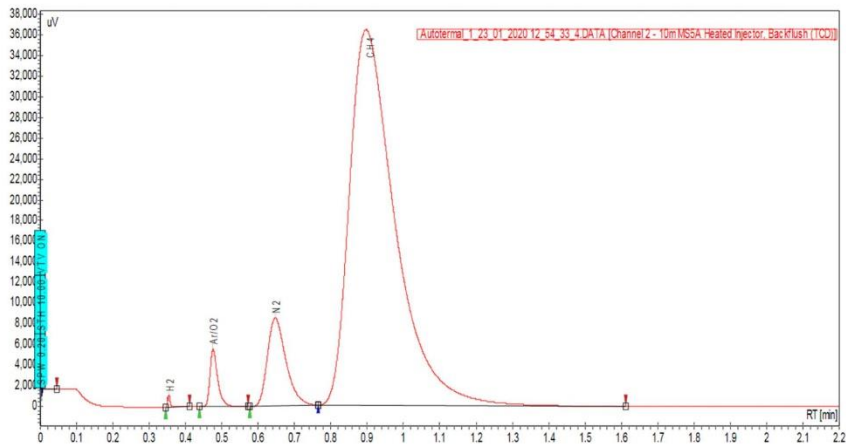
Index	Name	Time [min]	Quantity [%CAL]	Height [uV]	Area [Uv·min]	Area [%]
1	H2	0.28	46.51	444213.1	13069.6	76.169
2	CO	1.14	0	55.2	0.0	0.000

Figure S11. Raw GC spectrum of the molecular sieve (MS5A) channel with argon as carrier gas for H₂ analysis.

Chromatogram: Autotermal_1_23_01_2020_12_54_33_4_channel2

System: 490
 Method: 2017-SNG-Run
 User: aalarcon

Acquired: 23/01/2020 13:05:53
 Processed: 23/01/2020 13:09:02
 Printed: 24/08/2020 11:34:15



Peak Results:

Autotermal_1_23_01_2020_12_54_33_4.DAT[Channel 2-10m MS5A Heated Injector, Backflush (TCD)]

Index	Name	Time [min]	Quantity [%CAL]	Height [uV]	Area [Uv·min]	Area [%]
1	H2	0.35	0.00	1174.2	9.4	0.158
2	Ar/O2	0.47	0.00	5590.6	139.0	2.328
3	N2	0.65	0.00	8528.0	507.4	8.497
4	CH4	0.90	100.00	36392.2	5314.6	88.999

Figure S12. Raw GC spectrum of the molecular sieve (MS5A) channel using He as carrier gas for CH₄ and CO analysis.

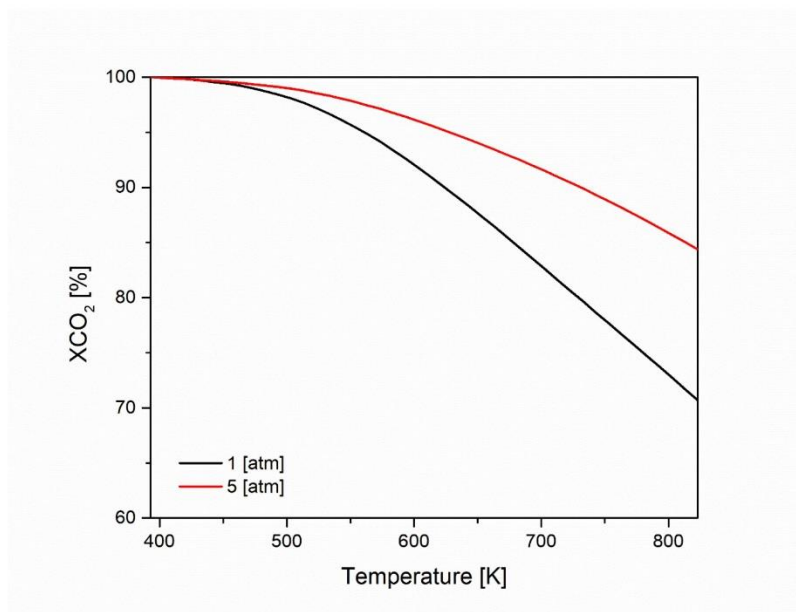


Figure SI4. Thermodynamics equilibrium: CO₂ conversion as a function of temperature and pressure at H₂/CO₂ molar ratio of 4.

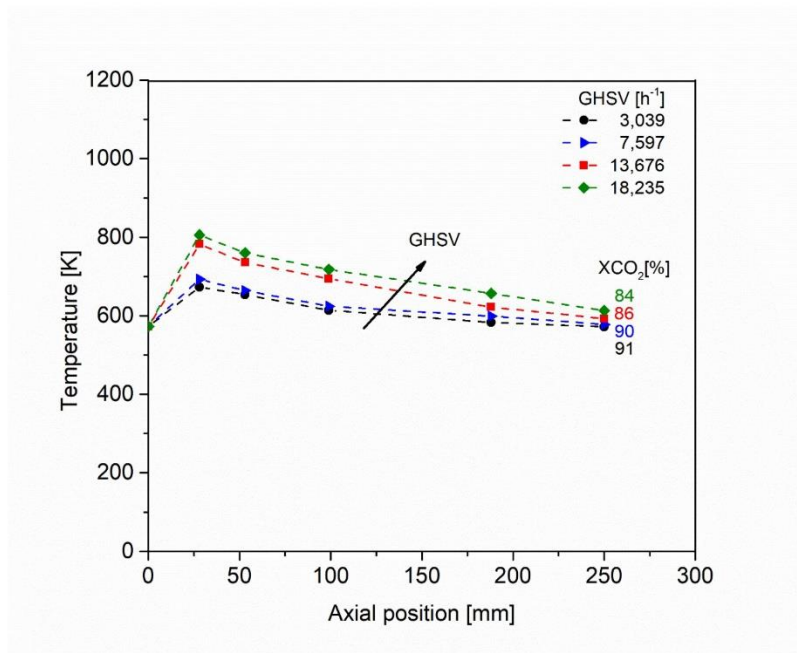


Figure SI5. Temperature profile heating the reactor at P=1 atm and $T_{\text{inlet}}=573\text{K}$.

Table S1. Simulation results at different reactor conditions of P, T_{inlet}, T_{air} and GHSV.

#	Reaction conditions					Results			Criteria: Yes or No	
	P	T _{inlet}	GHSV	T _{air}	ratio	XCO ₂	T _{max}	T _{outlet}	XCO ₂ ≥90	T _{max} ≤823
	[atm]	[K]	[h ⁻¹]	[K]	[-]	[%]	[K]	[K]	[%]	[K]
1	1	473	13,676	298	4	73	734	298	No	Yes
2	1	523	13,676	298	4	77	754	336	No	Yes
3	1 ^a	573	13,676	298	4	79	775	368	No	Yes
4	1	623	13,676	298	4	85	835	452	No	No
5	1	673	13,676	298	4	88	893	525	No	No
6	5	473	13,676	298	4	93	795	512	Yes	Yes
7	5	523	13,676	298	4	92	825	540	Yes	No
8	5	573	13,676	298	4	91	864	557	Yes	No
9	5	623	13,676	298	4	89	916	603	No	No
10	5	673	13,676	298	4	88	926	634	No	No
12	5	523	10,257	298	4	95	778	484	Yes	No
13	5	523	6,838	298	4	92	726	400	Yes	No
14	5 ^b	503	11,520	298	4	96	817	505	Yes	Yes
15	5	503	11,520	273	4	93	793	472	Yes	Yes
16	5	503	11,520	285.5	4	95	798	486	Yes	Yes
17	5	503	11,520	310.5	4	94	821	510	Yes	Yes
18	5	503	11,520	323	4	92	827	525	Yes	No
19	10	473	13,676	298	4	92	848	635	Yes	No
20	10	523	13,676	298	4	90	878	655	Yes	No
21	10	573	13,676	298	4	87	919	625	No	No
22	10	623	13,676	298	4	86	956	610	No	No
23	10	673	13,676	298	4	82	976	692	No	No
24	15	473	13,676	298	4	87	861	693	No	No
25	15	523	13,676	298	4	86	871	717	No	No
26	15	573	13,676	298	4	78	959	705	No	No
27	15	623	13,676	298	4	73	936	682	No	No
28	15	673	13,676	298	4	70	1049	780	No	No
29	20	473	13,676	298	4	81	920	765	No	No
30	20	523	13,676	298	4	80	940	785	No	No
31	20	573	13,676	298	4	73	1056	877	No	No
32	20	623	13,676	298	4	69	1158	953	No	No
33	20	673	13,676	298	4	68	1167	993	No	No
^a Data of the model validation										
^b Data of the reactor proposal										

Appendix: Ansys CFD model

ANSYS fluent solves the following equations for mass, momentum and energy.

Mass balance

The mass balance in the gas phase are written as (Eq. S1):

$$\frac{\partial}{\partial t}(\rho Y_i) + \nabla \cdot (\rho \vec{v} Y_i) = -\nabla \cdot \vec{J}_i + R_i \quad \text{Eq. S1}$$

where Y_i is the local mass fraction of each species i , \vec{J}_i is the diffusion flux of species i (Eq. 2), R_i is the net rate of production by chemical reaction (Eq. S3).

$$\vec{J}_i = -\left(\rho D_{i,m} + \frac{u_t}{S_{ct}}\right) \nabla Y_i - D_{T,i} \frac{\nabla T}{T} \quad \text{Eq. S2}$$

where, S_{ct} is the turbulent Schmidt number ($\frac{u_t}{\rho D_t}$ where u_t is the turbulent viscosity and D_t is the turbulent diffusivity), $D_{i,m}$ is the mass diffusion coefficient for species i in the mixture, and $D_{T,i}$ is the thermal diffusion coefficient.

$$R_i = M_{w,i} \sum_{r=1}^{N_R} \bar{R}_{i,r} \quad \text{Eq. S3}$$

where $M_{w,i}$ is the molecular weight of species i , and $\bar{R}_{i,r}$ is the Arrhenius molar rate of creation/destruction of species in reaction r .

Energy balance

The energy balance in the gas phase are written as (Eq. S4):

$$\frac{\partial}{\partial t}(\rho E) + \nabla \cdot (\vec{v}(\rho E + p)) = \nabla \cdot (k_{eff} \nabla T - \sum_i h_i \vec{J}_i + (\bar{\tau}_{eff} \cdot \vec{v})) + S_r \quad \text{Eq. S4}$$

The first three terms on the right-hand side represent energy transfer due to conduction, species diffusion, and viscous dissipation, respectively. S_r is the heat generation from chemical reaction of reaction R_i .

the E per unit mass is defined as:

$$E = h - \frac{p}{\rho} + \frac{v^2}{2} \quad \text{Eq. S5}$$

where sensible enthalpy h is defined for ideal gases as:

$$h = \sum_i Y_i h_i \quad \text{Eq. S6}$$

The energy balance in the solid phase is defined as:

$$\frac{\partial}{\partial t}(\rho h) + \nabla \cdot (\vec{v} \rho h) = \nabla \cdot (k \nabla T) + S_s \quad \text{Eq. S7}$$

where sensible enthalpy h is calculated for solid phase as:

$$h = \int_{T_{ref}}^T c_p dT \quad \text{Eq. S8}$$

The second term on the left-hand side of Eq. S7 represents convective energy transfer due to rotational or translational motion of the solid phase, while the

terms on the right-hand side are the heat flux due to conduction and volumetric heat sources within the solid phase, respectively.

Momentum balance

The flow regime assumed was axial with a plug flow model with turbulent movement. The standard k-ε two-equations model was considered for modelling turbulence. This model is based on transport equations for the turbulence kinetic energy (k) (Eq. 9) and its dissipation rate (ε) (Eq. 10).

turbulence kinetic energy (k):

$$\frac{\partial}{\partial t}(\rho k) + \frac{\partial}{\partial x_i}(\rho k u_i) = \frac{\partial}{\partial x_j} \left[\left(\mu + \frac{\mu_t}{\sigma_k} \right) \frac{\partial k}{\partial x_j} \right] + G_k + G_b - \rho \varepsilon - Y_M + S_k \quad \text{Eq. S9}$$

dissipation rate (ε):

$$\frac{\partial}{\partial t}(\rho \varepsilon) + \frac{\partial}{\partial x_i}(\rho \varepsilon u_i) = \frac{\partial}{\partial x_j} \left[\left(\mu + \frac{\mu_t}{\sigma_\varepsilon} \right) \frac{\partial \varepsilon}{\partial x_j} \right] + C_{1\varepsilon}(G_k + C_{3\varepsilon}G_b) - C_{2\varepsilon}\rho \frac{\varepsilon^2}{k} + S_\varepsilon \quad \text{Eq. S10}$$

The μ_t turbulence viscosity (Eq. 11) is calculated as:

$$\mu_t = C_\mu \rho \frac{k^2}{\varepsilon} \quad \text{Eq. S11}$$

The constant values ($C_{1\varepsilon} = 1.44$, $C_{2\varepsilon} = 1.92$ and $C_\mu = 0.09$) and the turbulent Prandtl numbers for ε and k ($\sigma_\varepsilon = 1.3$ and $\sigma_k = 1.0$) are established by the viscous model.

CURRICULUM VITAE



Andreina Alexandra Alarcón Avellán

Birthday: April 3, 1991

Nationality: Ecuadorian

Email: andreina612@gmail.com

Phone: +34631609125

Address: Carrer Roger de Flor 303 5 2a
Barcelona 08025 |Spain

EDUCATION

2017-Present

Nanoscience Ph.D.

Thesis: Catalyst and reactor design for carbon dioxide methanation
University of Barcelona (UB)
Barcelona-Spain

2016-2017

Renewable and sustainable energy M.Sc.

University of Barcelona (UB)
Thesis: Prediction of temperature profile on a CO₂ methanation reactor prototype
Barcelona-Spain

2008-2013

Petroleum Engineering B.Sc.

Escuela Superior Politécnica del Litoral (ESPOL)
Guayaquil-Ecuador

PROFESSIONAL EXPERIENCE

2019-Present

Researcher

Catalonia Institute for Energy Research (IREC)
Barcelona-Spain

2019

Visiting Scientific

INERATEC GmbH and Karlsruhe Institute Technology (KIT). (September to December)
Karlsruhe-Germany

2017-2019

Researcher

Catalonia Institute for Energy Research (IREC)
Barcelona-Spain

2014-2016

Professor

Escuela Superior Politécnica del Litoral (ESPOL)
Guayaquil-Ecuador

AWARDS

2016

Post-graduate scholarship

Walter Valdano Raffo Program (First Edition)
Escuela Superior Politécnica del Litoral (ESPOL)
Guayaquil-Ecuador

PUBLICATIONS

- **A. Alarcón**, J. Guilera, T. Andreu. An insight into the heat-management for the CO₂ methanation based on free convection. *Fuel Processing Technology*, (2020). <https://doi.org/10.1016/j.fuproc.2020.106666>.
- J. Guilera, T. Boeltken, F. Timm, I. Mallol, **A. Alarcón**, T. Andreu. Pushing the limits of SNG process intensification: high GHSV operation at pilot scale. *ACS Sustainable Chemistry & Engineering* 2020, 8, 22, 8409–8418. <https://doi.org/10.1021/acssuschemeng.0c02642>.
- **A. Alarcón**, J. Guilera, T. Andreu. Higher tolerance to sulfur poisoning in CO₂ methanation by the presence of CeO₂. *Applied Catalysis B: Environmental* 263, (2020) 118346. <https://doi.org/10.1016/j.apcatb.2019.118346>.
- J. Guilera, J.del Valle, **A. Alarcón**, J.A. Díaz, T. Andreu. Metal-oxide promoted Ni/Al₂O₃ as CO₂ methanation micro-size catalysts. *Journal of CO₂ Utilization* 30, (2019) 11-17. <https://doi.org/10.1016/j.jcou.2019.01.003>.
- **A. Alarcón**, J. Guilera, T. Andreu. Optimization of nickel and ceria catalyst content for synthetic natural gas production through CO₂ methanation. *Fuel Processing Technology* 193, (2019) 114-122. <https://doi.org/10.1016/j.fuproc.2019.05.008>.
- **A. Alarcón**, J. Guilera, T. Andreu. CO₂ conversion to synthetic natural gas: reactor design over Ni–Ce/Al₂O₃ catalyst. *Chemical Engineering Research and Design* 140, (2018) 155-165. <https://doi.org/10.1016/j.cherd.2018.10.017>.

CONFERENCES

- **A. Alarcón**. Synthetic natural gas production through CO₂ methanation process. Presented at 7th Jornada d'investigadors Predoctorals Interdisciplinària (JIPI). (2019). Barcelona, Spain.
- **A. Alarcón**, J. Guilera, T. Andreu. High activity, stability and tolerance to H₂S impurities by means of CeO₂ as a promoter in CO₂ methanation. Presented at SECAT. (2019). Cordoba, Spain.

- J. Guilera, **A. Alarcón**, J.H. Badia, T. Andreu. Optimal catalyst formulation and scale-up for their use in CO₂ methanation micro-reactors. Presented at 3rd Adding value to CO₂. (2019). Madrid, Spain.
- T. Andreu, J. Guilera, M. Biset-Peiró, **A. Alarcón**, J.R. Morante. Nanocatalysts for the sustainable production of synthetic fuels. Presented at 3rd Adding value to CO₂. (2019). Madrid, Spain.
- T. Andreu, J. Guilera, **A. Alarcón**, M. Biset-Peiró. Structured catalysts for synthetic natural gas production through CO₂ methanation. Presented at International Congress of Nanoscience and Nanotechnology. (2019). Quito, Ecuador.